The Effect of Thermal Aging and Boiling Water Reactor Environment on Type 316L Stainless Steel Welds

By

Timothy R. Lucas

B.S.A.S.T., Nuclear Science 2004
Thomas Edison State College

M.S, Nuclear Science and Engineering 2008
Massachusetts Institute of Technology

SUBMITTED TO THE DEPARTMENT OF NUCLEAR SCIENCE AND ENGINEERING
IN PARTIAL FULFILLMENT OF THE REQUIREMENTS FOR THE DEGREE OF

DOCTOR OF PHILOSOPHY IN NUCLEAR SCIENCE AND ENGINEERING
AT THE
MASSACHUSETTS INSTITUTE OF TECHNOLOGY

MAY, 2011

Signature of Author _____
Timothy R. Lucas
Department of Nuclear Science and Engineering
May 20, 2011

Certified by _____
Ronald G. Ballinger
Professor of Nuclear Science and Engineering and Material Science and Engineering
Thesis Supervisor

Certified by _____
Bilge Yildiz
Professor of Nuclear Science and Engineering
Thesis Reader

Certified by _____
Hannu Hänninen
Professor of Engineering, Design and Production, Aalto University, Finland
Thesis Reader

Certified by _____
Mujid S. Kazimi
TEPCO Professor of Nuclear Engineering
Chair, Department Committee on Graduate Students

The Effect of Thermal Aging and Boiling Water Reactor Environment on Type 316L Stainless Steel Welds

By

Timothy R. Lucas

SUBMITTED TO THE DEPARTMENT OF NUCLEAR SCIENCE AND ENGINEERING
IN PARTIAL FULFILLMENT OF THE REQUIREMENTS FOR THE DEGREE OF

DOCTOR OF PHILOSOPHY IN NUCLEAR SCIENCE AND ENGINEERING
AT THE
MASSACHUSETTS INSTITUTE OF TECHNOLOGY

MAY, 2011

Abstract

The thermal aging and consequent embrittlement of materials are ongoing issues in cast stainless steels and duplex stainless steels. Spinodal decomposition is largely responsible for the well known "475°C" embrittlement that results in drastic reductions in ductility and toughness in these materials, and this process is operative also in welds of either cast or wrought stainless steels where δ-ferrite is present. While the embrittlement can occur after several hundred hours of aging at 475°C, the process is also operative at lower temperatures, at the 288°C operating temperature of a boiling water reactor (BWR) for example, where ductility reductions have been observed after several tens of thousands of hours. An experimental study has been completed in order to understand how the spinodal decomposition may affect material properties changes in BWR pipe weld metals as well as the effects of the BWR environment on Type 316L stainless steel welds. This thesis also represents the first systematic and rigorous investigation of environmental fracture. In addition, weld metal centerline SCC crack growth rate has been quantified.

Material characterization includes SCC crack growth, in-situ fracture toughness, fracture toughness in air, as well as Charpy-V and tensile property evaluation as a function of aging time and temperature. SCC crack growth rate results in BWR normal water chemistry indicate an approximately 2X increase in crack growth rate over that of the unaged material. In-situ fracture toughness measurements indicate that environmental exposure can result in a reduction of toughness by up to 40% over the corresponding at-temperature air values. This has been termed "environmental fracture" Detailed analyses of the results strongly suggest that spinodal decomposition is responsible for the degradation in properties measured ex-environment. SCC crack growth rate and fracture toughness have been linked to the microstructural features of the Type 316L weld metal. Analysis of the results also strongly suggests that the in-situ properties degradation is the result of hydrogen absorbed by the material during exposure to the high temperature aqueous environment.

Acknowledgements

I wish to thank Professor Ballinger for taking me in and providing me with a challenging topic. I would also like to thank Professor Bilge Yildiz who represents the highest level of academic intensity. Her sound advice, grounded in genuine interest in student success, helped me to overcome some very difficult obstacles while at MIT. Furthermore, she challenged me on many levels but gave the required support to help me realize a greater potential. Additionally, Professor Hannu Hänninen provided valuable insight and support for this thesis. I also provided him with probably some of the most atrocious writing he has ever seen, which he helpfully corrected, at least 6 times. He helped me with a very practical education on the subject matter of this thesis and always maintained a very jovial attitude. Additionally, he facilitated many of the analytical methods in this thesis. A very special thanks to Tapio Saukkonen, who provided most of the detailed and practically artistic SEM micrographs through out this thesis. I also appreciate Van Christie for his valuable additions with the SEM. Olga Todoschenko's contribution with the TDS measurements was also greatly appreciated.

This project would not have been possible without the generous funding provided by the Tokyo Electric Power company.

On a more personal note, I should express endearing gratitude to Katerina Lucas as she compelled me to reach the extreme of education. I would also like to extend my appreciation to Professor Luisa Chiesa from Tufts University for her moral support for the duration of my Ph.D. studies at MIT. My friend and colleague, Dustin Langewisch, deserves recognition for all of his help and support along the way. Finally, I should thank my lab mates, Jon Gibbs, Mike Short, Sara Ferry, Mike Dunlevy and Joe Hubley for making the lab a very entertaining place to work. Lauren Ayers, my undergraduate researcher and friend, was instrumental in the completion of this work. She performed a great deal of the grunt work throughout the thesis. I owe her special thanks for her persistence and tenacity which is matched only by her intellect and talent in the lab.

There is one final lady in my life without which I could not have made it through the program. She has housed me and provided me with unending entertainment and distraction. She will be my vehicle to a different life. She is the good sailing vessel Slick.

For my father, grandfather and great-grandfather,
all of whom served the nuclear industry in their own right.

Table of Contents

List of Figures

List of Tables

List of Abbreviations

1T-CT	One inch Thick - Compact Tension specimen
A	Austenite Solidification mode
AF	Austenite-Ferrite Solidification mode
BCC	Body Centered Cubic
BWR	Boiling Water Reactor
CANDU	Canadian Deuterium Uranium Rector
CEFM	Coupled Environmental Fracture Model
CSS	Cast Stainless Steel
DAC	Data Acquisition and Control
DCPD	Direct Current Potential Drop
DSS	Duplex Stainless Steel
E-beam	Electron Beam
EAC	Environmentally Assisted Cracking
ECCC	European Creep Collaborative Committee
EDX	Energy Dispersive X-ray analysis
EPRI	Electric Power Research Institute
F	Ferrite Solidification mode
FA	Ferrite-Austenite Solidification mode
FCC	Face Centered Cubic
FN	Ferrite Number
GMA	Gas Metal Arc
GTAW	Gas Tungsten Arc Welding
HAZ	Heat Affected Zone
HELP	Hydrogen Enhanced Localized Plasticity
HIC	Hydrogen-Induced Cracking
IG	Intergranular
IGSCC	Intergranular Stress Corrosion Cracking
K	Stress Intensity Factor
K_{IC}	Critical Stress Intensity
K_{ISCC}	Critical Stress Intensity Required for SCC
LSE	Lower Shelf Energy
MMA	Manual Metal Arc
NRC	Nuclear Regulatory Commission
POSAP	Position Sensitive Atom Probe
RCS	Reactor Coolant System
SAW	Submerged Arc Welding
SZW	Stretch Zone Width
TEM	Transmission Electron Microscope
TEPCO	Tokyo Electric Power Company
TG	Transgranular
TIG	Tungsten Inert Gas
TTT	Time-Temperature-Transition
WRC	Welding Research Council

List of Symbols

(A)	Activity of product of species A
(B)	Activity of product of species B
(H^+)	Activity of hydrogen
(H_2O)	Activity of water
A	Absorption fraction of hydrogen
a	Overall crack length
a	Number of reactants A
A_C	Area of cathodic region
a_s	Crack length increment per step
A_T	Total area
$A\gamma$	Area of the austenite outside the cathodic region
A_δ	Area of the δ-ferrite
B	L_δ to R_C ratio
b	Number of reactants B
b	Thickness of the test specimen
c	Concentration
C_0	Initial concentration in the crack volume
C_1	Concentration in the crack volume following one fatigue cycle
C_b	Oxygen concentration in the bulk
c_h	Length past the mouth of the actual crack
C_m	Mechanistic constant describing unknown differences in material
C_{MEM}	Material-electro-mechanical variable
Cr_{eq}	Chromium percent equivalent
D	Diffusion coefficient
d	Number of water molecules
D_T	Total diffusion constant
D_γ	Diffusion coefficient for hydrogen in austenite, in units of cm^2/s
D_δ	Diffusion coefficient for hydrogen in ferrite, in units of cm^2/s
$D_{\delta\gamma}$	Distance from δ-ferrite core to dendrite boundary
e	Reaction potential
e^-	Exchange electron or equivalent
e^0	Standard potential
E_d	Difference between anode and cathode potentials
e_N	Potential after N cycles of fatigue
F	Faraday's constant, 96,500 coulombs per electron
f_γ	Volume fraction of austenite
f_δ	Volume fraction of ferrite.
G	Gibbs free energy
G_{Ox}	Molecular weight of the oxide
h	Actual crack length
I	Total current
i_C	Corrosion current
J_{IC}	Point of fracture toughness J_{IC}
K_I	Stress intensity factor

K_{IC}	Critical stress intensity
L_δ	Secondary dendrite arms length
M	Any metal species
m	Load line displacement
m_0	Actual crack mouth displacement
M_f	Mixing fraction
N	Number of fatigue cycles
N	Axis normal to the weld direction
n	Factor accounting for the number of triangles in a sample
n	Number of electrons exchanged
N_A	Avogadro's number
N_{H2}	Number of H_2 molecules produced
Ni_{eq}	Nickel percent equivalent
P	Axis parallel to the weld direction
P_{max}	Maximum applied load
P_{min}	Minimum applied load
Q	Direction of thickness
Q_{Ox}	Number of moles of oxide
R	Gas constant
R_C	Cathodic radius
R_E	Electrolyte resistance
R_M	Material resistance
R-value	Loading ratio in fatigue
T	Temperature or Time
t_{Ox}	Thickness of the oxide layer
V_0	Volume of the crack interior
V_{Ox}	Volume of oxide
$V_{\gamma\perp}$	Crack growth rate of the austenite in the perpendicular direction
V_δ	Crack growth rate of the δ-ferrite phase boundary
W_δ	Secondary dendrite arms width
X	Length on one side of dendrite cell
α	Area fraction
α	Iron-rich alpha phase
α'	Chromium-rich phase
α_C	Area fraction of the austenite acting as the cathodic region
α_γ	Area fraction of the austenite outside the cathodic region
α_δ	Area fraction of the δ-ferrite
γ	Surface energy
γ	Austenite
δ	Delta-ferrite
Δm	Small change in load line displacement applied in fatigue
Δm_0	Small change in actual crack mouth displacement applied in fatigue
θ	Angle of austenite fracture
ρ_{Ox}	Density of the oxide
σ	Sigma phase
σ_{ys}	Yield Strength

1 Introduction

Currently there are about 442 nuclear reactors providing approximately 18% of the world's electricity. This only encompasses the civilian power production reactors as there are many more nuclear reactors for military and research use [1]. In this thesis, the primary concern relative to the nuclear industry will be to focus on environmentally assisted cracking (EAC) of stainless steel welds and the effects of thermal aging on this phenomenon at reactor operating temperatures, primarily in the boiling water reactor (BWR) environment. EAC in nuclear reactors is not a new phenomenon. It has been occurring and been a topic of study since the dawn of the nuclear era. With the nuclear industry, there has always been a need for safe operation. As a result, much effort has been spent to understand and combat EAC in nuclear reactors. In 1979, Shao and Burns compiled operational reactor experience with intergranular stress corrosion cracking (IGSCC). They found that from the inception of the commercial nuclear industry to the date of their study there were at least 133 incidents of IGSCC with the earliest observed cracking in weld heat affected zones (HAZ) occurring in 1965. They further noted that the first occurrence of IGSCC in large diameter piping, was in 1978 in a German BWR [2]. In Sweden, all four nuclear generation sites have experienced IGSCC problems in at least one of the numerous BWRs on each site [3]. In Taiwan, BWR-6 Nuclear Power Station Unit-1 routine inspection found 10 HAZs that had undergone IGSCC after just five operating cycles. Most of the cracking occurred in the recirculation loop. Most of these events were repaired by weld overlay, and then had stress relief techniques applied [4].

As recently as just the last ten years three events in the US nuclear fleet have been attributed to stress corrosion cracking (SCC), a material process described in chapter 2, in piping. The following EAC events occurred in nickel-based alloys, such as Alloy 600, and the nickel weld metals Alloy 82 and 182, however, and are included for demonstrative purposes. In October 2000, the V.C. Summer nuclear power station found SCC in various welds in the reactor coolant system. The first weld between the nozzle and the reactor coolant system (RCS) hot leg was found to contain a small through wall crack allowing slight leakage of primary coolant. In October 2006, five different circumferential SCC cracks were found in the pressurizer system of the Wolf Creek Generating Station [5]. Finally, as recently as November 2010, a weld flaw at the Duane Arnold Energy Center in Iowa led to indications of SCC that had penetrated 70% through an RCS pipe wall weld. In the case of Duane Arnold, the weld was repairable by overlaying a new weld [6]. However, the weld cracking at V.C. Summer and Wolf Creek stations brought on industry wide evaluations and inspections of existing nickel-based alloy welds. Furthermore, the fact that there was, in the case of Wolf Creek, 5 individual cracking in one system caused the Nuclear Regulatory Commission (NRC) to call into question original structural integrity evaluations based on the known aging effects of nickel-based alloy welds [5]. SCC is not just limited to light water reactors, heavy water reactors such as Canadian Deuterium Uranium Rectors (CANDU) also have a history of environmental degradation. In 2008, Tapping reported on the ability of providing life extensions to the existing CANDU fleet as well as stressing proper design for future

reactors to engineer maximum corrosion resistance [7]. The research reactor at Chalk River in Canada developed a heavy water leak from the reactor vessel which contained high levels of tritium and lost the production ability of medical isotopes for some time [8]. In addition, the increased regulation, inspection and repair of welds will require increased expenditure as the existing reactor fleet ages.

Stainless steels are a favored material for nuclear and other industrial applications because they have a high degree of corrosion and environmental resistance, are easily formed and welded and have sufficient strength and toughness for a wide range of applications. Welding of stainless steels is a very common joining technique. In the case of nuclear reactors it is the most common method for joining permanent piping as it requires no flange or seal thus providing a continuation of the RCS boundary with no component to fail. The advantages of welding are in the ease of shaping, efficacy and cost, as well as the overall strength. The disadvantage of welds is that they require technical skill in order to implement correctly, and while better than a flange and seal, they are metallurgically different from the surrounding material, which can lead to EAC. Furthermore, little is known about the effects of long-term aging on stainless steel welds. There are literally thousands of welds in a nuclear power plant. They range in shape from small seal welds that may be only a single pass, to multiple pass welds butt-welding piping together. For the interest of this study, one weld type will be of primary interest – the Type 316L recirculation pipe multi-pass butt-weld found in many non-US BWRs.

The welding techniques require that a specified amount of delta (δ)-ferrite be present in the weld metal to prevent hot cracking. While the elimination of hot cracking is essential for a sound weld, the δ-ferrite can be unstable with respect to spinodal decomposition into an iron-rich α phase and a chromium-rich α' phase. Spinodal decomposition is largely responsible for the well known "475°C" embrittlement that results in drastic reductions in ductility and toughness in cast stainless steel [9]. Additionally, the process is operative in welds in either cast or wrought stainless steels where δ-ferrite is present. While the embrittlement can occur after several hundred hours of aging at 475°C, the process is also operative at lower temperatures, at the 300°C operating temperature of a boiling water reactor for example, where ductility reductions have been observed after several tens of thousands of hours. If one considers that the BWR piping design life is at least 40 years the possibility of ductility reduction in stainless steel welds cannot be overlooked. In addition to spinodal decomposition, sensitization and segregation will also be considered as aging mechanism.

BWR piping systems are constructed using stainless steels of several varieties, including wrought types 304, 304L, 316, 316L and cast versions with similar chemistries. Welds for these materials are typically made using electrodes of either the same composition or other chemistries such as type 308. The amount of δ-ferrite in a weld is a function of the ratio between the nickel equivalent (the higher the nickel equivalent the lower the amount of δ-ferrite for a given chromium equivalent) and the chromium equivalent. The higher the chromium equivalent the higher the amount of δ-ferrite for a given nickel equivalent.

In addition to the potential of weld embrittlement due to spinodal decomposition of δ-ferrite, there is little data available on the effect of long term aging on the crack growth behavior of stainless steel welds, which have suffered mechanical properties degradation, in high temperature aqueous environments typical of those that exist in BWR systems. There is thus a concern that current data base may not be conservative.

The BWR environment brings a great challenge to the weld. They must operate in a hostile environment, provide a high pressure boundary, function at elevated temperatures as well as undergo continuous operations for the current required life of 40 years, and possibly longer. Future reactor designs will be commissioned with an expected life time of 60 or even 80 years. Considering that the typical BWR operates at 288°C, then during the life of the weld, it will thermally age for up to 350,000 h. This gives plenty of time for SCC to occur in an already susceptible material and an aggressive environment. During this time it will undergo a wide range of phenomena, such as spinodal decomposition, stress relaxation, nucleation and growth, etc, that will affect the material properties of the weld. By the end of life, the weld, while fundamentally still the same material, will have a different strength, toughness, hardness, and resistance to fracture and SCC crack growth than at the beginning of life. Furthermore, the evolution of properties in the weld is complex. As will be shown in this study, some of these properties reach equilibrium, and some will reach a peak value and then fall off. In any case, understanding the nature of the evolution will be of great benefit to reactor design for elucidation of the material capabilities of welds throughout the life of a reactor.

Considering that the US has not started building a new reactor since 1979 and has not completed one since 1996 [10], the reactor fleet in this country is aging. Globally, there are about 80 reactors that have been in operation for more than 30 years, and 250 for more than 20 years. The initial expected lifetime for the reactors was typically 40 years. It is unlikely that these reactors will be shutdown if they can procure license extension. Additionally, there is little in the way of large scale energy production that can take their place until new reactors can be built. Thermal aging of welds has an impact on the re-licensing of the current reactor fleet. Sufficient data must be collected and analyzed relative to the current generation. While this thesis will not propose a decision in terms of plant life extension, the results will add to the current data universe that exists and will provide some insight into the changes of material properties. The material changes directly affect the functionality of a component at the expected normal loading, as well as the peak transient loading. Additionally, welds may be subject to cyclic loading, such as from pump vibrations, pressure induced shockwaves due to boiling, long-term cycling by plant heat-up and cool-down, or even large load cycling from external events such as earthquakes. Furthermore, it is conceivable that the shock loading during extreme accident scenarios could also be a major factor in weld failure. For any given reactor there is an operating history that is unique to that station. Along with the unique operating history are many plant specifics that can affect both the loading and aging of the weld system.

The preceding few pages should serve to put into context the importance of understanding the weld system and the aging effects that occur due to operating for an

extended period of time in the BWR environment. For the remainder of this thesis, there will be very little discussion related to the nuclear industry as a whole. The effort will focus on the performance of welds that are prototypical of those found in BWRs.

As a final note, there are several contributions through out this thesis. The key contributions are listed below:

- Evaluated SCC crack growth behavior of Type 316L welds as a function of weld ferrite content and thermal aging.
  - Connected SCC crack growth rate to the weld microstructure via optical and SEM analysis.
  - Established the likelihood that diffusible hydrogen generated at the crack tip is responsible for the SCC crack growth when exposed to the LWR environment.
  - Identified previously unrecognized phenomenon of Fatigue/SCC oxide precipitation difference.
  - Provided a geometrical correlation linking FN to SCC growth rates for the FA solidification mode.
- Explored in a systematic way for the first time the phenomena of "Environmental Fracture" in LWR environments
  - Established the likelihood that diffusible hydrogen generated at the crack tip is responsible for the reduction in toughness when exposed to the LWR environment.
  - Provided evidence that sufficient hydrogen can be produced and diffuse into the bulk material matrix to cause noted effects.
  - Identified previously undocumented brittle fracture occurring prior to the onset of crack blunting during in-situ fracture toughness testing.
- Expanded the data universe in reference to time, temperature, and ferrite number for thermal aging, utilizing high quality Alloy 316L welds, exactly duplicating those found in a BWR.

2 Background

In the primary environment of a nuclear reactor a high degree of cleanliness and purity must be maintained. Considering that the nuclear process inherently creates sources of radioactivity through activation and transmutation, it is desirable to keep the primary coolant free of any unnecessary chemical components. Furthermore, the primary boundary material itself must be chosen such that it is resistant to the primary coolant environment. The chosen material must be strong and tough enough to handle the pressures and temperatures that are found in a nuclear reactor. The material must be able to withstand radiation damage as well as be resistant to corrosion. Furthermore, the material must be able to be formed, machined and welded using approved methods. The material must be able to meet all of the above criteria while still economical. Of the metals that meet the above criteria, the most common materials used in primary coolant boundaries outside the steam generator are indeed stainless steels. In the United States, Type 304 is used extensively, while many reactors abroad use Type 316L. It is the second alloy that will be the focus of the study.

In order to join the stainless steels used in the pressure boundary, the main method employed is through gas tungsten arc welding (GTAW). Briefly, this method employs a tungsten welding tip that is moved at a given rate with an applied current. The electric arc produces a molten pool of filler metal, called the weld bead, which is led along by moving the welding tip. The entire process is covered with a gas blanket to prevent contamination by air. This method will be described in greater detail below. In addition, stainless steel and welding chemistry, solidification process, and the effects of aging will be discussed. Also, a brief synopsis of previous major stainless steel weld aging studies and results will be given.

2.1 Weld Definitions

Prior to any meaningful discussion on the metallurgy of welding, and in order to maintain consistency through out this study it is important to define a weld standard geometry as well as give some standard definitions. To accomplish this, recommendations by the *European Creep Collaborative Committee* (ECCC) [11] will be adopted. In describing the geometry, a Cartesian coordinate system is chosen with the axis as N, P, and Q. Figure 2-1 gives an illustration, where the axis are defined as:

- N is the axis normal to the weld direction described as + in the direction of lateral weld tip movement.
- P is the axis parallel to the weld direction, with + defined as the direction of weld tip movement.
- Q is the direction of thickness, with the + direction being defined as the part of the weld that is laid down first outward, or the inside of the pipe moving to the outside.

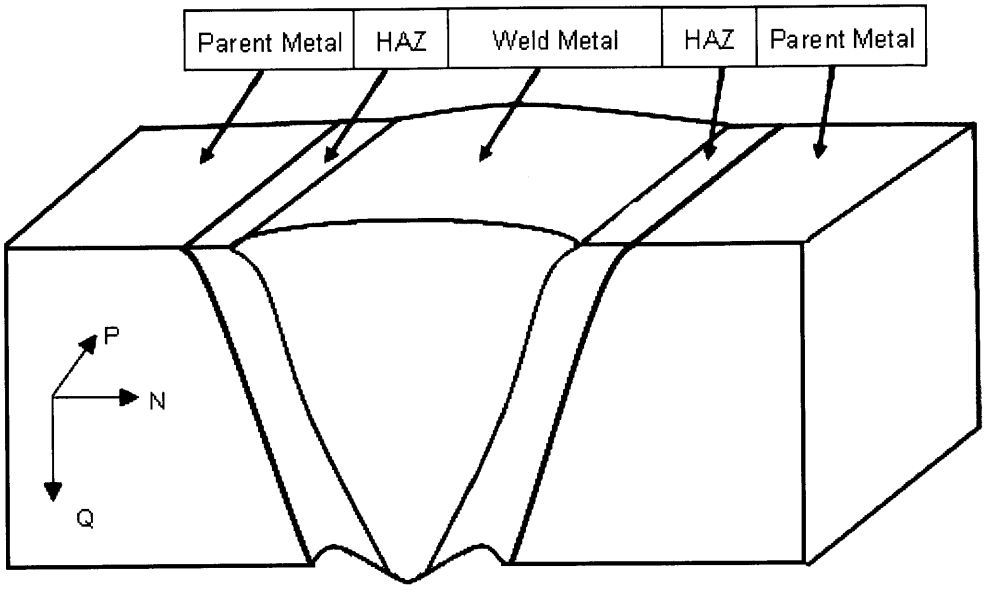

Figure 2-1 Visualization of weld geometry axis.

Furthermore it is important to note that the principle stress direction of interest in the manufacture of butt-welded piping for this study is the N axis. Hoop stresses would be along the P axis. Considering that the geometry of interest is a pipe, one might think that a cylindrical geometry is a better choice, however, the assumption is made that over the samples the radial change is negligible. Further definitions of interest are:

- Deposited Filler: filler metal that is used for the weldment.
- Fusion Line: the boundary between the parent metal and the weld metal.
- Heat Affected Zone: parent metal material that is not melted but is altered due to the welding process.
- Parent metal: the metals that are joined by welding, in the case of this study Type 316L.
- Weld Metal: the material that is both melted and retained in the construction of the weld, the weld metal is contained in the fusion zone, made up of deposited filler and melted parent material.
- Weldment: a joint between two parent metals containing both deposited filler metal and the heat affected zone.

2.2 Welding Process

Joining metals through a localized melting and resolidification with added filler metal is generally known as fusion welding. According to Lancaster, fusion welding using electrodes first dates from the late 19th century [12]. Fusion welding was a common technique for stove pipe construction beginning in the 1920's. The first implementation of fusion welding on large scale construction was performed during World War II in support of ship construction. Following the technological advances gained during the war years, welding advanced quickly and today there are over 150 different fusion joining

processes. This section will review GTAW which commonly used for stainless steels. GTAW, like many other welding methods, employs a movable welding tip, an applied filler metal, and is electrically driven, that is GTAW contains an anode and a cathode and the heat is controlled and delivered by electric current. [12]

2.2.1 Gas Tungsten Arc Welding

Previously known as tungsten inert gas (TIG) welding, GTAW is the most common method for joining stainless steels. It is also used for a wide range of other materials including challenging metals such as copper or aluminum which are difficult to weld due to their high heat conductance. A shielding gas is used in order to keep the weld pool oxygen free and to prevent the impurities in air from contaminating the weld pool. The cover gas is traditionally an inert gas such as argon, nitrogen, helium or a mixture thereof. However, for some applications hydrogen (not inert, thus the name change from TIG to GTAW) mixtures may be employed. GTAW normally applies current in DC, however for some specialized applications such as aluminum, AC is used. For high purity, low porosity welds, such as in Type 316L for nuclear applications, the electrode is the anode and the parent metal the cathode. Electrodes are made with tungsten and stabilized typically with thorium. For long life applications, the electrode is further stabilized with cerium, lanthanum, or yttrium. These elements increase the electrode life by reducing the work function, or the amount of energy to free an electron from the surface, and increasing the emissivity of the electrode. Cooling of the tungsten is also increased due to the increase in emissivity and this reduces tip melting, which prevents inclusions in the weld from deposition of the melted electrode in the weld. Weld metals tend to contain other contaminates as well. Sulfur is an impurity in the base and filler metals. Even with a shielding cover gas, there is still a chance for oxidation to occur in the weld pool due to the circulation of the cover gas jet emitting from the electrode-surrounding-nozzle. However, both oxygen and sulfur are needed in some amount to create proper penetration and wetting of the weld. Furthermore, manganese is also present to combine with the sulfur. The importance of removing these two contaminates is that it allows the weld metal to behave as a pure metal and to convectively cool in a uniform radial heat flux. Additionally, too much sulfur can lead to hot cracking. Oxide inclusions in the weld pool can form localized floating anodic spots that can distort the heat flux profile, consequently changing the shape of the fusion zone. GTAW is chosen as the main welding method in the nuclear industry due to the several advantages it allows: 1) by using a cover gas and no flux, the welds can be formed with a lower contamination rate, low amount of inclusions and low porosity compared to other welds; 2) the ease of the process lends itself to automation, especially helpful for pipe welds (known as orbital welding); 3) tungsten electrode life allows for long continuous welds; 4) because current is applied via a separate electrode, filler chemistry can be customized to each material and desired solidification mode. The major disadvantage of GTAW is the low filler deposition rate, resulting in a slow welding process. However, the cleanliness and predictability of the resulting weld make this the ideal candidate for the nuclear industry, and indeed any industry that requires high quality and high purity, such as the pharmaceutical and medical industries. [12]

2.3 Type 316L Stainless Steel

Type 316L stainless steel is a ternary alloy of the iron-nickel-chromium system. It is important to understand the role of the different weld filler metal alloying elements to fully understand the modes of weld solidification. Furthermore, many of the alloying elements, while small in concentration, will play a big role in the susceptibility to SCC and fracture [13,14]. Much of the material property characterization is controlled not by the iron-nickel-chrome base but by the purposeful addition of alloying elements and the incidence of impurities.

Figures 2-2 shows the pseudo-binary phase diagram for the iron-nickel-chromium system. Considering that each alloying element is a promoter of either austenite or ferrite solidification modes, they will be expressed in terms of chromium or nickel percent equivalent (Cr_{eq} or Ni_{eq}).

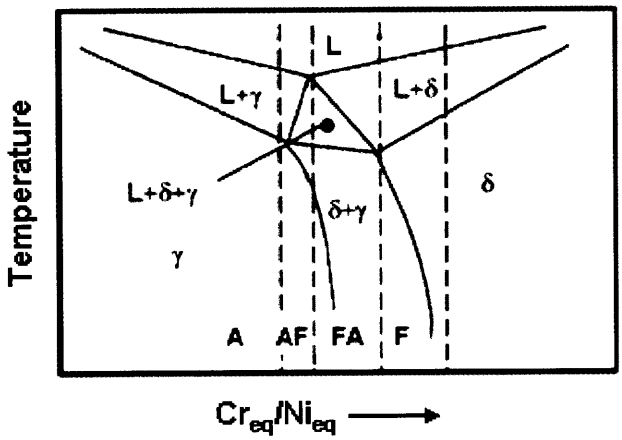

Figure 2-2 Iron-Nickel-Chromium pseudo-binary phase diagram, showing different weld solidification modes [9].

2.3.1 Chromium

Aside from the balance of iron, the next most abundant element in Type 316L stainless steel is chromium. The principle reason for the addition of chromium is for corrosion resistance. Oxides formed with chromium are both faster forming and more stable than those formed with iron alone. A normal definition of stainless steel is when the chromium content is above 13%. However, just 8% is required to form a protective passivation layer. Aside from the obvious advantage of corrosion resistance, chromium also is a substitution atom for iron and so provides some solid solution strengthening. Two drawbacks of chromium however are the readiness of forming carbides and the formation of embrittling phases in steels. Chromium typically forms $M_{23}C_6$ chromium-rich carbides in the presence of carbon. Chromium is also the main promoter in the formation of sigma (σ) phase in the iron-nickel-chromium system. Chromium is a ferrite promoter.

2.3.2 Nickel

In the ternary iron-nickel-chromium system nickel acts as an austenite promoter. In the iron-chromium system, above approximately 13% chromium the alloy will be a stainless steel and almost always be stable as a body centered cubic (BCC) ferrite at temperatures of 800°C and above. However, with additions of enough nickel, austenite can become a stable phase in any temperature below solidification. The nature of the austenite/ferrite relationship will become clear later. Nickel is neither a carbide former nor a promoter of intermetallic phases but is a solid solution strengthener.

2.3.3 Molybdenum

The addition of molybdenum is primarily what distinguishes between Type 304 and Type 316. In Type 316L the primary purpose of molybdenum is two fold, it increases corrosion resistance and increases strength and creep resistance at high temperatures. In the case of welds, it also serves as a stabilizer for ferrite and will promote formation and retention of ferrite upon solidification.

2.3.4 Manganese

The primary function of manganese is to scavenge sulfur. Without manganese, iron and sulfur will form sulfides that can lead to hot cracking. Manganese and sulfur combine, and are stable, at a relatively high temperature compared to the solidification of the alloy, thus the sulfur gets removed from the system in the form of manganese sulfide (MnS). These are ultimately manifested as inclusions in austenite, MnS inclusions are recognizable by their nearly perfect spheroidal shape in the weld metal. Manganese is an austenite promoter and stabilizer. It is particularly helpful in preventing martensitic transformation of austenite, but the effect is greatly dependant on the nickel concentration found in the alloy system.

2.3.5 Silicon

Silicon addition to stainless steels can have several deleterious effects including the formation of embrittling iron-silicides, the formation of σ-phase, and low-melting eutectics with nickel. However, silicon is necessary in welds for two reasons, it acts as the principle scavenger of oxygen (along with trace amounts of aluminum) and it decreases the viscosity of the weld pool, improving fluidity and wetting. Silicon is neutral in the formation of ferrite or austenite.

2.3.6 Carbon

In Type 316L, the L stands for low-carbon. Carbon is an austenite promoter, it also greatly reduces corrosion resistance through the formation of $M_{23}C_6$ carbides, where chromium can be removed. As Lippold points out, consider that there are nearly 4 times as many metal atoms as carbon atoms in $M_{23}C_6$, and the weight of chromium, the main element making up the $M_{23}C_6$, is about 4 times as heavy as a carbon atom, then one carbon atom removes 16 times as much chromium based on weight percent [9].

2.3.7 Sulfur

The addition of sulfur in stainless steels is principally to increase machinability. However, sulfur has many deleterious effects. Fortunately, with the addition of manganese, as well as proper control of the solidification process, most of the problems with sulfur are negated.

It is important to understand which alloying elements are promoters of austenite or ferrite in order to understand the solidification kinetics and the resulting, controlling, microstructure. Table 2-1 summarizes the role of each alloying element in terms of promoting austenite, ferrite, or neither.

Table 2-1 Solidification mode promoted by alloying elements in the Type 316L weld system.

Alloying Element	Promotes
Chromium	Ferrite
Nickel	Austenite
Molybdenum	Ferrite
Manganese	Austenite
Silicon	Neutral
Carbon	Austenite
Sulfur	Neutral
Copper	Austenite

2.3.8 Other Impurities

Two elements present in quantities of significance are copper and phosphorus. Copper promotes austenite and serves to precipitation harden the steel. Phosphorus is present only as an impurity and serves no purpose [9].

2.4 Weld Solidification Modes

The composition of alloying elements in Type 316L weld filler material lies at the intersection of four possible solidification mechanisms for the ultimate stable microstructure of the weld. Figure 2-2 shows the region of interest in the pseudo-binary phase diagram for the iron-nickel-chromium system. The solidification process leads to several endpoint microstructures and morphologies based on the initial chemistry as well as the cooling kinetics, controlled by weld tip speed as well as interpass temperature [15]. The discussion that follows describes efforts to predict and obtain the desired microstructure as well as what that microstructure will look like. In Figure 2-2, there are four modes of solidification identified: fully austenite (A); austenite-ferrite (AF); ferrite-austenite (FA); and purely ferrite (F). Each mode has a unique path to arrive at the final unique microstructure. In the case of Type 316L welding, FA is the desired solidification

path as it produces the most tortuous microstructure, and thus is most resistive to solidification cracking, compared to other solidification modes as will be discussed below.

2.4.1 Constitutional Diagrams

The first problem to be overcome in controlling the ultimate microstructure is to identify the equivalent chromium and nickel percentages. This is done through the use of formulas for plotting on the various constitution diagrams such as the Schaeffler, DeLong or WRC diagrams. Once the equivalents are known, it is merely a matter of locating them on the respective diagrams.

Schaeffler was the first to give a predictive diagram for welding of stainless steels in 1947 [16]. This was later followed by DeLong in 1956, who focused primarily on the 300 series of stainless steels [17]. DeLong and Long produced an updated version of the DeLong diagram in 1973 that took nitrogen content into account [18]. Finally in 1988 the Welding Research Council (WRC) produced the WRC-1988 diagram quickly followed by the WRC-1992 diagram [19]. The Schaeffler, DeLong and WRC-1992 diagrams are in Figures 2-3 through 2-5, respectively. Each has their own method of calculating the chromium and nickel equivalency, based on weighting of the elemental composition of the alloy and whether it is a ferrite or austenite promoter [19]. For a complete historical recounting of the evolution of these diagrams, please see a welding reference such as [9].

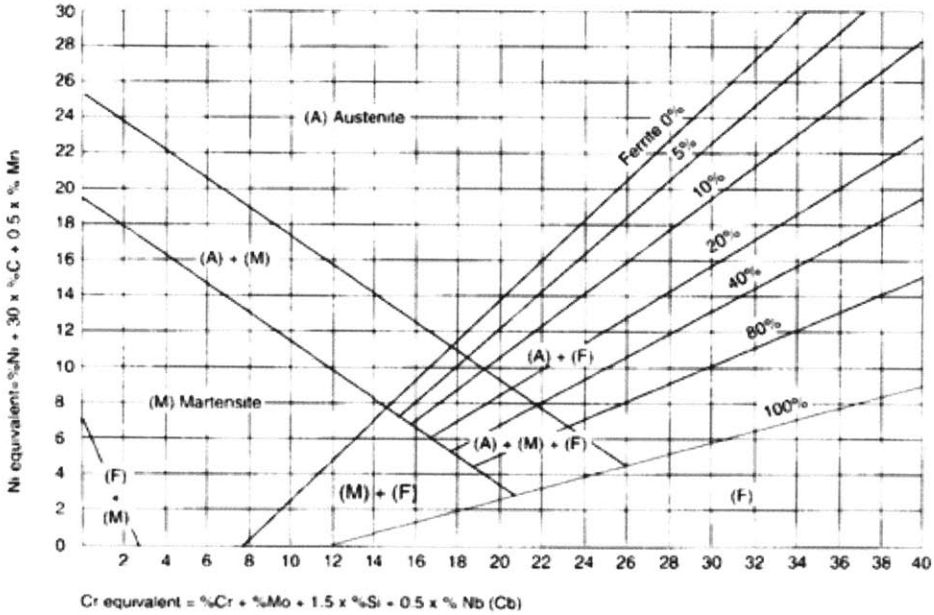

Figure 2-3 Schaeffler constitutional diagram [16].

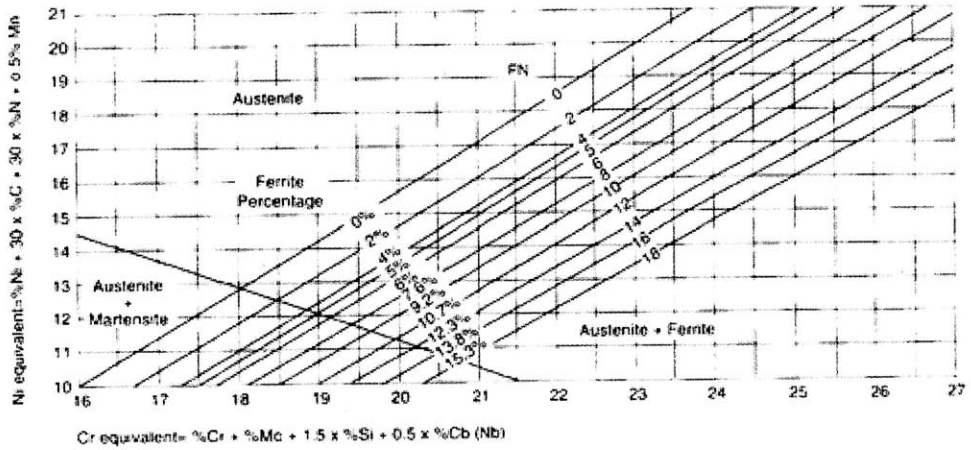

Figure 2-4 DeLong constitutional diagram [18].

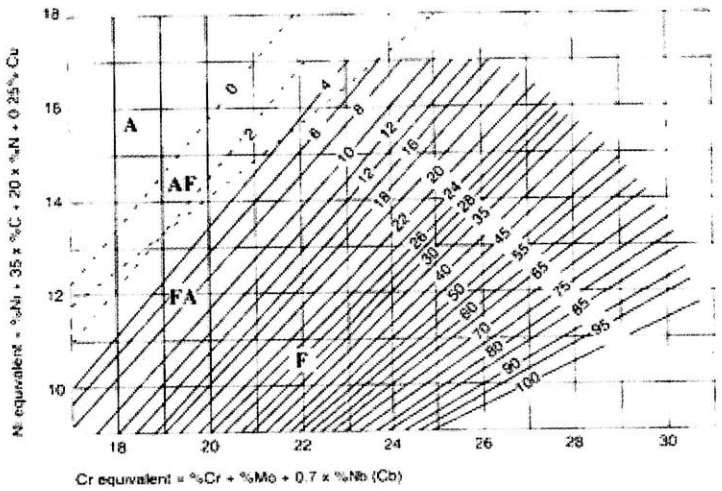

A, AF, FA,F stand for solidification modes
A : Austenitic single phase (γ)
AF : Primary phase (γ) + Eutectic Ferrite (δ)
FA : Primary phase (δ) + Peritectic / Eutectic phase (γ)
F : δ Single phase Solidification

Figure 2-5 WRC-92 constitutional diagram [19].

In order to evaluate the nickel and chromium equivalence, Schaeffler proposed the following equations:

$$Ni_{eq} = Ni + 0.5Mn + 30C \qquad [2\text{-}1]$$

$$Cr_{eq} = Cr + 2.5Si + 1.8Mo + 2Nb \qquad [2\text{-}2]$$

While Long and Delong use:

$$Ni_{eq} = Ni + 0.5Mn + 30C + 30N \qquad [2\text{-}1]$$

$$Cr_{eq} = Cr + Mo + 1.5Si + 0.5Nb \quad [2\text{-}2]$$

While the WRC uses:

$$Ni_{eq} = Ni + 35C + 0.25Cu \quad [2\text{-}3]$$

$$Cr_{eq} = Cr + Mo + 0.7Nb \quad [2\text{-}4]$$

2.4.2 Solidification Modes

As mentioned above, based on the chemistry there are four unique solidification modes that can result from the welding process of stainless steels. The solidification modes lead directly to unique microstructures. As shown above, it is possible to predict the solidification mode before hand. However, due to local variations in cooling rates and mixing with parent material, other solidification mechanisms are possible. The modes and resulting microstructures will be described below. In all cases the solidification takes place in a dendritic nature due to the rather slow rate of cooling. Furthermore, it is energetically favorable for the dendrites to grow along the <100> direction. This results in a nearly uniform crystallographic material. A summary of the process is shown in Table 4. Schematic and example microstructures are shown in Figures 2-6 and 2-7, respectively.

Fully austenitic solidification, known as mode "A" is when the liquid solidifies as primary austenite. There is no ferrite present at any time. The solidification structure is dendritic with a cellular structure. Segregation occurs during solidification which results in impurities and alloying elements being trapped at the dendrite boundaries, leading to the cellular appearance. In mode A solidification, there can be low melting point liquids that become trapped along the straight dendrites. This can lead to solidification cracking. Furthermore, the straight dendrite boundary has a higher wettability, aiding in liquid entrapment. [9]

The next form of solidification, "AF" or austenitic-ferritic solidification is slightly more complicated. When type A solidification is occurring, some ferrite promoting elements are rejected by the austenite and pushed to the dendritic boundaries in some concentration. When the concentration becomes high enough, these ferrite promoters cause the formation of ferrite. This ferrite is stable at room temperature due to the concentration of ferrite promoters and does not undergo a ferrite-austenite transformation. In this case, the ferrite, is formed from a eutectic and is manifested in an interdendritic or intercellular structure. [15]

The most complicated, yet most desirable solidification mode is the ferritic-austenitic mode, mode "FA". FA first solidifies as primary δ-ferrite, with a peritectic-eutectic reaction forming the initial austenite at the end of the solidification process. This reaction occurs in the region marked FA in Figure 2-2. When the solidification process is

complete and there is no more liquid, there is trapped austenite in between the δ-ferrite dendrites. As the weld bead cools, the δ-ferrite becomes unstable and transforms to austenite leaving only δ-ferrite at the core of the dendrite. The resulting structure can be either lathy or skeletal depending on the cooling rate. For a high cooling rate a lathy δ-ferrite morphology is present. When the cooling rate is low, a more skeletal type of δ-ferrite microstructure is noted. This microstructure is also referred to as vermicular. Finally, the interspacing of the secondary skeletal and dendrite arms is a function of the rate of cooling. The FA solidification mode provides the most beneficial microstructure for welds as it creates the most tortuous path for solidification cracking. Furthermore, the nature of the kinetics limits the surface wettability and low-melting temperature phases. This is the solidification mode that will be studied for the remainder of the study. [15]

The final solidification mode as the Cr_{eq}/Ni_{eq} is increased is the type "F" or fully ferritic solidification mode. When there are not enough austenite promoters, the solidification mode shifts from FA to solely F. Following complete solidification, the dendrite structure starts to cool, and the δ-ferrite loses stability and undergoes transformation to austenite starting from the dendrite boundaries. The degree of transformation depends ultimately on the Cr_{eq}/Ni_{eq} as well as the cooling rate. A low cooling rate and low Cr_{eq}/Ni_{eq} result in an acicular structure, while a higher cooling rate results in less diffusion from the δ-ferrite to the austenite, leading to larger δ-ferrite grains and keeping the austenite trapped at the grain boundaries. This structure is known as the Widmanstätten structure. These types of microstructures are rare in austenitic stainless steels due to the high Cr_{eq}/Ni_{eq} ratios required; they are more common to duplex stainless steels. [15]

Table 2-2 Solidification path of different solidification modes [15].

Solidification Mode	Solidification Sequence	Solid-State Transformation	Resulting Morphology
A	$L \rightarrow (L + A_P) \rightarrow A$	None	Cellular Dendritic A Cellular A
AF	$L \rightarrow (L + A_P) \rightarrow (L + A_P + F_E) \rightarrow (A_P + F_E)$	$F_E \rightarrow A_T$	Interdendritic F Intercellular F
FA	$L \rightarrow (L + F_P) \rightarrow (L + F_P + A_E) \rightarrow (F_P + A_E)$	$F_P \rightarrow A_T$	Intercellular A Vermicular F Lacy F Blocky F
F	$L \rightarrow (L + F_P) \rightarrow F_P$	$F_P \rightarrow A_w$ $F_P \rightarrow A_T$	Widmanstätten A Massive A Cellular F

Symbol	Meaning
L	Liquid
F	Ferrite
A	Austenite
P	Primary
E	Eutectic
T	Transformed
W	Widmanstätten

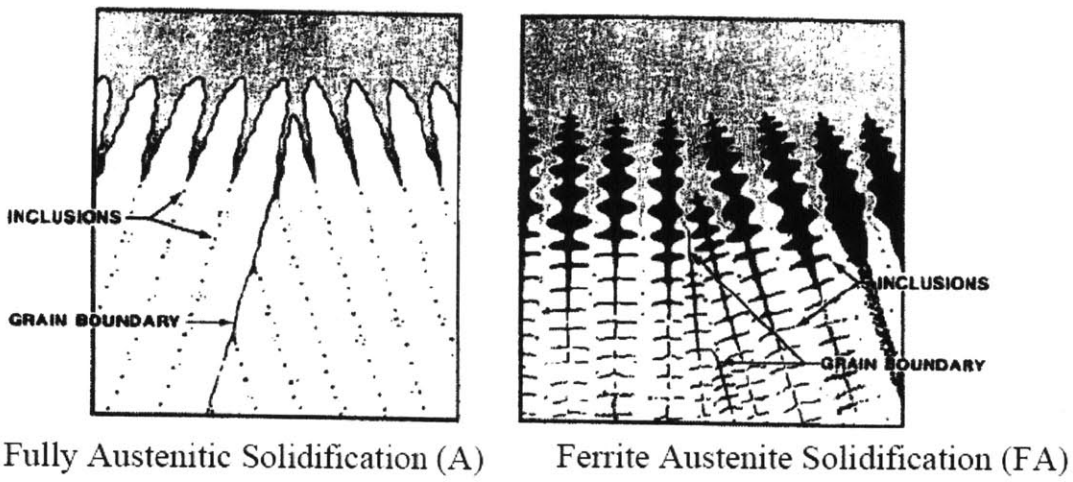

Figure 2-6 Schematic of solidification modes A and FA [9].

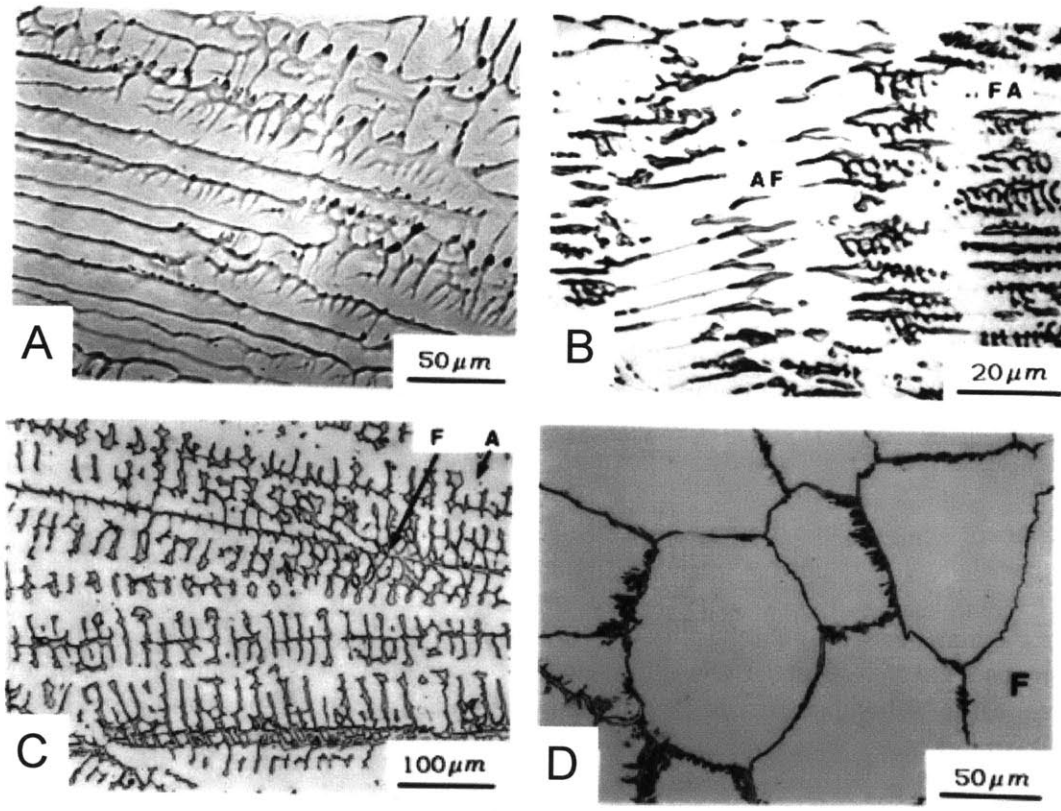

Figure 2-7 Solidification mode microstructure, A - Type A, B - Type AF, C – Type FA, D - Type F [15].

The FA mode of solidification is the normal mode for welding in nuclear power plants. In fact it is required by nuclear construction codes that at least 5% δ-ferrite be present. The actual resulting dendritic structure of the welds for this study will be shown in the next

chapter, however, at this point it is beneficial to discuss the implications of δ-ferrite in the microstructure. As already stated, the δ-ferrite is present to prevent hot cracking. The welds used for nuclear service have to maintain their integrity for the life of the plant. Austenite is known to be stable for long aging periods. Unfortunately, δ-ferrite is known to be susceptible to multiple aging mechanisms that ultimately can result in embrittlement. Spinodal decomposition, a process where the δ-ferrite beneath the solubility curve undergoes a kinetic process to form a chromium-rich, iron-depleted α' phase and a chromium-depleted, iron-rich α phase. In addition there is the possibility of the formation, precipitation and growth of the chromium-rich σ-phase, which is also known as an embrittling agent as well as a cause for local corrosion. Finally, the austenite is an FCC structure while the δ-ferrite is a BCC structure, so there is an inherent mismatch that will lead to grain boundary mismatches and residual micro-stresses. The entire weld system contains a great deal of residual stress, which can be up to the yield point of the material [20]. It is normally of great benefit to stress relieve welds as the residual stresses can lead to increasing susceptibility to cracking and have an impact on both tensile strength and toughness. However, as will be evident from the time-temperature-transition (TTT) diagram in Figure 3-3, heating the welds to a temperature where stress relief could occur would lead to the formation of σ-phase, the impact of which would likely be worse than the initial residual stress state. The residual stress combined with the possible kinetics of δ-ferrite aging lead to a very challenging aging problem for the nuclear fleet. What is known is that in general, as stainless steel welds age, the microstructural changes lead to an increase in hardness and tensile strength and a decrease in Charpy-V toughness [20]. However, there is very little data available for Type 316L welds in piping aged at reactor operating temperatures and time scales.

2.5 Weld Aging

It is well known that δ-ferrite is aged by two primary processes, spinodal decomposition and the growth of the chromium-rich σ-phase [20]. For the purposes of this study, the aging conditions were controlled to preclude the growth of the chromium-rich σ-phase. For this reason, only spinodal decomposition will be discussed at length.

The concept of spinodal decomposition was first proposed by Hillert's thesis in 1956 [21]. Together Cahn and Hillard published a seminal paper modeling the phenomena in 1958 [22]. Essentially, the process consists of a metastable phase, in the case of this study - δ-ferrite, being beneath the solubility curve and decomposing to form two separate but stable phases, for δ-ferrite a chromium-rich, iron-depleted α' phase and a chromium-depleted, iron-rich α phase. The governing equations as described by Cahn and Hillard are shown in Eq. 2-5.

$$\frac{\partial c}{\partial t} = D\nabla^2(c^3 - c - \gamma\nabla^2 c), \qquad [2\text{-}5]$$

where: D is the diffusion coefficient
c is the concentration

γ is the surface energy

In the case of Type 316L stainless steel, spinodal decomposition has been shown to be a reult of the chromium and iron interaction with nickel being merely a bystander. In 316, the composition of chromium is 16-18% and 65 to 72 % iron. In a BCC crystalline structure this is the ferrite phase [23]. Figure 2-8 shows an AB binary system Gibbs free energy as a function of concentration. The spinodal is not at the point of the lowest Gibbs free energy, this would correspond to the miscibility gap, but rather the inflection point. If the weight percent is between the compositions for A and B then the system is favorable for spinodal decomposition, thus leading to a separation of the root phase, in the case of this study δ-ferrite decomposes to a chromium-rich, iron-depleted α' phase and a chromium-depleted, iron-rich α phase. This separation is manifested in nano-scale structural changes. [24]

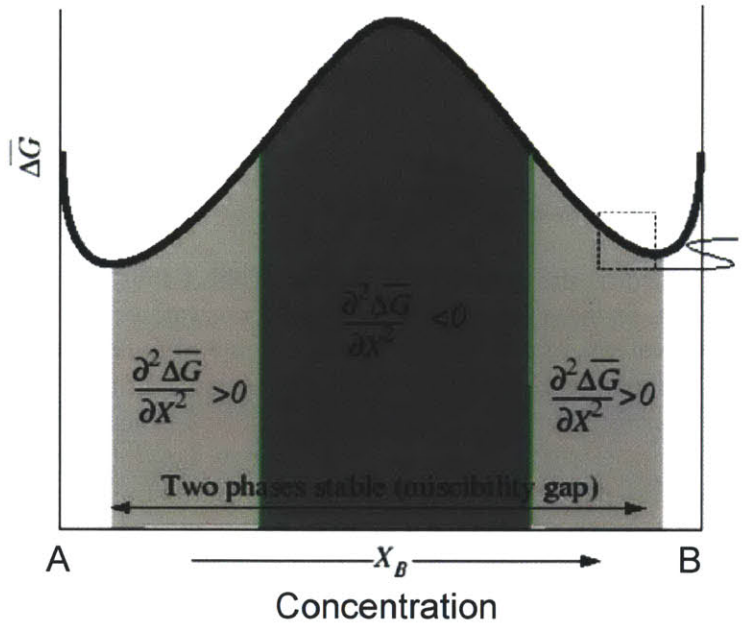

Figure 2-8 AB binary system at a given temperature in the range of the miscibility gap [25].

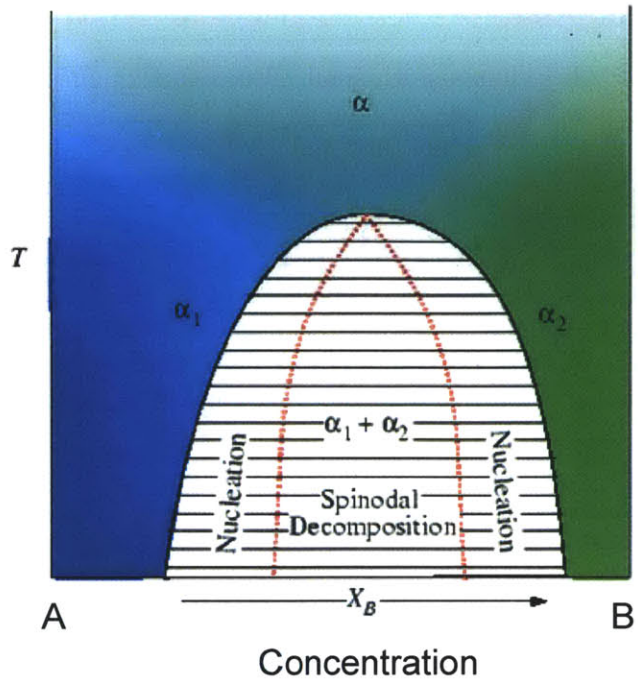

Figure 2-9 Solubility curve and spinodal [25].

The spinodal is defined as the points of inflection of the Gibbs free energy curves of a composition A and B, or the points where the second derivatives are equal to zero. If the first and second derivatives of free energy with a change of composition of A and B are plotted versus a temperature normalized to the systems critical point, or reduced temperature, then four regions of interest can be identified. This is shown schematically in Figure 2-9. Where $\partial^2 G/\partial c^2 > 0$ or above the spinodal curve to the $\partial G/\partial c$ curve, the two phase region must decompose by nucleation and growth, above $\partial G/\partial c$ the two phases no longer exist independently. $\partial^2 G/\partial c^2 = 0$ is the spinodal, as already defined. In the area under the spinodal curve, where $\partial^2 G/\partial c^2 < 0$ components of the alloy will diffuse apart as diffusion reinforces compositional changes.

What is interesting is that when the composition causes $\partial^2 G/\partial c^2 < 0$ the diffusion is in a sense uphill. The sign of the diffusion coefficient changes at the spinodal leading to a buildup in concentration as opposed to the usual diffusion or separation described by Fick's first law.

The products of spinodal decomposition occur in a spatially periodic fashion. This allows for use of Fourier transforms for the study of the concentration with time. However, due to the limits associated with both the understanding of spinodal decomposition as well as the assumptions of the models used to describe it, anything beyond minute concentration changes must be studied numerically. However, two results can be developed assuming linear and concentration-independent diffusion coefficients (valid only for very small fluctuations). The first is that the decomposition does not occur right at the spinodal but instead must be at some point where $\partial^2 G/\partial c^2$ is more negative. The second is that the

spatially periodic nature of the compositional changes is inversely proportional to the concentration where $\partial^2 G/\partial c^2 = 0$. From this it is possible to predict the wavelength, which is measurable. δ-ferrite, for example, has a measured wavelength of 5 nm [26].

There is both a time and temperature dependence for spinodal decomposition. The actual preferential concentration for the spinodal changes with temperature. Copetti and Elliot were quite successful in numerical simulations of the spinodal decomposition process [27]. Their results demonstrated that at the onset of spinodal decomposition, there are several wavelengths each growing in amplitude at different rates. The rate of growth and the final amplitude are dictated by temperature, whereas the final concentration is dictated by the fastest growing wavelength. The simulations showed a shorter wavelength and a steeper interface for the fastest growing wavelength. After the concentration and wavelength are set, the two phases then undergo coarsening, further increasing the compositional gradient, often consuming remaining shorter wavelengths [27]. While this is discussed in a 2-dimensional sense, when a third dimension is added the phase-composition takes on a tangled structure that is normally described in direct observation as mottled. Figure 2-10 illustrates the evolution of the compositional gradient for different wavelengths at different times.

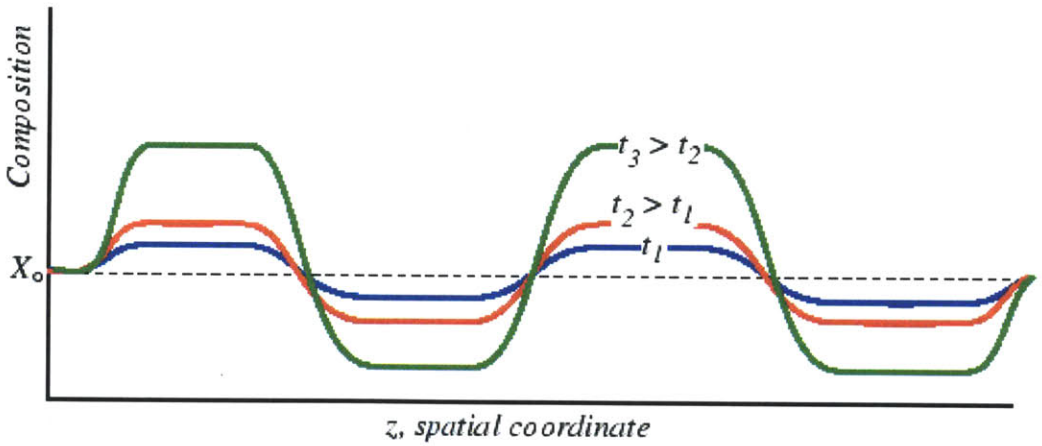

Figure 2-10 Growing amplitude and coarsening boundary in the dominant wavelength [25].

There have been numerous transmission electron microscope (TEM) and atom-probe studies primarily focused on spinodal decomposition with a side interest on the effects on material properties. Briefly, some of the studies of relevance that focus primarily on spinodal decomposition are described now. The first physical observation occurred using a TEM in 1980 by Kubo and Wayman analyzing β-brass. In addition they found that relaxation of elastic constraints during TEM foil manufacturing aided the spinodal decomposition process [28]. Brenner et al. in 1982, first used atom-probe analysis to study ferritic stainless steels as well as investigating the change of hardness caused by spinodal decomposition. The effects of spinodal decomposition were shown to increase hardness with aging. Using first generation atom-probe analysis, Brenner et al. showed that the spinodal indeed had a dominant period and amplitude. Initially at 13% chromium,

values as high as 80% chromium where found. They described the decomposed morphology as irregular, interconnected and vein like [26]. In 1990, Brown et al. investigated the cast stainless steel CF3. Their results were very similar to Brenner's in terms of increasing hardness, however the physical observation of the spinodal was increased by position sensitive atom probe (POSAP). POSAP allowed the entire spinodal to be viewed atom for atom instead of a small random averaged area in Brenner's work. As a result, they found first that the addition of nickel increased the rate of decomposition, where it was previously thought to be a bystander in spinodal decomposition of the Fe-Cr system. Austenite in the alloy also increased the initial rate of spinodal decomposition as well as the rate of hardening. Furthermore, POSAP analysis showed definitive compositional fluctuations, wavelength and amplitude for spinodal decomposed material [29]. Abe and Watanabe have studied welds that are very similar to those in this study. Primarily they were first interested in quantifying spinodal decomposition for aging at 335°C and the changes of nano-hardness in the weld. Their welds were Type 316L in thick wall piping, with two ferrite contents, one resulting in AF and the other in FA solidification modes. They found that for the AF mode, the ferrite hardened with aging out to 20,000 h and then began to soften. In the FA mode, it continued to harden, but at a much lower rate. In observing spinodal decomposition they utilized a TEM and noted mottling. They also found that ferrite etching increased with aging and hardness. They attributed all observed effects to spinodal decomposition [30]. Using a very high resolution TEM, in 2009, Hättestrand et al. where able to perform a very detailed inspection of duplex stainless steels and the effects of cold working on spinodal decomposition [31]. They found that the hardness increased as a function of aging time and temperature. However, they also added the variable of cold working effects on the spinodal decomposition. They found that cold working increased the rate of hardening and retarded the formation of α'-nucleation that is often found along with the spinodal decomposition. Furthermore, the high resolution of their TEM allowed them to study the γ/δ-boundary in greater detail than previously possible. They found that in cold-deformed duplex stainless steels there was an α'-denuded zone along the γ/δ-boundary at elevated aging temperatures which did not exist in the unstrained material at lower aging temperatures. Figure 2-11 is taken from their 2009 paper and shows the γ/δ-boundary for the spinodally decomposed material. They found that cold working raised the temperature where spinodal decomposition was the preferred mechanism over nucleation and growth. They attributed this to the influence of coherency strains [31].

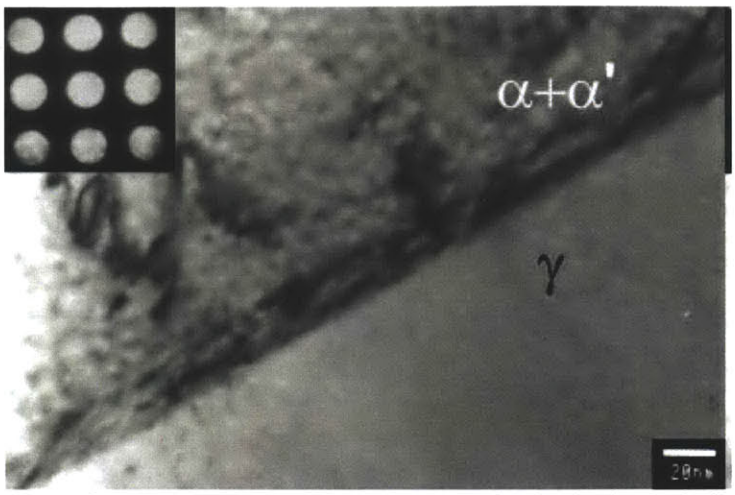

Figure 2-11 A ferrite/austenite phase boundary. Mottled contrast in the ferrite grain is present also in the immediate vicinity of the austenite grain [31].

2.6 Environmental Effects

There are two primary environmental effects of concern to this study. They are SCC and "environmental fracture", or the environmental effect on fracture toughness. SCC has been studied extensively and only a brief history and explanation of it will be provided here. Environmental fracture has a much shorter history, only being formally identified in 2007 [32].

2.6.1 Stress Corrosion Cracking

SCC requires three conditions in order to occur: 1) a susceptible material, 2) a tensile stress, and 2) a corrosive environment. In order to better understand SCC it is important to consider these three conditions individually and then how they interact in a symbiotic manner to cause crack growth.

A material must be susceptible to stress corrosion. This typically means that the material must be a metallic alloy, although pure metals, polymers, and ceramics may also be susceptible under the right conditions [33]. The materials are often ductile in nature and usually form a protective passivation layer such as an oxide film. Many of the susceptible materials typically are corrosion resistant, yet they are still at risk for SCC. In the case of this study, austenitic stainless steels are used in many aggressive environments, however they are known to undergo SCC.

The stress that is required for SCC is always tensile in nature at the crack tip. This stress can be either externally applied, or come from internal residual stresses from machining, cold working, or welding. In operation, external stresses may come from pressurization, mechanical support or fitting. The applied load is usually static in nature. Furthermore, it

is less than the critical stress intensity required for material failure (K_{IC}) but there is a critical stress intensity required for SCC, which will be referred to as K_{ISCC}.

The environment is usually aqueous in nature. By having a liquid medium, there is an increased mode for ion transport, conductivity and an opportunity for enrichment of species at the crack tip. The aggressiveness of the environment is known to increase with temperature, as well as contaminates such as chlorides or hydroxides. It is also well known that the corrosion potential is a function of oxygen content. However, the potential in the crack and at the crack tip may be very different than that of the bulk environment.

Propagation of the crack occurs in two parts, initiation and then growth. Initiation usually occurs at surface flaws. These flaws can be remainders of initial forming, for example, ridges due to machining or welding. They may also be general corrosion crevices or pits that have grown in a geometry that can then transition to SCC. In either case, the surface flaw or feature is a preexisting flaw to SCC that acts as an occluded space to give a required electrochemical environment to cause initiation and growth. Growth can be either transgranular (TG) or intergranular (IG) or a combination of both. In the case of TG fracture, the crack path ignores the overall grain structure and will go through the grain giving a fracture surface that is often crystallographic in nature. Conversely, in IG growth it is the grain boundary that is being attacked and so the fracture surface shows the grain as it has undergone decohesion with the grains on the opposite crack face. In SCC there is often little or no removed material, but primarily separation of the surfaces. The fracture surfaces often appear brittle even though the overall material may be ductile. A brief summary of some of the SCC models will be presented here. Later, for analytical purposes, the relevant models will be described in greater detail. [33]

The widely referenced deterministic Ford-Andresen, or slip-dissolution, model was published in 1988 [34]. This was the culmination of 60 years of research by several researchers into oxide film rupture and its role in crack propagation. The crack path follows a preferential corrosion path, such as a grain boundary or slip plane. As the oxide film is occasionally ruptured when there is a sufficient strain in the parent material. The surface is then bare of the protective oxide layer and susceptible for attack by the environment [34]. There is considerable debate surrounding this model, see for example Hall for a complete critique of the Ford-Andresen model [35,36]. Shoji et al. built upon the Ford-Andresen model by providing more detailed crack tip strain rate calculations [37]. In 2010, Shoji et al. reformulated the principle equations concerning oxidation kinetics and strain field description as questioned by Hall. This resulted in a better prediction of SCC in some austenitic stainless steels [37].

The biggest critic in the literature of Ford-Andresen and Shoji appears to be M.M. Hall. Hall published the film rupture – active path corrosion model in 2009 [38]. This model is a mathematical description of the anodic current density as a function of constant strain rate. The physical explanation for the model was provided by Raicheff in 1967 [39]. They noted that current density reaches a plateau despite the increasing strain. The physical theory was that the rate of current density change balanced the formation of new active

surface with the dissolution of the unprotected surface. The addition of this model provides for a mathematical expression relating anodic current, strain rate and crack tip velocity.

The coupled environmental fracture model has been in constant development and improvement by Macdonald et al. [40]. The model is very close to the Ford-Andresen slip-dissolution model but couples the internal and external environments and places a restriction of charge conservation throughout the cracking system. As with the Ford-Andresen model, crack growth is via anodic dissolution but considers the cathodic reactions to be the rate limiter to crack growth. Macdonald's model yields similar accuracy as slip-dissolution. However, the constants are easier to obtain. As with all SCC models to date, there is considerable controversy and an ongoing dialogue between researchers. Macdonald thoroughly explains the evolution of his model and gives retort to the latest criticism in [40].

Aaltonen et al. proposed another alternative model known as the selective dissolution – vacancy creep model [41]. He mainly studied Alloy 600. However, the model still holds relevance to other materials as well. First proposed in 1996, his model focused on oxidization at the crack tip leading to vacancy formation at the oxide/metal interface. The buildup in concentration of the vacancies leads to diffusion into the matrix. The vacancies then influence dislocation mobility, shear localization, and the matrix defect structure. As the vacancies accumulate near the crack tip, voids are created and the crack propagates, exposing new metal for oxidation and the process repeats. [41]

Another mechanism was proposed by Scott in 1993 [42]. Essentially an oxide layer would form at the crack surface, leading to a layer of diffused oxygen atoms at the grain boundaries. This would lead to embrittlement of the matrix by oxide formation. This mechanism can be active in nickel-based alloys. [42]

In 1985 Jones proposed a model that was meant to explain both SCC and corrosion fatigue [43]. The essence of the model was such that vacancies formed by anodic dissolution at film rupture sites would migrate as divacancies to lattice sites in the bulk material in the vicinity of the crack tip. In the case of corrosion fatigue, the divacancies come from internal vacancy sources. In either case, the divacancies accumulation leads strain hardening and to brittle fracture in the vicinity of the crack tip. [43]

Scully proposed a simplified model in 1975 that described crack front propagation as a series of slip-step movements. The surface of the crack tip would be initially covered by a protective film, but undergoes mechanical shear exposing a slip plane of the base metal. Corrosion and repassivation ensues on the crack tip and the corrosion occurs fast enough that there is incremental crack growth before the surface is completely passivated. There must be a balance between strain rate, corrosion and passivation, if one were higher the mode of fracture, or protection would dominate and SCC would not occur. Scully proposed that this occurred under a constant charge and strain rate. He acknowledged the limitations of the simplistic model for never taking into account crack morphology, creep strain rate, cold working, heat treatment etc. [44]

The wide range of potential models for SCC is a clear demonstration that mechanisms are not entirely understood. In each case there is an acknowledgement of the environment, the strain and the material properties, however as of yet, there is no overarching explanation. While it is likely that any successful model must take into account the trifecta needed for SCC, few models incorporate all the aspects. For the purpose of this thesis however, only a general understanding of the process and the many variables are needed. There will be no attempt to create an SCC correlation and indeed, due to the highly unique nature of the material microstructure compared to wrought materials, many of the existing models may not even be applicable.

2.6.2 Environmental Fracture

The term "environmental fracture" refers to a reduced fracture toughness of a material following exposure to environment. Hixon et al. first formally identified the phenomenon in 2007 [31]. Previously, other researchers, had seen similar environmental impact, such as Andresen in alloy 182 weld metals [45]. The behavior has often been attributed to experimental error, but was shown to be a real effect [31]. To date there has been very little research into this topic. Most fracture toughness studies in welds focus on thermal aging effects tested in air and will be discussed below.

2.7 Previous Weld Metal Studies

There have been numerous previous studies on welds of all sorts. For the purpose of this review, GTAW welds in Type 316L will be the focus. However, occasionally a relative alternative will be discussed. Welding properties studies on this subject have been active since the 1950's, and aging impact on welds has been studied since the 1960's [46]. A review of previous research cannot possibly be all inclusive. However, the major studies for Type 316L welds in the temperature range and environment of interest will be discussed. In reference to the conditions for this study, the actual data universe is quite small. First, the focus will be on studies that look strictly at mechanical properties, such as Charpy-V, tensile properties and fracture toughness. Next are those whose main concern is SCC, many of which contain mechanical property testing.

2.7.1 Aging Effects on Properties

Vitek et al. in an aging study in 1991 focused on Type 308 stainless steel welds [13]. The plate welds containing approximately 10% δ-ferrite were subjected to nano-indentation, Charpy-V, tensile, and fracture toughness characterization. Welds were aged at 475°C for up to 20,000 h. It was found that the hardness of the austenite phase remained constant while that of the ferrite phase increased by as much as 100%. The Charpy-V upper shelf energy fell most in the first 1000 h and continued a slight decline after that. Fracture toughness followed a similar trend and tensile properties remained largely unaffected. Fractography indicated that carbide precipitation as well as spinodal decomposition played a role in the property changes. Unfortunately, there was also G-phase precipitation that impacted the results. [13]

NUREG/CR-6428 authored by [20] in 1996 is a study that focuses on Charpy-V energy and fracture toughness. The study focused on Type 304/308 welds but contained data from many previous tests on Type 316 as well. Furthermore, the data pool given also shows SMAW, SAW, and GTAW welding results. The welds used all contained between 4 and 9 % δ-ferrite. They were made in piping rings. However, the direction of testing was for the fracture surface to open circumferentially, with fracture occurring along the PQ plane (similar to this study) but in the P direction. NUREG/CR-6428 also did not utilize tensile testing but instead relied upon correlations of the Charpy-V data to tensile properties. The study found similar trends to Vitek, where there is a general decrease in Charpy-V energy, and a slight decrease in toughness initially, for the Type 304/308 welds. For Type 316 studies given, the fracture toughness changed little in each study while the Charpy-V energy dropped with aging. What is interesting from the data universe concerning fracture toughness is that there is a large inconsistency among reported data. For any given weld type and age, data scatter covers approximately 300 to 500 kJ/m^2. This shows an initial difficulty in quantifying effects on welds.

The most complete review of the data universe comes from Mills in 1997 [47]. In the review, fracture toughness and Charpy-V energy values are presented for Type 304 and 316 welds, base metals, and HAZs. The data shows again that there is little change in fracture toughness values and a drop in Charpy-V energy during early aging and relatively little change after that. It is also noted that fracture toughness values drop as testing temperature is increased. Often in this study, the δ-ferrite content is not given. [47]

Nayak et al. were primarily interested in the embrittlement of Type 316L welds. Figure 2-12 is a sample from a study of the aging and temperature impacts on the rate of embrittlement. Nayak used lower shelf energy (LSE) as a descriptive mechanism for aging effects on welds. In Figure 2-12, the increase in aging results in an increase in the embrittlement of the 316 stainless steel. Also evident is that as ageing time increases, the stainless steel continues to embrittle but at a slower rate. Nayak et al. thought this to be evident of spinodal decomposition [48].

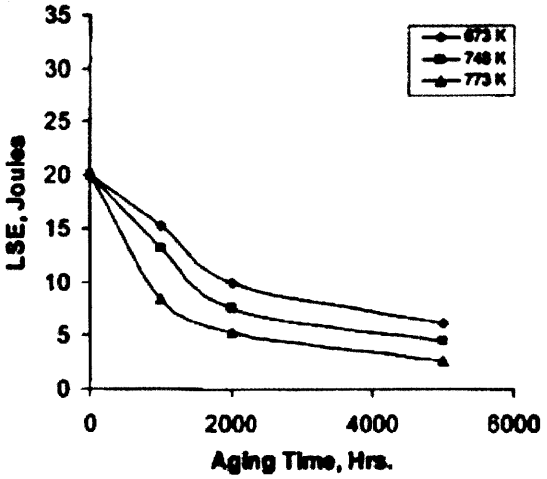

Figure 2-12 Lower shelf energy as a function of aging time and temperature [48].

2.7.2 Stress Corrosion Cracking

The number of material, environments and methods of SCC studies is extensive. For welds, the literature is fairly extensive, although the majority of the studies focus on the HAZ or the fusion line or in environments that are not related to the nuclear industry. The number of studies on austenitic stainless steel welds subjected to BWR conditions to promote SCC crack growth along the weld centerline is quite small. Those will be reviewed here.

While not actually a weld study, Berry et al. produced castings that solidified with the same microstructure as Type 316 welds. The initial inference was that with aging, the surface energy would change based on the kinetics of spinodal decomposition. They showed that in the ferrite cores of the dendrites, the surface energy decreases as a function of aging. In this way, the Griffith fracture criterion is met with smaller stress intensity. The cracking was aligned with the dendrite structure, and was found to occur preferentially along the gradients predicted by the modified Cahn-Hillard equation. [49]

Utilizing a bead-pile style of weld, where the beads are just freely stacked without actually joining anything, Shaikh et al. studied the effects of aging on SCC in welds in 1992 [50]. The weld filler metal was Type 316L with an average ferrite number of 7. The weld was heat treated at 600°C for up to 2,000 h. This led to significant carbide and sigma phase precipitation. Yield strength decreases as a result. The actual SCC tests were performed in heated $MgCl_2$ solution, and so occurred under a very different environment than BWR chemistry. The results, however, were that the cracking occurred in a transgranular manner through the austenite and also along the austenite/ferrite boundary. [50]

Type 308 and 316L welds were subjected to a simulated BWR environment by Hamada and Yamauchi, reported in 2001 [14]. Their welds were meant to simulate those found on

the pressure vessel and as such were subjected to the same post-weld heat treatment as with a reactor pressure vessel, in this case up to 610°C for 40 h. Then in order to accelerate aging at 288°C they aged the material at 500°C for 25 h. These materials were machined as slow strain rate specimens and U-bend specimens for SCC testing. The environment was oxygenated pure water. Hamada and Yamauchi found that the Type 308 welds either sensitized or became healed depending on the length of the heat treatment, while the Type 316 performed in a superior manner demonstrating resistance to sensitization. This was believed to be due to the higher δ-ferrite content (8-15%), and low carbon content (<0.03 wt%) suppressing the carbide precipitation. [14]

The effects of loading and water chemistry on the weld and HAZ were performed by Lu at Tohoku University in Japan and reported in 2008 [51]. The research focused on Type 316L welds and heat affected zones subjected to both oxygenated as well as hydrogenated environments. The welds had a ferrite number of between 10 and 14 depending on location. Crack length was measured using alternating current potential drop. Crack growth rates for the hydrogen water chemistry were much less than for the oxygenated water. In all cases, however, they were between 1 and $3x10^{-10}$ m/s. The fracture morphology of the weld metal was interdendritic in nature. [51]

2.7.3 Materials Similar to Welds

While welds are a special material in terms of their bead by bead creation and the unique resulting microstructure of parallel dendrites there are other materials that are similar in nature. Both duplex stainless steels (DSS) and cast stainless steels (CSS) are similar in that they both contain δ-ferrite. In the case of DSS the δ-ferrite content is much higher than that of the welds. Furthermore, these are wrought materials. For CSS, the δ-ferrite content, and indeed the rest of the material composition is quite close to stainless steel welds. However, CSS are formed by casting and as such do not develop the highly heterogeneous microstructure of welds. While studies of DSS and CSS are not fully relevant, they have been studied much more extensively than austenitic stainless steel welds. With the wealth of data that the studies bring, and the similarities of the materials, parallels can be drawn in terms of material response, especially in terms of aging and γ/δ-interface. While the review of studies is no way exhaustive, and other studies will be brought up later, those presented here are general examples of what can be found elsewhere.

In 2006, Roychodhury et al. reported on findings concerning hydrogen's influence on fracture toughness and hardness in DSS. They found that increasing the hydrogen content led to an increase in hardness, particularly in the austenite phase. They were most interested in investigating the effects of charged hydrogen on the initiation toughness of fracture, the stretch zone width (SZW) and the tearing resistance. They found that charged hydrogen reduced the fracture toughness as well as the tearing resistance. They were unable to evaluate the SZW in hydrogen samples as it was not evident under SEM. The primary mode of fracture in the stable tearing region was by cleavage in ferrite and micro-void coalescence in the austenite. Separation and crack growth also occurred significantly on the γ/δ-interface [52].

Pumphrey and Akhurst, Stangwood and Druce, and Chung and Lean all published studies concerning CSS in 1990. They were all concerned with the aging effects on the cast material. Separately, they arrived at the conclusions that the hardness increased with age, and fracture toughness and Charpy-V energy decreased. In each case this was attributed to spinodal decomposition [53, 54, 55]. Pumphrey and Akhurst were concerned primarily with as-cast and aged CF3 material but Stangwood and Druce were also interested in welds of CF3. Chung and Lean obtained actual material from in-service BWR's. They studied CF3, CF8 and CF8M. They found that spinodal decomposition was primarily responsible for the aging effects and also that the toughness was further degraded by precipitation of $M_{23}C_6$ carbides at the γ/δ-interface. They also suggested that it maybe impossible to ever develop a working correlation for the effects of spinodal decomposition across a wide range of materials as there are too many variables affecting the kinetics. Even in materials of the same composition, thermodynamic and fabrication effects make modeling difficult. In 1996, Bethmont et al. found similar results as above. They also noted that the fracture toughness tests in air never underwent unstable fracture and that the scatter in their data was due primarily to tearing through microstructural variation. [56]

To date there is no single complete study that has taken into account the variability that occurs in the welding process across chemistry and aging. This thesis is the first systematic attempt to study the mechanical properties, SCC crack growth, fracture mechanics, and most novel, in-situ fracture toughness as functions of both ferrite number and aging time at different temperatures for consistent welds prototypical of those found in BWRs. There is a very limited data universe for the real conditions of BWR operation and therefore it is very difficult to make any prediction or study based on existing data. One of the goals of this study is to provide for a solid foundation of well founded and qualified data that is relevant to the nuclear industry and the BWR operating conditions in specific.

3 Project Description

A program has been carried out to investigate the effect of long-term thermal aging on mechanical and corrosion properties, including SCC growth behavior and fracture toughness as well as the effect of the environment on fracture toughness. Specifically, the following properties were investigated: (1) SCC crack growth rate in normal BWR chemistry environments, (2) the effect of environment on in-situ fracture toughness, (3) the fracture toughness properties without exposure to the BWR environment, (4) tensile properties, (5) hardness, (6) residual stress, (7) Charpy-V energy, and (8) trapped hydrogen content.

In order to explore the effects of spinodal decomposition on SCC and material properties, an exact example of a BWR pipe was obtained and welded in the same way as though it were going into a plant under construction. The pipe was schedule 240, 600 mm, Type 316L stainless steel, fabricated by forging at Japan Steel Works and welded by the Electric Power Research Institute (EPRI). The weld metal chemistry was controlled to provide two ferrite numbers, 10 and 14. These two key materials are designated as "low-ferrite" and "high-ferrite", respectively. After welding, the material was sectioned into the appropriate sample blank size and then thermally aged when needed. This process created a weld library that is prototypical of several aging times and conditions of welds that would be found in a BWR. Figure 3-1 shows the complete sample matrix for the Type 316L weldments. Sample identification numbers are indicated. Since the weld production effort provided for a very large and complete library of welds, it was not possible to test every condition. As noted in Figure 3-2, a select subset of weld materials was actually tested.

Figure 3-3 shows the iron-chromium TTT diagram in the region where spinodal decomposition occurs in the iron-chromium alloy with time and temperature of experimental aging and BWR operation noted. Key variables under the matrix are aging time and temperature as well as the amount of δ-ferrite in the welds. As is illustrated by Figure 3-1, the test program provided aging times that at operating temperature simulates those of actual BWR operation. As previously mentioned, material property tests consisted of normal tensile testing, hardness, residual stress, fracture toughness, fatigue crack growth rate as well as SCC crack growth rate testing. Each SCC test was completed with an in-situ fracture toughness test. The key physical metallurgy variable is the characterization of the degree of spinodal decomposition as a function of the thermal aging for a given initial δ-ferrite content. The welds were also extensively examined using standard metallographic, micro-analytical (SEM, micro-hardness), and industrial (Magne-Gage, etc.) techniques to determine the amount of δ-ferrite present and to fully characterize the welds. Upon completion of the weld property studies, further effort was made to gather insight into the principle reasons for the noted effects. Specifically, nano-indentation and residual stress analysis as well as post-mortem inspection using optical and SEM microscopy were used. Further details on each step will be provided in their respective subsections of the report.

The goal of this thesis will be to develop an understanding between the initial state of a weld and the degree of properties degradation for any combination of time and temperature that would be achievable during BWR operation. The long ultimate aging times will assure that insight developed by the program can be extrapolated to end of life conditions.

			J_{IC} Fracture Toughness						Crack Growth Rate		Tensile				Charpy V-Notch						Macro Hardness
			25 °C			288 °C			288 °C		25 °C		288 °C		25 °C			288 °C			
Low δ-ferrite	As Welded		6	38	84	64	92	112	44	102	41A	41B	83A	83B	115A	115B	115C	2A	2B	2C	65
	300 °C	5,000	45	108	37	107	39	53	117	87	3A	3B	52A	52B	82A	82B	82C	99A	99B	99C	8
		20,000	113	49	20	48	50	109	42	96	111A	111B	36A	36B	104A	104B	104C	57A	57B	57C	25
		40,000	106	61	95	11	60	98	97	101	89A	89B	105A	105B	62A	62B	62C	35A	35B	35C	
	400 °C	1,000	23	89	15	119	31	128	27	123	78A	78B	58A	58B	51A	51B	51C	110A	110B	110C	13
		5,000	28	118	22	125	34	75	32	124	122A	122B	14A	14B	18A	18B	18C	126A	126B	126C	30
		10,000	33	81	17	120	9	90	21	80	121A	121B	1A	1B	24A	24B	24C	66A	66B	66C	129
	430 °C	1,000	59	70	98	76	56	26	55	79	72A	72B	63A	63B	7A	7B	7C	77A	77B	77C	127
		5,000	4	12	85	16	103	73	74	5	47A	47B	100A	100B	40A	40B	40C	71A	71B	71C	116
		10,000	10	69	91	54			43	114	19A	19B	67A	67B	93A	93B	93C	29A	29B	29C	94
High δ-ferrite	As Welded		144	160	199	193	211	259	173	238	225A	225B	132A	132B	219A	219B	219C	142A	142B	142C	187
	300 °C	5,000	250	134	155	210	248	260	157	207	214A	214B	198A	198B	147A	147B	147C	202A	202B	202C	192
		20,000	156	190	188	194	179	150	205	254	253A	253B	148A	148B	180A	180B	180C	196A	196B	196C	186
		40,000	223	189	221	239	255	140	243	151	154A	154B	137A	137B	136A	136B	136C	257A	257B	257C	164
	400 °C	1,000	237	184	256	138	240	174	244	185	236A	236B	170A	170B	224A	224B	224C	169A	169B	169C	226
		5,000	245	182	234	183	200	166	232	167	242A	242B	176A	176B	241A	241B	241C	175A	175B	175C	197
		10,000	233	177	229	171	228	172	227	168	203A	203B	181A	181B	195A	195B	195C	230A	230B	230C	235
	430 °C	1,000	139	261	163	251	161	217	178	249	143A	143B	258A	258B	153A	153B	153C	252A	252B	252C	131
		5,000	135	215	133	212	152	204	162	218	165A	165B	220A	220B	130A	130B	130C	246A	246B	246C	231
		10,000	149	216	146	201	222	145	206	141	159A	159B	209A	209B	191A	191B	191C	213A	213B	213C	247

Figure 3-1 Complete sample matrix for all material blanks.

			J_{IC} Fracture Toughness						Crack Growth Rate		Tensile				Charpy V-Notch						Macro Hardness
			25 °C			288 °C			288 °C		25 °C		288 °C		25 °C			288 °C			
Low δ-ferrite	As Welded		6	38	84	64	92	112	44	102	41A	41B	83A	83B	115A	115B	115C	2A	2B	2C	65
	300 °C	5,000	45	108	37	107	39	53	117	87	3A	3B	52A	52B	82A	82B	82C	99A	99B	99C	8
		20,000	113	49	20	48	50	109	42	96	111A	111B	36A	36B	104A	104B	104C	57A	57B	57C	25
		40,000	106	61	95	11	60	98	97	101	89A	89B	105A	105B	62A	62B	62C	35A	35B	35C	
	400 °C	1,000	23	89	15	119	31	128	27	123	78A	78B	58A	58B	51A	51B	51C	110A	110B	110C	13
		5,000	28	118	22	125	34	75	32	124	122A	122B	14A	14B	18A	18B	18C	126A	126B	126C	30
		10,000	33	81	17	120	9	90	21	80	121A	121B	1A	1B	24A	24B	24C	66A	66B	66C	129
	430 °C	1,000	59	70	98	76	56	26	55	79	72A	72B	63A	63B	7A	7B	7C	77A	77B	77C	127
		5,000	4	12	85	16	103	73	74	5	47A	47B	100A	100B	40A	40B	40C	71A	71B	71C	116
		10,000	10	69	91	54			43	114	19A	19B	67A	67B	93A	93B	93C	29A	29B	29C	94
High δ-ferrite	As Welded		144	160	199	193	211	259	173	238	225A	225B	132A	132B	219A	219B	219C	142A	142B	142C	187
	300 °C	5,000	250	134	155	210	248	260	157	207	214A	214B	198A	198B	147A	147B	147C	202A	202B	202C	192
		20,000	156	190	188	194	179	150	205	254	253A	253B	148A	148B	180A	180B	180C	196A	196B	196C	186
		40,000	223	189	221	239	255	140	243	151	154A	154B	137A	137B	136A	136B	136C	257A	257B	257C	164
	400 °C	1,000	237	184	256	138	240	174	244	185	236A	236B	170A	170B	224A	224B	224C	169A	169B	169C	226
		5,000	245	182	234	183	200	166	232	167	242A	242B	176A	176B	241A	241B	241C	175A	175B	175C	197
		10,000	233	177	229	171	228	172	227	168	203A	203B	181A	181B	195A	195B	195C	230A	230B	230C	235
	430 °C	1,000	139	261	163	251	161	217	178	249	143A	143B	258A	258B	153A	153B	153C	252A	252B	252C	131
		5,000	135	215	133	212	152	204	162	218	165A	165B	220A	220B	130A	130B	130C	246A	246B	246C	231
		10,000	149	216	146	201	222	145	206	141	159A	159B	209A	209B	191A	191B	191C	213A	213B	213C	247

Figure 3-2 Complete sample matrix for all material blanks, specimens tested highlighted in red.

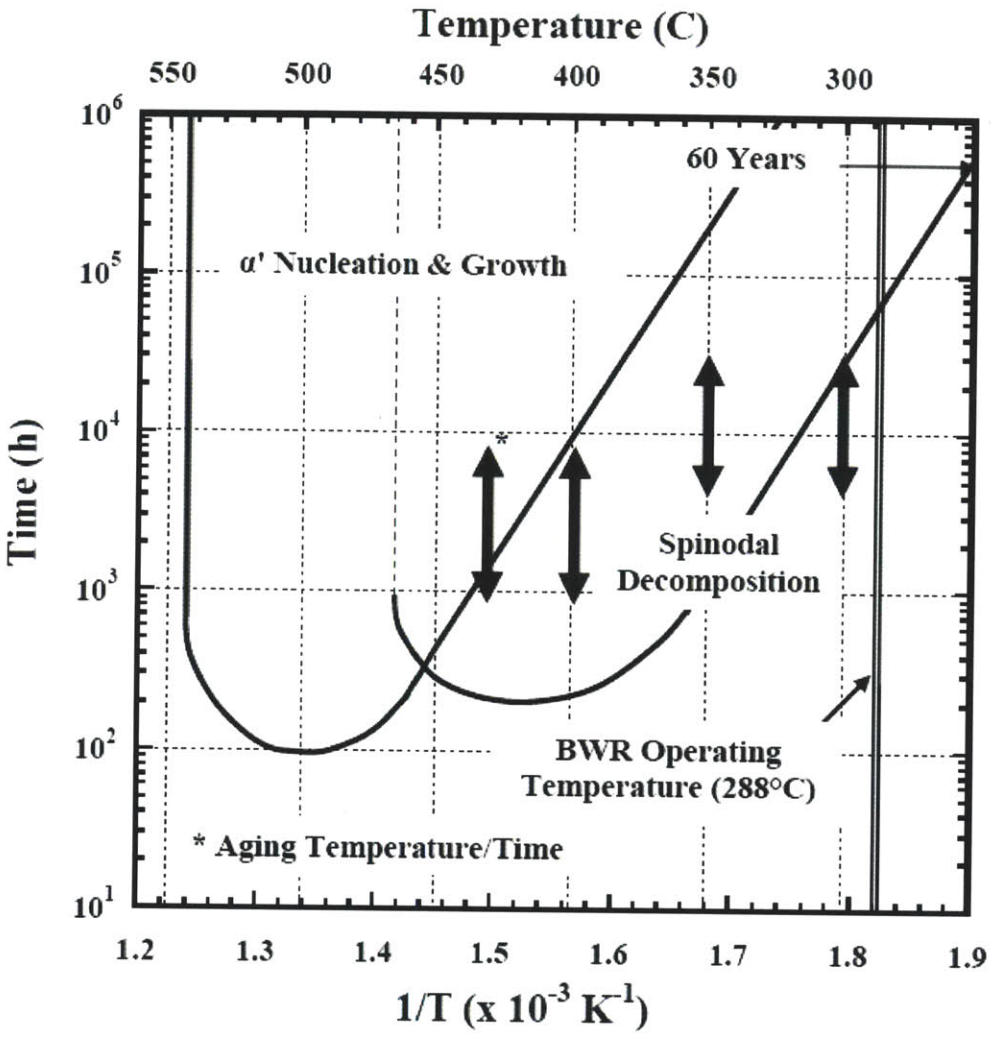

Figure 3-3 Time-Temperature-Transition (TTT) diagram for an Fe-Cr alloy in the region of spinodal decomposition with the project time/temperature aging matrix indicated by vertical arrows. Also shown is the BWR operating temperature [57].

4 Experimental Techniques

The overarching purpose of the study was to evaluate the effects of thermal aging on the mechanical properties of Type 316L stainless steel weldments. Prior to performing experiments weldment samples had to be constructed and aged properly. Once the base material was fabricated and treated it is used to construct the actual samples of three geometries for individual tests. Samples were fabricated to perform standard stress-strain testing via tensile tests, hardness mapping, residual stress analysis, and 1T-CT (one inch thick, compact tension) specimens were used for fracture toughness, fatigue crack growth and stress corrosion cracking crack growth rate measurements.

4.1 Weldment Fabrication

Sections of 600 mm diameter, schedule 240 (42 mm wall), Type 316L stainless steel pipe were obtained through the efforts of Professor Tetsuo Shoji at Tohoku University. The pipe and welding configuration is shown schematically in Figure 4-1. Weld wire material was obtained with two 316L compositions. Table 4-1 shows the weld wire chemistries, including the ferrite numbers. The weld wire chemistries were designed to achieve the desired ferrite content in the pipe/plate welds. The pipe was sectioned into 6 rings, and was delivered to the EPRI NDE Center in Charlotte NC. Figure 4-2 A shows the packaged rings as received at the NDE Center.

Table 4-1 Weld wire chemistries, chemical balance is iron.

Specification	C	Mn	Si	S	P	Cr	Ni	Mo	Cu
316L-WO21437	0.022	1.85	0.44	0.001	0.021	19.34	12.68	2.51	0.26
316L-HT94789	0.015	1.75	0.35	0.014	0.017	19.2	12.3	2.61	0.05

The welding was performed using an automated gas tungsten arc method with two heats of 316L filler metals at the EPRI NDE Center in accordance with ASME Boiler & Pressure Vessel Code with qualified weld procedures and non-destructive testing. Weldments were created using a fully nuclear qualified procedure complete with full ultrasonic inspection, Appendices A through C in reference [57] contain the complete documentation for the welding and inspection processes. All materials, procedures and geometries are consistent with BWR recirculation piping, allowing the study to exactly replicate the desired conditions.

For this study, the weld chemistry has already been shown in Table 4-1 above. It is straight forward to calculate the chromium and nickel equivalence as well as the resulting ferrite number and percent. This is tabulated in Table 4-2 for each of the respective models. For this study, all of the solidification is predicted to occur in mode FA resulting in a primarily face-centered cubic (FCC) austenitic material with some retained BCC ferrite.

Table 4-2 Equivalent chromium and nickel and resulting ferrite number.

	Material Designation	Cr_{eq}	Ni_{eq}	Ferrite Number (FN)
Schaeffler or DeLong	Low-Ferrite	22.5	14.3	10
	High-Ferrite	22.3	13.6	14
WRC-92	Low-Ferrite	21.9	13.5	10
	High-Ferrite	21.8	12.8	14

Six welds were made joining Type 316-pipes with a thickness of 41 mm and 600 mm in diameter. Three of the pipe welds were with one heat of 316L, and three pipe welds with the other. Figure 4-2D shows the pipe welding set-up which utilized an orbital GTA welder while rotating the pipe.

The sections were then divided as follows: (1) ½ of one of each of the two ferrite number welds were shipped to Tohoku University. The remaining rings were shipped to MIT, (2) 1 between-weld ring was shipped to MIT. The remaining rings were shipped to Tohoku University. Figure 4-2E shows a photograph of two of the weld rings as received at MIT. The weld rings were marked and stamped before cutting, shown in Figure 4-2 B and F. Table 4-3 gives the EPRI weld identification number and the corresponding sample numbers for final fabrication. In this way, careful custodial control of all samples was maintained. The pipes were then saw cut to allow for blanks of different sizes. The largest blanks are sized for making 1T-CT specimens for J_{IC} and SCC growth rate testing. Medium sized blanks are sized for making transverse weld tension specimens with 6.35 mm diameter. Small blanks were cut for Charpy-V impact specimens. [57]

Samples are then aged at temperatures of 430°C, 400°C and 300°C for times up to 40,000 h. The long ultimate aging times assure that correlations developed by the program can be extrapolated to end of life conditions. Table 4-4 shows the thermal aging matrix. Aging times and temperatures were selected to increase the speed of thermal aging yet prevent microstructural changes not present in the BWR environment (such as σ-phase formation). Maximum aging temperature was limited to 430 °C in order to prevent excess carbide and σ-phase per the TTT graph in Figure 3-3.

Table 4-3 Material weld identification number corresponding to specimen blank number.

Specimen Source	
Weld ID Number	**Specimen Numbers**
316L WO21437-1	1-64
316L WO21437-2	65-129
316L WO21437-3	Spare (1/2 to Tohoku)
316L HT 94789-1	130-195
316L HT 94789-2	196-261
316L HT 94789-3	Spare (1/2 to Tohoku)

Table 4-4 Thermal aging matrix.

Aging Time (h) \ Aging Temperature (°C)	300	400	430
1,000		●	●
5,000	●	●	●
10,000		●	●
20,000	●		
40,000	●		

Figure 4-1 Pipe weld-ring configuration.

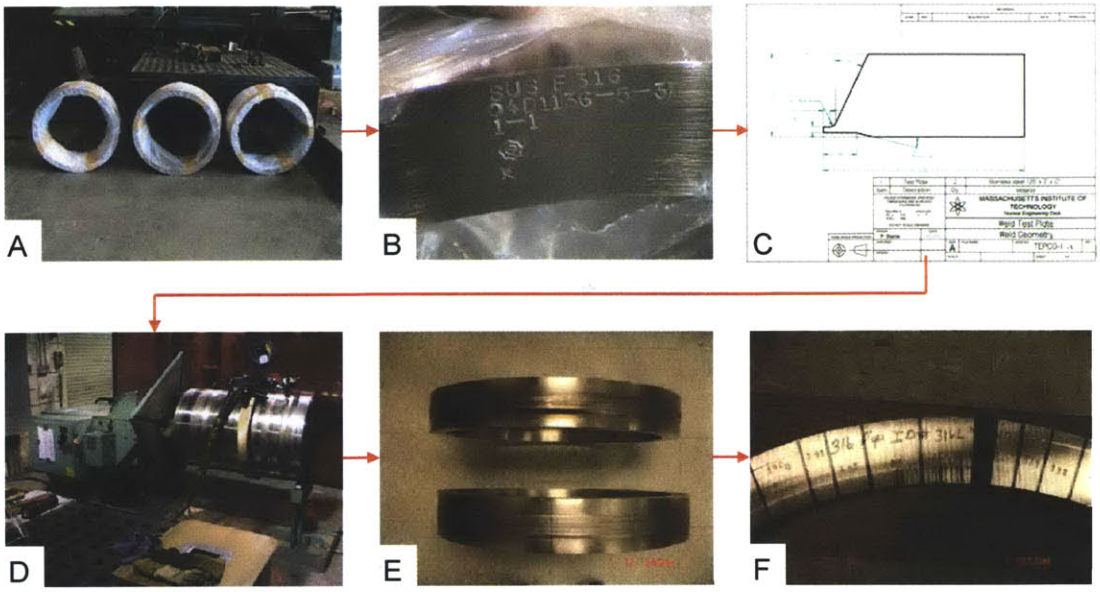

Figure 4-2 Weld construction process: A) forged pipe rings, B) rings stamped, C) diagram for cut in rings in preparation for welding, D) orbital welding of rings, E) completed welds, F) welds sectioned into blanks and labeled.

4.3 Weld Characterization

Verification of the expected microstructure was performed via optical microscopy on a Zeiss inverted microscope. Welds were cut on the principle planes and analyzed at 50X, 100X, 200X and 500X. The weld cross-section was polished using increasing grits of abrasive paper to 1200 grit and finished with a 0.06 μm alumina suspension. The sample was then etched with Kalling's reagent. In this section, the results of the initial weld characterization will be presented. Figure 4-3 shows the NQ plane of the weld, the boxes in the figure represent areas of greater magnification presented below.

The parent metal is a normal forged alloy. As expected this contains a normal crystalline structure following the traditional randomly oriented grain nature of such materials. Figure 4-3 illustrates the base and weld metal.

The HAZ and fusion line are shown in Figure 4-3C.1. In the HAZ it is normal in wrought stainless steel welds for the HAZ to undergo recrystallization and grain growth resulting in larger crystals. In this material, however, the grains of the HAZ are not exceptionally larger than those of the base metal. Furthermore, the crystalline orientation of the grains in the HAZ serves as seeding for the growth of the dendrites in the weld metal.

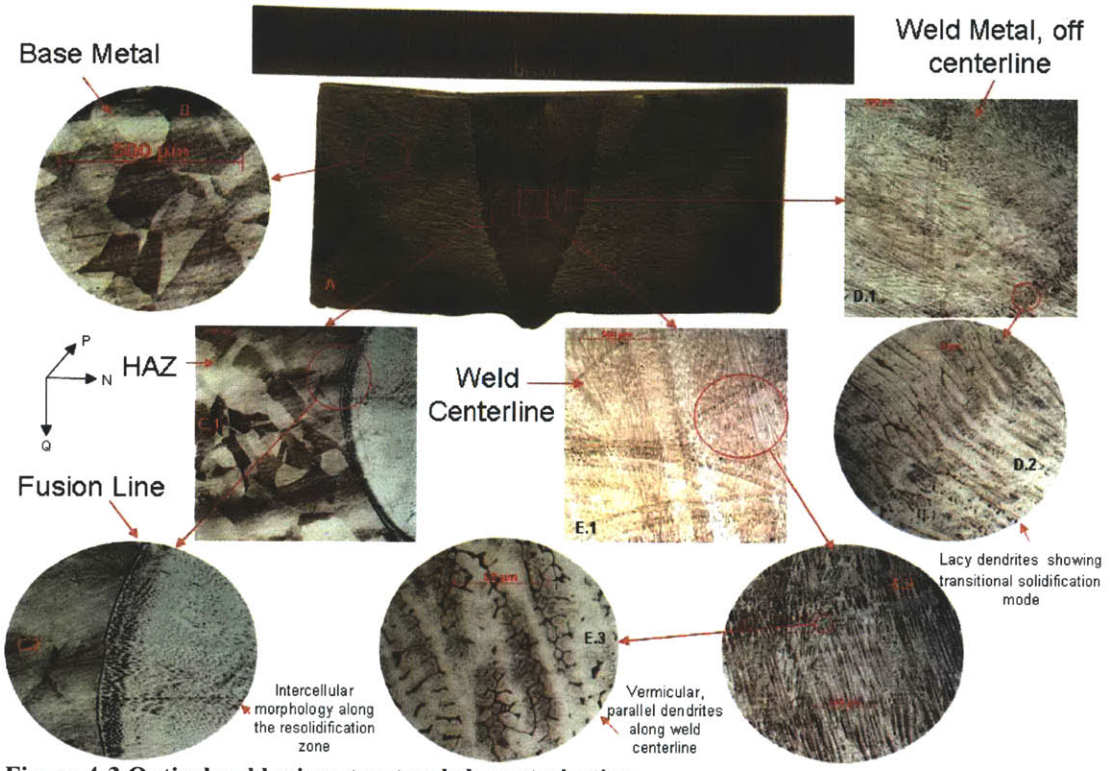

Figure 4-3 Optical weld microstructural characterization.

Along the fusion line, there is a very thin area called the resolidification zone, shown in Figure 4-3C.2. In this area where the dendrites that will define the weld metal begin to grow. The resolidification zone is made up of parent metal that has melted with the weld filler metal. There is a large amount of ferrite in this fine region and numerous other precipitants are found there. The structure and size of individual weld passes can be noted by the cyclic repetition of this area as seen in Figure 4-3.

The area in the weld metal closest to the fusion line shows an area where the dendrite formation has not quite become the dominant mechanism of solidification. As shown in Figure 4-3C.2, there are large areas of cellular austenite. This is due to the weld wire chemistry combining with the parent metal and forcing an A type solidification. Furthermore, only certain grains of the parent material will spawn dendrite growth, those being the grains with the energetically preferential crystalline direction facing the dominant direction of cooling. An example of this is shown in Figure 4-3C.1. Moving toward the weld centerline and the first real dendrites begin to form. These can be seen as extending from only certain grains of certain staining. The staining intensity is a function of grain orientation. Notice that in this region the dendrites form perpendicular to the fusion line, as this is the direction of cooling. In the center of the weld they will run parallel in the Q direction. In Figure 4-3D.2 transition from cellular to lacy dendrite structure is noted. This is due to leaving the melt area which is influenced by the parent chemistry but still maintaining a cooling rate high enough to form lacy ferrite for the given chemistry in the FA mode. As the cooling rate slows, the weld melt still maintains the FA mode but the δ-ferrite takes on a skeletal form at the core of the dendrite. This

occurs moving closer to the weld centerline, which also leads to the direction of dendrite growth gradually turning toward the Q direction. As can be noted in Figure 4-3E.2 there are often weld bead boundaries where dendrite direction can continue in a similar direction, seeded by the previous weld pass, or grow in alternative yet complimentary crystallographic directions. Figure 4-3E.1 shows that there are three separate boundaries of interest occurring on unique scales – 1) the skeletal δ-ferrite core and its interface with the austenite, on the order of one micron; 2) the complete dendrite structure, on the order of 10-20 microns wide and 3) the weld bead itself, on the order of 1 mm. As has already been mentioned, the dendrites in the center exhibit skeletal δ-ferrite cores and grow parallel in the Q direction, for example see Figure 4-4. The weld centerline area is shown along the PN plane in Figure 4-4. Here the dendrites and δ-ferrite cores can be viewed end on. It is interesting to note that the skeletal δ-ferrite present has varying numbers of secondary dendrite arms and they do not always maintain the same shape. It is in this region where the material properties will be inspected. Figure 4-4 shows the parallel dendrites, and their spacing in the region of interest for testing purposes.

Clearly the nature of welds is one of significant inhomogeneity. Unlike normal wrought materials, the difficulty of studying welds is complicated by the unique structures found in the weld metal. Predictably, the weld properties are a function or the geometry and the location in the weld. For this reason it is very important to test as close to the same region as possible. Furthermore, the dendrites along the weld centerline boundaries that run orthogonal to direction of applied force in the tests of this study are parallel in nature. For these reasons, understating the microstructure of the weld and maintaining a consistency of testing location is of utmost importance.

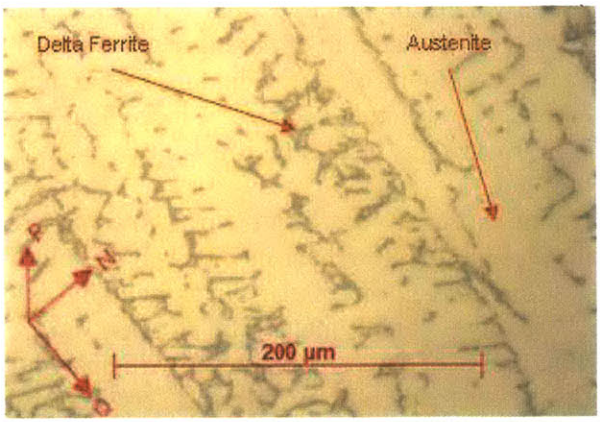

Figure 4-4 Optical micrograph showing dendrite spacing, austenite and delta ferrite in an as-welded, low-ferrite material. In materials testing, cracking will be in the Q direction.

4.4 Tensile Testing

Standard tensile testing was performed at 25°C for the entire sample matrix and at 288°C for those matrix points representing aging at 400°C. Testing was carried out in accordance with ASTM E8 on an Instron 8500R load frame [58]. Elevated temperature testing was conducted in a 6.9 kW Thermocraft furnace. Tensile specimens were of the

standard specimen dimensions of 25.4 mm gauge length as specified in ASTM E8. Two samples are machined from each weld blank, yielding different weld fusion zone content in each gauge length. The weld center line was in the middle of the gauge length and the sample was machined such that it represents the principle stress direction. The purpose of the tension testing was to identify uniaxial tensile strength as defined by a 0.2 mm/mm offset and the ultimate tensile strength prior to fracture. The specimens were labeled with the blank number and "A" for the wider portion of the weld and "B" for bottom portion of the weld. Figure 4-5 shows the dimensions of the specimen used. The diameter of the specimens was set at 6.35 mm in order to include at least 10 grain boundaries across the diameter per ASTM E-8 specifications. Figure 4-5 shows the approximate parent material, HAZ and weld metal zones contained in each specimen.

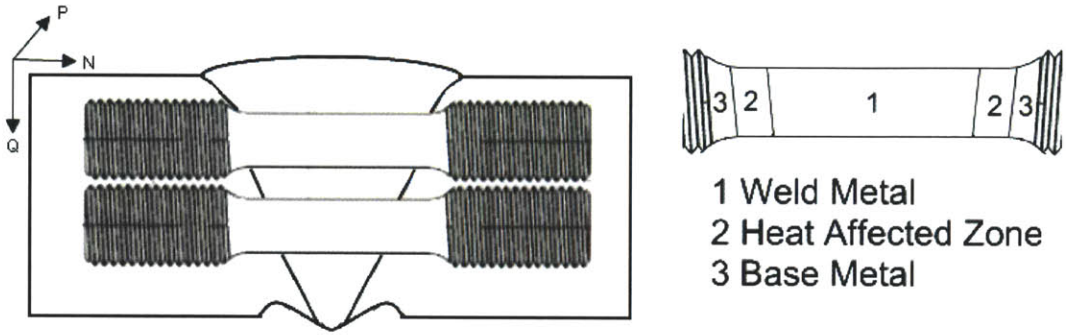

Figure 4-5 Tensile specimen weld location and constituency.

4.5 Fracture Toughness Testing

Fracture toughness testing was completed using 1T-CT specimens machined such that the fracture surface was coplanar with the center line of the weld in the PQ plane. The 1T-CT specimen was constructed and the fracture toughness tests were carried out in accordance with ASTM E1820 [59]. Precracking was performed always to the same a/W value of 0.58 as it can be shown that the properties of a weld change as a function of location in the weld. Crack length was measure using the direct current potential drop (DCPD) method. For samples in air, load is applied by an Instron® 8500R load frame with temperature elevation provided by a 6.9 kW Thermocraft furnace. In-situ testing is performed in the SCC apparatus as described below. For all tests the strain rate is 0.025 to 1.27 mm/min with data taken continuously by the data acquisition and control (DAC) system.

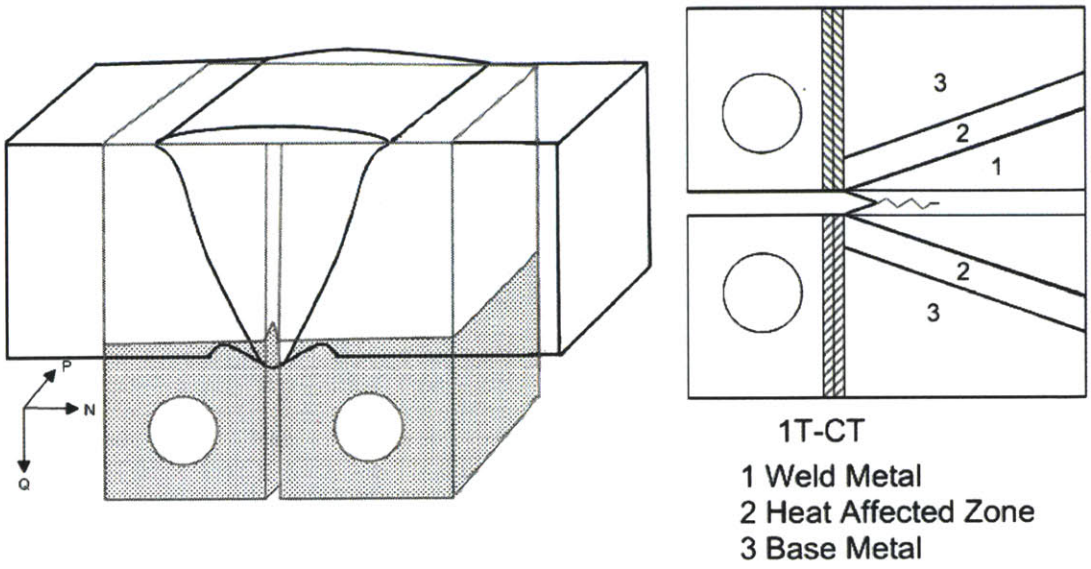

Figure 4-6 Drawing showing EB weld location for fracture toughness/SCC crack growth specimens.

Further details of the construction of the 1T-CT specimen will now be described. Figure 4-6 illustrates the sample used for all fracture toughness, fatigue crack growth rate and SCC growth rate testing. Since it was used in such a wide variety of tests the construction of the samples will only be described once. Since the wall thickness of the pipe is less than 63.5 mm, extra material was E-beam welded onto the blanks cut from the pipe and plates. The EB welding process was chosen for its high energy density resulting in essentially no distortion and minimal heat-affected zone. 1T-CT specimens were then machined using an electro-discharge process. The dimensions are consistent with ASTM E-647 and E-1820 and the International Cooperative Group on Environmentally Assisted Cracking standards. Figure 4-6 shows the orientation of the compact tension specimen blanks that were produced to accommodate for the fact that SCC grows from the inside diameter to the outside diameter. Figure 4-6 also shows the orientation to the weld [59,60].

Sample preparation for 1T-CT specimens begins with one compressive stroke that reaches the maximum stress intensity that will be applied during precracking. This is done in order to create a plastic zone in order to initiate the crack. Following the initial compressive stroke, the precracking is performed in 5 steps with decreasing K in each step, each step length is chosen to be longer than the plastic zone created by the previous step. This is repeated until an a/W of 0.58 is reached.

Fracture toughness testing is not as common as other forms of material characterization and the process will be briefly described. As stated above, the crack is sharpened using fatigue precracking. Fracture toughness testing was initiated from the lowest applied load in the last step of precracking. The test was performed in constant strain rate. The same method is used in-situ but at a slower strain rate. Temperature is maintained at within 3°C of the test temperature in accordance with [59]. In the beginning of the fracture toughness test, the crack tip was sharp, illustrated as point 1 in Figure 4-7. As the stress intensity

builds up, the crack tip begins to blunt, shown as seen at point 2. The crack tip continues to blunt until completely stretched, the radius of the circle which is formed is the stretch zone width (SZW). This is illustrated as point 3. At this point, the crack propagation behaves as a series of tensile specimens. Once the crack has grown 0.2 mm, which is delineated by the 0.2 mm offset line, shown in Figure 4.7, in the fracture toughness graph, the point of fracture toughness, J_{IC}, is recorded. Following this point, the material undergoes stable tearing. This is point 4 in Figure 4.7. The slope of the stable tearing zone demonstrates the required energy to maintain crack propagation - the lower the slope, the easier to maintain crack growth. Stable tearing is maintained for up to 4 mm prior to securing the test. [61]

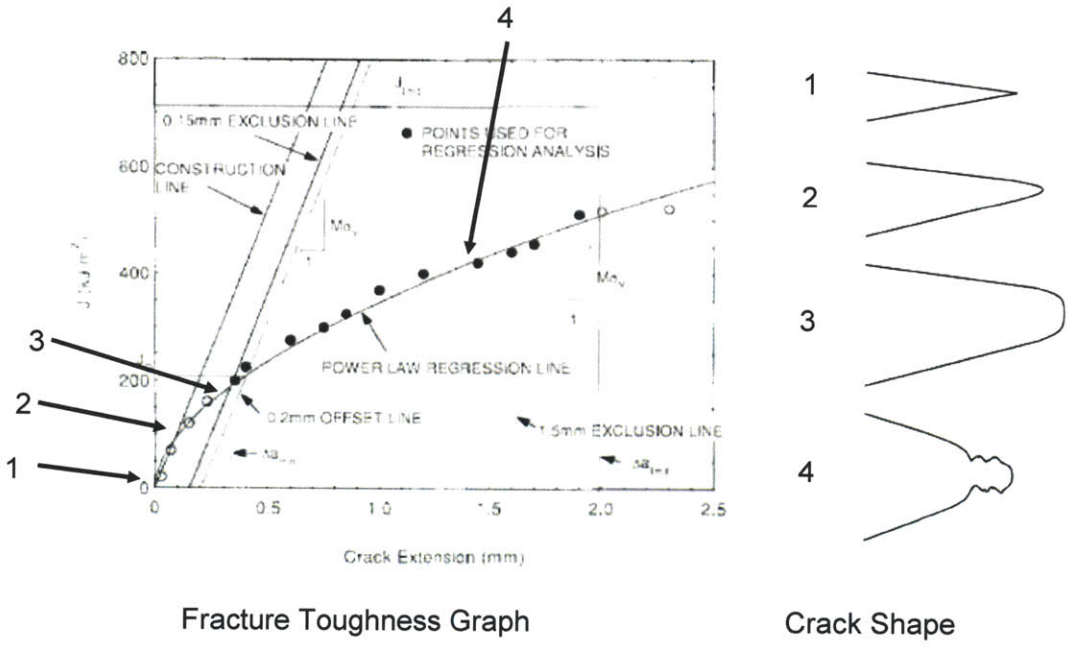

Figure 4-7 J-R Curve construction and corresponding crack tip shape [59].

4.6 Stress Corrosion Cracking and Fatigue Crack Growth Rate Testing

Stress corrosion cracking experiments were conducted in normal boiling water reactor conditions of 300 ppb oxygen, 10.5 MPa, and 288°C. The experiment consists of three main parts, environmental control, loading and DAC. The environment was controlled using a custom built water purification system connected to a 3.8 l autoclave. The purpose of the water purification system was to maintain the exacting chemical standards of the BWR environment. An autoclave maintained the sample and surrounding water at 288°C and, with the assistance of a charging pump and back pressure regulator, at 10.5 MPa and a dissolved oxygen concentration of 300 ppb. Loading of the sample was applied and controlled by an Instron® 8800MR load frame and controlled by a custom program receiving input from the DAC system. The DAC measured all relevant parameters of the system including temperature, pressure, load, chemistry as well as providing loading patterns from a preprogrammed routine and emergency shutdown

protection. Measurement of crack length was conducted using the DAC via the DCPD method and averaged over 10 data points to give crack length based on the changing resistance of the sample with crack growth. Standard 1T-CT specimens as described above and in ASTM E1820 were used with the sample machined such that the cracking occurs along the center line from the root of the weld, propagating toward the outside of the weld along the PQ plane. The sample was precracked in air in accordance with ASTM E1820, and then transferred to the BWR environment. At this point the sample underwent a series of sine wave loading at decreasing frequency and increasing R-value (P_{min}/P_{max} where P is the applied load) as a slow approach to constant loading. This data was recorded for the purpose of comparison to establish fatigue crack growth rate date. The final step prior to constant loading was usually a trapezoidal load pattern giving a nearly constant load for some duration. In this way the crack is preconditioned and sharpened for SCC to occur. Furthermore, the preconditioning usually lasted approximately 1700 h before constant stress intensity factor (K) loading was achieved. This was to ensure proper stabilization of the environmental factors prior to the commencement of SCC crack growth rate testing. SCC was usually noted after more than 500 h at static loading and allowed to run until a steady CGR is reached. Environmental tests, termed, in-situ, were completed with a standard fracture toughness test as in section 4.5.

Figures 4-8 and 4-9 show photographs of the autoclave and environmental test system. Figure 4-10 shows a schematic representation of the environmental test system. Figure 4-8 shows the water feed and makeup system while Figure 4-8 shows the inside of the autoclave installed in the servo-electric fatigue/slow strain rate machine. The autoclave system was fully instrumented for oxygen, hydrogen, pH, and conductivity measurement for both the inlet and outlet water. The corrosion potential was measured using both Pt and Cu/Cu_2O reference electrodes placed in the autoclave immediately adjacent to the test specimen. The test specimen was insulated from the grips via ZrO_2 inserts in the grips and washers. All of the hot sections of the autoclave/piping system are constructed of titanium. The low temperature metal components in the loop are made from stainless steel. Distilled and demineralized water was supplied to the makeup system (the right hand side of Figure 4-8) from the laboratory water supply system. The makeup system then circulates the water through a demineralizer/filter system to assure cleanliness. Makeup water was supplied to the autoclave system where chemistry could be adjusted from a hydrogen overpressure to an oxygen overpressure. Provision was made for injection of chemicals as well as for gas purging. Treated water was then supplied to the autoclave using a circulating piping system. Water conductivity as low as 0.05 μS/cm was routinely achieved.

The system was capable of operation over the oxygen range from essentially zero (< 2 ppb) to air (or oxygen) saturated conditions with adjustable conductivity. Flow paths were as follows: water from the glass main water column is drawn through a booster/recirculation pump where it splits. The majority of the water mixes with the demineralized and filtered water that had exited the autoclave and returns to the glass column. This recirculation is necessary for mixing when impurities are injected and also to aid in mixing in dissolved gases. The circulation rate was 12 l/h, leaving the

booster/recirculation pump and going to the charging pump where the pressure increased to 10.5 MPa. This water was heated in the regenerative heat exchanger and preheater before entering the autoclave. The autoclave also has an external heater to maintain a constant temperature. The water leaving the autoclave is cooled in the regenerative heat exchanger and cooler before reducing pressure to about 0.04 MPa at the back pressure regulator. Conductivity was then measured before the water is demineralized, filtered, and returned to the glass column. A dissolved O_2 meter is placed on a separate sampling line before the demineralizer and empties to drain. A separate make-up water loop is provided for any water losses that may occur during the multiple month testing.

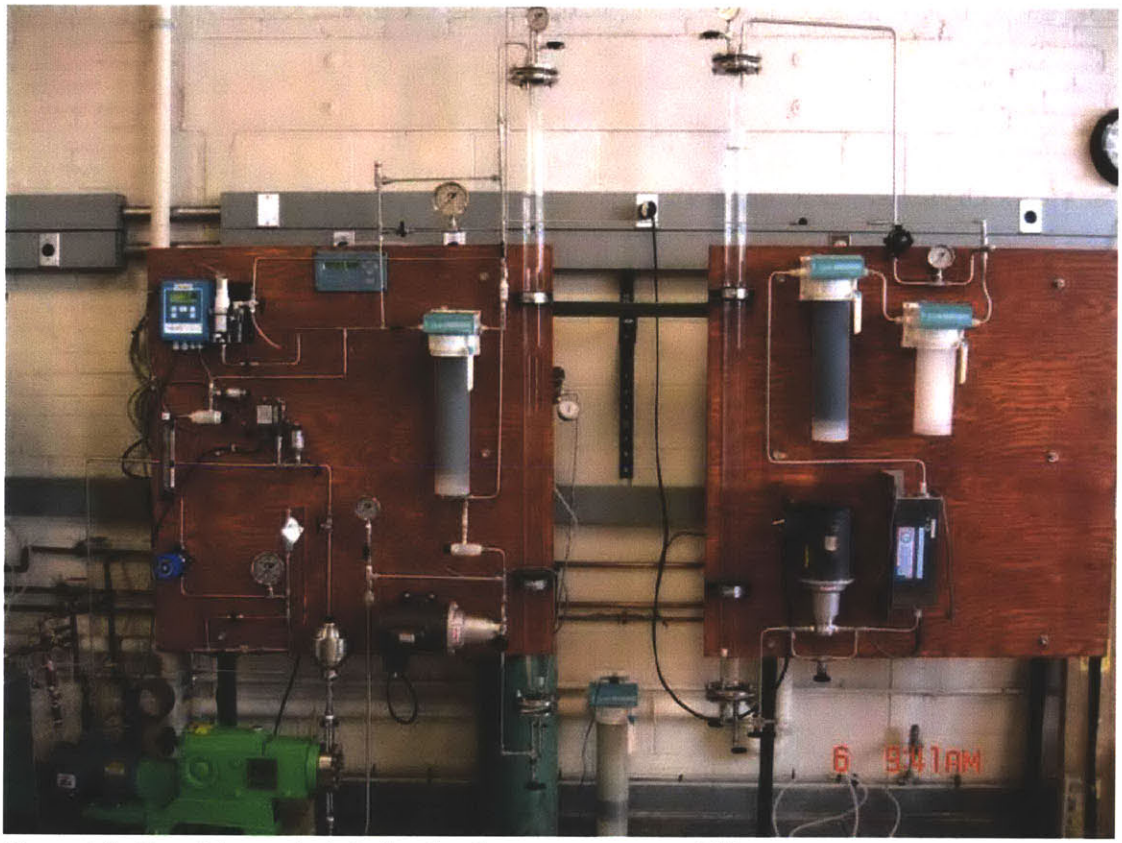

Figure 4-8 Chemistry control, feed and make-up water system [57].

Figure 4-9 Photograph of autoclave internals with completed SCC/ in-situ fracture toughness specimen installed.

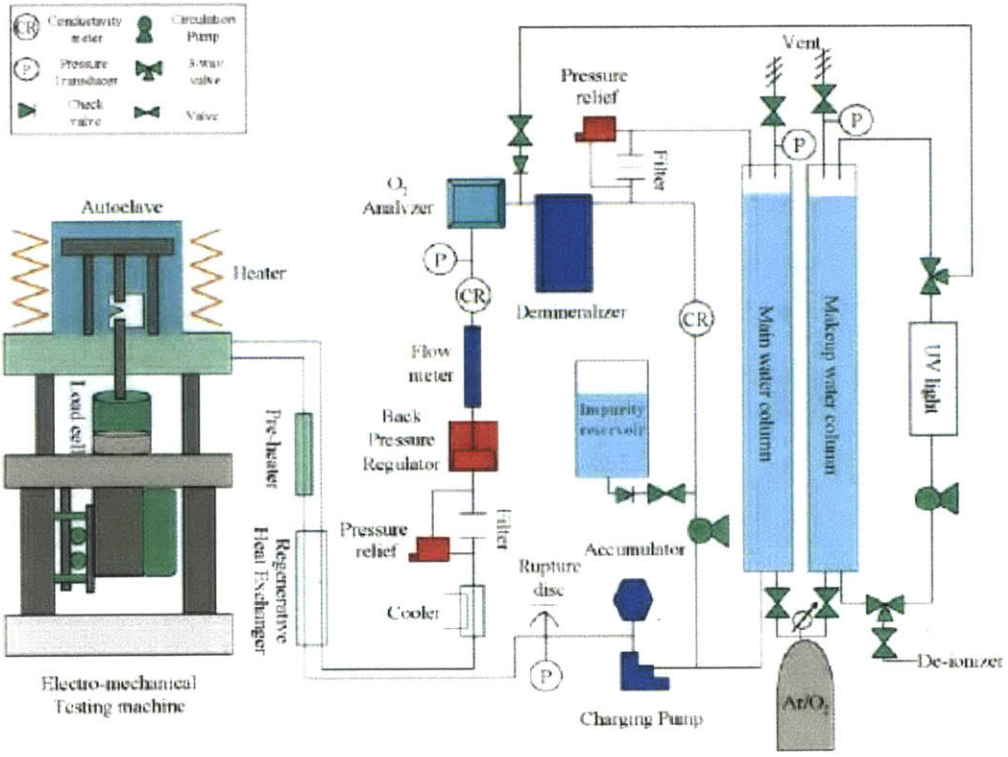

Figure 4-10 Schematic representation of environmental test system [57].

Charpy-V Impact Testing

Notched Bar Impact testing, also known as Charpy-V notch impact testing, was carried out in accordance with ASTM E23 [62]. The purpose of Charpy-V impact testing was to

measure a material's fracture energy during high strain rate fracture. This was accomplished by placing a notched specimen into a calibrated pendulum apparatus which swings and impacts with a known force. After fracture of the sample the pendulum continues to reach some height. By comparing the initial and final height of the pendulum the absorbed energy, and therefore fracture energy, can be obtained. Charpy-V impact testing was performed by Massachusetts Materials Research Inc, of W. Boylston, MA, USA. Testing was performed at 25°C and 288°C over the entire sample matrix. Samples were machined such that the plane of fracture was co-planer with the weld center line, occurring on the PQ plane along the centerline. Furthermore, fracture occurs in the radial direction. Figure 11 shows the orientation of the specimens with the V-notch facing the weld root. Three samples are machined from each weld blank which yielded varying degrees of weld fusion zone in each sample. The specimens were labeled by the blank number and either "T", "M", or "B" for "top," "middle," and "bottom", respectively.

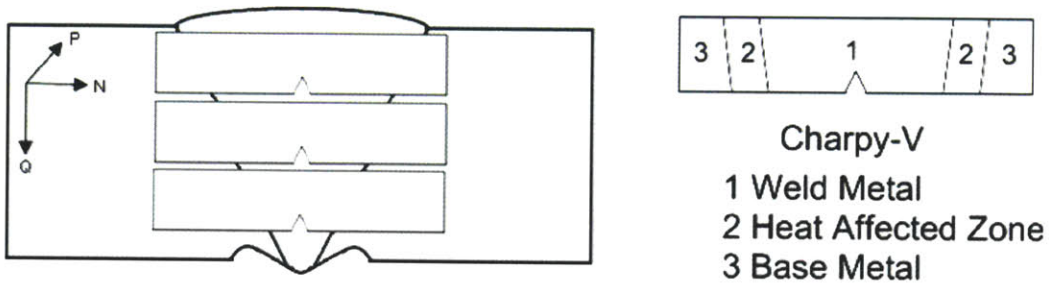

Figure 4-11 Indication of Charpy-V notch machining locations.

5 Results

The results of the material property characterization are summarized below. The general trend for tensile properties showed that with time there was a slight increase then a decrease in yield strength but an increase in ultimate tensile strength. SCC crack growth rate increases with aging time and in-situ fracture toughness decreases for high-ferrite and increases with low-ferrite material. In-situ fracture toughness is much lower than that of equivalently aged air samples.

5.1 Tensile Testing

Tensile testing has been completed on all samples at 25°C and on the 400°C high- and low-ferrite materials at 288°C. The data is shown graphically in Figures 5-1 through 5-4 and in Table 5-1. Figure 5-4 shows a typical stress-strain curve obtained for the tensile tests. The fracture surfaces of the tensile specimens were analyzed using a scanning electron microscope (SEM). Figure 5-5 shows the ductile nature of the fracture at 288°C, which is typical of all the tensile specimens. Fracture occurred on the PQ plane of the weld, and as such, any fractography of the fracture surface is along that face.

The most dramatic change was noted in the first 1000 h of aging, with the full effect of the spinodal decomposition reaction occurring by 5000 h. The data sets inflect and show a slight drop in tensile strength. It should be noted, however, that testing weld specimens comes with a great deal of difficulty as each weld structure is made up of a series of parallel but arching dendrite patterns. As a result, the location in the gauge length where plastic deformation occurs can have an impact on data scatter. In the high temperature testing, plastic deformation, tearing and failure frequently occurred in the heat affected zone region, as this is the softest and weakest area. The graphical data only shows data points where this did not occur.

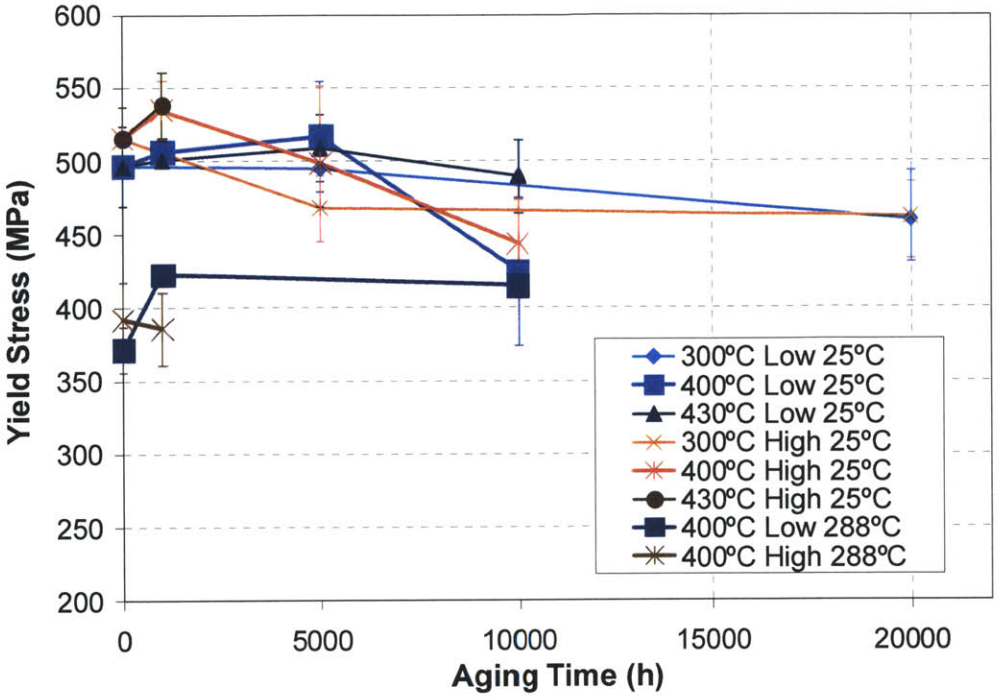

Figure 5-1 Yield stress as a function of aging time, temperature and ferrite number at 25°C and 288°C in air testing conditions.

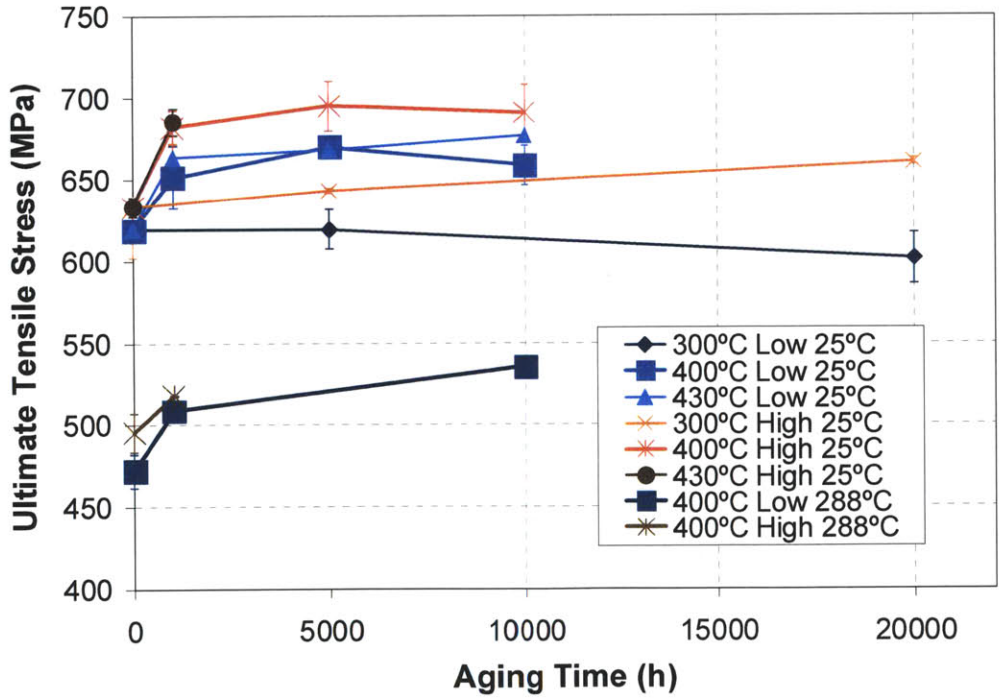

Figure 5-2 Ultimate tensile stress as a function of aging time, temperature and ferrite number at 25°C and 288°C in air testing conditions.

Table 5-1 Tensile Testing Summary.

				Tensile Properties							
Ferrite Content	Aging Temperature	Aging Time (h)	Sample #	Yield Stress (MPa)	Average Yield Stress (MPa)	Ultimate Tensile Stress (MPa)	Average Ultimate Tensile Stress (MPa)	Elongation (%)	Average Elongation (%)	Reduction in Area (%)	Avg. Reduction in Area (%)
Low δ-ferrite 25 °C	As-Welded	0	41A	470	**497**	602	**619**	31	**26**	59	**54**
			41B	524		636		21		49	
	300 °C	5,000	3A	498	**494**	632	**620**	30	**30.5**	65	**65**
			3B	490		607		31		65	
		20,000	111A	486	**460**	585	**601**	27	**25**	54	**57**
			111B	434		617		23		60	
	400 °C	1,000	78A	498	**506**	633	**652**	39	**34.5**	64	**61.5**
			78B	515		671		30		59	
		5,000	122A	479	**517**	663	**671**				
			122B	554		678					
		10,000	121A	374	**424**	647	**659**	36	**35**	80	**73.5**
			121B	474		672		34		67	
	430 °C	1,000	72A	500	**501**	656	**664**	33	**26.5**	64	**70.5**
			72B	503		673		20		77	
		5,000	47A	486	**509**	666	**669**	28	**26**	56	**56.5**
			47B	532		672		24		57	
		10,000	19A	464	**489**	677	**677**	32	**34**	78	**66.5**
			19B	514		678		36		55	
High δ-ferrite 25 °C	As-Welded	0	225A	537	**516**	639	**633**	33	**30**	69	**67**
			225B	495		627		27		65	
	300 °C	5,000	214A		**468**	642	**644**	42	**36.5**	80	**74**
			214B	468		645		31		68	
		20,000	253A	431	**462**	659	**661**	28	**32**	64	**68**
			253B	493		663		36		72	
	400 °C	1,000	236A	555	**535**	693	**683**	36	**29.5**	69	**75**
			236B	515		672		23		81	
		5,000	242A	552	**499**	712	**696**	37	**37**	77	**79**
			242B	446		681		37		81	
		10,000	203A	414	**444**	674	**692**	35	**34.5**	78	**77**
			203B	474		709		34		76	
	430 °C	1,000	143A	516	**538**	694	**686**	24	**20.5**	59	**70**
			143B	561		678		17		81	
		5,000	165A	468	**447**	685	**675**	37	**34.5**	80	**80**
			165B	425		665		32		80	
		10,000	159A	409	**450**	659	**671**	58	**47**	80	**79**
			159B	491		683		36		78	
Low δ-ferrite 288 °C	400 °C	0	83a	387	**372**	462	**472**				
			83b	356		483					
		1,000	58a	423	**423**	513	**509**				
			58b	423		504					
		5,000	75a	283	**271**	481	**482**				
			75b	260		483					
		10,000	1b	415	**415**	536	**536**				
High δ-ferrite 288 °C	400 °C	0	132a	417	**392**	484	**496**				
			132b	367		507					
		1,000	170a	410	**386**	519	**518**				
			170b	361		518					
		5,000	176a	354	**378**	532	**530**				
			176b	402		529					
		10,000	181a	424	**387**	547	**533**				
			181b	349		520					

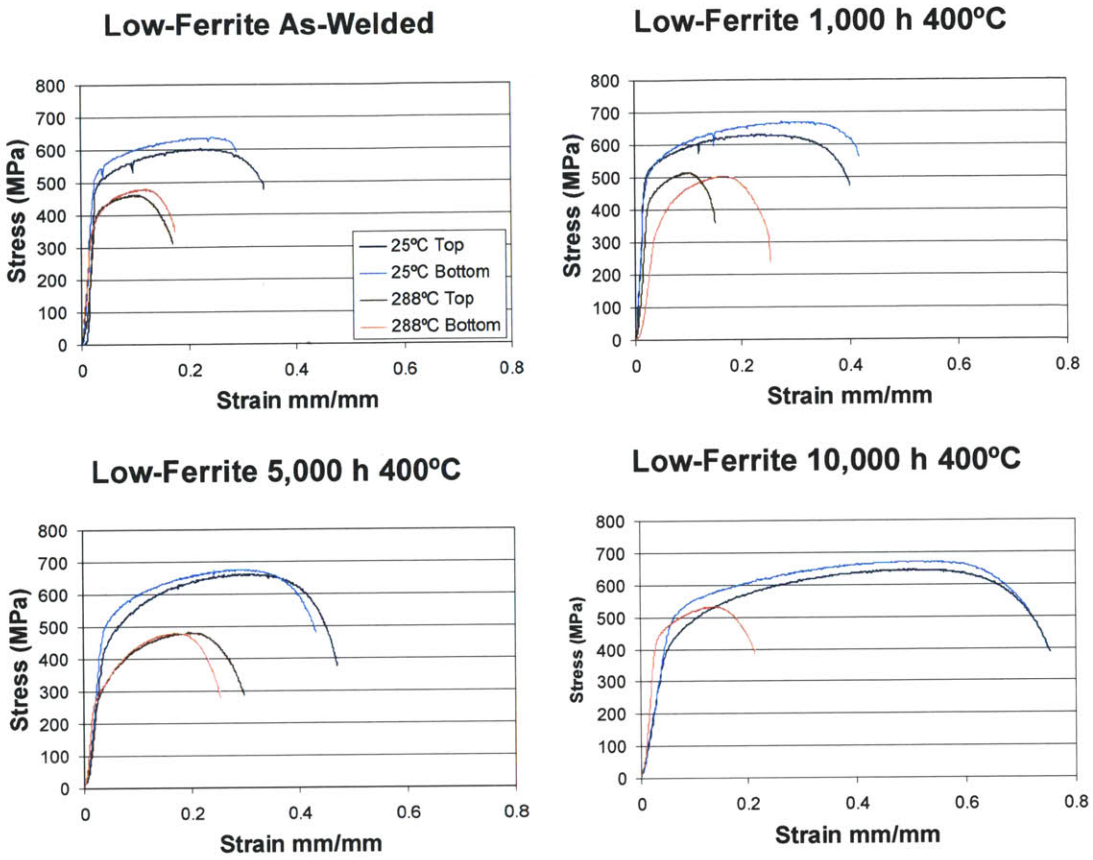

Figure 5-3 Low-ferrite tensile data showing lower strength and integrated toughness in the elevated temperature test.

The data for the as-welded material shows similar trends as for the as-welded fracture toughness behavior to be shown later. In a tensile test the area under the stress-strain curve is indicative of toughness, in Figure 5-3 it is clear that the higher temperature tests result in lower strength and toughness. Material labeled "Top" is from the outside of the weld, while that labeled "Bottom" is from closer to the root of the weld. Furthermore, the difference in toughness can be seen as a function of aging and ferrite number.

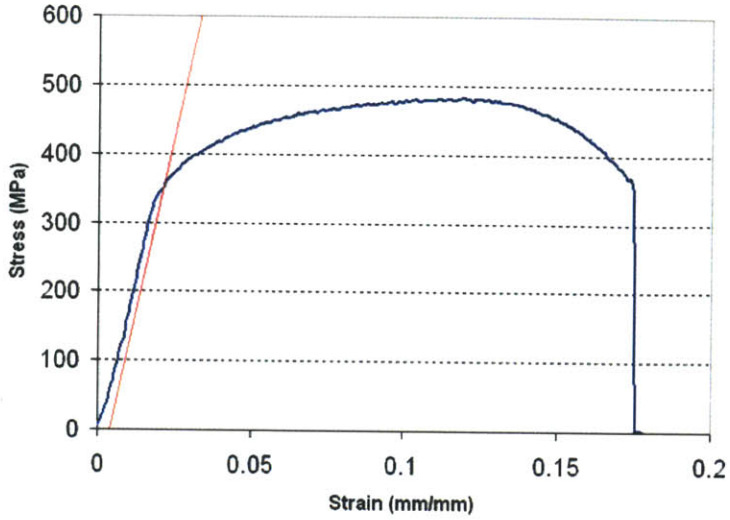

Figure 5-4 Stress-strain plot for low-ferrite, as-welded sample tested at 288°C

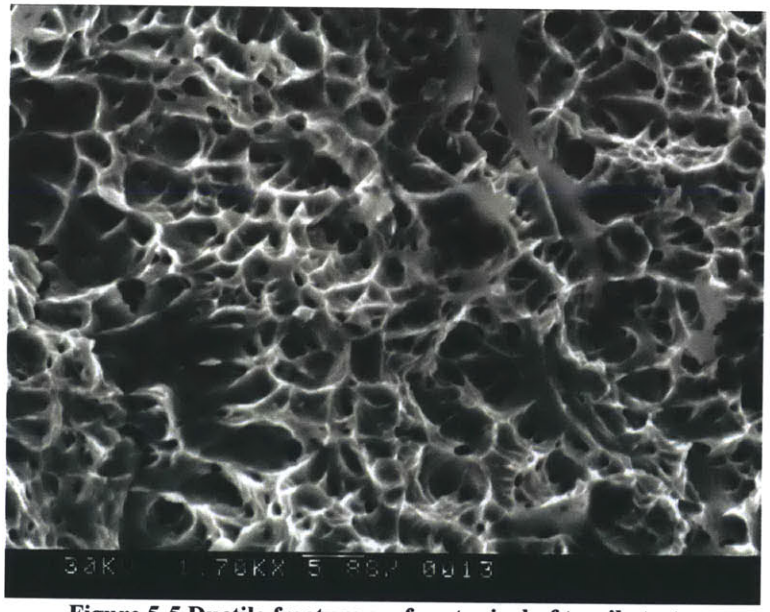

Figure 5-5 Ductile fracture surface typical of tensile tests.

Further inspection of the fracture surfaces yielded several inclusions of interest, which are not shown, each analyzed with energy dispersive x-ray (EDX) spot analysis. Iron-chromium-rich inclusions, silicon-rich oxide, and an almost completely iron oxide particle were noted. All of these inclusions can serve as nucleation sites for fracture. However, it should be noted that there were not many inclusions within the resolution of this particular SEM. In the fracture toughness section, more inclusions will be identified. SEM and EDX for the tensile specimens was performed using a TOP-CON ABT-150 SEM.

5.2 SCC Crack Growth

SCC crack growth rate testing was performed for 4 conditions representing 400°C high- and low-ferrite, as-welded and 5,000 h aged points on the testing matrix. It should be noted that it was not possible to test all points on the matrix as SCC crack growth rate tests last from between 2,000 h to 8,800 h in the longest case. However, each specimen yielded numerous data points. While the test can be summed as giving a fracture toughness value, a stable SCC and fatigue crack growth rate, each material in reality provides several data points, insight into the particular fracture phenomena and an opportunity to tailor each test to explore unique conditions. Furthermore, while each test is of either an unaged or 5,000 h aged sample, due to the length of testing at temperature, there is aging occurring at 288°C which in the case of the 8,800 h test can be considered quite significant.

Specimens were pre-cracked in air and then tested in high purity water containing 300 ppb dissolved oxygen at 288°C. A "standard" testing sequence was used to assure that SCC crack growth would be achieved and steady state rates would be measured. This required transitioning the crack from transgranular to interdendritic by fatigue loading with a gradually increasing load ratio, R-value (P_{min}/P_{max}) and a gradually decreasing frequency.

5.2.1 SCC Crack Growth Data

Figure 5-6 shows a summary of all of the SCC crack growth data produced in the program plotted against the general disposition-line data for Type 316 stainless steel in high purity water [63]. In general, the data fall within the "universe" of data for wrought material under simulated BWR conditions. It is important to note that the actual condition of the test specimen is changing during the test. For example, test # 238 (high-ferrite, as-welded) lasted 8,600 h. Thus, while the initial condition was unaged, the actual test conditions varied during the test since, in effect, aging at 288°C during the test was taking place. The "double aging" effect is no doubt one variable in the large scatter that appears in the SCC crack growth data. Welds should normally have a considerable scatter due to the fact that they have an inherent variability in the microstructure and residual stress.

Average SCC crack growth rate for as-welded and 5000 h aged at 400°C high- and low-ferrite is shown graphically in Figure 5-7. It is clear that there is a marked increase in both high- and low-ferrite crack growth rates as a result of thermal aging. During each test, conditions were carefully controlled. In comparing each ferrite number, it is evident that there is a larger aging impact on the high-ferrite material than the low-ferrite material, indicating that the change in SCC resistance is occurring partly as a result of the increase in δ-ferrite content, as that is the main variable in the weld. Indeed, in SEM and optical microscopy of the fracture surface we can see that there is preferential cracking occurring along the δ-ferrite dendrite core region as will be discussed below.

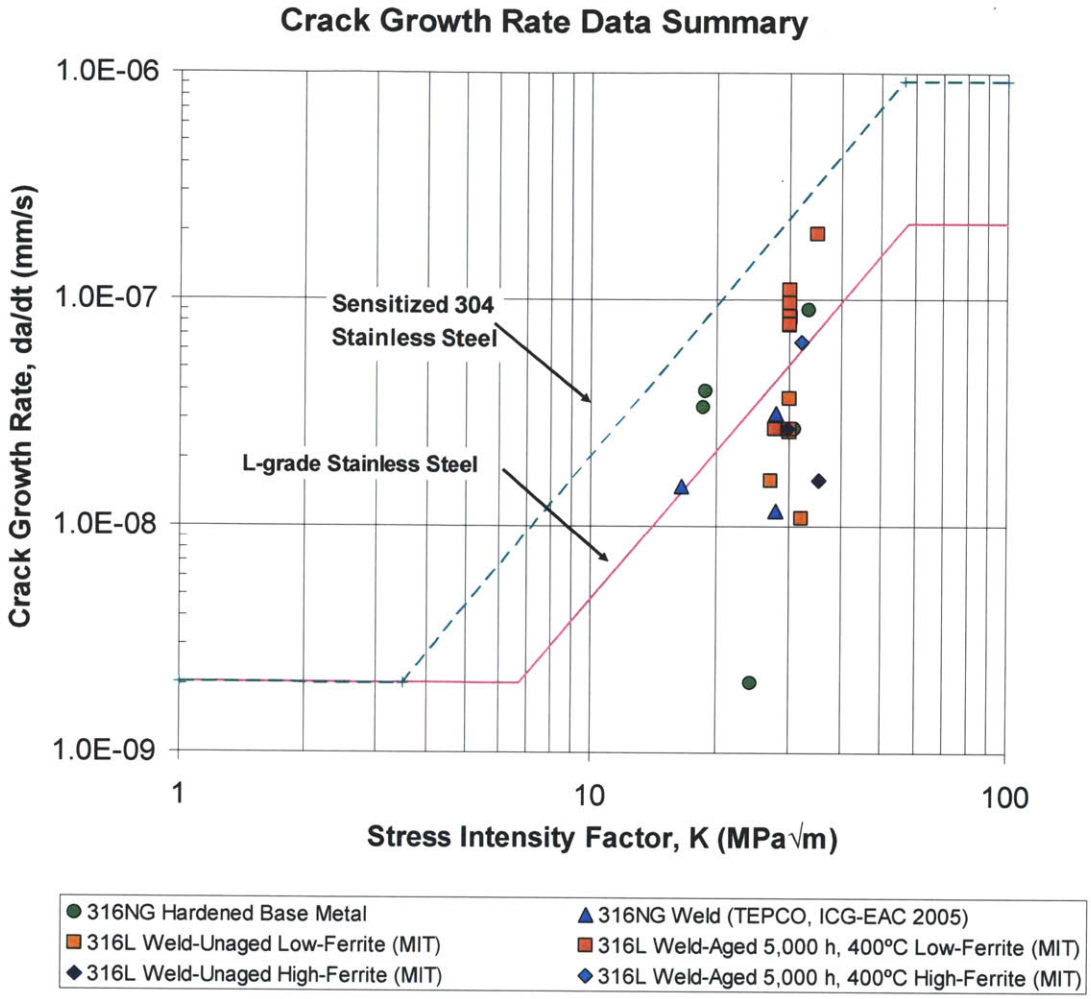

Figure 5-6 Summary of average SCC crack growth rates plotted with Type 304 and 316L design lines [63].

Comparing with SCC growth rate (1.1~2.6 x 10^{-8} mm/s) of as-welded material, the aged weld shows approximately an approximate order of magnitude higher SCC growth rate (0.9~2.1 x 10^{-7} mm/s) at constant loading conditions. Spinodal decomposition and consequent local re-distribution of chromium in δ-ferrite and an increase in precipitation size due to growth are believed to be mainly responsible for the increased SCC growth rate in thermally aged welds. Once again, the crack path is largely interdendritic, as will be shown in the fractography below.

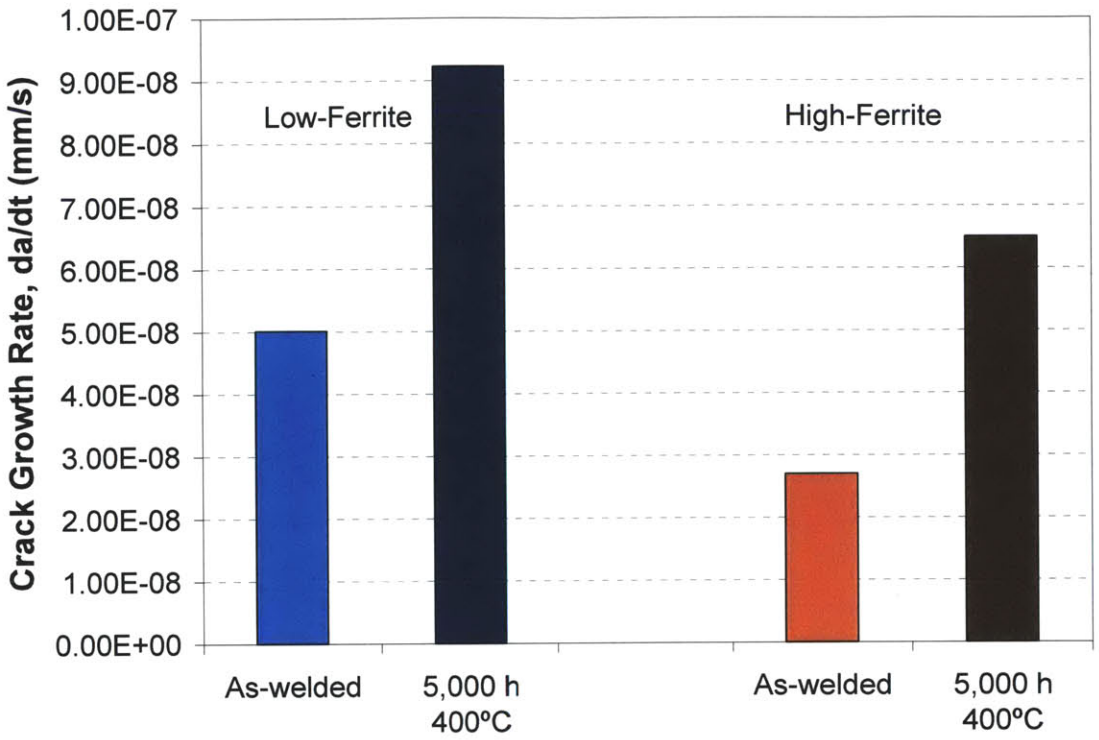

Figure 5-7 Average SCC crack growth rate for K of 30 MPa√m.

The standard procedure to prepare the 1T-CT specimens for in-situ testing was to perform routine in air precracking beginning with one compressive stroke to less than the maximum allowed load. This was followed by cyclic loading with successive decrease in K_{max} until the final a/W was reached. Once the sample is placed in-situ and the environment meets specifications, the crack is further grown under fatigue. The final crack sharpening step is a trapezoid, followed by constant loading, where SCC initiates and propagates.

Figure 5-8 shows the test record for a low-ferrite as-welded test. The figure shows the test plan and crack growth record, metallography of the material will be shown below. The crack was conditioned for SCC through 8 steps, initially increasing K_{max} and R-value and then logarithmically decreasing frequency of fatigue. The only issue of note is the flat area occurring in step 3 between approximately 50 and 300 h. During this time a filter became clogged and the test was unloaded until repair was available. Finally in the 8th step a trapezoid approach to constant loading was used. Step 9 was constant loading and SCC was noted after approximately 500 h of hold time. The maximum crack growth rate that was seen in the SCC region was 8.33×10^{-8} mm/s at a K value of 30.41 MPa√m. The observed crack growth rate is plotted in Figure 5-6 as well. Figure 5-9 shows the chemistry during the test. Both conductivities and electrochemical potential (ECP) of the bulk environment were recorded in order to verify that proper chemistry is maintained. ECP was recoded with a Cu/Cu_2O electrode. Dissolved oxygen is also kept steady at 300

ppb. Upon completion of testing, samples are removed from the autoclave and split in half for post-mortem analysis.

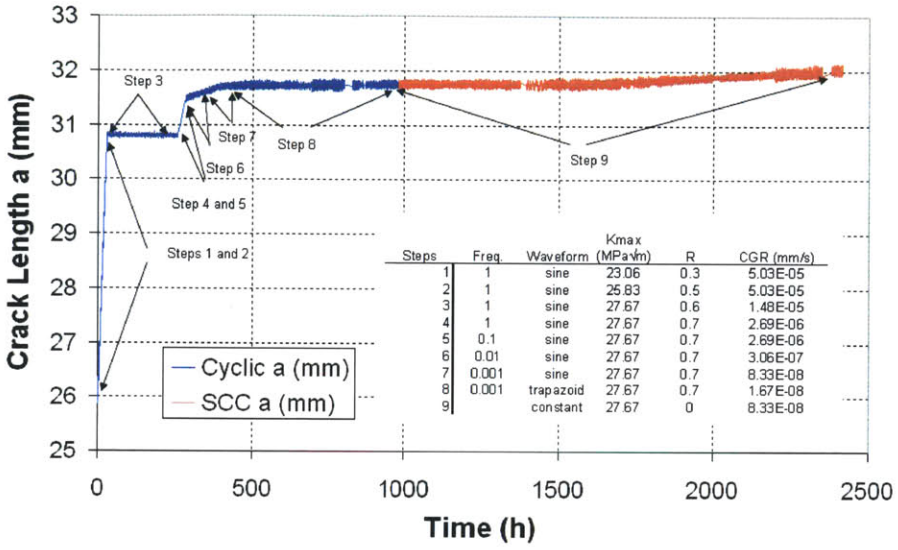

Figure 5-8 Crack Growth Rate (CGR) data for unaged, low-ferrite material.

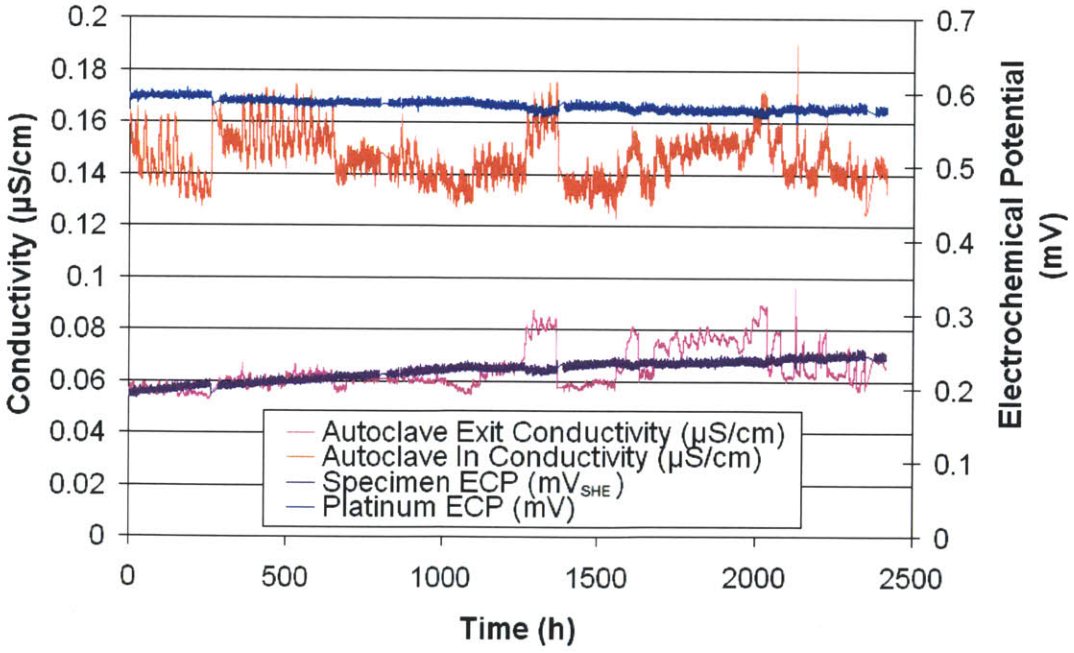

Figure 5-9 Chemistry during the crack growth rate experiment.

5.2.2 As-Welded SCC Fractography

An SEM micrograph montage is shown in Figure 5-10. The step changes are highlighted in red. Step 9 and beyond will be the focus of the fractography Figure 5-11 shows a clear change in the fracture morphology when the constant loading began. Also visible in Figure 5-11 are the secondary crack extensions created during SCC.

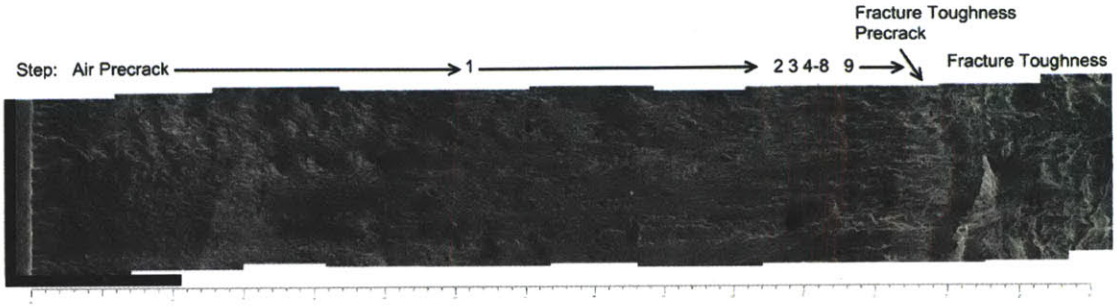

Figure 5-10 SEM micrograph montage of low-ferrite as welded material showing crack front progression through all stages of precracking and testing. SCC occurred during step 9.

In the micrograph in Figure 5-11, SCC secondary cracks are clearly visible. Note that the cracks are approximately 100 to 200 μm apart. Furthermore, in Figure 5-11 a columnar transgranular structure is visible in the precracking area, also with a similar spacing to interdendritic SCC. This spacing is dictated by the weld's dendritic structure that evolves during cooling. The montage of Figure 5-10 was also done in order to validate DCPD data. In all cases initial DCDP data contains less than 8% error over optically measured values. This is due in part to the use of side grooves in the 1T-CT sample construction.

For further post-mortem studies of the SCC region, half of the specimen was sectioned further in the crack area. This allowed examination along the plane normal to the welding direction, the NQ and PN planes. The samples were then mounted and polished to 0.05 μm finish. Polished samples are etched using Kalling's reagent, as in all optical fractography.

Figures 5-1 through 5-26 are micrographs obtained from the as-welded low-ferrite material. Similar fractography was obtained for all SCC samples, however, to demonstrate the main mechanisms of SCC in welds, only this sample is shown. For the aging discussion, another sample will be shown.

Optically, Figure 5-19 shows the secondary crack path propagation occurring along or seeking dendritic boundaries. Unfortunately due to the nickel coating and Bakelite mounting the etching was not as clear as desired. In Figure 5-21, parallel fracture is occurring in succession. This is likely preferential slip based on the crystallographic (111) planes for FCC austenite. Dendrites grow preferentially on the <100> crystallographic direction.

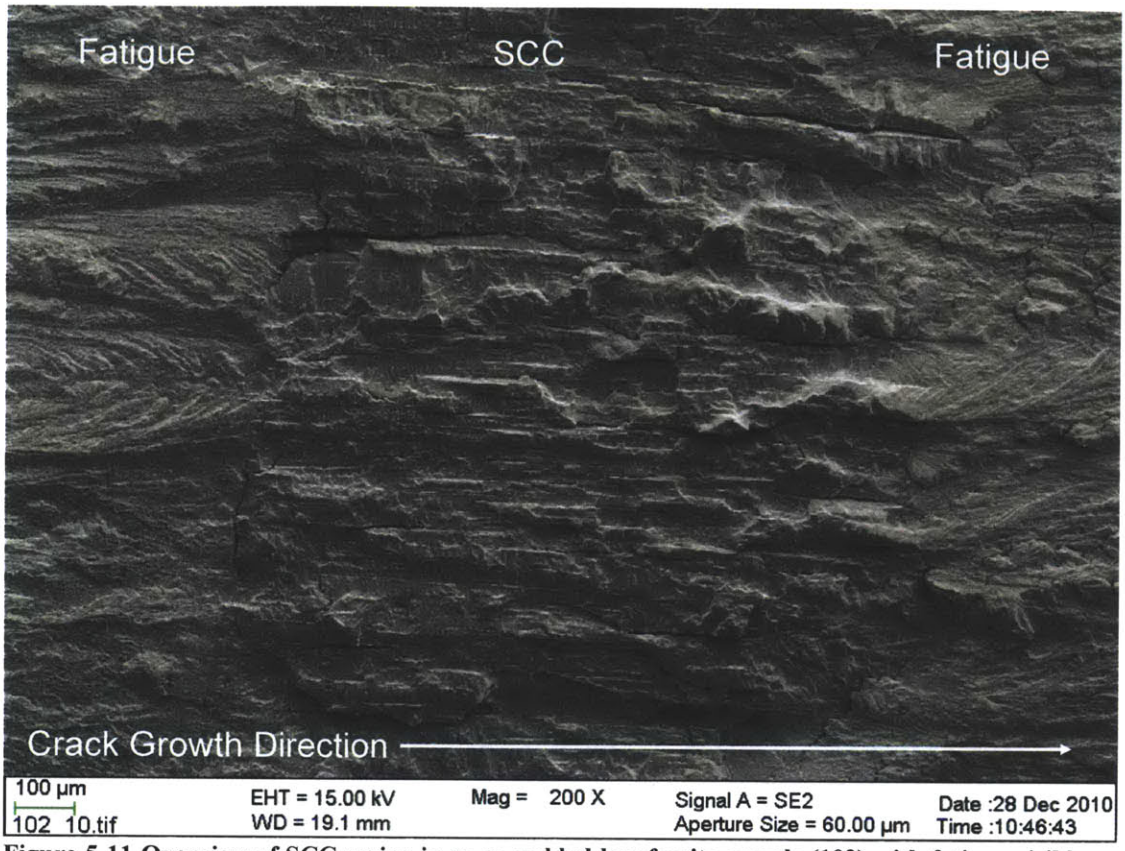

Figure 5-11 Overview of SCC region in an as-welded low-ferrite sample (102) with fatigue visible on both sides of the SCC region.

Figure 5-11 above shows a clear overview of the SCC region. Crack growth is from left to right, and this image is taken on the PQ plane, which is the main cracking face and situated normal to the applied load. Unless otherwise shown in a fractograph, this is the plane of viewing. The SCC region is bordered on each side by fatigue regions. On the left is the crack sharpening region leading to SCC, while on the right is the crack sharpening and front straightening region leading to the fracture toughness testing, to be discussed in the next section. There are several interesting features of note that can be seen in Figure 5-11. First, there are features in the fatigue region, these are carried through into the SCC region. Second, there are features in the SCC region that are carried through into the next fatigue region. The SCC secondary cracks occur with a spacing of approximately 100 µm, on the order of a few dendrites spacing. Furthermore, the SCC crack propagation front is not straight and the mechanism appears transgranular and illustrates a brittle surface. Finally, there is an oxide precipitation that is present on the fatigue surfaces that is not present in the SCC region. This in itself indicates that the chemistry at the SCC crack front is different than the chemistry at the fatigue crack front, most likely due to pumping action, as will be discussed later. Specifically, the solubility of the oxidized species is exceeded in fatigue but not in SCC. This has not been identified before but is clearly visible in the microstructures of other studies, such as [64][51]. Also, this would indicate that the precipitation occurs at the crack front.

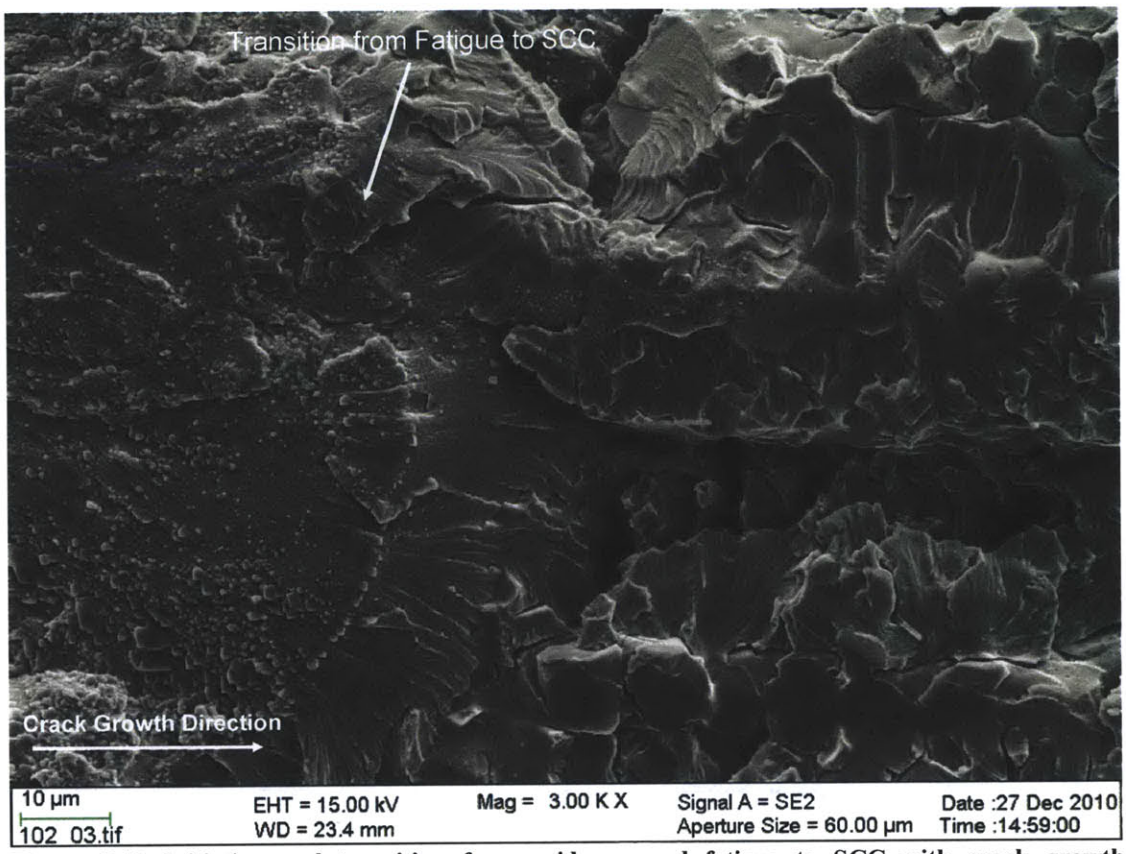

Figure 5-12 Initiation and transition from oxide covered fatigue to SCC with crack growth continuing along weld morphology.

Figure 5-12 shows a higher magnification of the transition from fatigue to SCC. It is clear that the transition occurs in a stepped manner, visible by the change of oxide precipitation and crack morphology. Initially, cracking is occurring in both the austenite and γ/δ phase boundary in the direction of crack growth. While it is not expected that they will crack at the same rates, and indeed they do not, what is important is that they are starting to crack at the same time and in the same direction. A further increase in magnification, shown below in Figure 5-13 yields even more insight. First, there is a clear difference in fracture morphology between the ferrite and the austenite phases. This is expected as they have different crystal structure. Austenite has a brittle appearance while δ-ferrite has a rounded, less brittle appearance. Also manifesting themselves in this image are precipitations. EDX confirms that these are chromium-rich carbide particles. The carbides weaken the δ/γ boundary and allow for accelerated crack growth along the boundary.

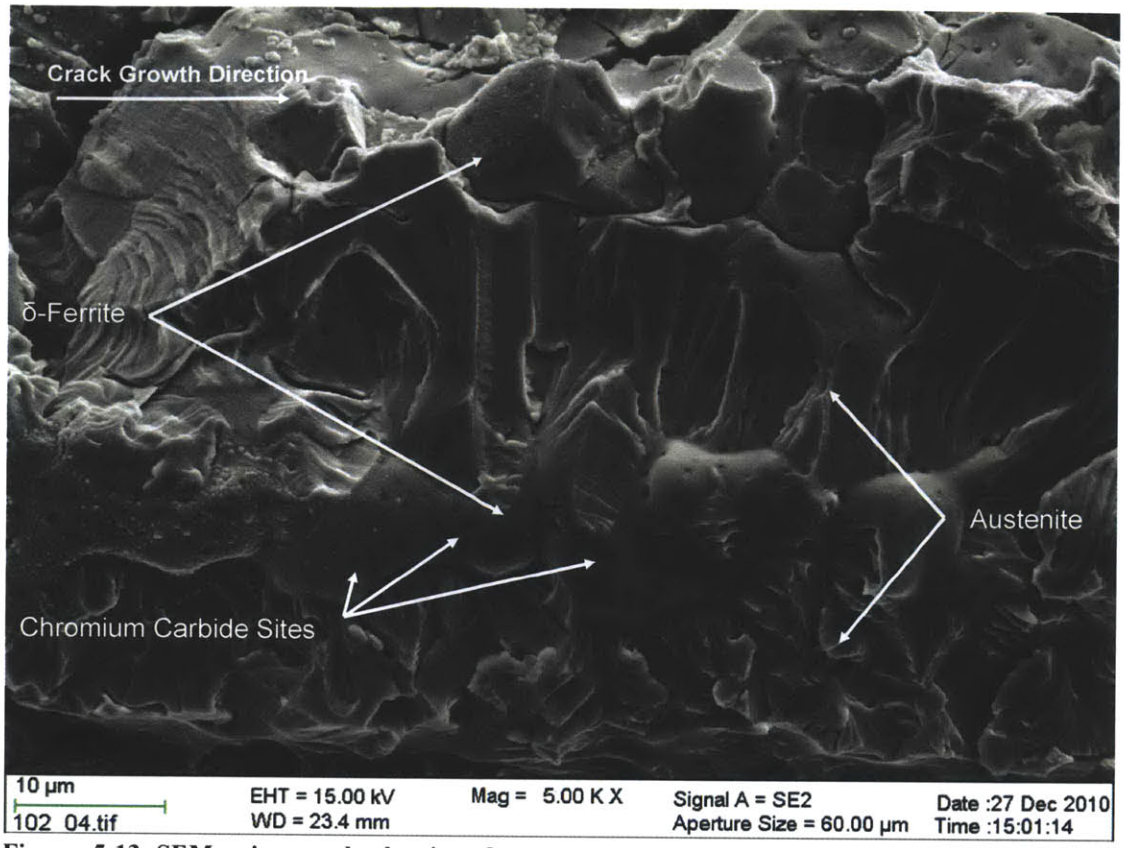

Figure 5-13 SEM micrograph showing the presence of carbide precipitation on the δ-ferrite boundaries and perpendicular brittle cracking in austenite.

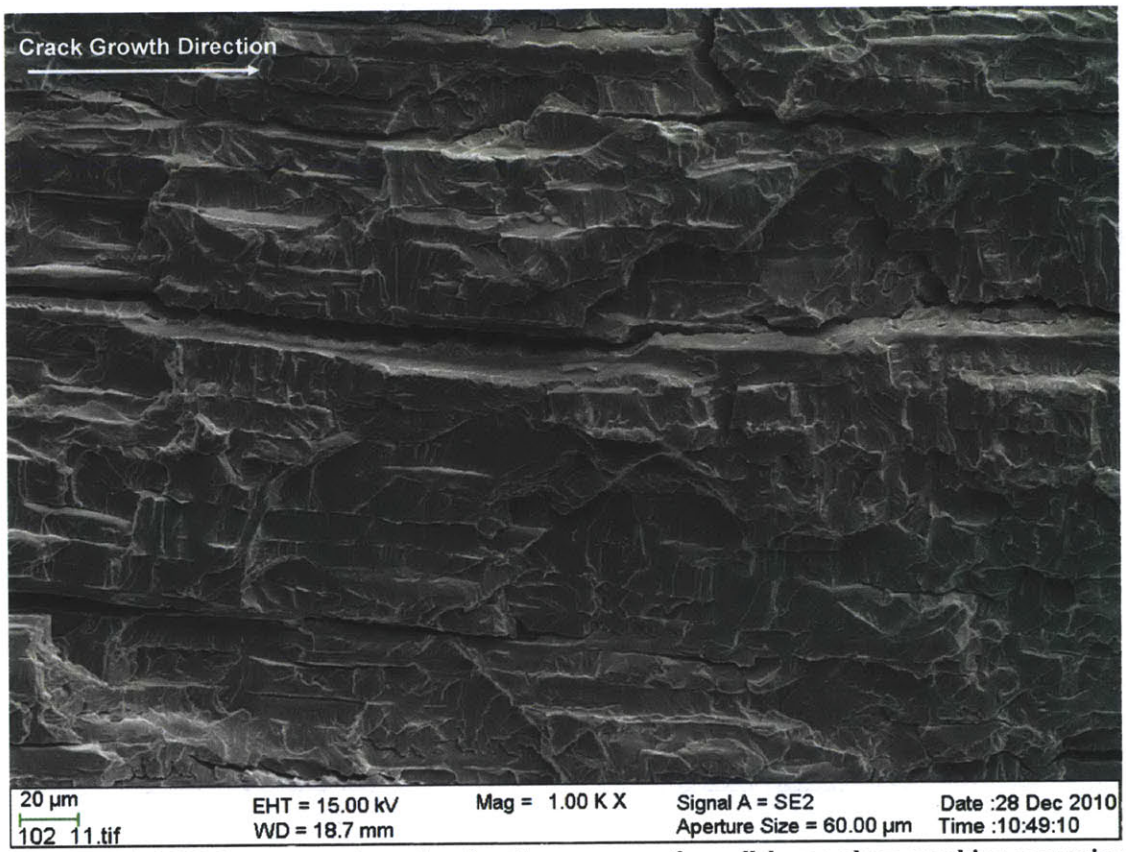

Figure 5-14 SCC fracture surface, showing the presence of parallel secondary cracking occurring along δ-ferrite dendrite cores.

Propagation of the SCC crack proceeds with little or no macroscopic deformation. What is important to note now, and will be explained shortly below is that the propagation likely occurs first in and along the δ-ferrite/austenite boundary. Then the δ-ferrite boundary cracking is followed by the austenite cracking. So the crack front moves forward along the δ-ferrite boundary and the rate of crack growth is tempered by a slower cracking in austenite. Looking closely at the nature of the austenite, however, shows that the fracture direction is not parallel with the over all crack growth direction but instead extends out laterally from the δ-ferrite/austenite interface until meeting lateral cracking coming from the other direction. This is shown in Figures 5-15 and 5-16, below. After some time, secondary cracking links up the δ-ferrite dendrite cores laterally, long after the initial cracking fingers have propagated along the δ-ferrite boundary.

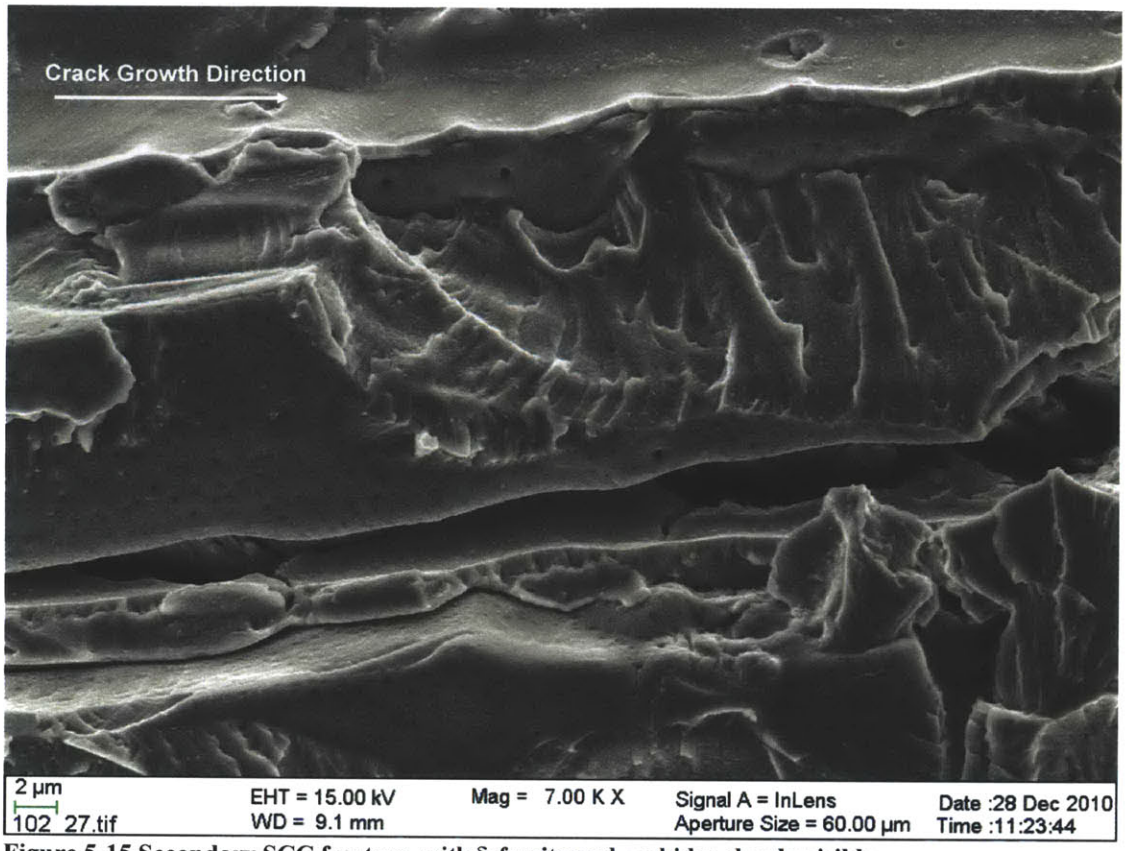

Figure 5-15 Secondary SCC fracture, with δ-ferrite and carbides clearly visible.

After sectioning the sample in both the PQ and PN planes for further analysis, several important details emerge. First, in Figure 5-16 and 5-17 below, the actual path of a secondary crack can be identified. In the PN plane, the dendrite δ-ferrite cores are visible, they are viewed end on and crack direction is normal to the plane. It is clear that the secondary crack is propagating through the austenite, and only occasionally passes though the δ-ferrite cores. The lighter etched area surrounding the δ-ferrite core is a cathodic area from the δ-ferrite anodic influence. There is also localized pitting occurring in the lighter etched area, this could be due to MnS inclusions present through out the austenite but made visible due to the cathodic nature of the area. In the third figure of the PN series, Figure 5-18 below, tertiary cracks can be seen initiating as the secondary crack propagates along. Finally when viewed from the NQ plane, shown optically in Figure 5-19, similar behavior is noted, but it is clear that the secondary cracks are moving in the forward direction as well. Also, it seems that there is the beginning of evidence of the importance of slip planes.

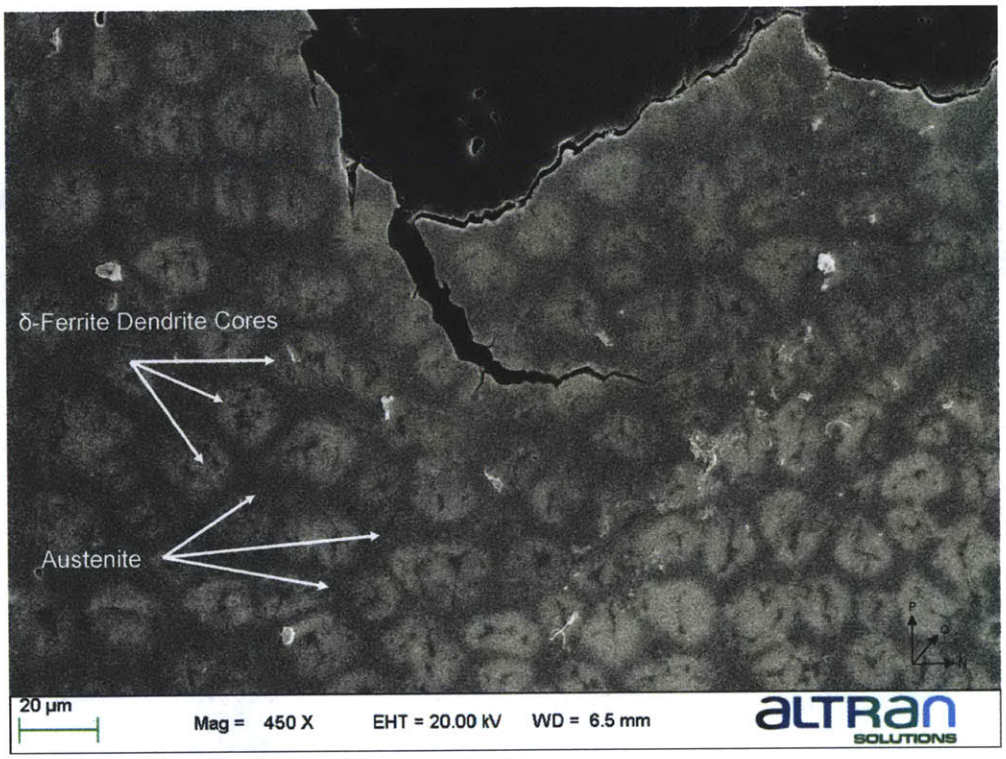

Figure 5-16 Secondary fracture path shown in the NP plane.

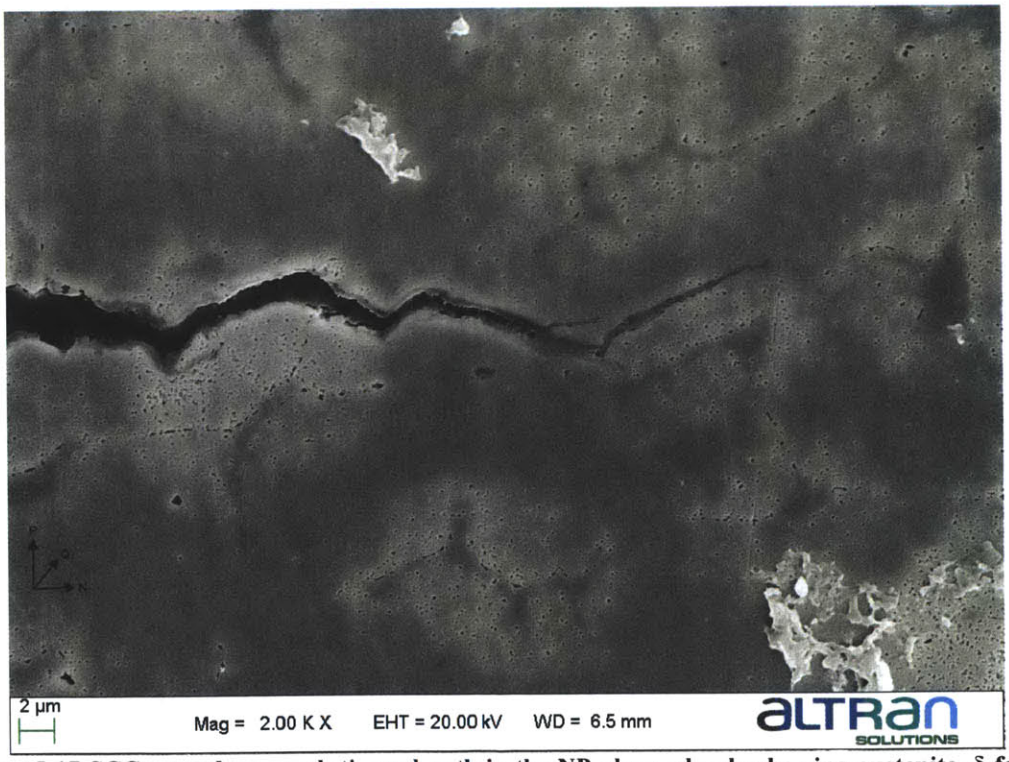

Figure 5-17 SCC secondary crack tip and path in the NP plane, clearly showing austenite, δ-ferrite and a lightly etched area surrounding the δ-ferrite, also visible is micropitting that may be MnS inclusions made visible.

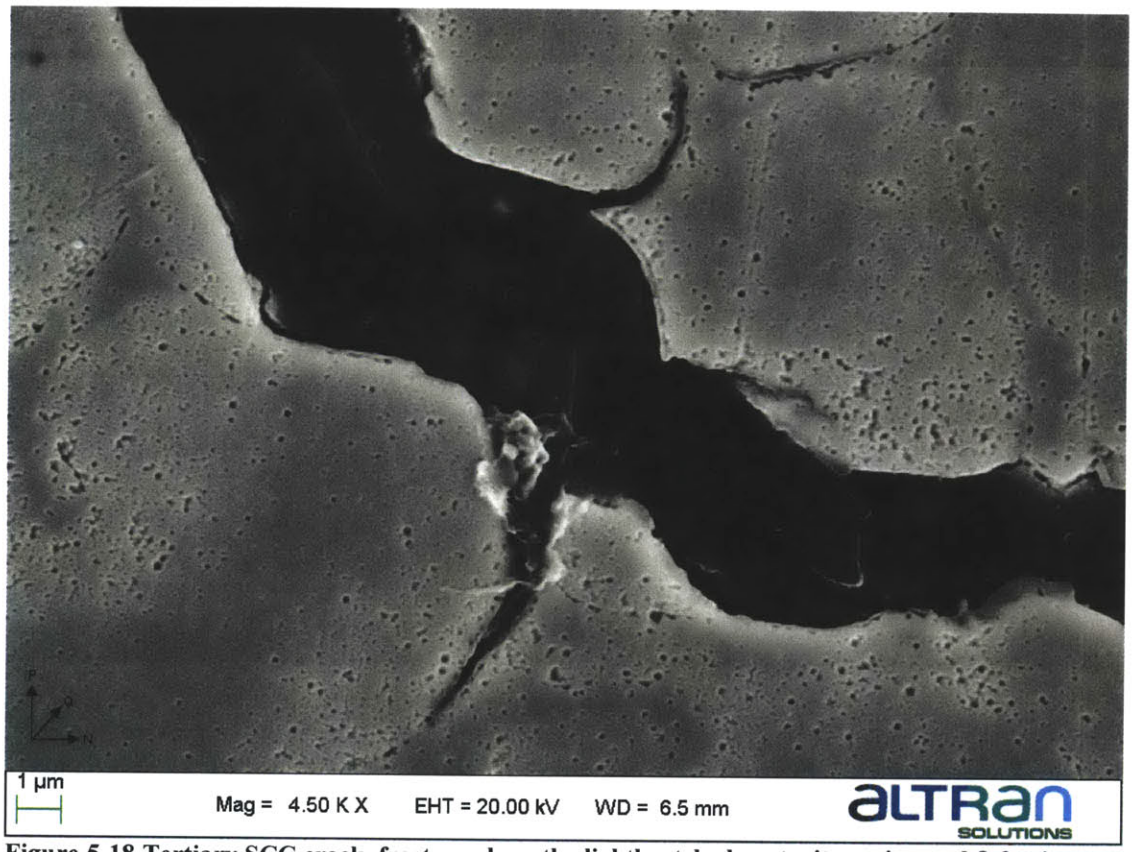

Figure 5-18 Tertiary SCC crack, fracture along the lightly etched austenite region and δ-ferrite core boundary.

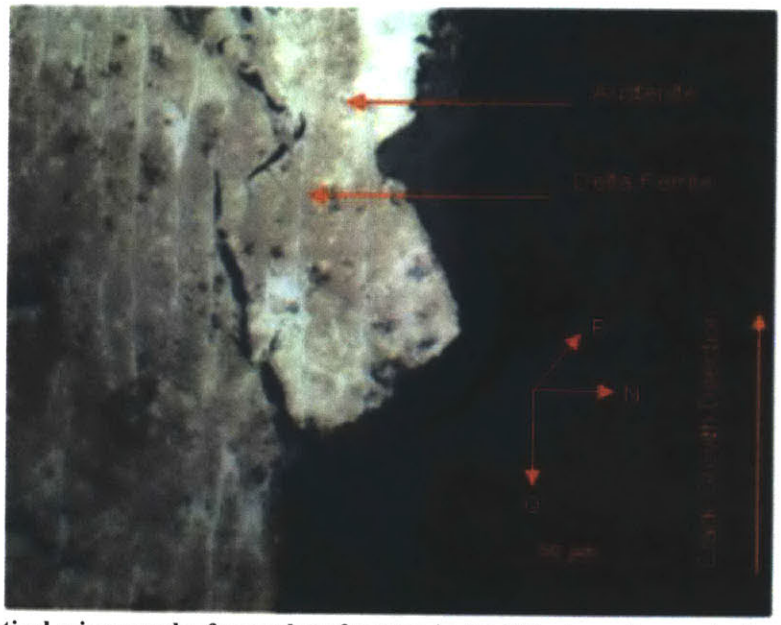

Figure 5-19 Optical micrograph of secondary fracture in the NQ plane, demonstrating preference for δ-ferrite for forward propagation.

Electron back scatter detection was used on an unetched PN-plane SCC surface. The results are shown in Figure 5-20 and 5-21. What is interesting to note is first the structure of the δ-ferrite cores. They are aligned in a very periodic manner as would be expected. More importantly, secondary crack propagation along the δ-ferrite dendrite cores is quite visible. Along the fracture surface, in this case the top of the image, there are many occurrences of dendrite cores being fractured. Interestingly, there are no MnS inclusions or chromium-rich carbide precipitates visible in this, or any of the other, electron back scatter images.

In Figure 5-22 below, a higher magnification of the austenite fracture surface is shown. Three features of significance are evident here. First is that the fracture is occurring laterally to the main crack growth direction, as discussed before. Second, the influence of carbides can be seen. Interestingly, the degree of material deformation around the carbides would indicate that they are not significant mechanistically in promoting fracture. Finally, what is very striking in the austenite is that the influence of slip is highly important to crack propagation. The equiaxial crystallographic nature of weld dendrite growth allows for a unique environment in which to consider the propagation of SCC. The main reason for this being that it is possible to have a material made of long parallel grains all grown on the same crystallographic direction, so slip occurs in a similar way in every grain, as opposed to wrought materials which have more or less random crystallographic orientation. So in a sense SCC in welds removes at least one of the degrees of freedom found in wrought materials. The optical image of the NQ plane, shown in Figure 5-23 clearly shows that cracking which is not occurring along the δ-ferrite interface is propagating along slip planes seeking more favorable fracture paths. Thus, the proposed mechanism for crack propagation in the austenite region must be one where slip mechanisms play a dominant role.

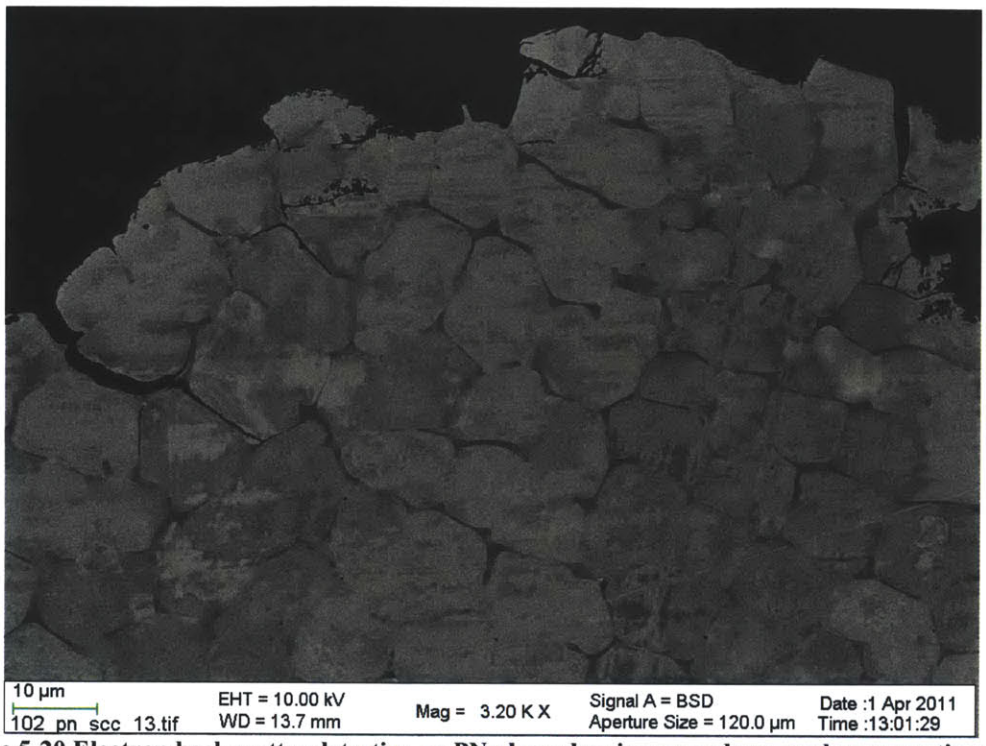

Figure 5-20 Electron back scatter detection on PN plane showing secondary crack propagation along δ-ferrite dendrite boundaries.

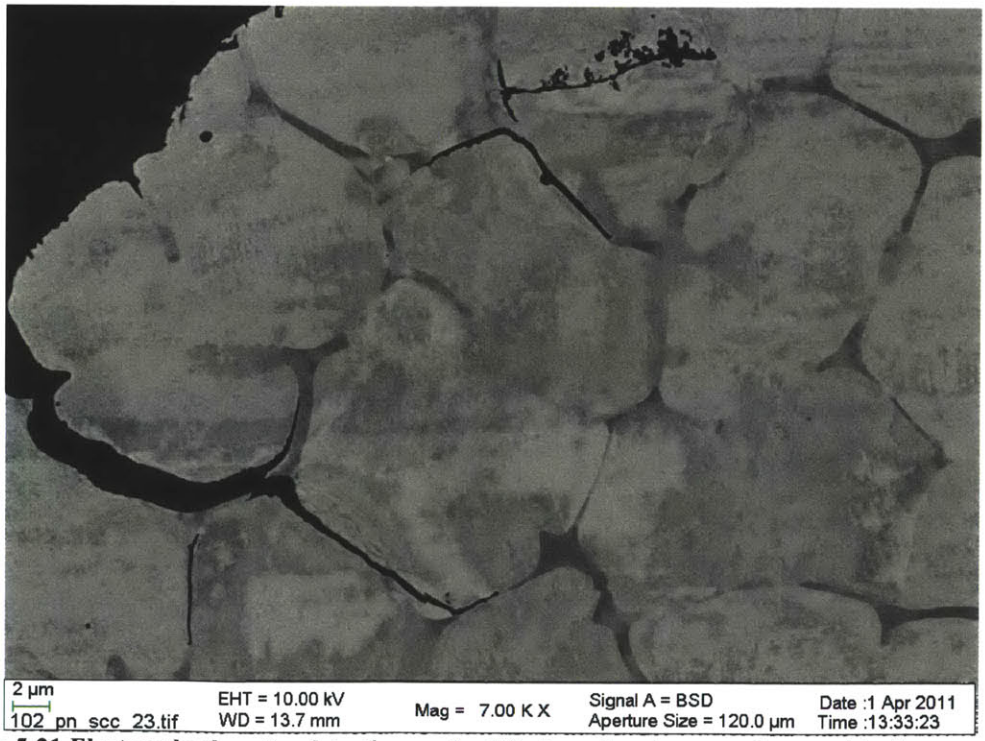

Figure 5-21 Electron backscatter detection on the PN plane showing secondary and tertiary cracking preference for δ-ferrite boundaries.

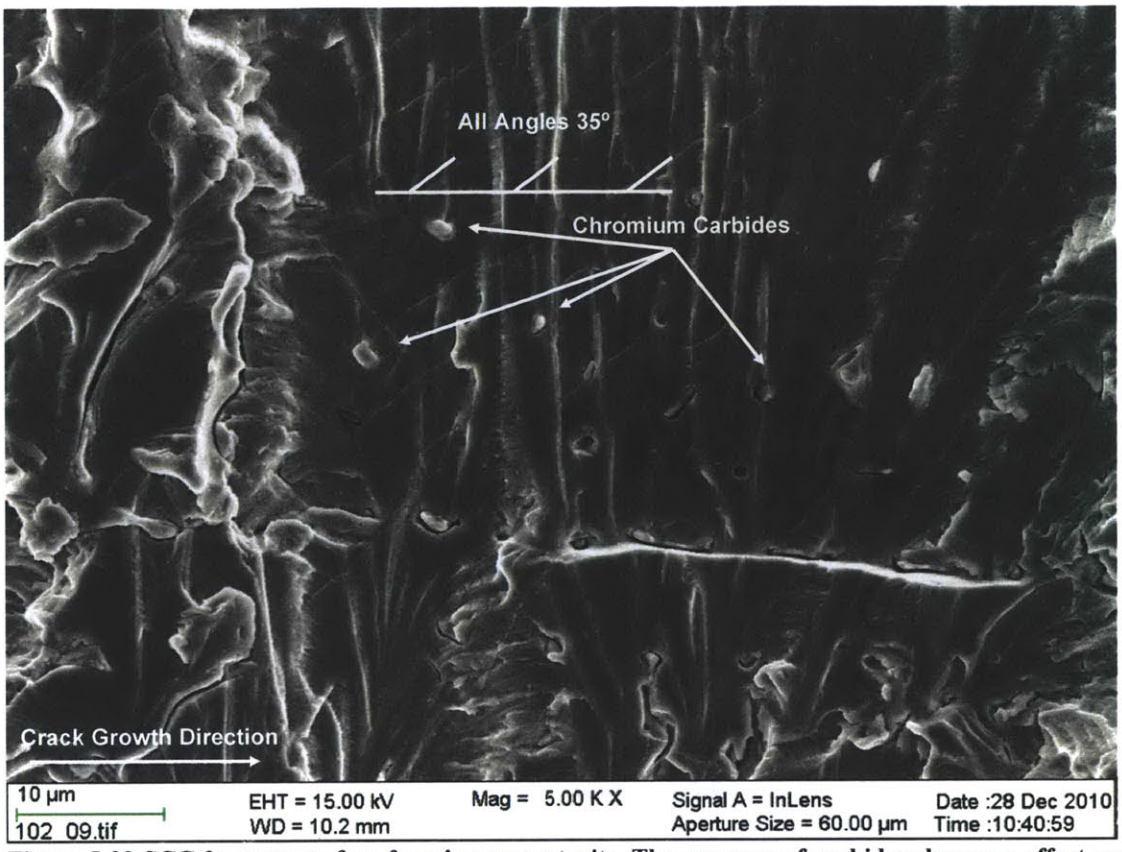

Figure 5-22 SCC fracture surface focusing on austenite. The presence of carbides shows no effect on crack propagation or in causing plastic deformation. Also visible are numerous parallel slip planes.

Figure 5-23 Optical micrograph on the NQ plane clearly showing the effects of preferential slip on cracking.

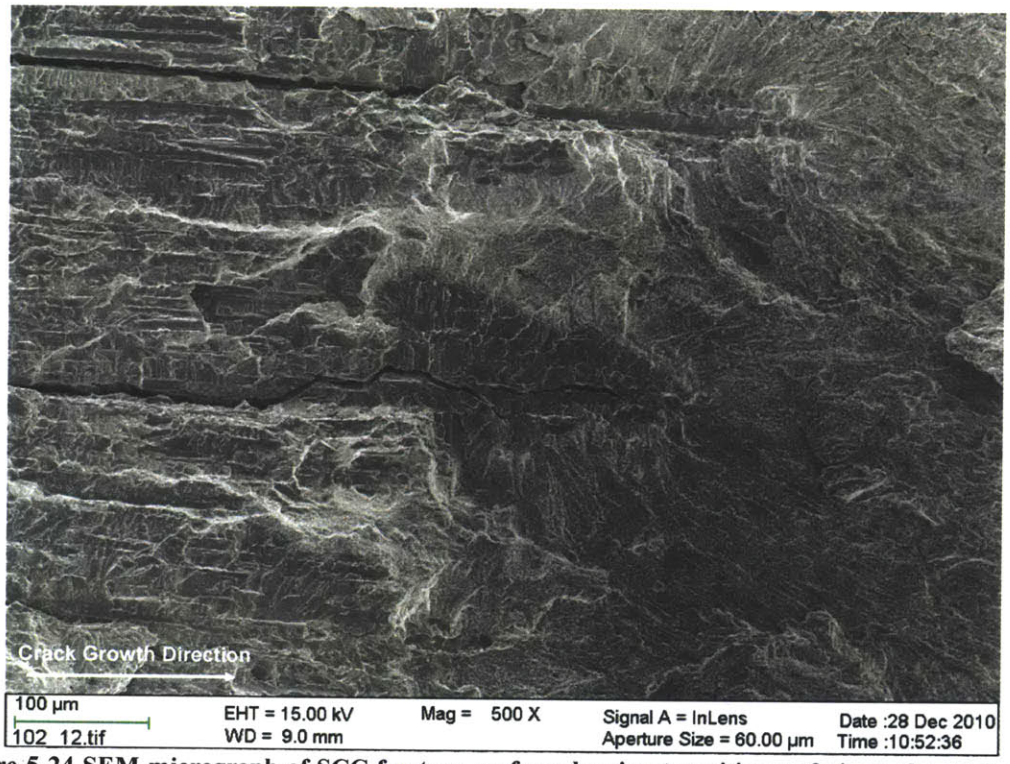

Figure 5-24 SEM micrograph of SCC fracture surface showing transition to fatigue, the preference for fracture along the δ-ferrite structure is clear.

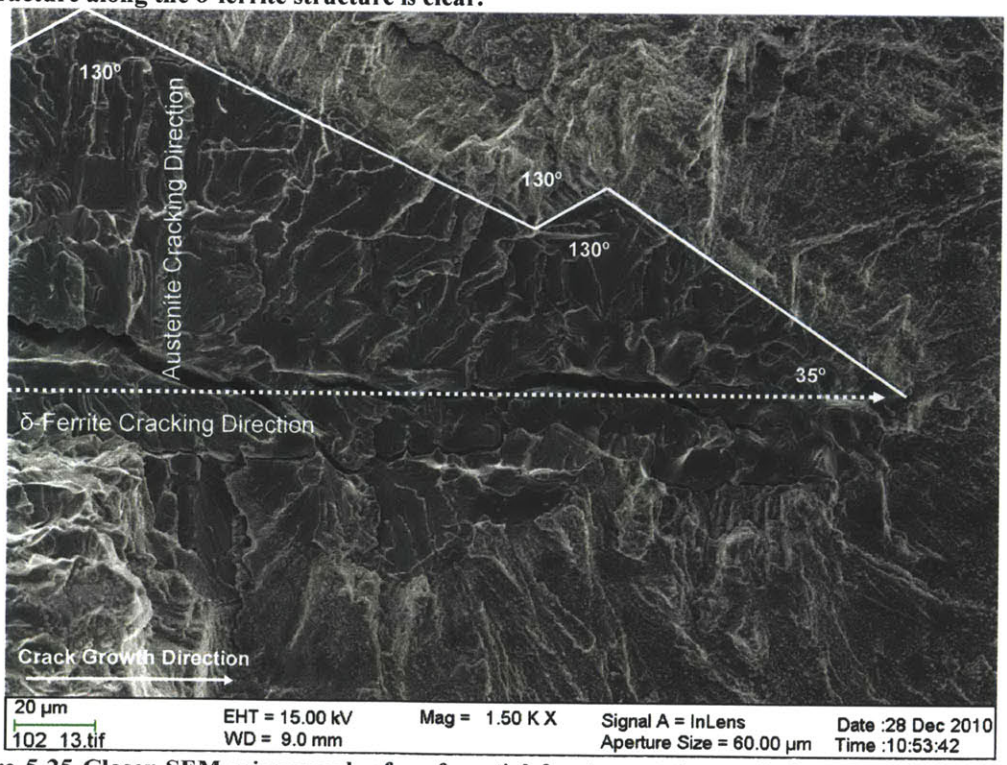

Figure 5-25 Closer SEM micrograph of preferential fracture at the crack front. Also visible is the change in oxide structure as the loading is changed to fatigue. Preferential, and periodic slip is noted in the austenite.

The two fractographs above, Figures 5-24 and 5-25, show the end of the SCC region where it interfaces with the next fatigue region. Beginning with Figure 5-24, two forward reaching fingers along the δ-ferrite structure are visible showing that indeed the δ-ferrite boundary region is cracking first and fastest. There are also microstructural features that extend into the fatigue region. In Figure 5-25, several angles are shown as well as the direction of cracking of both the austenite as well as the δ-ferrite. The angles are all reconcilable by considering that they are occurring in regular BCC and FCC crystals. In BCC the {111} close packed plane fracture angle is 35°. Since the δ-ferrite growth is in the <110>, according to the Kurdjumov-Sachs relationship, the austenite must be oriented in the <111> direction [65]. This means that the close packed {110} plane of the austenite lies at 45° however, there can be translational movement yielding a perceived slip angle of 35°. The 130° angles are approximately the slip angle expected with the 45° slip angles of FCC that is rotationally translated. Finally the spacing of the dendrites and the crystallographic plane of preferential slip demonstrates that the rate of δ-ferrite boundary cracking is slowed by the austenite needing to keep up with the δ-ferrite in order to provide a movable crack front.

Figure 5-26, again demonstrates that the lack of oxide precipitation in the SCC region is clearly visible in the electron back scatter image. However, it is noted that there are 3-4 striation marks without the oxide precipitation indicating that the process creating it takes some time to initiate. Perhaps this is due to cyclic enclave mass transport needing time to transport in the bulk environment.

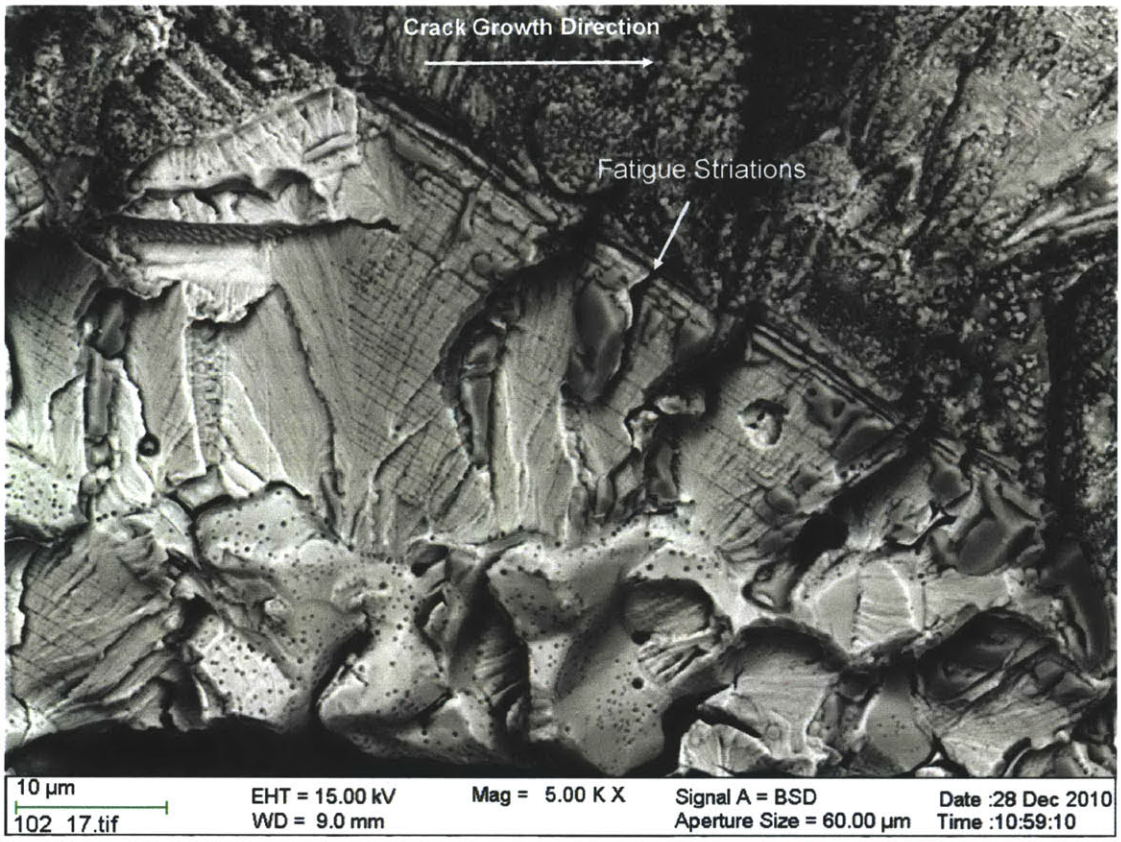

Figure 5-26 Electron backscatter micrograph of the transition of SCC to fatigue. Microstructural mechanisms such as carbide precipitation, slip in austenite and preferred cracking along the δ-ferrite boundary are visible. Also visible on the border between SCC and fatigue are 2 to 3 fatigue striations prior to oxide precipitation.

5.2.3 Aging Effects on SCC Fracture Surface

The impact of aging on SCC is shown in Figures 5-27 to 5-31 from high- and low-ferrite material, respectively. Each sample was aged for 5,000 h at 400°C. The most prominent difference between the aged material and the as-welded material is that the δ-ferrite is covered in oxide precipitant. This is quite visible in Figure 5-27. The implication is that spinodal decomposition is causing chromium redistribution, in to chromium rich and chromium depleted phases. The impact is such that the areas of increased chromium do not provide further protection, while the decrease in chromium in the α' phase causes a loss of protection. Even though this is happening on a 5-10 nm wavelength, the summed impact is a loss of protection. In Figures 5-28 oxide is forming along slip lines. As shown in Figure 5-29, the δ-ferrite takes on a brittle mode of fracture, completely separating from the austenite matrix. Behavior in this extreme was not seen in as-welded material. The influence of chromium carbides can be seen in Figure 5-30. Originally it was suspected that the chromium carbides would grow with aging, however, clear evidence of this could not be found. They do, however, undergo oxidation as the surrounding matrix has become sensitized.

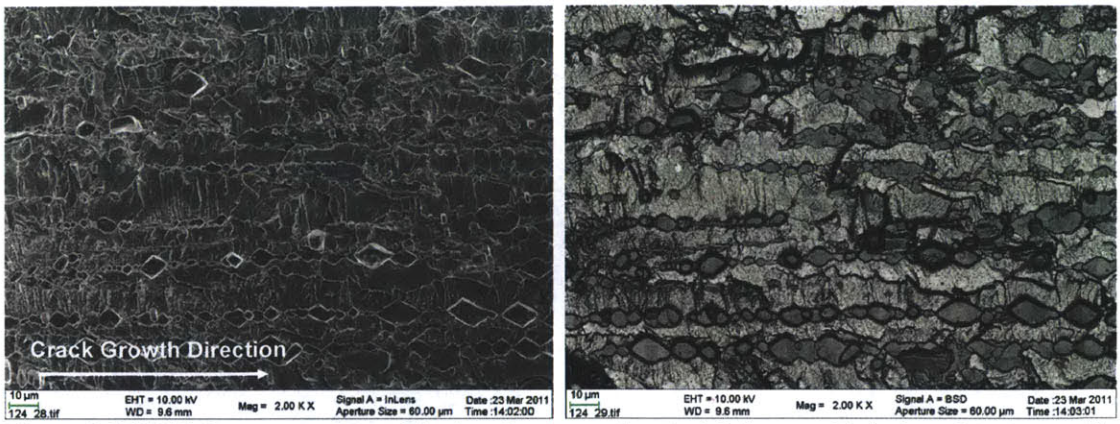

Figure 5-27 SCC fracture surface of the low-ferrite aged material shown with in-lens detector on the left and backscatter detector on the right. Oxides completely cover the δ-ferrite dendrite cores.

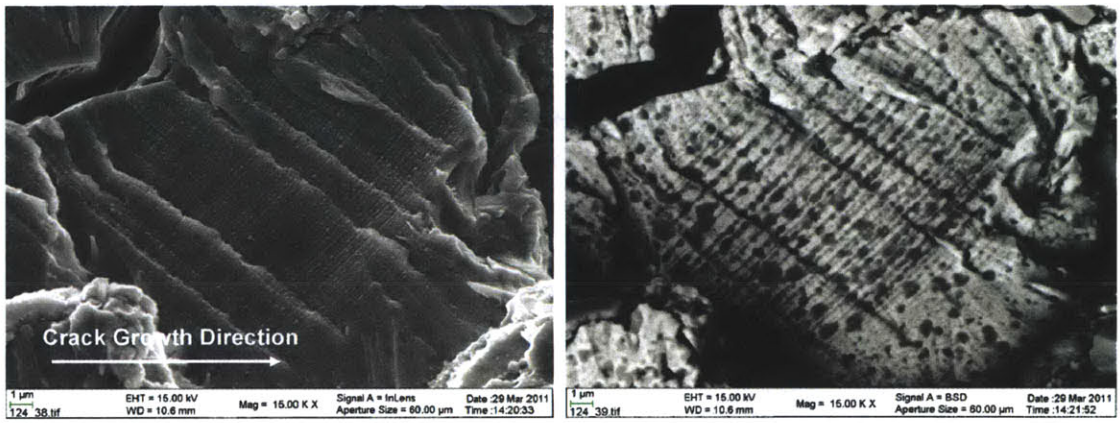

Figure 5-28 The importance of slip in SCC of austenite shown with in-lens detector on the left and backscatter detector on the right. The dark areas show oxide growth on the slip planes.

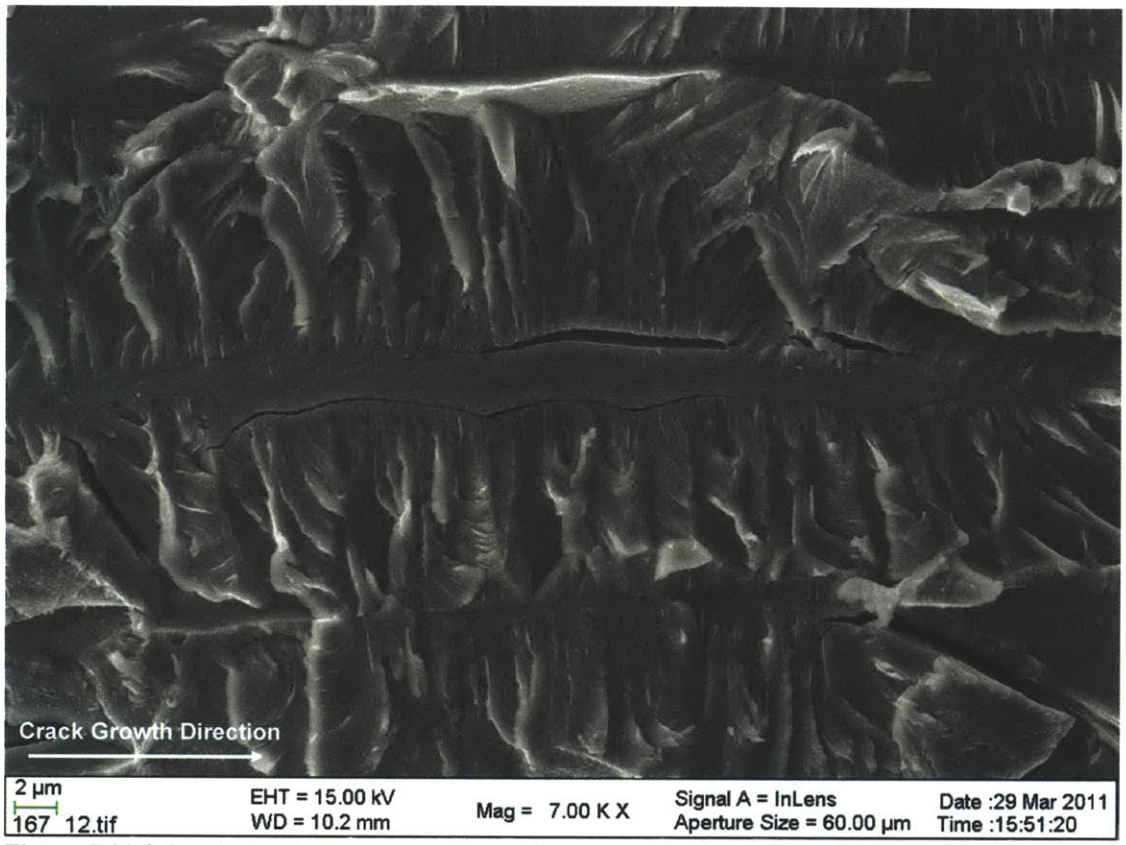

Figure 5-29 δ-ferrite dendrite cores separating from austenite in high-ferrite aged material. Also, δ-ferrite is cracking transgranularly in this sample.

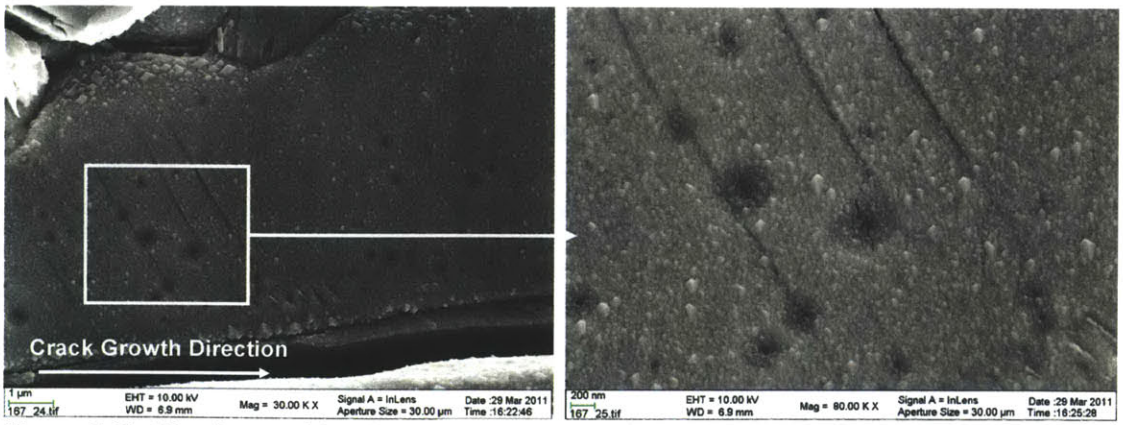

Figure 5-30 Slip planes with oxide developing around chromium carbides on δ-ferrite boundary. White box indicates location of micrograph on the right.

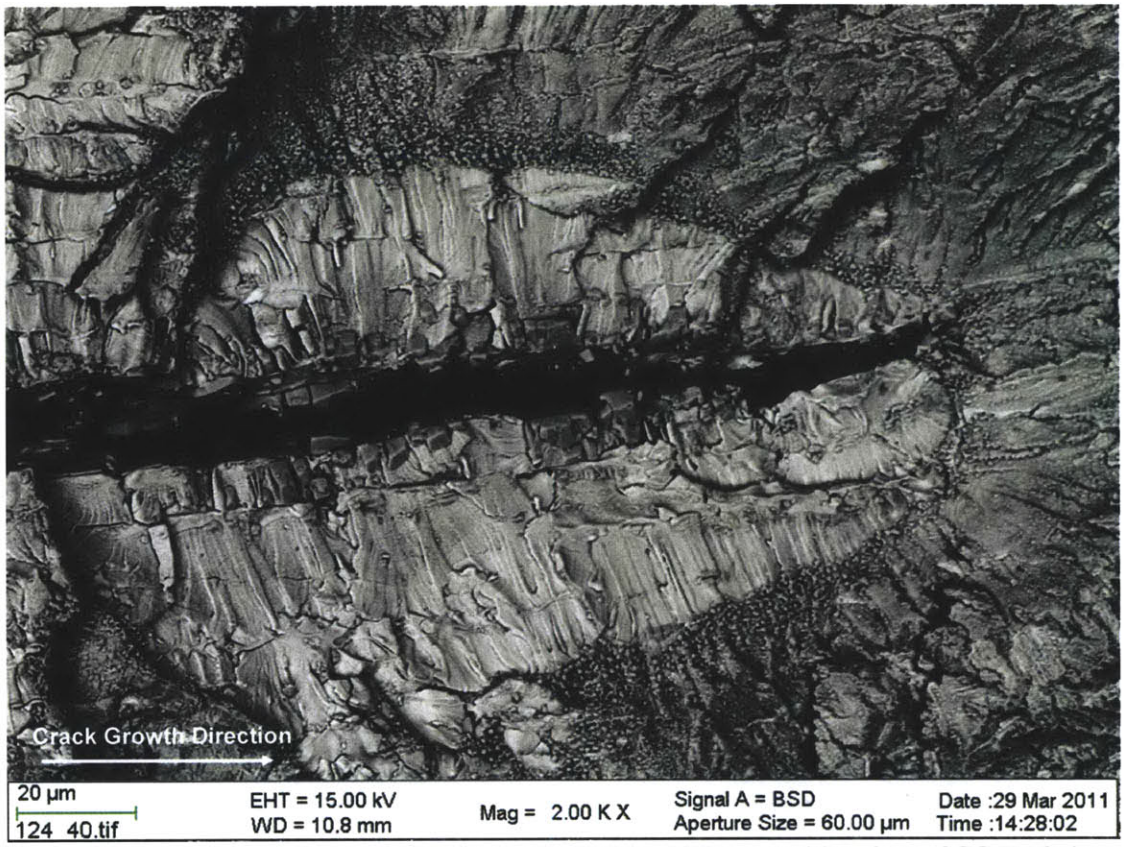

Figure 5-31 Electron back scatter detector micrograph of the transition from SCC to fatigue, demonstrating all aspects of SCC noted in this study. This is the high-ferrite aged sample.

The electron back scatter image in Figure 5-31 provides evidence of all the important mechanisms occurring during SCC. To summarize what has been noted in the SCC section:

- SCC is initiating in both austenite and along the δ-ferrite boundary.
- Propagation occurs first along the δ-ferrite boundary due primarily to the presence of chromium carbides.
- The chromium carbides along the δ-ferrite boundary sensitize the material and provide sites for oxidation.
- Fracture in austenite occurs laterally to the direction of the main crack front. Furthermore, fracture occurs along the planes of preferential slip, which are prone to oxidation.
- The fast cracking along δ-ferrite fingers are tempered by the slower cracking in the austenite.
- Microstructural features are visible and influence both fatigue and SCC crack propagation and cross the boundary between them.
- Aging embrittles the δ-ferrite resulting in brittle transgranular cracking and weakening of the γ/δ boundary and making it more susceptible to cracking.

- Spinodal decomposition causes a loss of passivation ability in the δ-ferrite, enhancing crack growth. Furthermore the impact of aging on crack growth rate is higher in the high-ferrite material, indicating that the mechanism is controlled by the δ-ferrite content.
- Oxide precipitation is deposited on the fracture surface of the fatigue region, but not on the SCC region. This indicates that fracture mechanism depends on transport and indicates that the environment in the SCC region is unique.

5.3 Fracture Toughness Results

Fracture toughness was evaluated for the as-welded and 400°C aged high- and low-ferrite material for both 25°C and 288°C in air. Where applicable, this was then compared to the in-situ results for high- and low-ferrite at 288°C, 300 ppb O_2 water after more than 2,000 h in the environment. The fracture toughness was evaluated in accordance with ASTM 1820-01, and crack length measurement was performed using DCPD. All results are shown in Table 5-2 and graphically in Figure 5-32. Results are summarized below with the data presented in different of formats in Figures 5-32 through 5-38. The results of fracture surface characterization are shown in Figures 5-40 through 5-58.

5.3.1 Fracture Toughness as a Function of Aging and Ferrite Content

J-integral based fracture toughness testing was completed in air at room temperature for both high- and low-ferrite material aged from 0 to 10,000 h. Figure 5-32 shows a graphical representation of the results. The in-situ fracture toughness is up to 40% less tough than the equivalent condition air result. For the evaluation performed in air, the general trend, which is also seen in the tensile and Charpy-V material characterization results, is that the material reaches a peak in toughness at the 1,000 h data point and falls off gently from there. The exception being the 5,000 h aged high-ferrite condition which has a dip in the average value. What is important is that the final value at 10,000 h is still of higher toughness than that of the initial as-welded material. The in-situ performance gave differing results. First, it should be noted that since the tests were only conducted at as-welded and 5,000 h aging, in the interest of testing efficacy, if there is a peak at 1000 h, it has been missed. For the trends that can be noted, low-ferrite in-situ material increased in fracture toughness while the high-ferrite in-situ did just the opposite.

The general trend of each series is that the 25°C results showed the highest toughness, followed by the 288°C air conditions. The in-situ test gave the lowest fracture toughness value, clearly demonstrating an environmental effect on fracture toughness. In the 5,000 h aged material, the same comparison can be made for both high- and low-ferrite. The complete data for low-ferrite material is presented graphically in Figure 5-33 in ranked order with the corresponding data included in Table 5-3. Similarly for high-ferrite, see Figure 5-34 and Table 5-4. In Figures 5-35 and 5-36, the data for the as-welded and 5,000 h aged material is shown. Figures 5-37 and 5-38 show the actual $J/\Delta a$ plots as calculated with the measure point of fracture toughness, J_{IC}, noted as a diamond for each test at each condition for various aging times. This allows a comparison of the crack blunting, shown

in the slopes prior to the diamond, the actual J_{IC} and then the stable tearing modulus, or the steady slope after J_{IC}. It can be seen that the in-situ cracks blunt much slower, based on the slope before the fracture toughness point. J_{IC} comes at a much lower value for in-situ, than for the air conditions which. Following the stretch zone and J_{IC} the final important area on the graph is the stable tearing region. The slope of this line indicates the resistance to constant tearing with a well developed fracture occurring with a blunt crack. As the air slopes are near parallel, this indicates that similar tearing resistance is present. The in-situ stable tearing modulus, however, becomes nearly flat in some parts indicating almost unstable fracture. This is yet another indication from the data of the impact of the environment on fracture toughness of the material as it takes much less energy to cause fracture propagation in-situ than in air conditions.

Error in Δa was corrected by comparison of DPCD measurement to optical and SEM measurements. Error in J is estimated by propagating the known error in the load cell and distance transducer. The error propagates through the J-integral calculation to be less than 2% which is smaller than the data point on the graphs in Figures 5-32, 5-37 and 5-38.

At first the trend of fracture toughness decreasing with elevated temperature seems counterintuitive, however, it closely matches the results reported in NUREG/CR-6428 [20]. Furthermore, comparative stress-strain curves of air test conditions with aging are shown in the tensile-test section. As the area beneath the stress-strain curve is related to toughness, it is clear that the tensile data shows the same trends as the fracture toughness results. Individual in-situ test details are given in Appendix A. As was mentioned earlier, the trend in toughness shows an apparent toughness that is higher after 1,000 h aging and drops off gradually with additional aging. This trend is also present in the tensile and hardness data. The trend is most likely an artifact due to high residual stresses in the welds that are relaxed during the aging process. Residual stress analysis will be discussed in greater detail in the discussion chapter. Furthermore, there is the spinodal decomposition embrittling the δ-ferrite which changes the weld metal properties. Hardness mapping (discussed below) shows that the location in the weld has a large effect on properties and that the variation of physical properties is as much a function of position in the weld as any of the other variables. One possible explanation of the trend in air toughness is that the welds have not been stress relieved and so the residual stresses are such that they cause the fracture toughness and strength to decrease with increasing temperature. Instrumented hole drilling has been used to determine residual stresses for high-ferrite samples at room temperature for 400°C aged specimens. The reasons for the environmental effect on fracture toughness are not as obvious and will be discussed in greater detail in the fracture surface analysis.

Table 5-2 Complete fracture toughness results.

Average Valid Fracture Toughness Properties for Alloy 316L Welds at 400°C Aging

	Test Condition	Aging Time (h)	J (kJ/m^2)	K (MPa√m)
Low-Ferrite	25°C in air	0	153	181
		1,000	208	211
		5,000	207	210
		10,000	204	209
	288°C in air	0	130	158
		1,000	159	175
		5,000	163	177
		10,000	152	171
	In-situ	0	87	140
		5,000	110	145
High-Ferrite	25°C in air	0	174	193
		1,000	264	245
		5,000	190	208
		10,000	241	234
	288°C in air	0	153	171
		1,000	191	191
		5,000	199	195
		10,000	190	191
	In-situ	0	135	161
		5,000	106	143

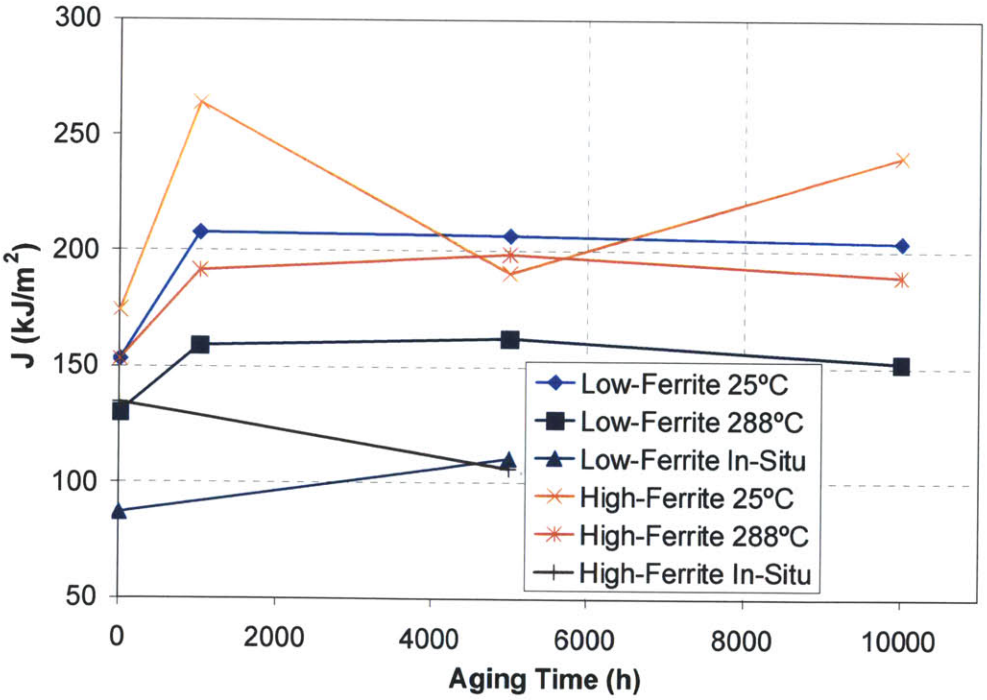

Figure 5-32 Graphical representation of fracture toughness data as a function of aging at 400°C and ferrite number.

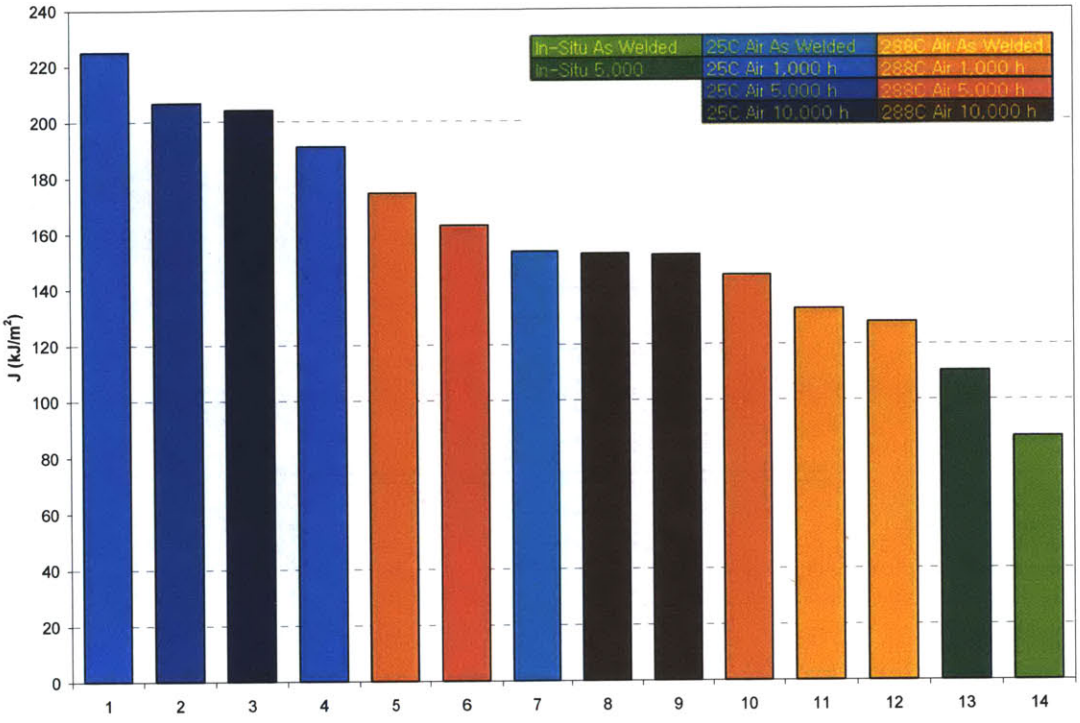

Figure 5-33 Ordered summary of low-ferrite J-based fracture toughness values, aging time at 400°C and condition noted by color.

Table 5-3 Low-ferrite fracture toughness results

Fracture Properties for Low-Ferrite Alloy 316L Welds			
Rank	**Test Condition**	**J (kJ/m²)**	**K (MPa√m)**
1	Low-Ferrite 25°C Air 1,000 h	225	219
2	Low-Ferrite 25°C Air 5,000 h	207	210
3	Low-Ferrite 25°C Air 10,000 h	204	209
4	Low-Ferrite 25°C Air 1,000 h	191	202
5	Low-Ferrite 288°C Air 1,000 h	174	183
6	Low-Ferrite 288°C Air 5,000 h	163	177
7	Low-Ferrite 25°C Air As Welded	153	181
8	Low-Ferrite 288°C Air 10,000 h	153	171
9	Low-Ferrite 288°C Air 10,000 h	152	171
10	Low-Ferrite 288°C Air 1,000 h	145	166
11	Low-Ferrite 288°C Air As Welded	133	159
12	Low-Ferrite 288°C Air As Welded	128	157
13	Low-Ferrite 288°C In-Situ 5,000 h	110	145
14	Low-Ferrite 288°C In-Situ As Welded	87	140

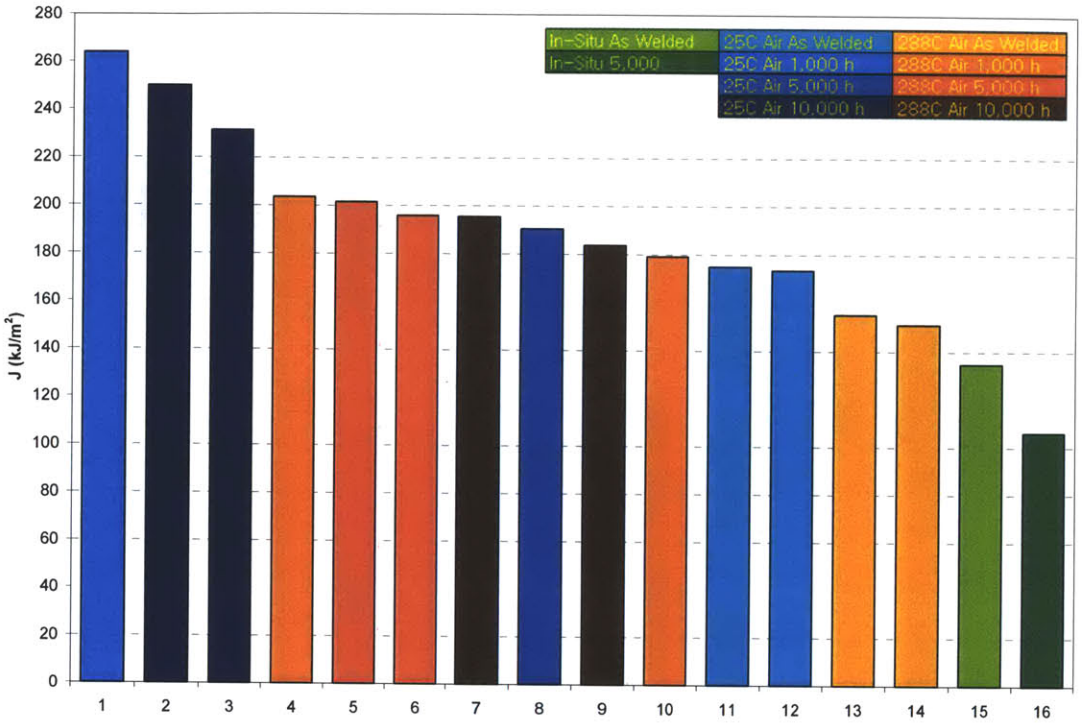

Figure 5-34 Ordered summary of high-ferrite J-based fracture toughness values, aging time at 400°C and condition noted by color.

Table 5-4 Low-ferrite fracture toughness results

Fracture Properties for High-Ferrite Alloy 316L Welds			
Rank	**Test Condition**	**J (kJ/m²)**	**K (MPa√m)**
1	High-Ferrite 25°C Air 1,000 h	264	245
2	High-Ferrite 25°C Air 10,000 h	250	238
3	High-Ferrite 25°C Air 10,000 h	231	229
4	High-Ferrite 288°C Air 1,000 h	204	198
5	High-Ferrite 288°C Air 5,000 h	202	197
6	High-Ferrite 288°C Air 5,000 h	196	194
7	High-Ferrite 288°C Air 10,000 h	195	194
8	High-Ferrite 25°C Air 5,000 h	190	208
9	High-Ferrite 288°C Air 10,000 h	184	188
10	High-Ferrite 288°C Air 1,000 h	179	185
11	High-Ferrite 25°C Air As Welded	175	193
12	High-Ferrite 25°C Air As Welded	174	193
13	High-Ferrite 288°C Air As Welded	155	172
14	High-Ferrite 288°C Air As Welded	151	170
15	High-Ferrite 288°C In-Situ As Welded	135	161
16	High-Ferrite 288°C In-Situ 5,000 h	106	143

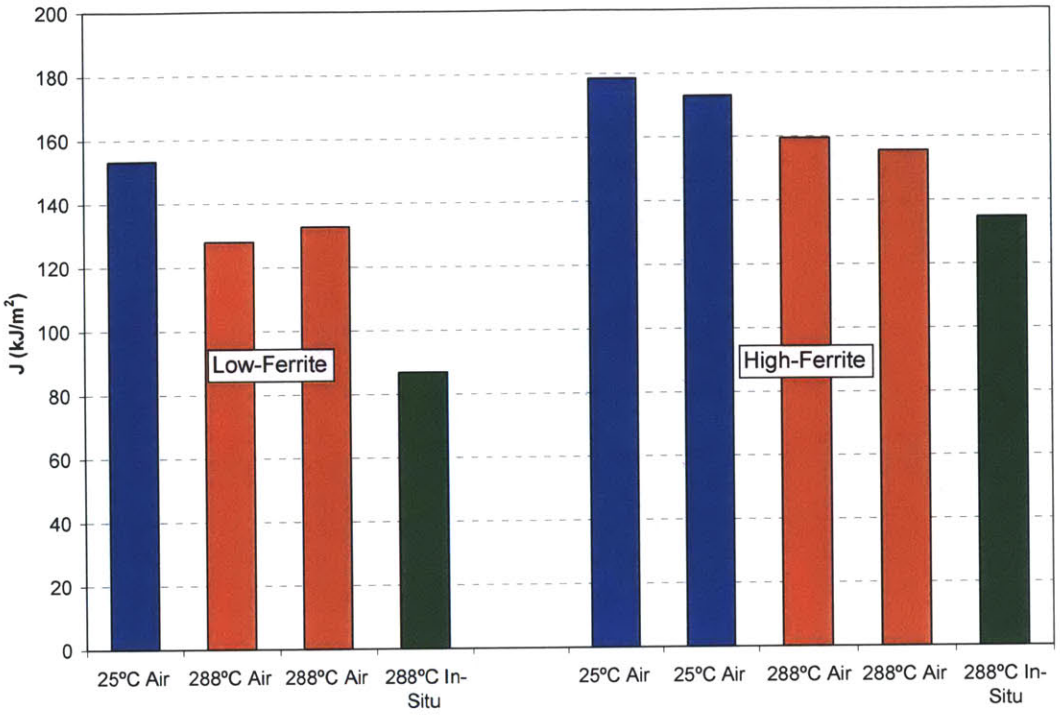

Figure 5-35 As-welded fracture toughness data.

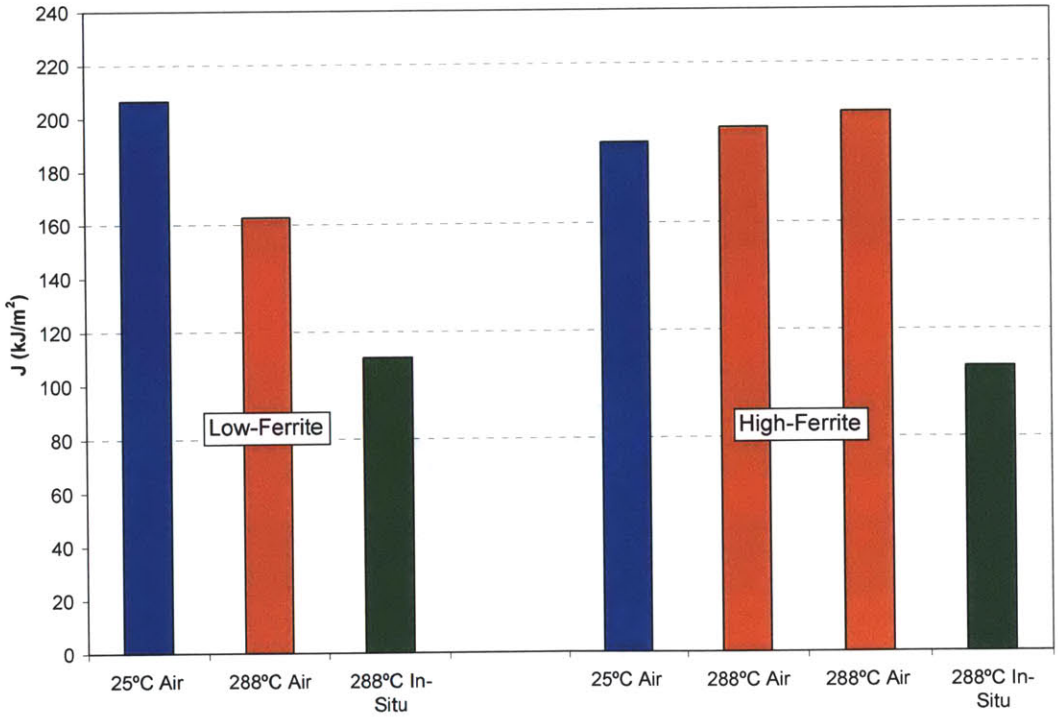

Figure 5-36 Material aged for 5,000 h at 400°C fracture toughness data.

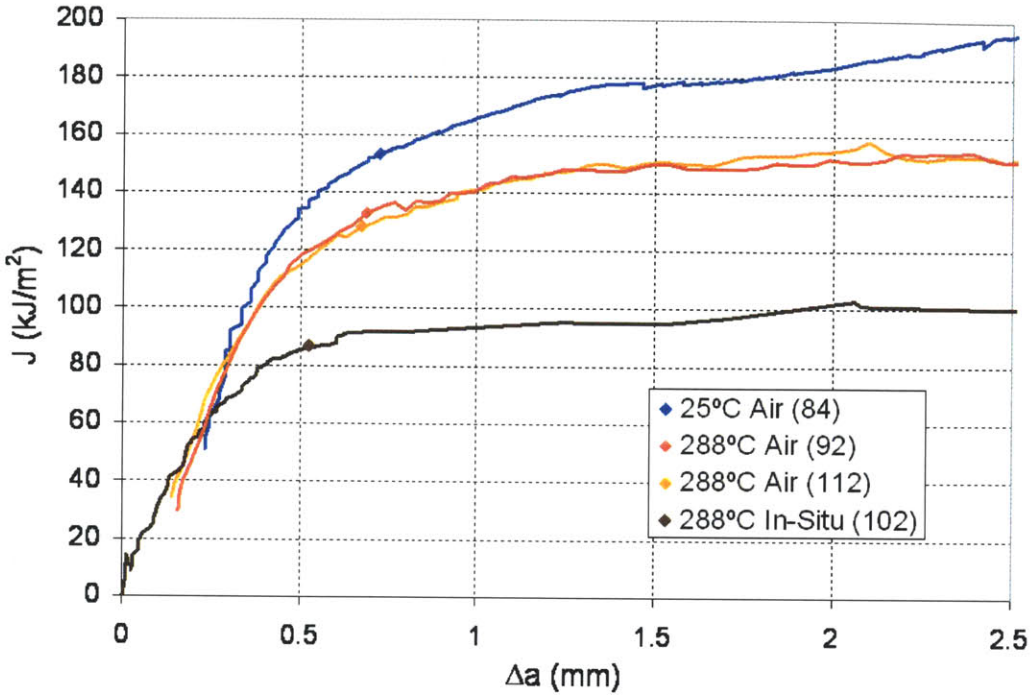

Figure 5-37 Low-ferrite as-welded J-R curves with J_{IC} noted by a diamond on the curve. Prior to the diamond is the stretch zone and afterwards is the stable tearing region.

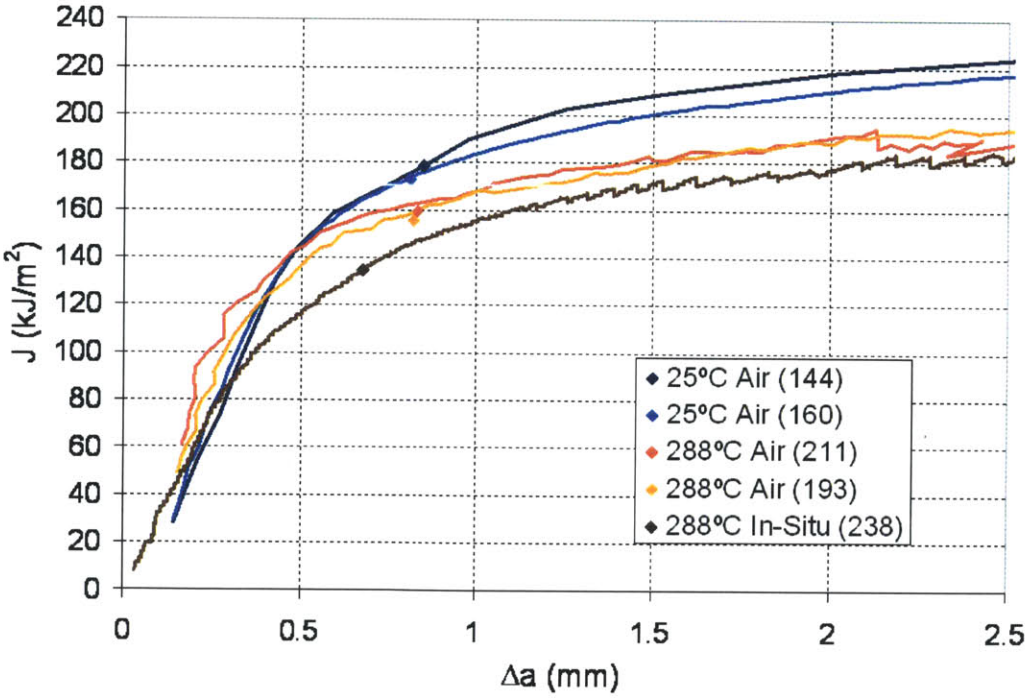

Figure 5-38 High-ferrite as-welded J-R curves with J_{IC} noted by a diamond on the curve. Prior to the diamond is the stretch zone and afterwards is the stable tearing region.

5.3.2 In-Situ Fracture Toughness

During testing in the early part of the overall project an unusual behavior was observed when testing an unaged, low-ferrite material. After an exposure of approximately 1850 h and during a low frequency fatigue portion of the test, an unstable fracture condition developed resulting in rapid fracture of the material. While this behavior was highly unusual a complete examination of the test record indicated that there was no malfunction of the test. Thus, the observed behavior was considered as a real effect. Based on an analysis of the test record it was estimated that the fracture toughness of this sample was approximately 75 MPa$\sqrt{m}$. However, direct comparison with literature data was difficult primarily because the test was being conducted in load control which magnified the instability once it began. Fracture toughness tests are normally conducted in displacement control in accordance with ASTM E1820 procedures [59]. None-the-less, the observed instability prompted the program to conduct informal discussions with industry and national laboratory scientists. In these discussions it was discovered that this unstable fracture phenomenon has been observed by a number of investigators but that these investigators discounted the phenomenon as being a result of some kind of experimental error. As an example of another noted event, Andresen reported similar behavior for cold-worked stainless steel and Alloy 182 weld metals. Figure 5-39, from [45], shows a case of unstable fracture for cold-worked stainless steel tested in oxygenated water at 288°C. The tests in this program were very carefully controlled as were those of Andresen and it is very unlikely, that the unstable fracture was due to a test system malfunction. The actual cause for this behavior required a more extensive, deliberate, investigation. At least partially as a result of the work in this thesis, the effect of the environment on the fracture toughness, termed "Environmental Fracture" has been highlighted as an emerging issue by the industry.

As a result of the unstable crack growth observation, the project began conducting in-situ fracture toughness tests at the end of each SCC crack growth test. At the end of an SCC test a fatigue step was added, with an R of 0.7, to the test program to allow further exploration of environmental fracture using a standard J-R test in accordance with ASTM 1820. As the results show, there is a significant reduction in fracture toughness when tested in the actual environment. When a "standard" displacement controlled test is performed the fracture toughness reduction is similar to the load controlled instabilities that have been observed. Moreover, the question must be asked: is this phenomenon an issue that the industry needs to be concerned about? The only potential scenario where this phenomenon may be relevant would be in the case where a sudden, rapid displacement occurs where there is an already existing SCC crack present. Such a situation could possibly exist during an earthquake. Under any other operating situation a rapid loading situation would not occur.

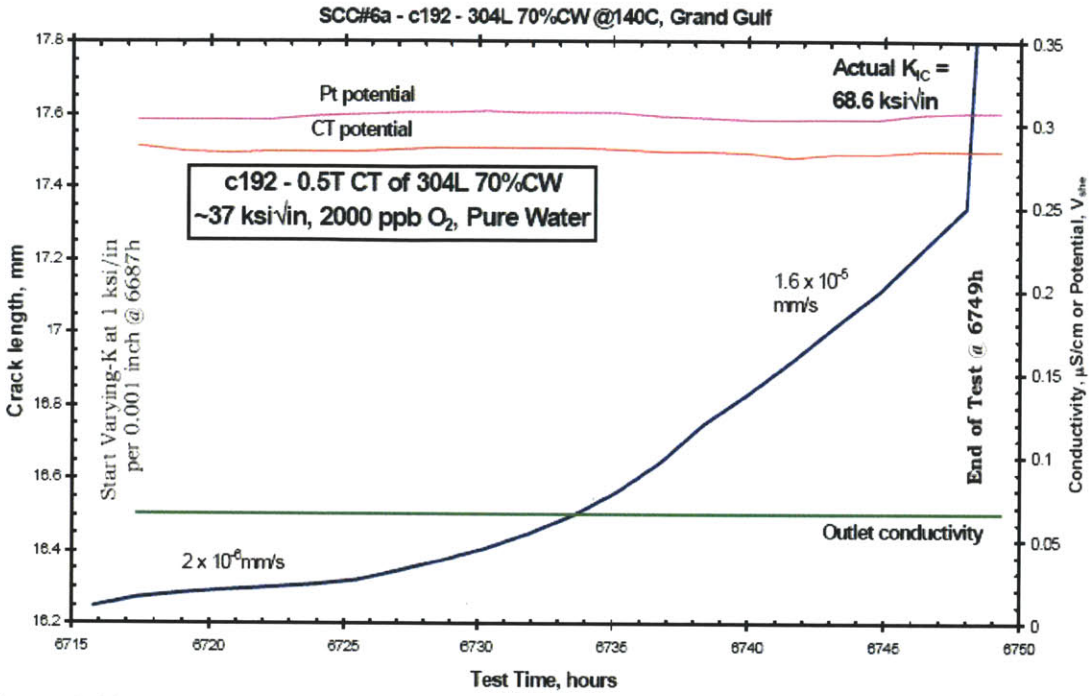

Figure 5-39 Example of unstable crack propagation in cold-worked stainless steel. Crack was growing at a stable rate of 1.6 x 10^{-5} mm/s when a sudden and complete fracture occurred [45].

5.3.3 Fracture Toughness Test Fractography

Post-mortem analysis was performed on the fracture toughness samples using both optical and SEM microscopy. Samples are sectioned using wire electro-discharge machining and/or cooled band and diamond saws to allow inspection in the planes perpendicular to the fracture surface. Optical samples were mounted and polished with the final polish being performed by 0.05 µm silica suspension. The samples where then etched in Kalling's reagent for 15 s to highlight the δ-ferrite. In general, the fracture toughness behavior in air showed the typical crack blunting region, transition to ductile fracture, and stable ductile tearing controlled primarily by inclusions. In-situ test however, yielded a more unique fracture surface. Rather than have a smooth transition from fatigue to crack blunting, there is an area of brittle fracture which occurred prior to blunting. This was the main indication of environmental fracture. The fracture surface analysis will be discussed in three parts: 1) overview, 2) stretch zone and 3) the stable tearing region. These areas are shown in Figures 5-40 through 5-66. These images were taken from low-ferrite as-welded material and for the aging from high-ferrite 5,000 h aged material. However, this behavior is representative of all the in-situ test conditions.

5.3.3.1 Overview

The photograph in Figure 5-40 shows the areas that were analyzed using an SEM. All of the material in Figure 5-40 is low-ferrite, as-welded material. On the left is material tested in-situ sample, in the middle is the 288°C air condition and on the right the 25°C air condition. There are two items which are immediately obvious, particularly between

the in-situ and air conditions: 1) the oxidation that has occurred on the in-situ condition, as well as the varying oxidation on the fracture surface is not present on the air conditions, and there is heat tinting that has occurred on the high temperature conditions; 2) the lateral-contraction of the samples follows the fracture toughness value, the 25°C air condition has the highest fracture toughness value and in-situ condition the lowest. The very small amount of lateral contraction on the in-situ condition indicates that it was far less tough than the others. The samples were analyzed using a Zeiss ULTRA 55 field emission gun SEM.

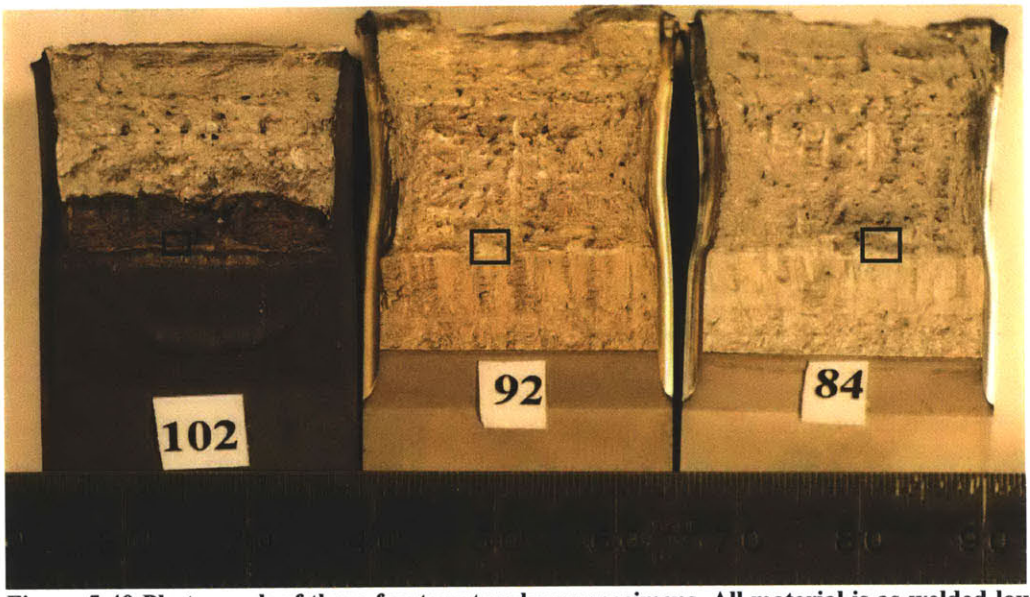

Figure 5-40 Photograph of three fracture toughness specimens. All material is as-welded low-ferrite. The material on the right was tested in air at 25°C, the middle material was tested in air at 288°C and material on the left was tested in-situ. The black boxes represent areas of further inspection.

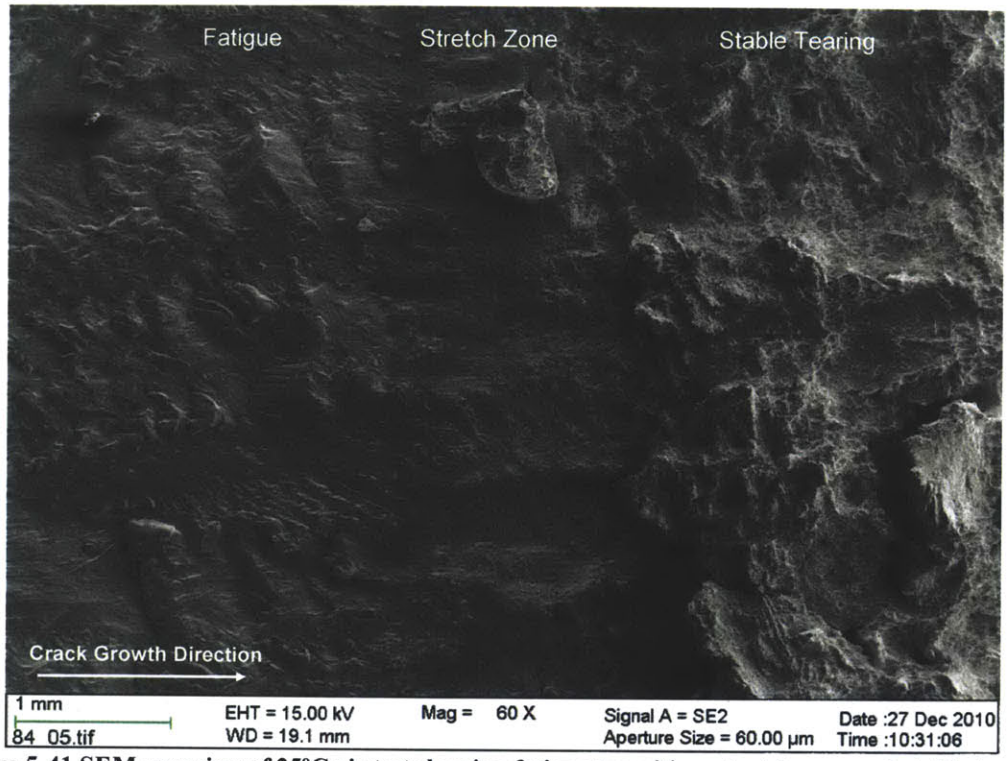

Figure 5-41 SEM overview of 25°C air test showing fatigue transition, stretch zone and stable tearing.

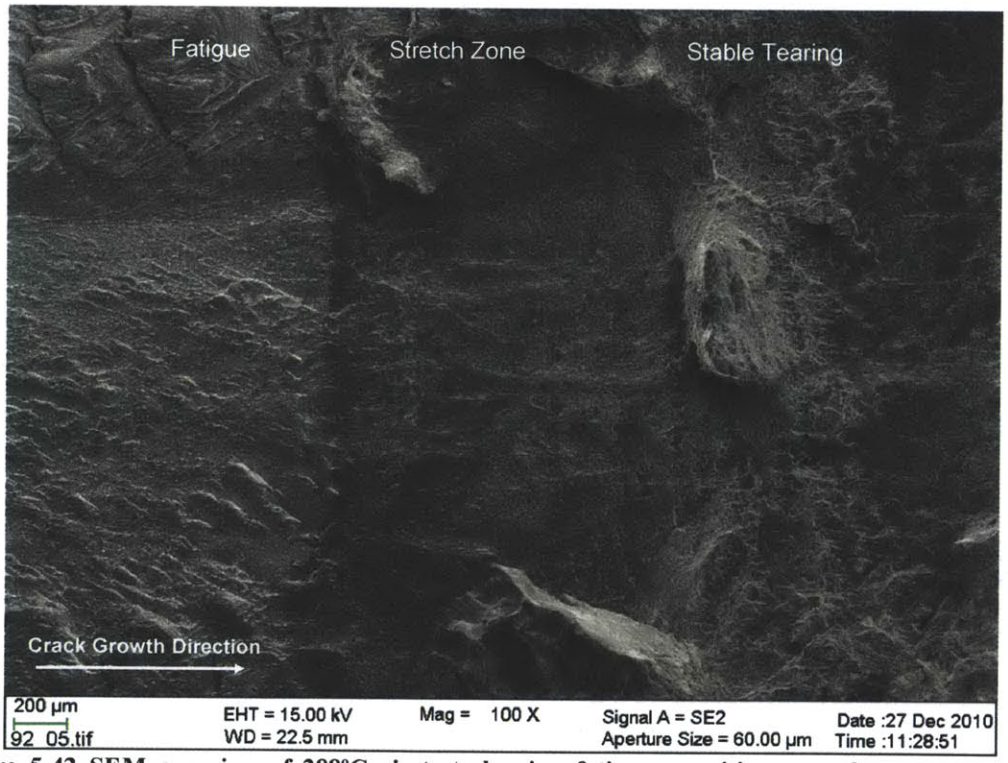

Figure 5-42 SEM overview of 288°C air test showing fatigue transition, stretch zone and stable tearing.

Figures 5-41, 5-42, and 5-43 are SEM micrographs representative of the entire test area in each specimen. In each of them the fatigue, stretch zone and stable tearing zone is visible. Figure 5-41 and 42, the air samples, show very similar features with a clear transition from fatigue to the stretch zone, and then the onset of ductile tearing to finally fully developed stable tearing. There is some, small amount of microstructural continuity in the fatigue to stretch zone transition. The features of the stable tearing region appear to occur on the same length scales previously discussed, that of the weld bead size and that of the dendrite size. Conversely, in the in-situ sample micrograph, even at a relatively low magnification, there are two striking features visible. The first is a brittle region at the onset of the stretch zone, dividing the fatigue and the stretch zone regions. It is postulated that this is an instant fracture that occurs at the beginning of the test at a relatively low J value as it happens prior to crack tip blunting. This brittle instability also follows microstructural features that begin in the fatigue region. The second feature of note in the in-situ sample is that in the crack blunting region, there are small cracks perpendicular to the fracture surface that are not present in the air tests. These features will be examined in greater detail in the stretch zone section immediately below. The size of the actual SZW is usually in indicator of toughness. However, due to the uneven crack front found in welds, estimating the size of this is difficult. The areas chosen for closer analysis were purposefully large and do not represent an average SZW.

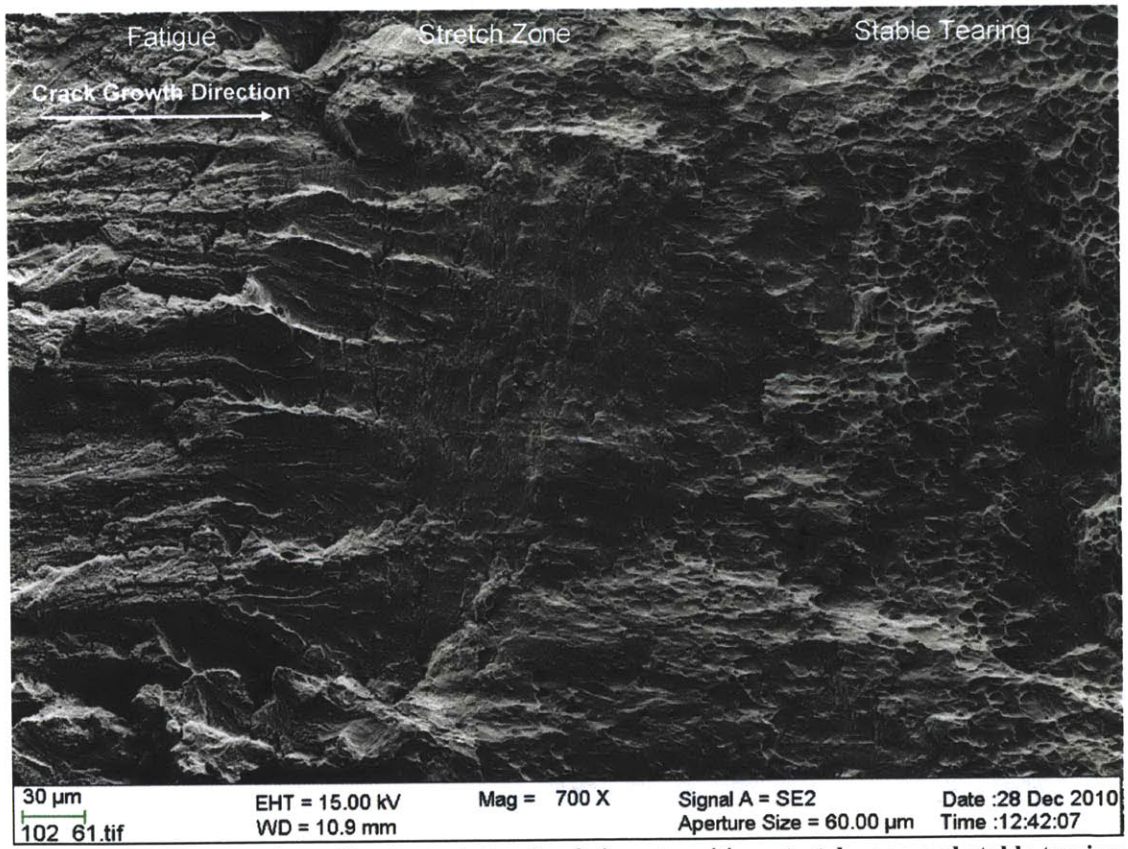

Figure 5-43 SEM overview of in-situ test showing fatigue transition, stretch zone and stable tearing. The region of brittle fracture as well as stretch zone width slip-step fracture is visible.

5.3.3.2 Stretch Zone

The stretch zone is the area where the crack tip transitions from the sharp tip produced in fatigue to the blunt tip that develops in the beginning of the fracture toughness test. As the material deforms plastically, the resulting tip is rounded with a radius on the order of size of the stretch zone. This is seen as a flat area in the sample, shown for example in Figure 44. Rather than act as a sharp tip with a point of singularity, the fracture front acts as a series of continuous tensile specimens. In this way, part of the stretch zone also highlights the transition to stable ductile fracture. Figures 5-44 through 5-53 show the fatigue-fracture toughness transition, the crack blunting region and the transition to ductile tearing region for each test condition. Additional fractography of the brittle area found in the in-situ conditions are also shown.

Figures 5-44 through 5-46 show the fractography of the material tested in 25°C air, while Figures 5-47 through 5-51 are of the 288°C air condition. The microstructural features in each material are close enough that they will be discussed together. Figure 5-44A (25°C air condition) and Figure 5-47A (288°C air condition) show a high magnification of the fatigue transition. Figures 5-44B and 5-47B show a higher magnification image. While it appears that there are striations both before and after the transition, in fracture toughness testing these are most likely the traces of operating active slip systems and in any case they are not due to the brittle fracture noted in the in-situ condition. Figures 5-45A and 5-48A show the blunting region with the onset of ductile fracture. This region is characterized by a smooth face with protracted ductile dimpling open in the direction of crack growth.

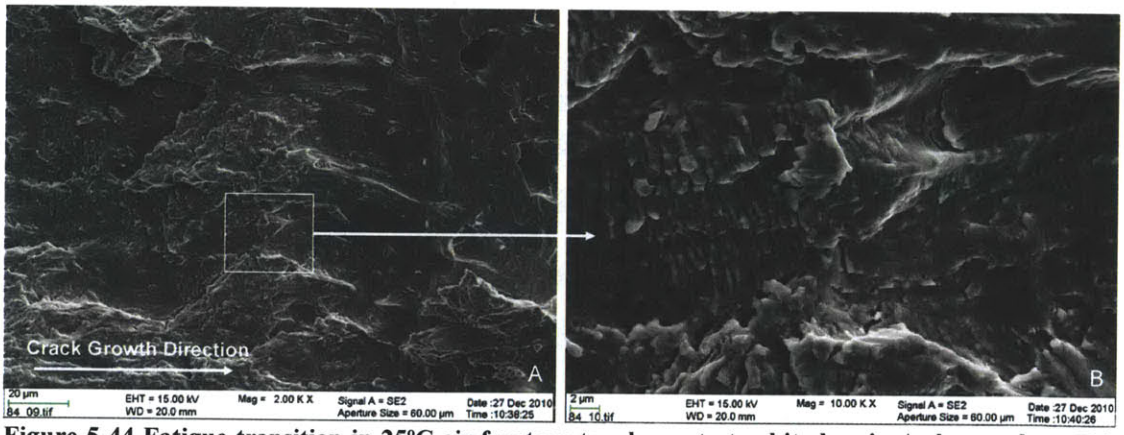

Figure 5-44 Fatigue transition in 25°C air fracture toughness test, white box in A shows where B is taken.

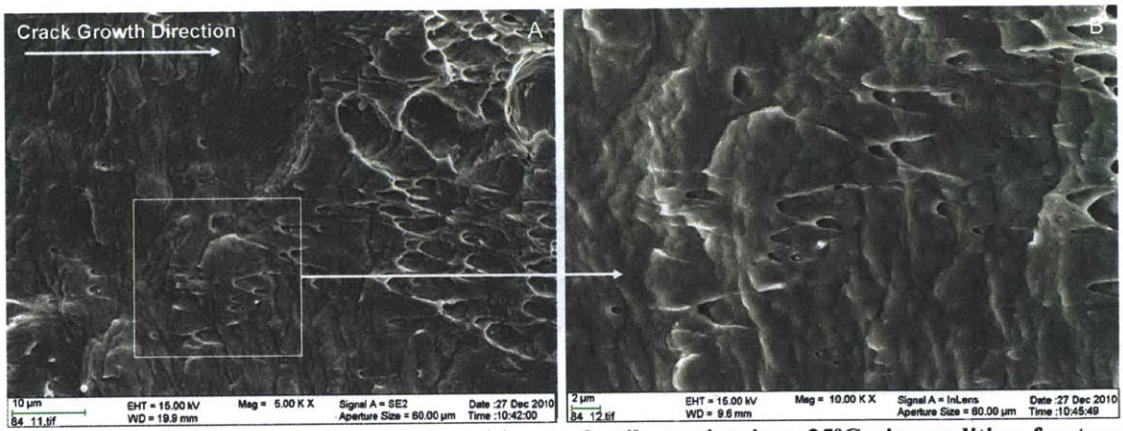

Figure 5-45 Crack tip blunting and transition to ductile tearing in a 25°C air condition fracture toughness test, white box in A shows where B is taken. MnS inclusions are noted as being the source of ductile fracture in austenite.

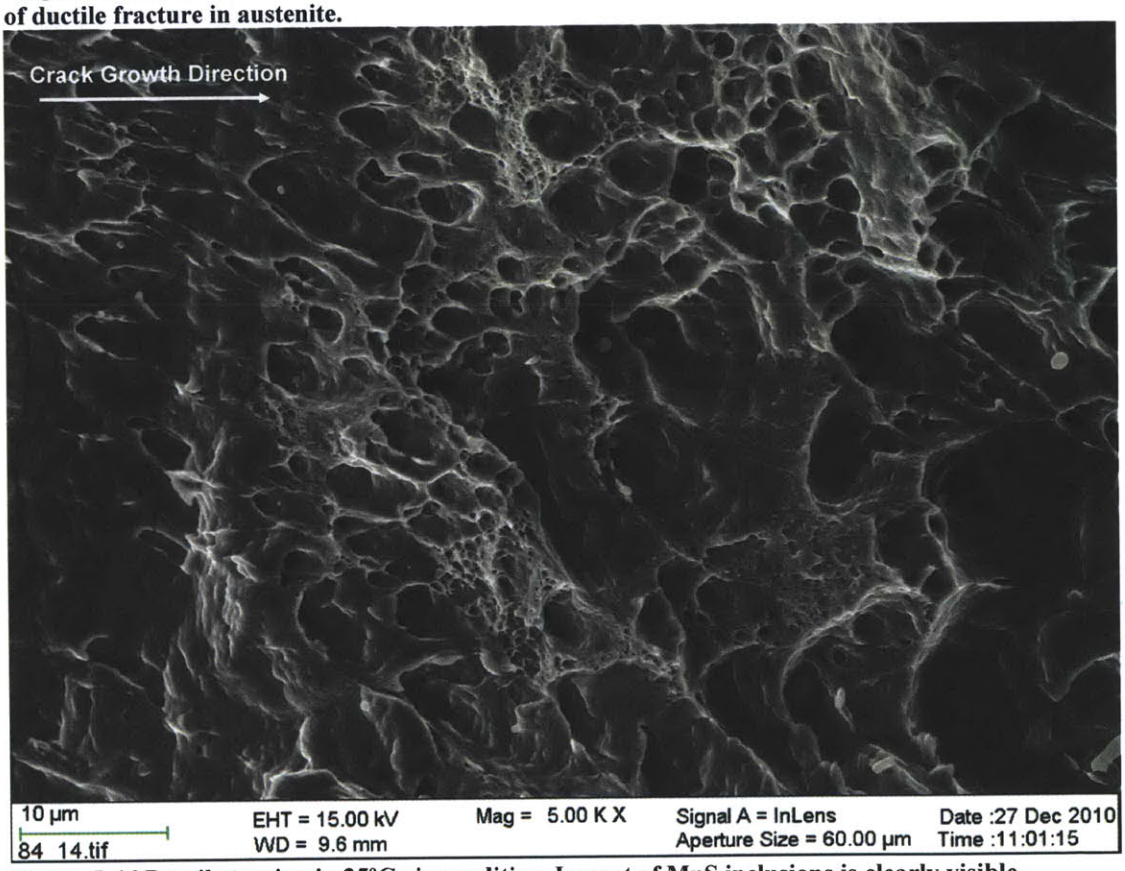

Figure 5-46 Ductile tearing in 25°C air condition. Impact of MnS inclusions is clearly visible.

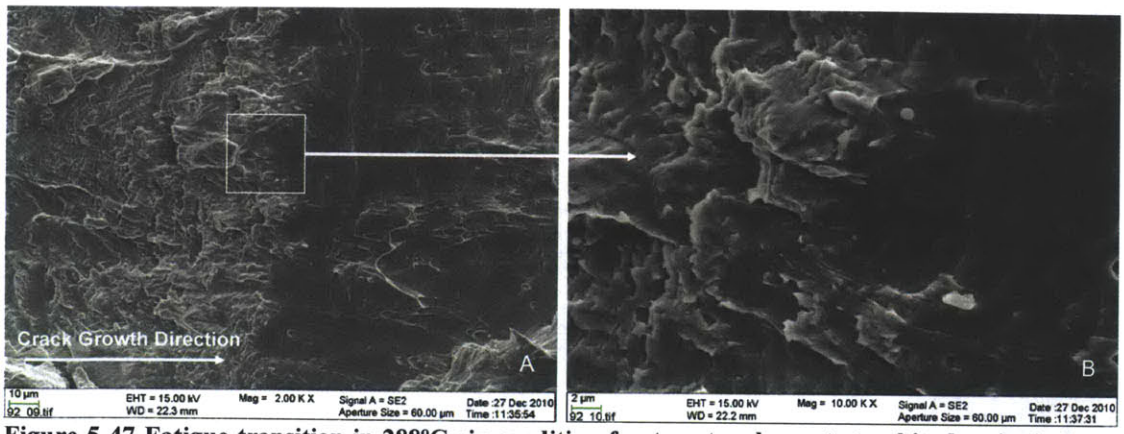

Figure 5-47 Fatigue transition in 288°C air condition fracture toughness test, white box in A shows where B is taken.

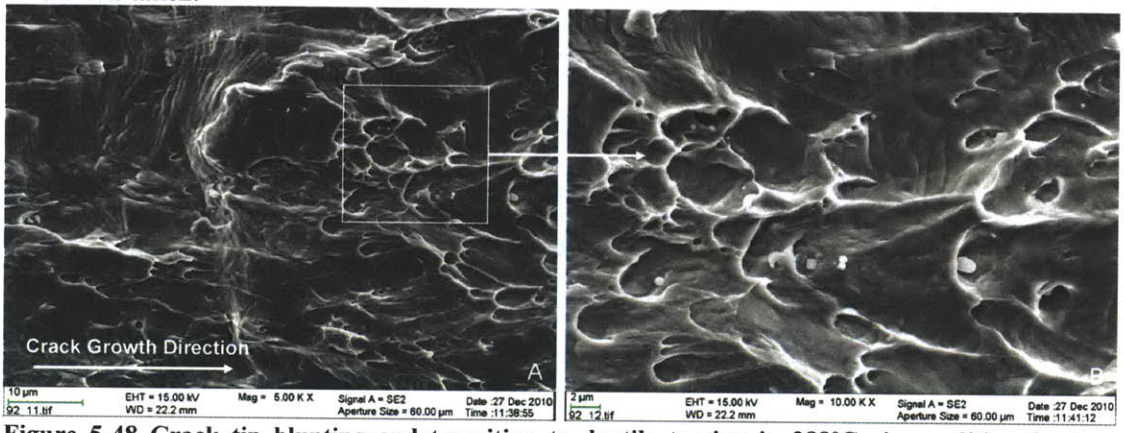

Figure 5-48 Crack tip blunting and transition to ductile tearing in 288°C air condition fracture toughness test, white box in A shows where B is taken. MnS inclusions are noted as being the source of ductile fracture in austenite.

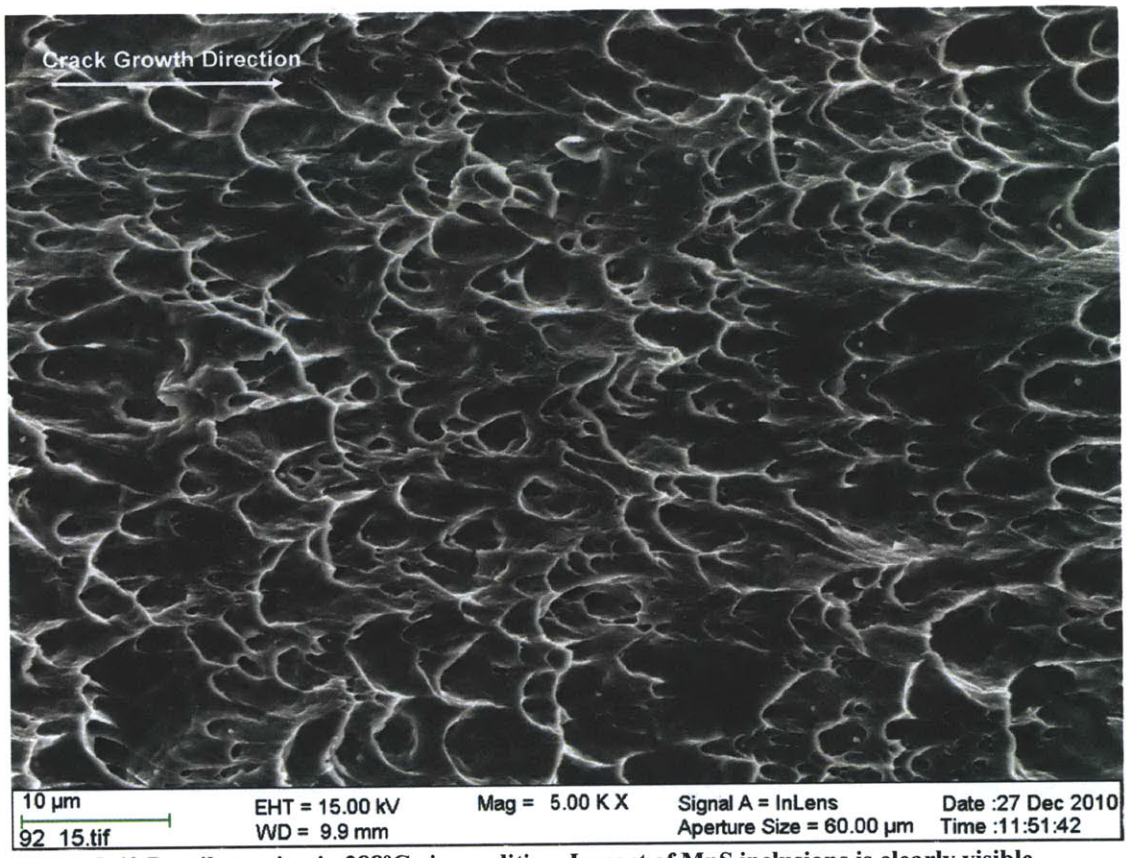

Figure 5-49 Ductile tearing in 288°C air condition. Impact of MnS inclusions is clearly visible.

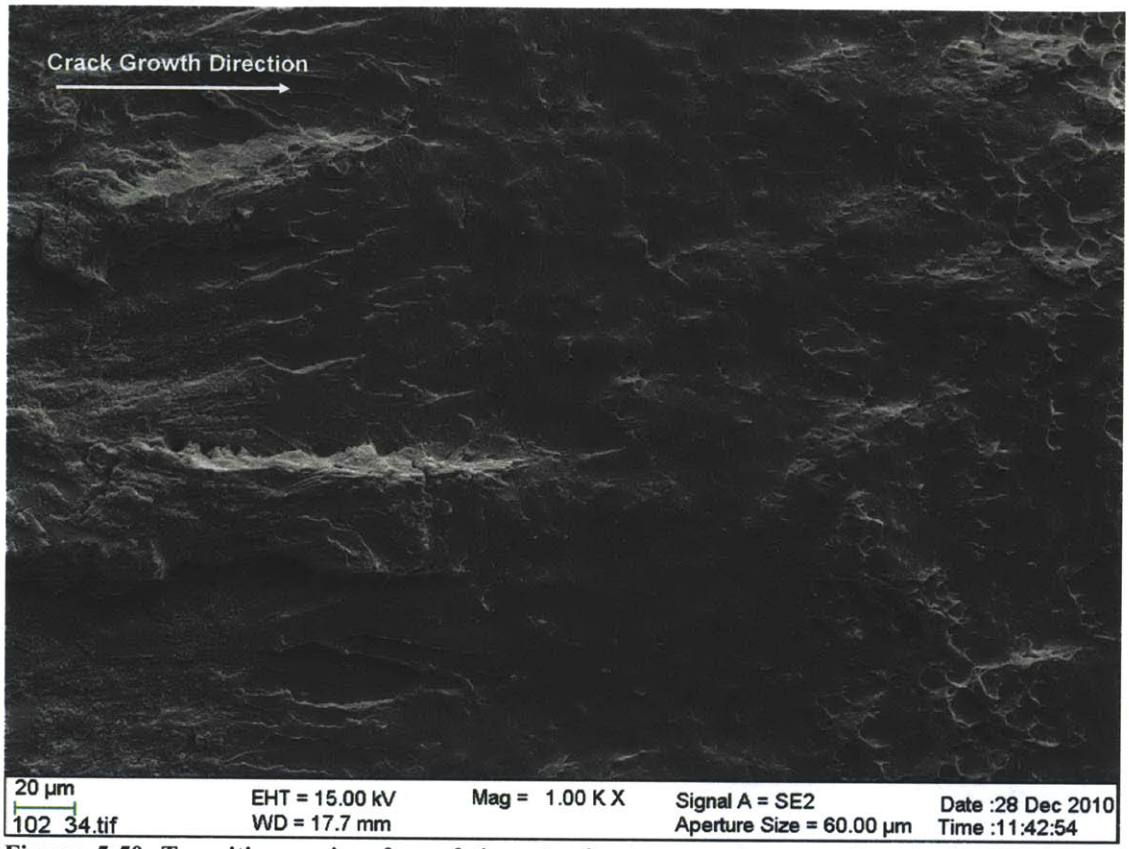

Figure 5-50 Transition region from fatigue to fracture toughness testing during in-situ test conditions. Brittle fracture is visible and is approximately the size of the cyclic fatigue plastic zone.

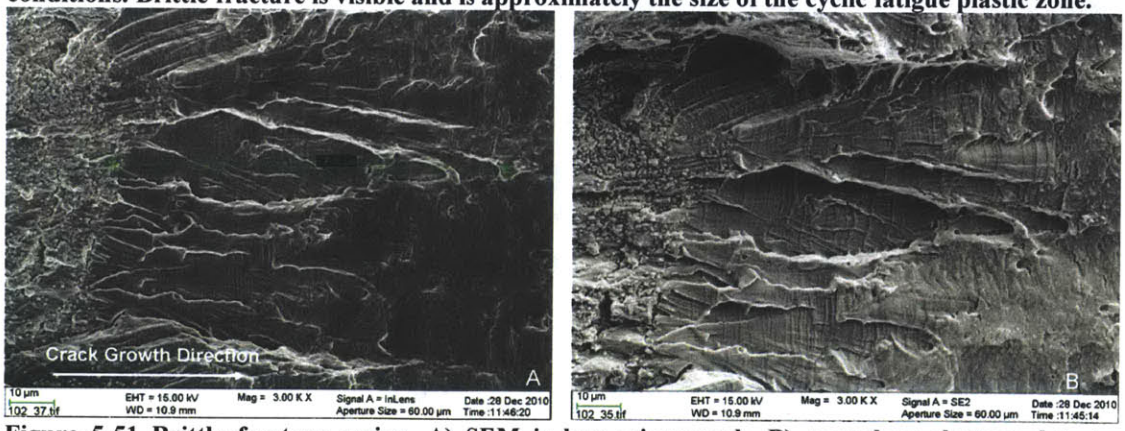

Figure 5-51 Brittle fracture region. A) SEM in-lens micrograph, B) secondary electron detector image.

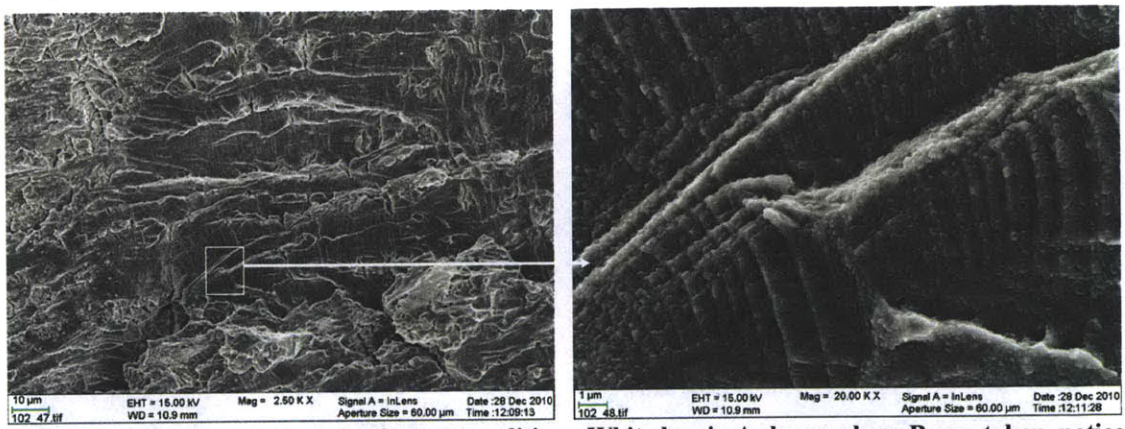

Figure 5-52 Brittle area from in-situ test conditions. White box in A shows where B was taken, notice the protracted slip steps.

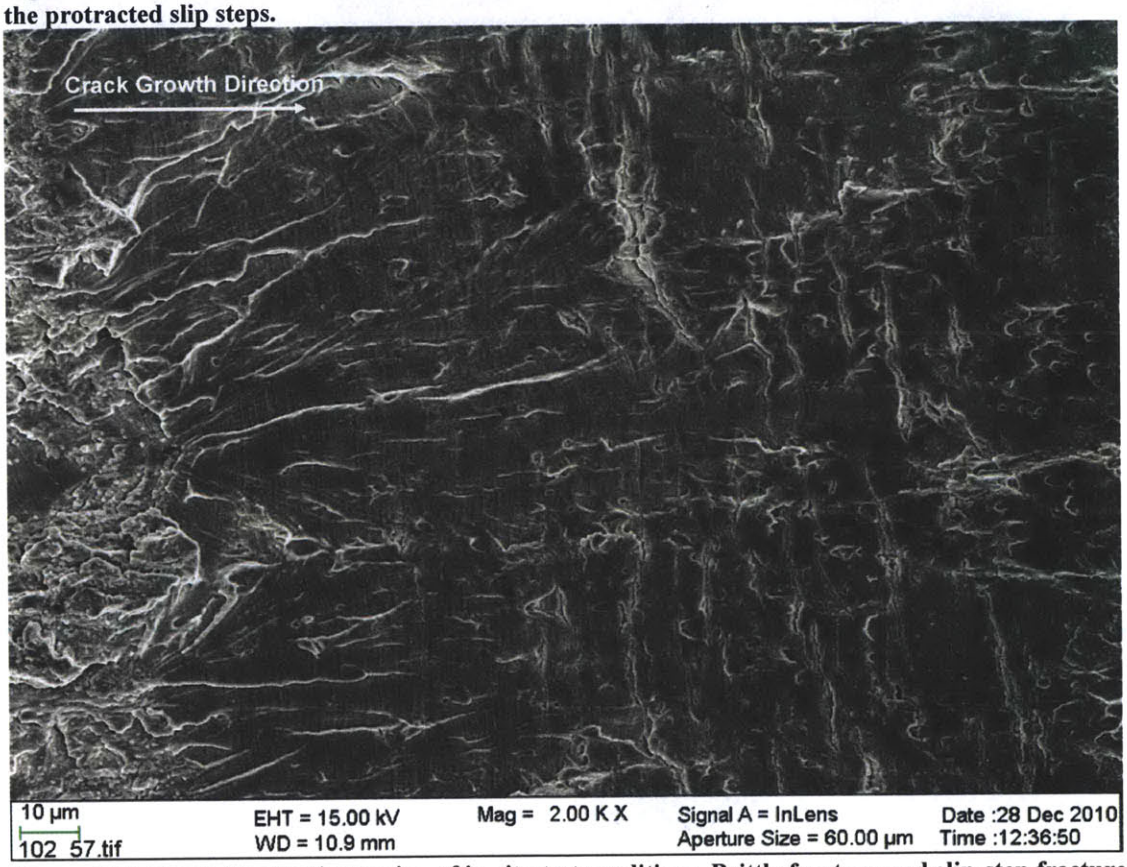

Figure 5-53 Crack tip blunting region of in-situ test conditions. Brittle fracture and slip-step fracture in the stretch zone are visible.

At the focal point of each of these is an inclusion, in this case, EDX shows mainly manganese sulfide (MnS), shown in 5-45B and5-48B. MnS is quite recognizable due to its nearly spheroidal shape. In the transition region, regular dimple structure is noted as expected for ductile fracture, shown in Figure 5-46 and 5-49. Again, MnS is present as an inclusion.

The in-situ condition fractography is shown in Figures 5-50 through 5-52. The entirety of the stretch zone is shown in Figure 5-50. The brittle zone and the slip-step fracture already noted above will be the focus of this portion of the discussion as the ductile regions of the stretch zone appear very similar to the air samples. Figure 5-51 clearly shows the brittle area. The brittle area was measured and found to be approximately 100 μm. This is approximately equivalent to the cyclic plastic zone calculated for the fatigue stress intensity in plain strain conditions that would have formed in the fatigue crack tip sharpening step prior to the fracture toughness test. This is calculated using the stress intensity, K and the yield stress, σ_{ys} equation 5-1 [61]:

$$r = 0.033\frac{\Delta K^2}{\sigma_{ys}^2}, \qquad [5\text{-}1]$$

For this material, the plastic zone is calculated to be 53 μm. This type of cyclic plastic zone is normally characterized by a cellular dislocation structure, and in air, the dislocation structure shows very little impact on the initial blunting [61]. However, the environment must play a role in causing a rapid fracture instead of simple crack tip blunting. Figure 5-51B shows a much greater contrast of the same area as Figure 5-51A, clearly highlighting the brittle nature of this brittle zone. This zone is present in every in-situ fracture toughness test condition. This condition is also visible in other researcher's micrographs, but never noted, leading to the conclusion that this is the first reporting of a new material fracture phenomenon, see, for example, [64], shown later. Figure 5-52A and 5-52B show that slip occurs in the brittle area. Another feature that has not been noted before is the shear fracture, clearly visible in many of the figures but best illuminated in Figure 5-47. At this time it is believed that this is shear occurring at 45° into the fracture surface. Interestingly, Figure 5-48 shows dendrites from an air sample at 25°C in the stretch zone of a fracture toughness test in the NQ plane. The normally straight dendrite cores are bending slightly as indicated by the straight red lines. This does not happen in the samples where testing is done in the BWR environment. These two results, the brittle zone in the cyclic plastic zone region and the shear fracture, indicate that the cause of the environmental degradation on fracture toughness affects the material by limiting the plastic deformation. Hydrogen is well known to cause a reduction in ductility.

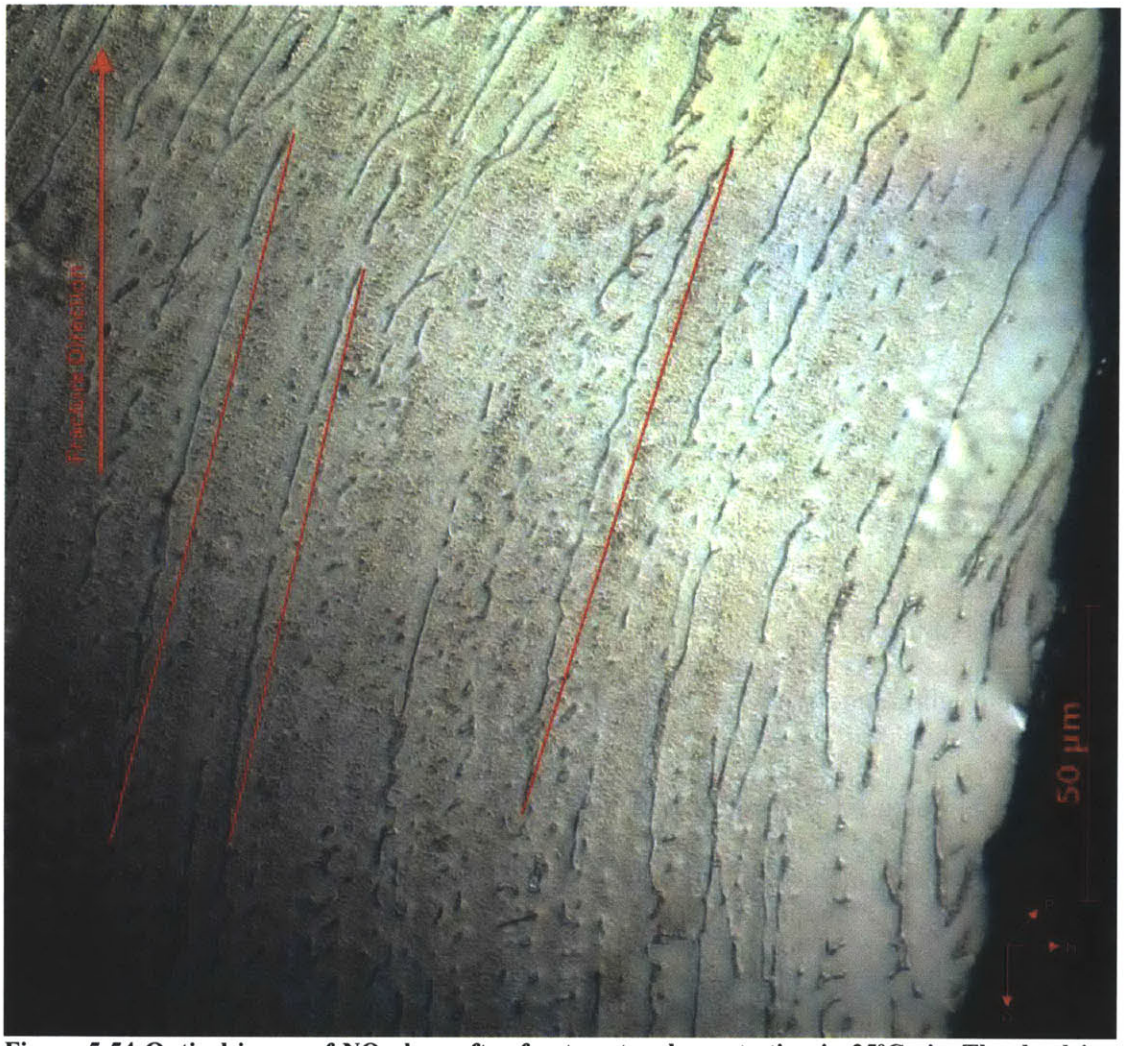

Figure 5-54 Optical image of NQ plane after fracture toughness testing in 25°C air. The dendrites clearly deform. This does not occur during in-situ fracture toughness testing.

5.3.3.3 Stable Tearing Region

The fracture surfaces in the stable tearing region showed clear ductile failure, as is evident in the SEM micrographs in Figure 5-55, 5-56, and 5-57, 25°C air, 288°C air and in-situ samples, respectively. These figures show several important features and interactions which occur. In Figures 5-55A and 5-56A, the air conditions, there are clearly two different size dimple arrangements present. In the larger dimples, the presence of MnS inclusions can be seen as spheroidal inclusions in Figures 5-55 and 5-56, though noticeably absent from the in-situ condition shown in Figure 5-67. It is believed many of them have dissolved in high temperature water. The larger dimples are believed to be occurring in the austenite phase as that is where it would be likely to find the MnS inclusions due to manganese being an austenite promoter. In the δ-ferrite phase, it is believed the inclusions are much smaller, beyond the resolution of the SEM. The dimples are consequently smaller in size. This allows the visibility of some underlying material structure in the stable tearing region. Figures 5-55B and 5-56B are much higher

magnification, where the small size of the MnS inclusions can be resolved. Also, in the smaller dimples, even at 30,000 X magnification, no inclusions can be identified. Also, not visible, because it is too large is the largest scale of interaction, the size of the weld beads, 1-3 mm. However, on the in-situ conditions, there is less of tearing of on this scale. However, in air, it is normal to see a crack meandering in the form of large delaminating flaps, forming at crack arrestors created by the weld bead boundaries or other dendritic morphology changes. The second scale of the fracture was on the scale of the austenite/ferrite interfacial continuum, shown in Figure 58, in a 25°C air sample, cross-sectioned in the PN plane.

Figures 5-59 through 5-61 show SEM images of dendrite delamination occurring in an as-welded high ferrite material tested at 25°C in air. This particular microstructure is found only when lathy ferrite is present. Figures 5-59 through 5-61 are gradually increasing magnification of the same area. The lighter areas of the micrograph show what is believed to be δ-ferrite, while the lower, darker larger portion is likely austenite. However, due to the close chemical composition of these two phases in this material it was not possible to use EDX to distinguish between the two.

Figures 5-62 through 5-64 are taken perpendicular to the fracture surface of high-ferrite material tested at 25°C in air. Parallels between the dendrite grain structure and aligned grain structure of forged materials can be drawn. The equiaxial nature of the dendrites is similar to mechanical fibering. In the case of Figure 5-62, the crack is progressing from the bottom of the micrograph to the top and clearly changes direction. It is noticeable that the dendritic structure changes from a laminar arrangement to a confused morphology causing the meandering path. This sort of dendrite morphology serves as a crack arrestor, forcing a change in crack path as shown in Figure 5-63. There were several cases where this exact behavior was noted. Furthermore, hardness testing indicates that confused morphology is on average ~1% softer and up to 5% softer than the laminar dendrite structure. The effect of the softer structure should be that it was tougher and acts as a crack arrester. Deformation of the dendrites under load is illustrated in Figure 5-64. Ultimately this leads to tensile necking behavior manifesting crack deflection and creating a meandering path, making the material tougher. As stated in the stretch zone section, this mechanism of deforming the dendrites and creation of a longer meandering crack path is not as active in the in-situ samples. What this means is that there are less mechanisms to resist ultimate fracture in-situ.

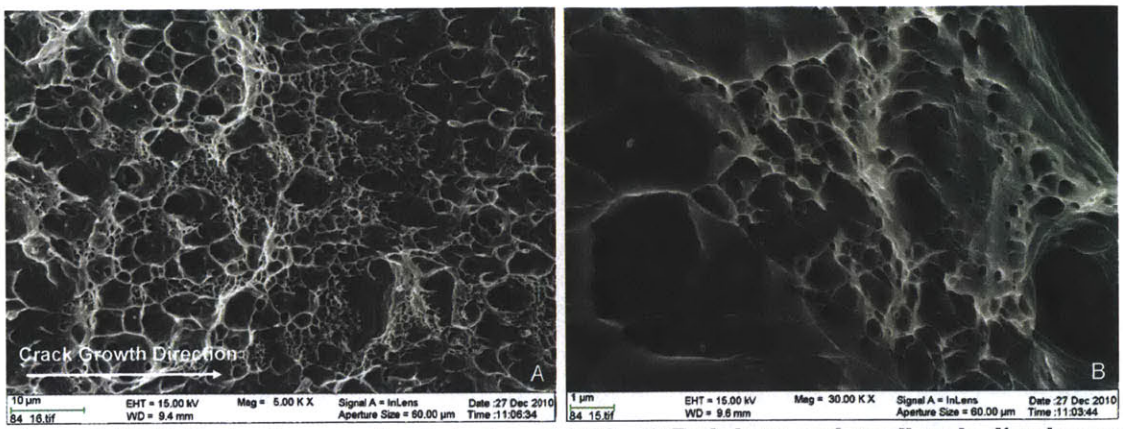

Figure 5-55 Stable tearing zone in air testing at 25°C. A) Both large and small scale dimples are formed. The small scale dimples are believed to be in δ-ferrite and large in austenite. B) Higher magnification of small dimples. Austenite dimples contain MnS inclusions while δ-ferrite do not.

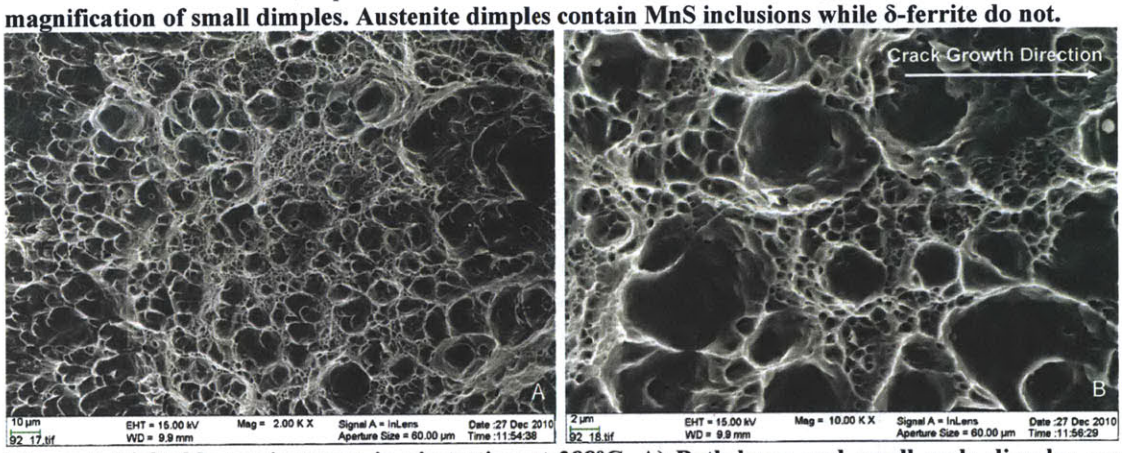

Figure 5-56 Stable tearing zone in air testing at 288°C. A) Both large and small scale dimples are formed. The small scale dimples are believed to be in the δ-ferrite and large in austenite. B) Higher magnification of small dimples. Austenite dimples contain MnS inclusions while δ-ferrite do not.

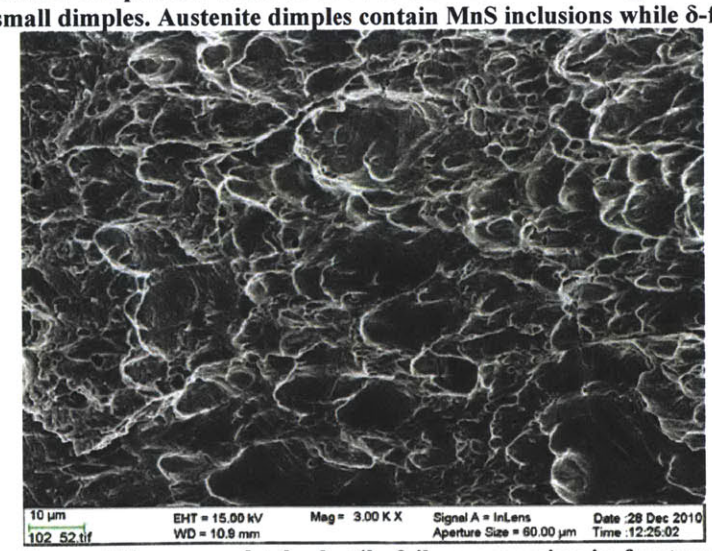

Figure 5-57 In in-situ conditions completely ductile failure occurring in fracture toughness testing. The lack of MnS inclusions is due to their dissolution in high temperature water.

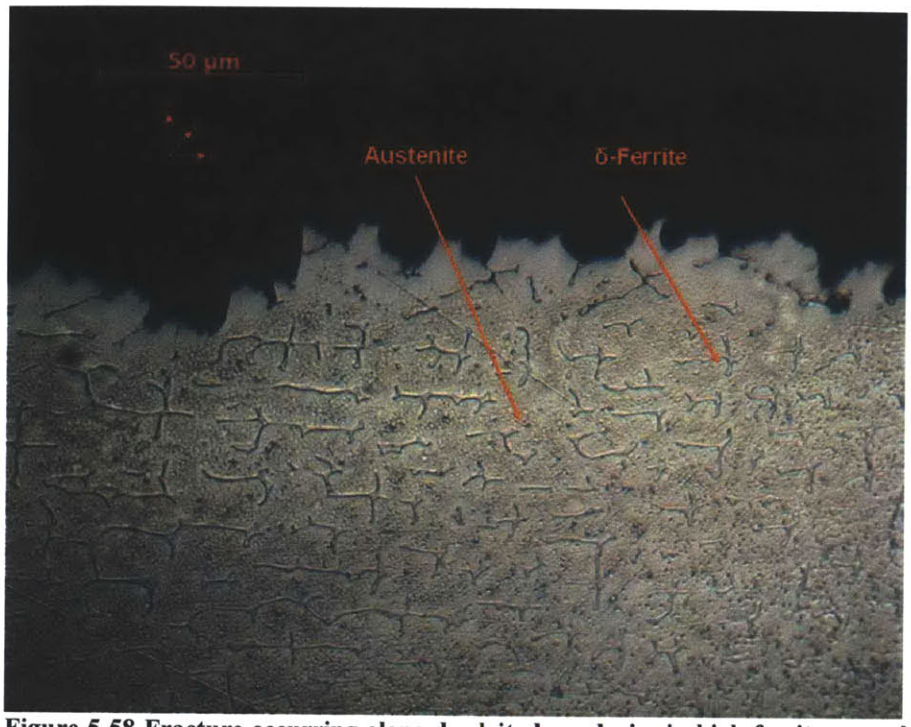

Figure 5-58 Fracture occurring along dendrite boundaries in high-ferrite, as-welded material tested in air at 25°C.

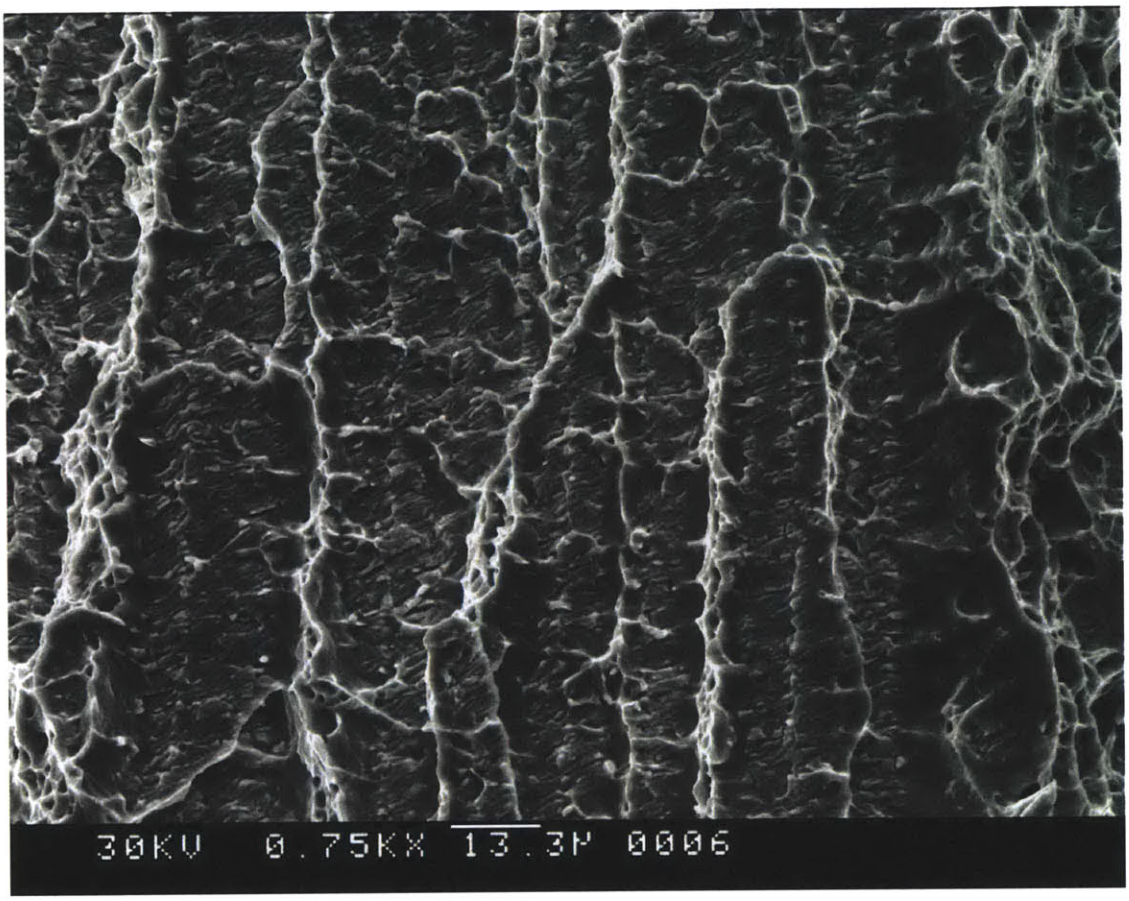

Figure 5-59 SEM micrograph as a result of delaminating at δ-ferrite boundaries in a high-ferrite, as welded material tested at 25°C in air. This type of morphology is only found when lathy ferrite is present.

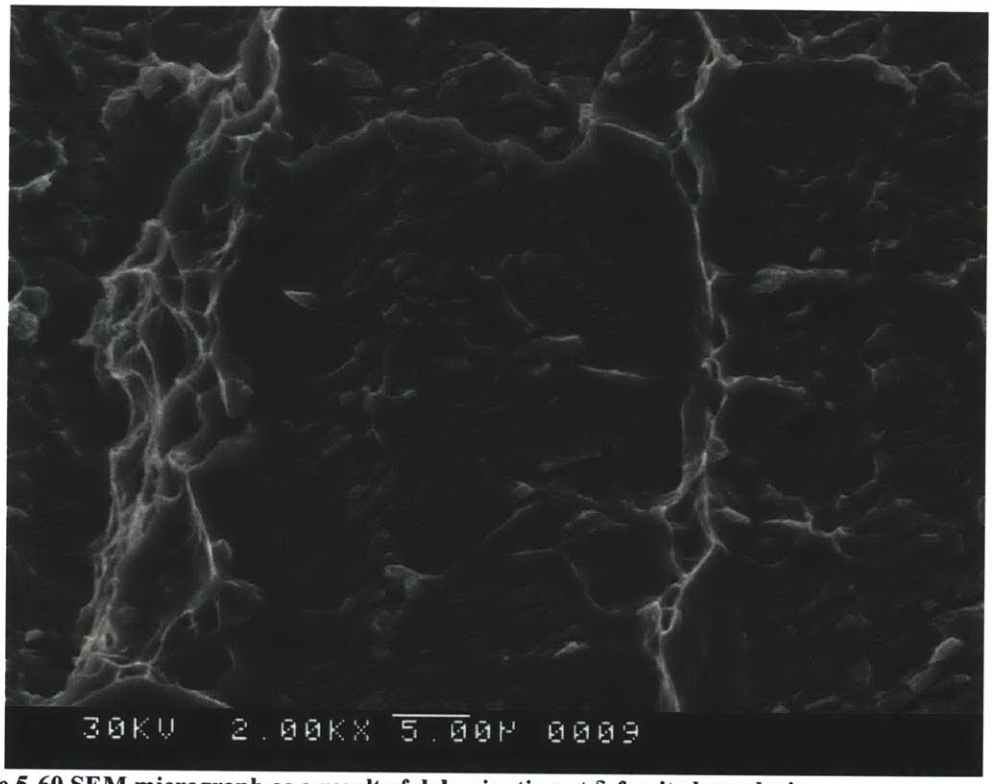

Figure 5-60 SEM micrograph as a result of delaminating at δ-ferrite boundaries.

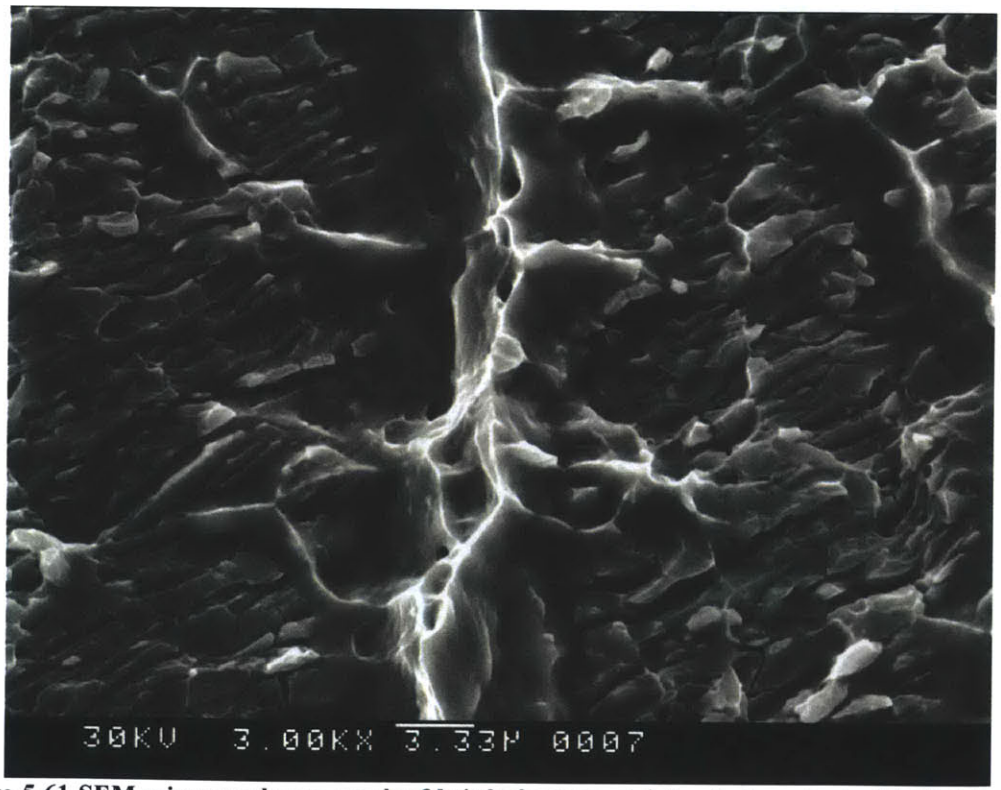

Figure 5-61 SEM micrograph as a result of brittle fracture at δ-ferrite boundaries highlighting the brittleness δ-ferrite.

Figure 5-62 Crack propagation follows a meandering path when encountering a different dendrite morphology which acts as a crack arrester.

Figure 5-63 A closer view of the change in δ-ferrite morphology acting as a crack arrester.

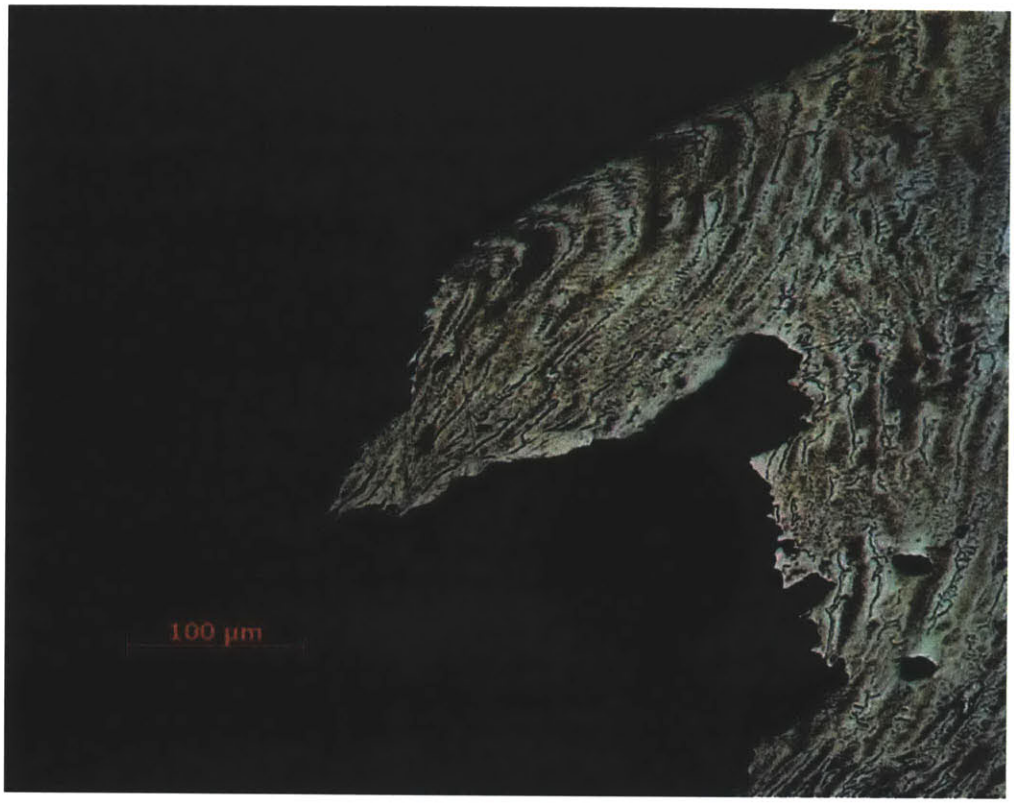

Figure 5-64 Deformation of dendrites after fracture under an applied load leading to a meandering crack path resulting in tougher material.

5.3.4 Conclusions of Fracture Toughness Testing

The results from the air fracture toughness in general showed little change in terms of aging effect for both 25°C and 288°C testing. The material actually got immediately tougher with aging. Considering however, that the environment has a clear degrading effect on toughness, the thermal aging mechanisms are of less importance for fracture toughness. The program to study environmental fracture in this thesis is the first systematic effort to identify the effects of the environment on what has been traditionally thought of as a strictly material property. Notable observations that will be important later include:

- In the material tested in air, classical fracture mechanics adequately explains what is occurring in the stretch zone - the fracture initiates by first blunting the fatigue sharpened crack tip and moves to ductile tearing.
- In-situ behavior is not adequately described by classic fracture mechanics, for two reasons:
  - Prior to crack tip blunting, there is a brittle fracture that occurs which is on the scale of the cyclic plastic zone in fatigue.
  - Cracking is occurring in slip planes while the crack is blunting.
- In the stable tearing region, both in air and in-situ, ductile fracture is aided by MnS inclusions. There is also fracture in and along the δ-ferrite.

However, crack arrest and meandering is more evident in air test conditions than during in-situ conditions.

- Furthermore, deformation mechanisms which are active in air leading to bending and necking of the dendrite structure both in the stretch zone and the stable tearing region are not present in-situ.
- Without the mechanisms of fracture resistance, such as plastic deformation, crack meandering, and the confused complex morphology they create, it is clear that in-situ tested conditions could have a lower fracture toughness.

It can be verified that the observed "environmental fracture" behavior is real and results in a very significant reduction in the fracture toughness of the material. The implication for structural integrity under dynamic loading conditions such as would exist during hypothetical accident situations needs to be evaluated.

5.4 Hardness Mapping and Microstructure

Hardness mapping was performed in order to identify the property changes as a function of location in the weld. Cross-sections of large welds, on the NQ plane sections were polished to a 0.06 μm and etched using Kalling's reagent. Hardness mapping was performed for weld cross-sections for both high- and low-ferrite as-welded, and 400°C aged 1,000 h and 5,000 h material. Only the high-ferrite samples are shown here. Figure 5-65 shows a schematic of the testing orientation and area.

Hardness mapping was performed using a Leco Model LM 247/AT hardness tester with a Vickers indenter. Figure 5-66 shows the maps for high-ferrite welds aged from 0 to 5,000 h at 400°C. In Figure 5-67 a sample indention is shown for comparison to the dendrite size. The average trends are shown in Figure 5-68. It is illustrated that the hardness increases and then exhibits a more gradual decrease. This correlates to the tensile test results noted in Figure 5-1 for material of the same aging. It is evident in the hardness maps that the hardness varies both horizontally and vertically in the welds. If we consider this in respect to the tensile test data and sample location, then the reason for data deviation in those tests becomes clear. The weld properties change depending on location. For this reason it is very important that all fracture toughness and crack growth rate test samples be taken from roughly the same location in the weld, as was done in this study. Furthermore, this clearly demonstrates that hardness data for welds that is reported in the literature in a non-mapped format can lead to very different conclusions based on the location of sampling in the weld or HAZ region. The centerline and root of the weld tend to have the highest hardness. The hardness decreases with the distance from the centerline radially. The HAZ is clearly visible and is noticeably softer than the weld metal but harder than the base metal. Finally, the lowest hardness is found in the base metal.

There are several factors that can affect the hardness of the weld metal. The most common reason given in the literature is based on dendrite spacing. The closer the dendrites the harder the material [30]. Based on the ferrite volume fraction, and thus the dendrite spacing, the anticipated effect is that higher ferrite numbers should be harder.

This is indeed the case with high-ferrite consistently showing higher hardness than low-ferrite samples. Another aspect of weld morphology that is not mentioned in the literature is the shape and angular dependence of the dendrite in reference to indention. Referencing Figure 4-4 in the experimental description, it is evident that the weld metal does not contain completely uniform dendrite morphology. Along the fusion line the dendrites are not fully developed, nor is the weld chemistry the same. There are differences in ferrite number and morphology as the dendrite cores shift from nucleation, to lathy ferrite to the final skeletal form found along the weld centerline. Furthermore, there are multiple weld passes that have an impact. Finally in some areas, the dendrites are being loaded on their short axis, or some other angle rotated about the axis of the Vickers tip. This results in slightly different crystallographic planes of exposure. As hardness and tensile properties correlate, and it is well known that there is a directional dependence on tensile properties in crystals, it is natural to expect to see the same behavior over a hardness map of a varying dendrite morphology [61]. The hardness mapping gives the clearest indication of the highly variable nature of weld metal, further demonstrating that there are many sources of inherent error based on the location of testing in the weld metal.

In terms of aging, there are three primary mechanisms that are active simultaneously, that may be acting in concert. First, there is spinodal decomposition which has already been shown to cause hardening in the δ-ferrite. If the weld metal is considered from a composite mechanics standpoint, then the δ-ferrite core and the surrounding austenite make up two phases with the carbides acting at the interphase region. So a change in one of the regions would have an effect on the overall composite system. This brings up the second mechanism, which is a growth and coarsening of the carbide particles in the interphase region. Finally, some researchers have theorized that the hardness is directly related to residual stress and strain fields associated with weld solidification mechanics [66]. Figure 5-69, from Morra, shows, for example, the crystallographic mismatch between δ-ferrite and the austenite in Type 304 stainless steel [67]. Such a mismatch can lead to dislocation pile-ups and would have impact on the micro-stress and -strain field. The next section discusses stress relaxation with time.

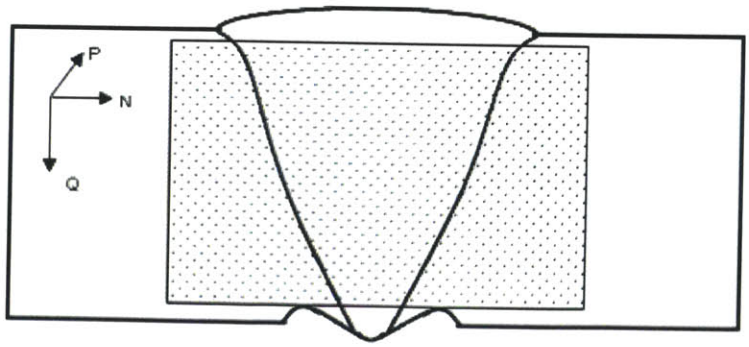

Figure 5-65 Schematic of hardness mapping area.

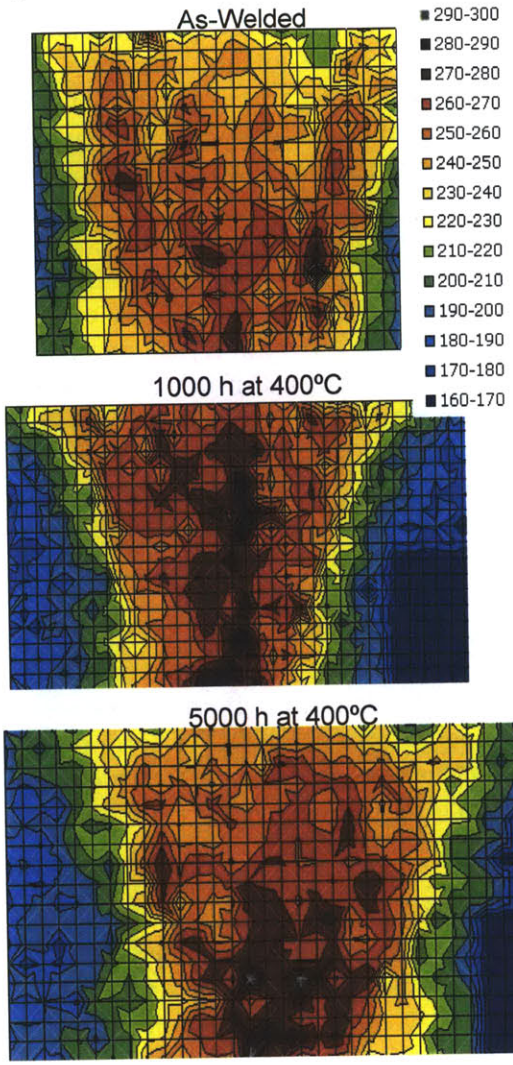

Figure 5-66 Hardness maps of high-ferrite material as-welded and aged at 400°C for 1,000 and 5,000 h.

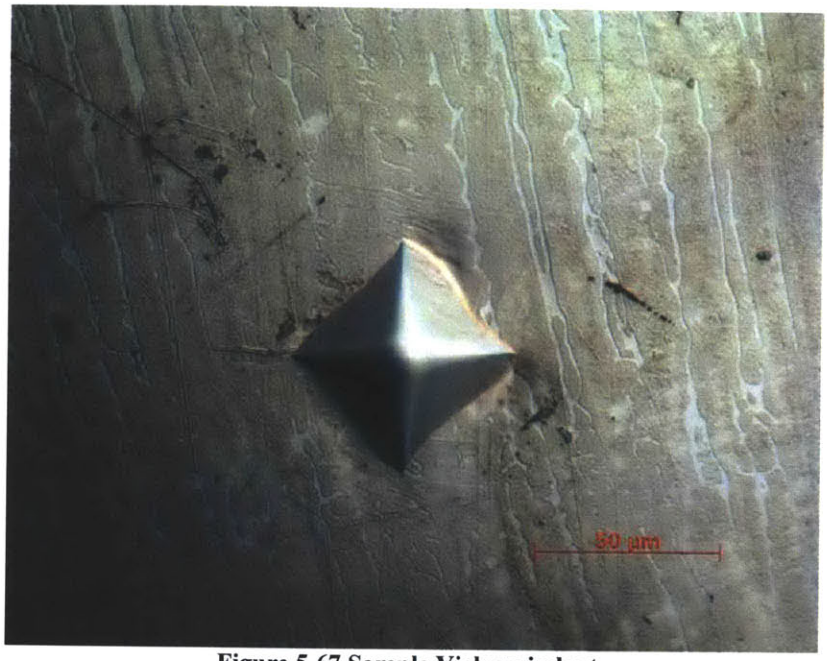

Figure 5-67 Sample Vickers indent.

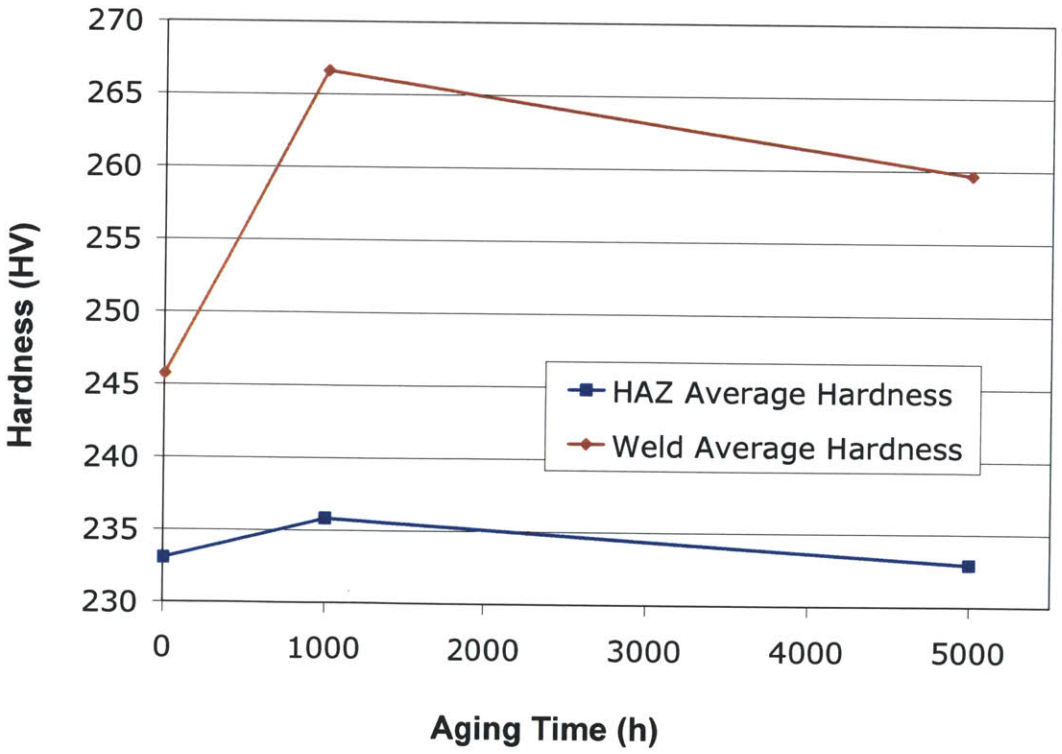

Figure 5-68 Average Vickers hardness value for high-ferrite material as a function of aging at 400°C for heat-affected zone and weld metal.

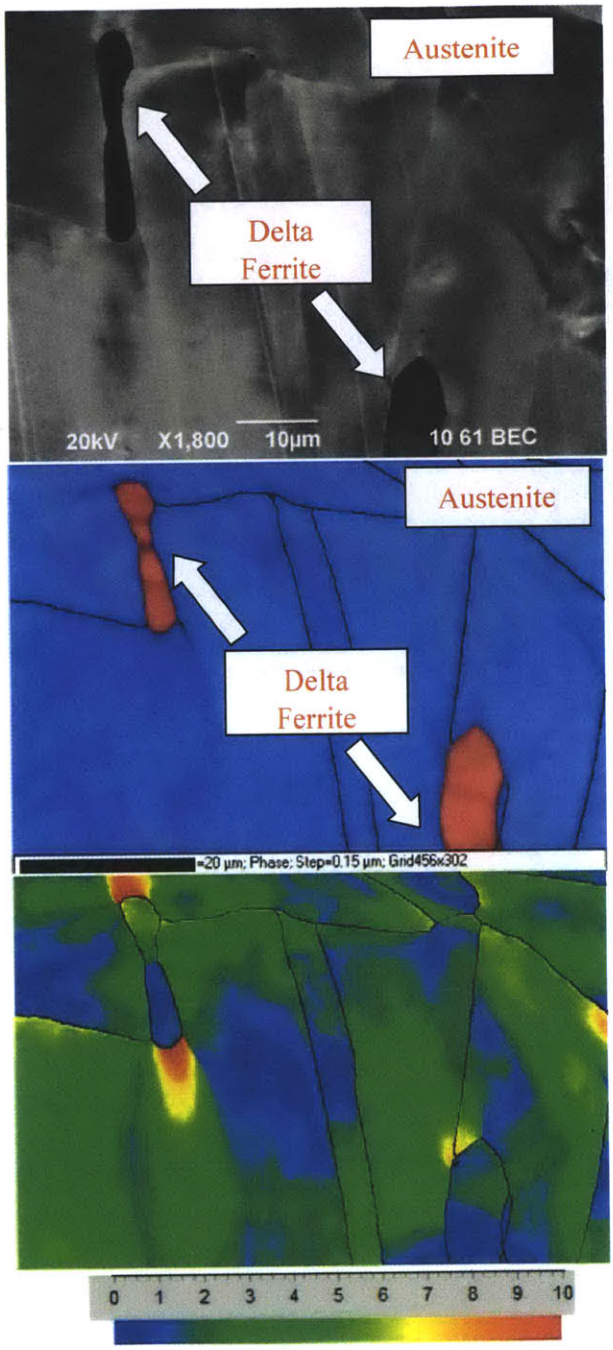

Figure 5-69 SEM electron backscattering diffraction image and missorientation map for Type 304 stainless steel containing delta ferrite. Upper: BSE image, Middle: phase map, Lower: missorientation map (Used with permission of Dr. Morra of GE Global Research Center).

5.5 Residual Stress Analysis

Nuclear power plant welds are not stress relieved due to their size and the potential for precipitation of undesirable phases at the temperatures required to allow stress relaxation. As previously mentioned, the lower toughness and tensile properties noted at 288°C versus 25°C is peculiar. In general, it is expected that increasing the temperature would actually make a material more ductile and therefore tougher. However, this was not the case. This leads to a need to determine the amount of residual stress within the weld metal as a potential cause.

High-ferrite samples were polished and prepared for residual stress analysis. Four material conditions were analyzed: as-welded, aged 1,000, 5,000, and 10,000 h at 400°C. Initially it was attempted to use X-ray diffraction in order to determine the residual stress. However, due to the extreme texture of the dendritic structure, this was not possible. It was determined that an instrumented center hole drilling method in accordance with ASTM E837-01 would be the method of analysis [68]. Samples where sent to Lambda Research, Inc. in Cincinnati, OH, for the performance of this test. Lambda electro-polished the surfaces of the samples to remove the surface layer where any residual stresses from the saw cutting and polishing would be located.

The actual measurement was made at the weld metal geometrical center on each sample. Residual strain was measured using a rectangular electrical resistance strain gauge. Hole machining was performed using an air-driven high-speed carbide tool. The hole penetrated a total of 1 mm, which is 40% of the strain gauge rosette centerline diameter. Figure 5-70 shows the sample and analysis point configuration and stress direction.

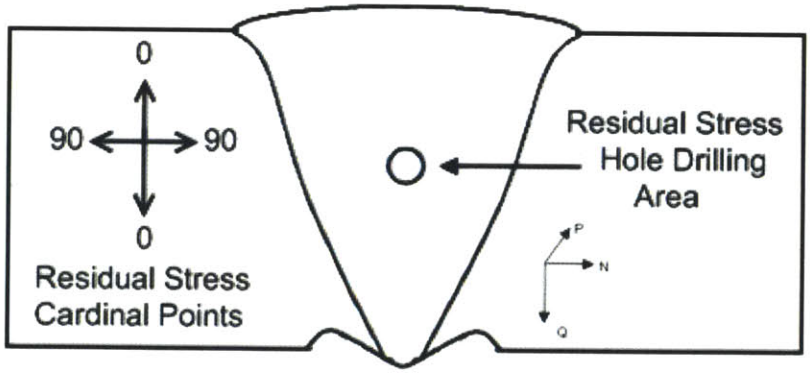

Figure 5-70 Weld metal showing location of test hole as well as the geometrical residual stress directions.

The results of the residual stress analysis are presented in Figures 5-71 through 5-77. If the overall average of the residual stress of each hole is taken for each aging time and graphed as a function of aging time the same trend that has been noted in the tensile and hardness properties is seen again. The trend was such that largest change in residual stress is in the first 1,000 h of aging followed by gradual decrease in compressive stress to 5,000 h and then a gradual increase to 10,000 h. This is shown in Figure 5-71. The hole

depth shown is from 0.2 to 0.8 mm in order to neglect surface and end effects. In Figure 5-71, only the average stress of each condition is shown. However, all of the conditions are under overall compressive stress even though at some depths there is residual tensile stress noted. The results of each sample are shown in Figure 5-72 though 5-75. Shown is the minimum and maximum stress as well as the average stress as a function of hole depth. In general, the as-welded sample retains the most compressive stress. There is a directional dependence of the residual stress. Figure 5-77 shows the absolute directional dependence of the residual stresses. In general, the residual stress direction is between 60 and 90 degrees in the direction of loading. This means that the residual stress is complimenting the actual loading direction of concern. It should be noted that the nature of the stress is expected to be similar through out the weld. However, the directional dependence may change based on the dendritic orientation. Furthermore, qualifying the impact of the residual stress on material properties is not possible as the machining of the samples relieves an unknown amount of the stress. Furthermore, when fracture toughness analysis is performed, the majority of the fracture resistance in the material comes from the plastic component of the J-integral, where the residual stresses would have already been relieved by plastic deformation.

The question of the cause of the decrease in compressive stress still remains. In addition, residual stress testing was done on 400°C aged samples. Plants actually operate closer to the 300°C aging temperature. So it is possible, though unlikely, that the stress relaxation mechanism may not be active.

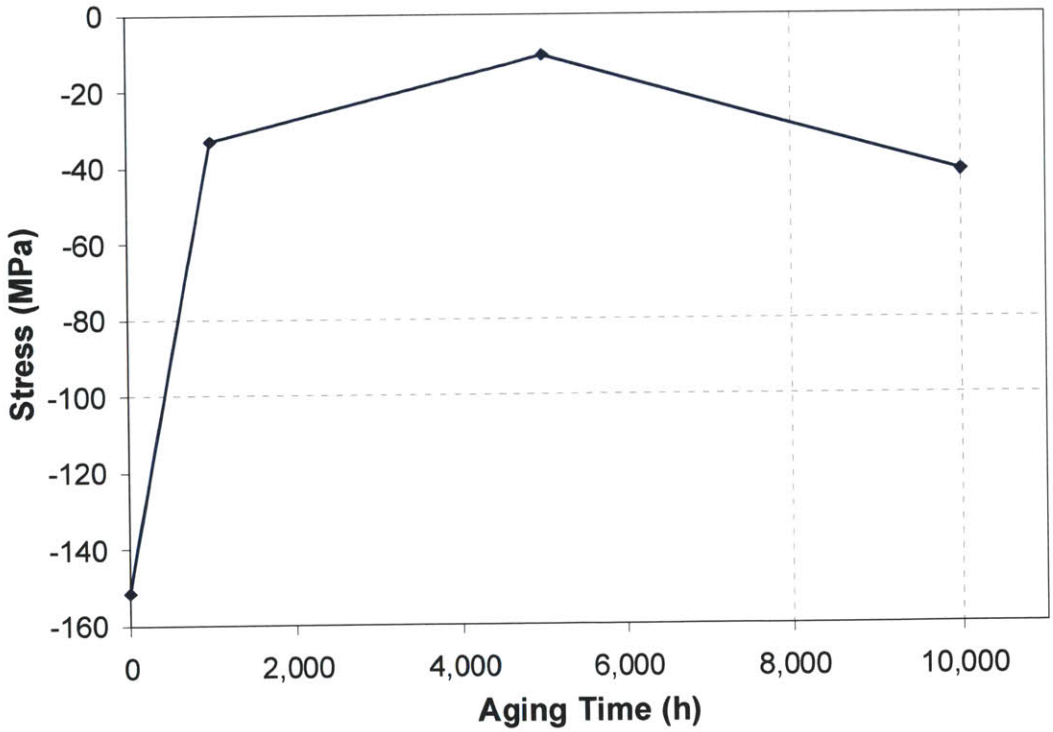

Figure 5-71 The overall average of the residual stress for each aging condition from 0.2 to 0.8 mm hole depth shown as a function of aging time. Of note is that the results exhibit the same trend as many of the material property characterization tests.

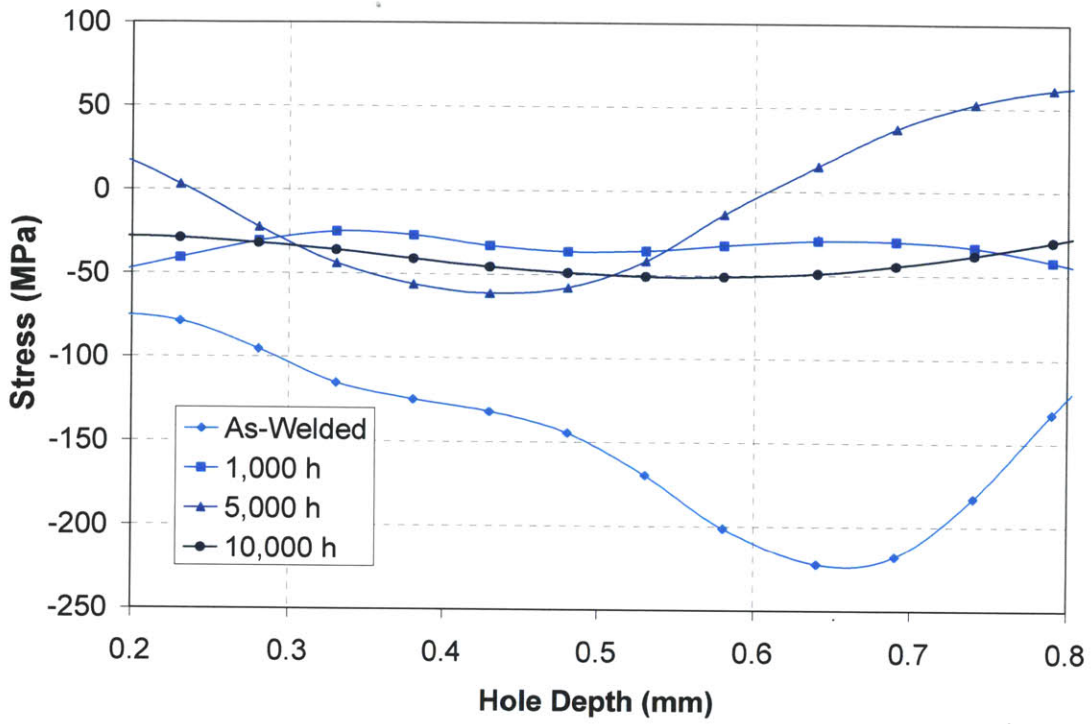

Figure 5-72 Average residual stress for each high-ferrite material aged at 400°C as a function of hole depth. The average is taken from 0.2 to 0.8 mm in order to remove surface and hole-end effects.

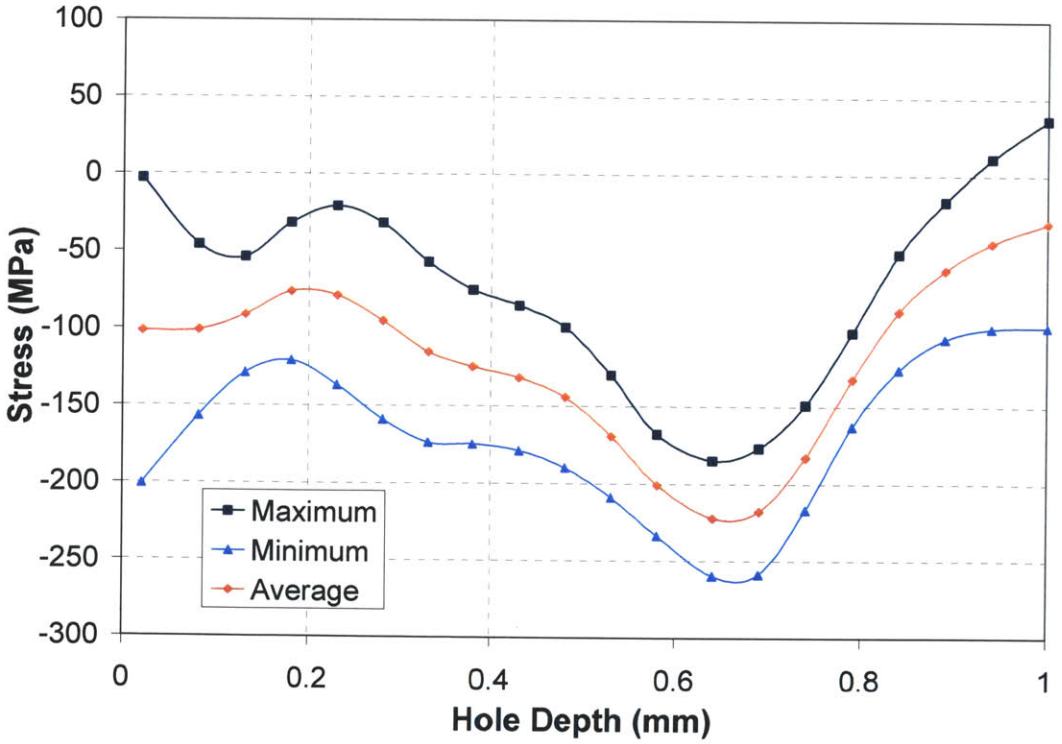

Figure 5-73 Maximum, minimum and average residual stress for the as-welded high-ferrite material.

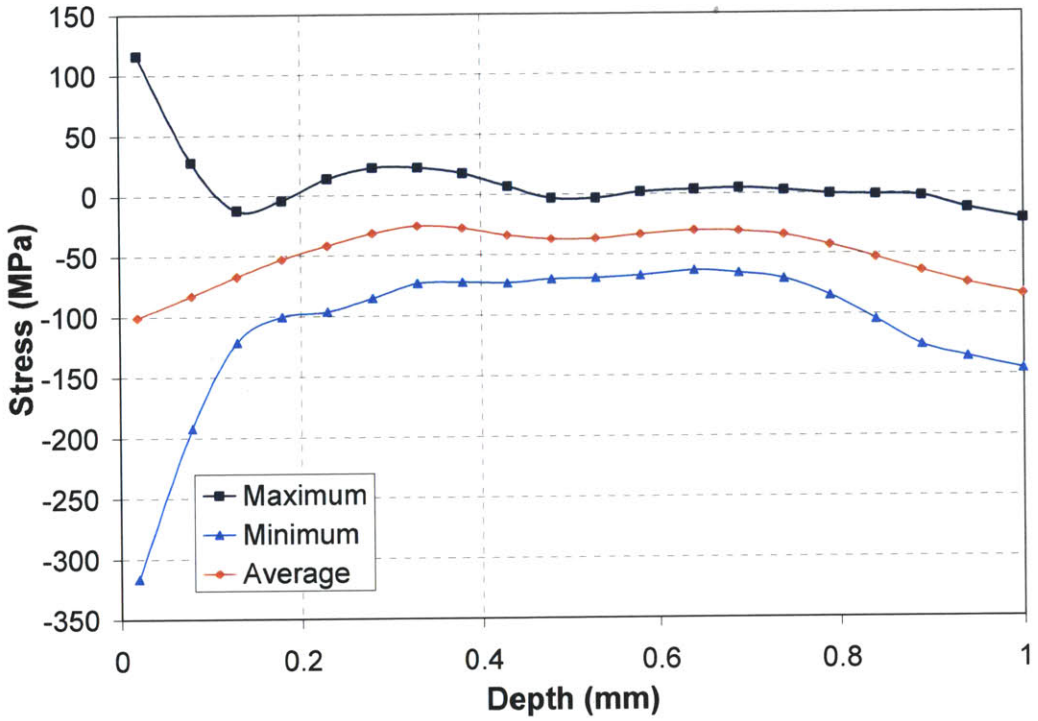

Figure 5-74 Maximum, minimum and average residual stress for 1,000 h, 400°C aged, high-ferrite material.

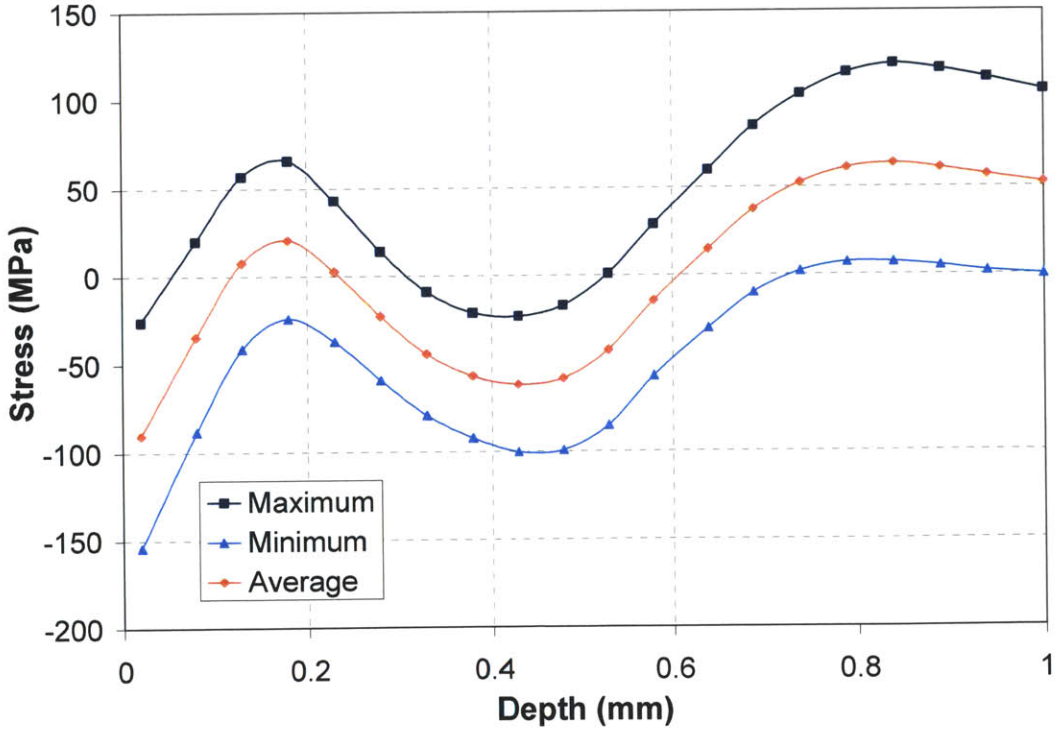

Figure 5-75 Maximum, minimum and average residual stress for the 5,000 h, 400°C aged, high-ferrite material.

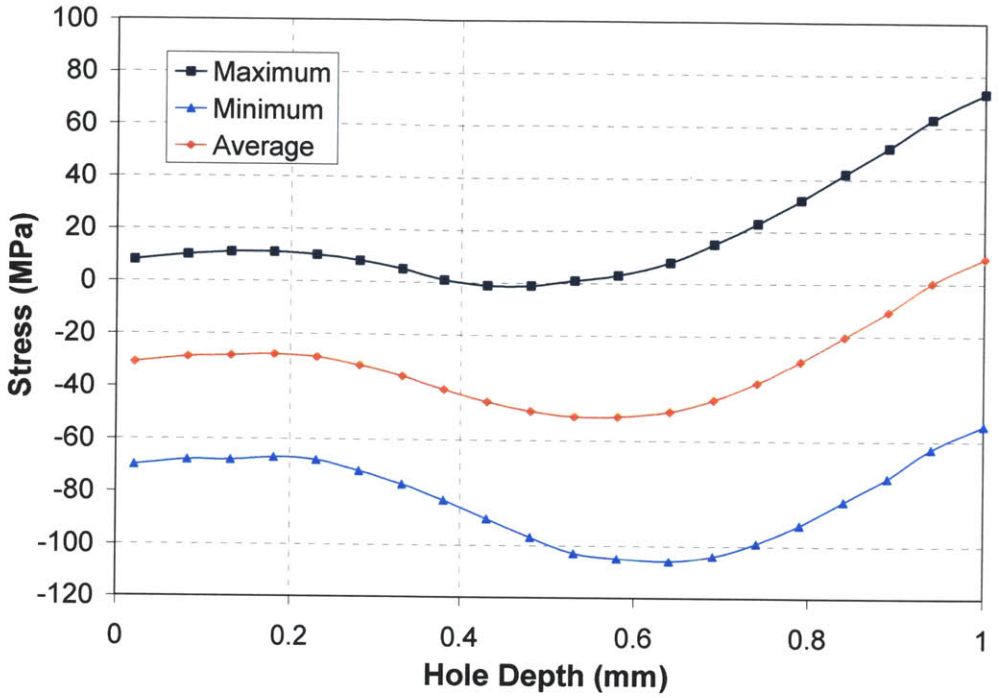

Figure 5-76 Maximum, minimum and average residual stress for the 10,000 h, 400°C aged, high-ferrite material.

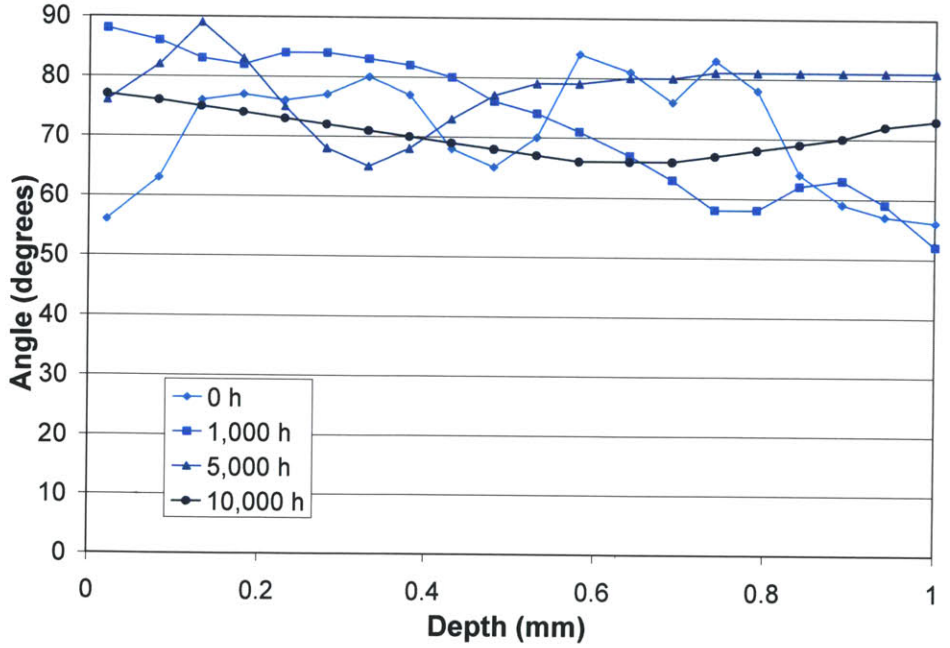

Figure 5-77 Absolute directional angle of stress. The results being mostly between 65 and 90 degrees as shown in the cardinal points in Figure 5-70, indicates that the residual stresses are complimentary to the loading stresses.

5.7 Charpy-V Testing

The trends in the Charpy-V data, a general decrease with aging time at temperature, are consistent with that reported by others such as [48]. For another example, Charpy-V data from Pumphrey and Akhurst for cast stainless steel (CF3) with approximately 13% ferrite as a part of a study in which a direct comparison between thermal aging, mechanical properties and the spinodal decomposition was measured and demonstrated a similar decrease with aging time [53].

5.7.1 Charpy-V Impact Energy as a Function of Aging Time and Ferrite Content

The data for material aged at 400°C is shown in Figure 5-80. The results of all tests are tabulated in Table 5-5. There was, however, an experimental mistake made, in that the material as-welded and aged for 1,000 h was tested in a different orientation relative to the fracture path used elsewhere in the study. The 5,000 h and 10,000 h materials where fractured in directions consistent with the rest of the study. For this reason, the trends seen in Figure 5-80 should not be viewed as ideal. In each case, the data for 300°C aging at 5,000 h was used as an alternative as-welded condition since very little change would have occurred in that material. This trend is shown by dashed lines in Figure 5-80.

The vertical bars in Figure 5-80 represent the range of observed values. The three samples averaged for each data point came from different locations within the weld (bottom, middle, top) so it was expected that there would be a considerable scatter in the data. This expectation is further reinforced by the observation of a change in the spatial hardness distribution with aging time and temperature. While there is considerable data scatter, in the elevated temperature aged data there is often a slight increase in Charpy-V impact energy at the longest aging time for this series, this will be addressed below in the discussion of the fractography. The trend in the higher temperature behavior, apart from the anomalous behavior at 400°C/10,000 h, is for saturation.

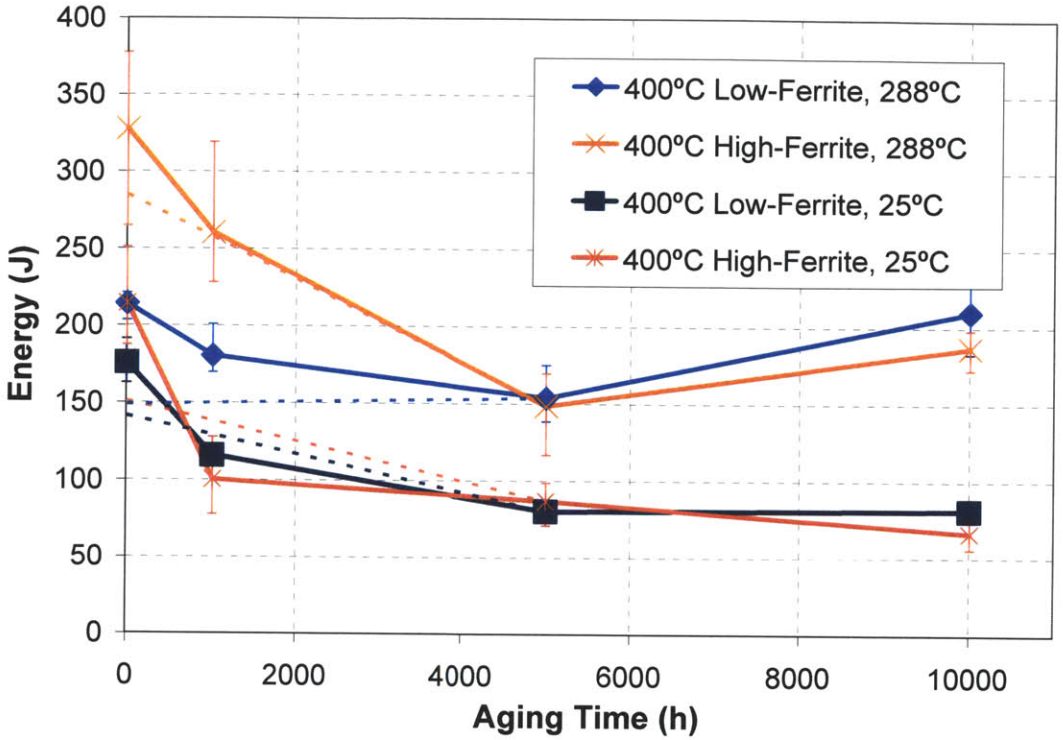

Figure 5-78 Charpy-V impact energy on high- and low-ferrite material aged at 400°C as a function of aging time. Dotted line represents extrapolation from 300°C aging data.

Table 5-5 Complete Charpy-V impact energy data.

Charpy V-Notch Impact Energy (J)

Ferrite Content	Aging Temperature	Aging Time (h)	25°C				288°C			
			Outside	Middle	Root	**Average**	Outside	Middle	Root	**Average**
Low-Ferrite	N/A	0	191	163	174	**176**	221	203	218	**214**
	300 °C	5000	162	127	135	**141**	146	161	138	**149**
		20000	125	119	149	**131**	178	156	188	**174**
	400 °C	1000	111	114	122	**116**	171	169	201	**180**
		5000	81	82	77	**80**	175	148	138	**154**
		10000	79	86	79	**81**	183	186	260	**210**
	430 °C	1000	108	129	123	**120**	184	155	210	**183**
		5000	77	94	77	**82**	161	125	142	**143**
		10000	73	73	111	**86**	136	148	142	**142**
High-Ferrite	N/A	0	205	251	187	**214**	340	377	264	**327**
	300 °C	5000	123	167	163	**151**	285	317	252	**285**
		20000	79	122	147	**116**	278	273	241	**264**
	400 °C	1000	77	127	95	**100**	319	235	228	**260**
		5000	71	98	91	**87**	159	117	169	**148**
		10000	60	56	83	**66**	198	172	190	**187**
	430 °C	1000	66	61	65	**64**	225	301	247	**258**
		5000	53	53	71	**59**	205	207	197	**203**
		10000	45	68	72	**62**	183	195	197	**192**

5.7.1 Charpy-V Impact Test Fractography

Regardless of the direction of fracture in the sample relative to the dendrite direction, the fractography was still valid and demonstrated that the data trends were what would be seen in any case of direction. However, the absolute change may not be valid for a detailed discussion. The behavior demonstrated first a decrease in shear lip size, then an increase after 5,000 h aging. Shear lip size is indicative of the impact toughness but is also orientation dependent, so it is not possible to draw a detailed conclusion from this [61]. The fracture path, as in fracture toughness testing, showed evidence of crack arrestor behavior, especially noticeable in the more ductile longer aged samples.

Fractography will focus on high-ferrite material tested at 288°C and aged at 400°C. Figure 5-81 shows that the Charpy-V energy was controlled by the austenite, which is expected as it makes up the majority of the material. Very interesting, however, is that the δ-ferrite exhibited brittle cleavage fracture. At high magnification, as shown in Figure 5-82, the δ-ferrite was brittle most likely due to high free carbon and nitrogen interstitial content. Figure 5-83, which is for 5,000 h aged at 400°C material, shows quite the opposite behavior, the material behavior was ductile in both austenite and δ-ferrite when near where the fracture is initiated. The strain rate increases as the Charpy-V hammer proceeds through the material [61]. When the strain rate gets high in the end of the test, the δ-ferrite again behaved in a brittle manner, shown in Figure 5-84. By this time in the aging, spinodal decomposition has occurred completely, and weakened the δ-ferrite. At 10,000 h the material is regaining toughness and demonstrated complete ductile failure in both phases throughout the fracture surface. This is likely due to the diffusion of interstitial carbon and nitrogen from the δ-ferrite, precipitating as carbides, mitigating the loss of toughness caused by spinodal decomposition. Carbon and Nitrogen diffusion are known to affect the Charpy-V properties ferritic steels [70].

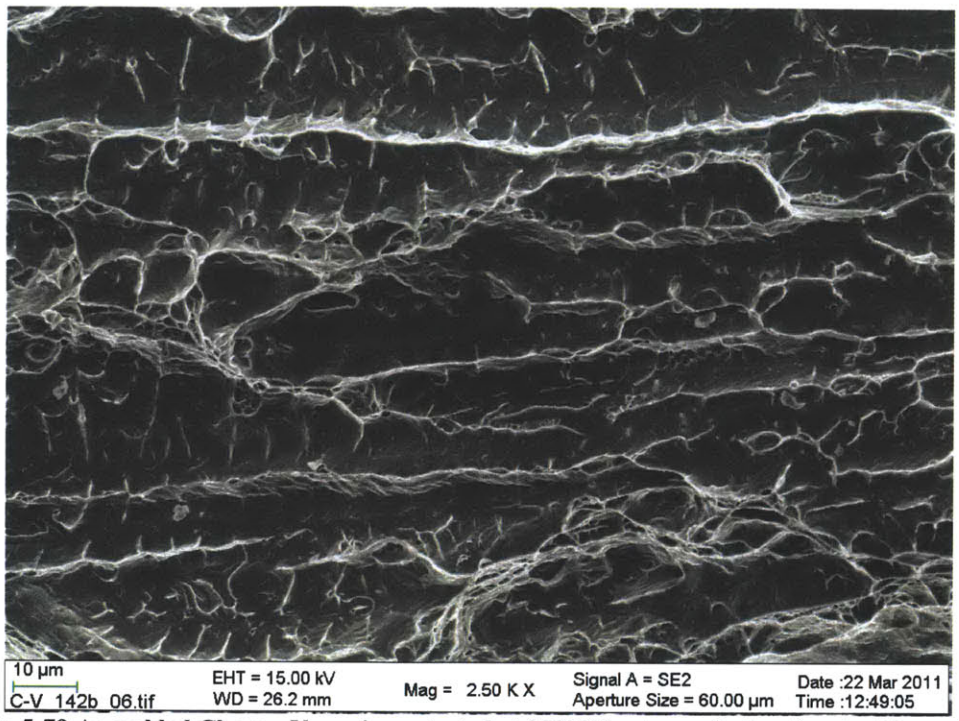

Figure 5-79 As-welded Charpy-V specimen, tested at 288°C fractograph showing ductile austenite and brittle δ-ferrite.

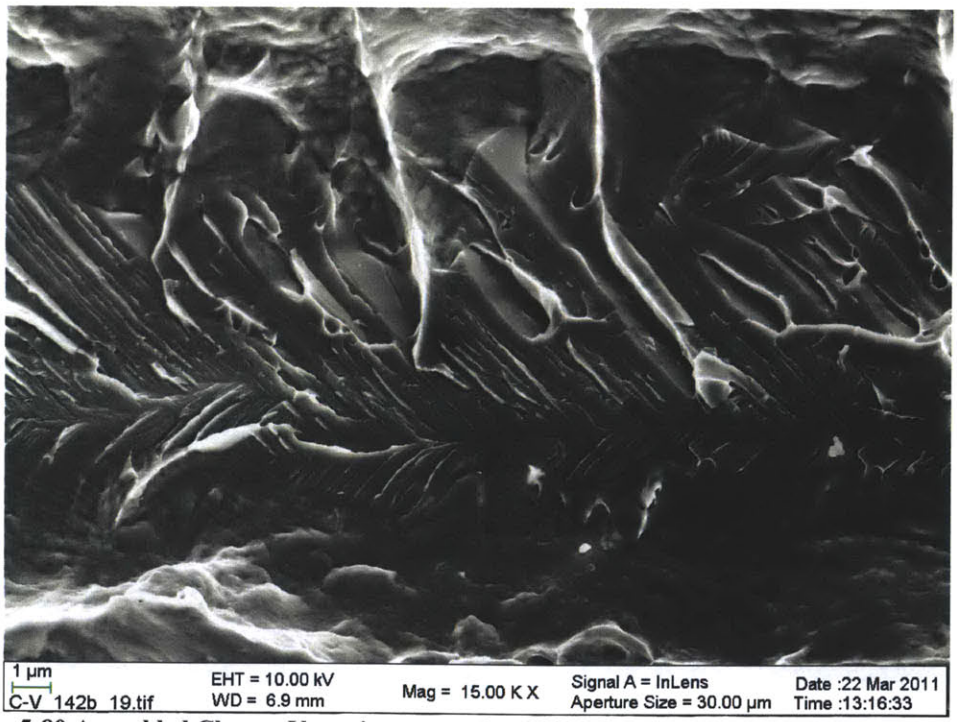

Figure 5-80 As-welded Charpy-V specimen, tested at 288°C fractograph showing ductile austenite and brittle δ-ferrite exhibiting chevron type cleavage patterns.

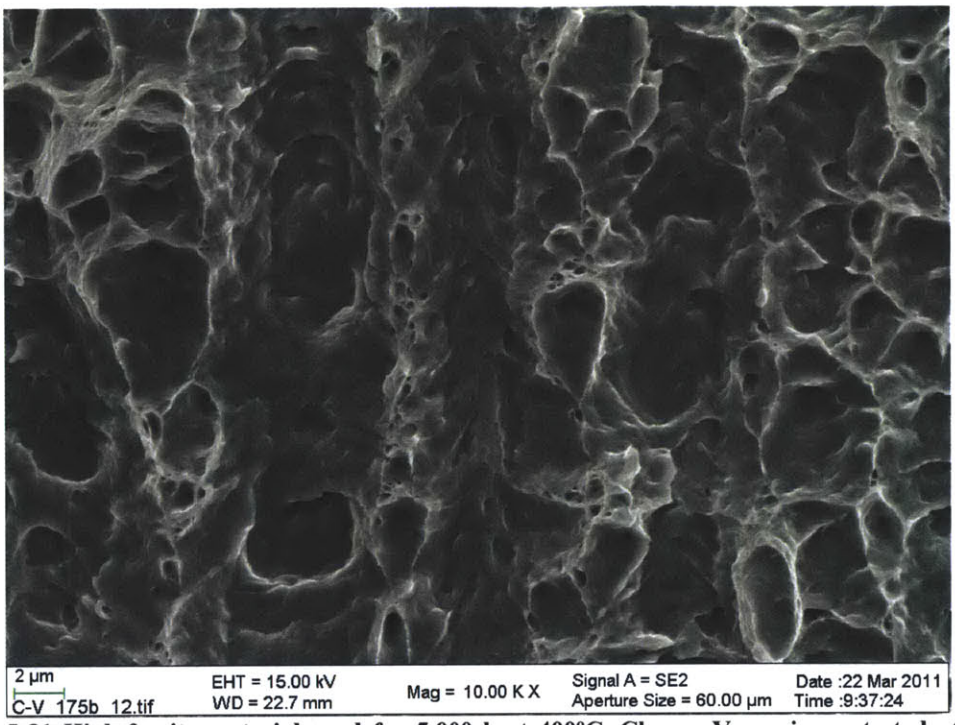

Figure 5-81 High-ferrite material aged for 5,000 h at 400°C, Charpy-V specimen, tested at 288°C fractograph showing ductile austenite and ductile δ-ferrite, this is taken close to the initial V-notch tip.

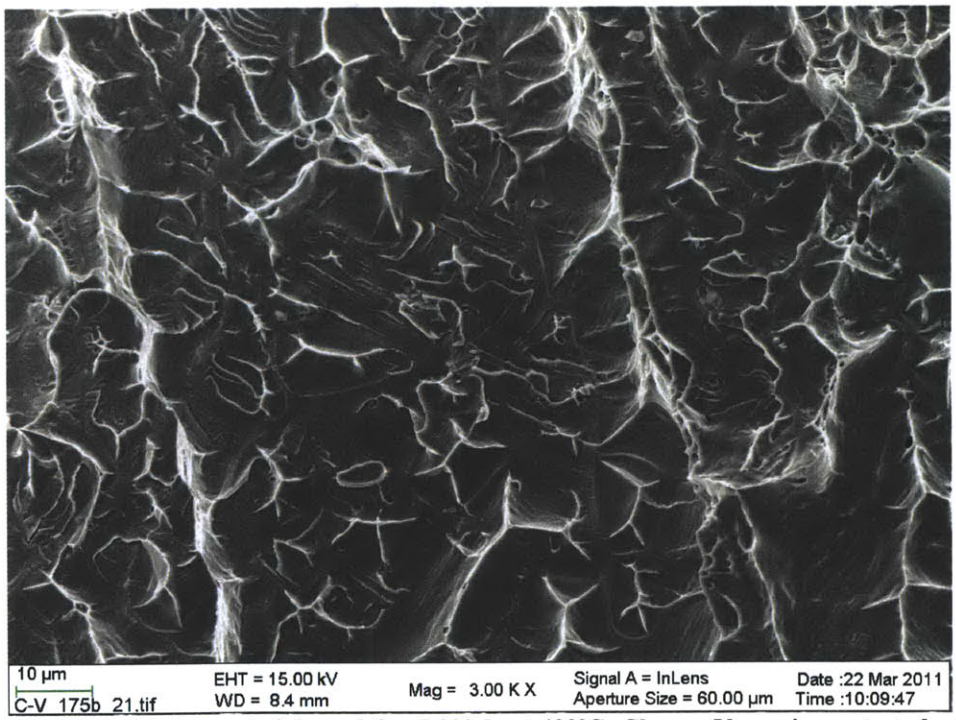

Figure 5-82 High-ferrite material aged for 5,000 h at 400°C, Charpy-V specimen, tested at 288°C fractograph showing ductile austenite and brittle δ-ferrite, this is taken farther from the initial V-notch tip than Figure 5-81.

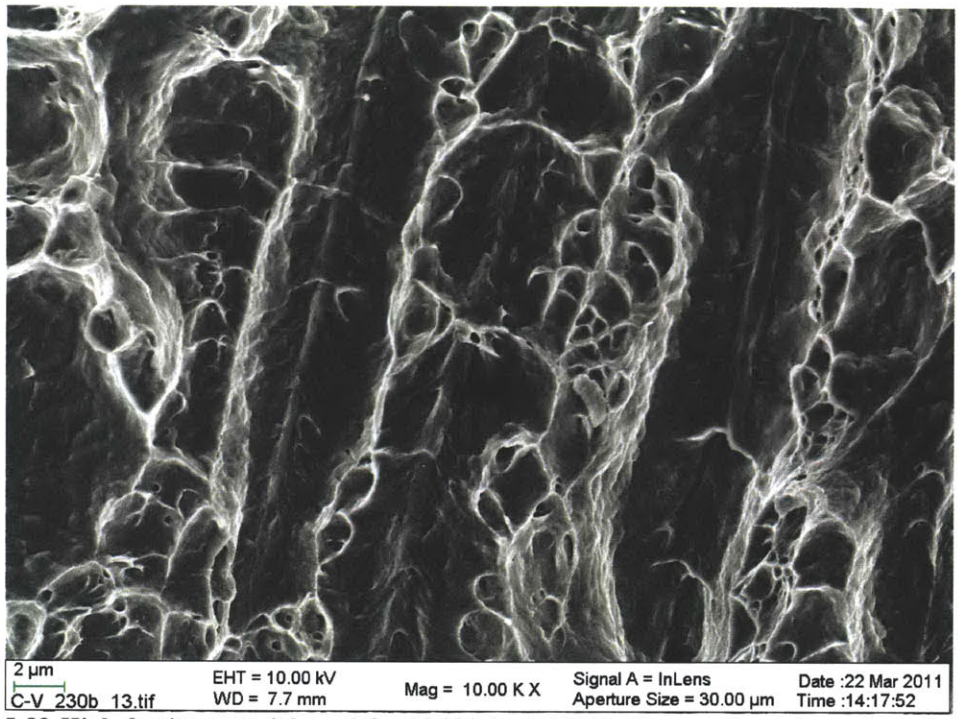

Figure 5-83 High-ferrite material aged for 10,000 h at 400°C, Charpy-V specimen, tested at 288°C fractograph showing ductile austenite and ductile δ-ferrite clearly visible. This behavior was noted throughout the sample at this aging condition.

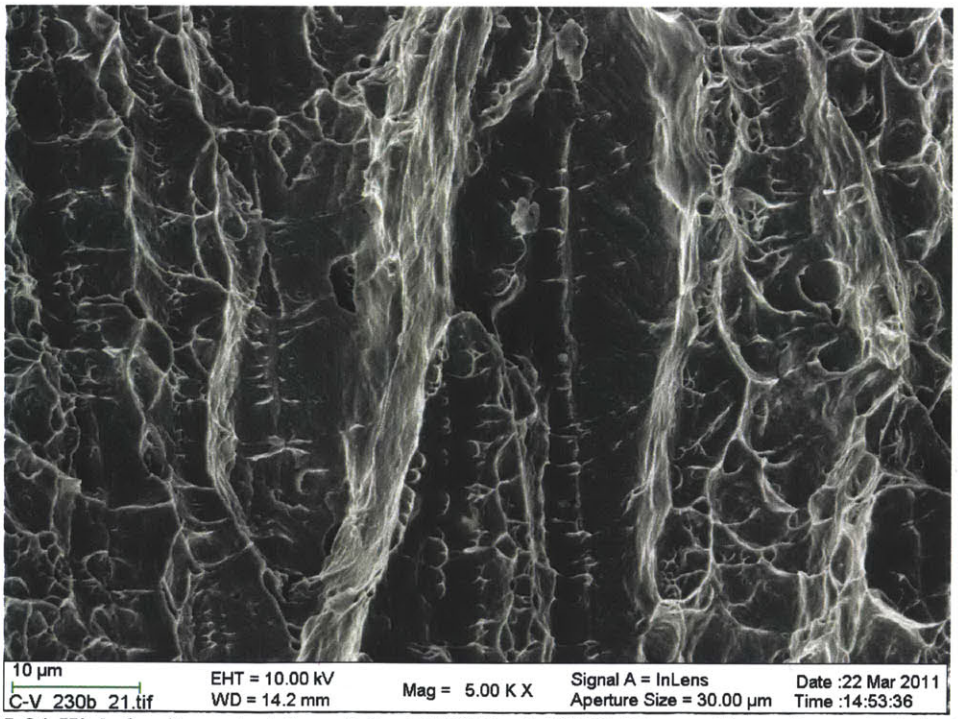

Figure 5-84 High-ferrite material aged for 10,000 h at 400°C, Charpy-V specimen, tested at 288°C fractograph showing ductile austenite and ductile δ-ferrite. This behavior was noted throughout the sample at this aging condition.

5.6 Effects in Fatigue

Standardized fatigue crack growth rate testing was not performed during this study. However, parts of the experimental series required a sharpened crack tip, which is achieved through fatigue as previously discussed. However, there are both effects of aging and the environment on the precracking regions.

In the case of aging, the main mechanism that can be noted is the embrittling of the δ-ferrite and the weakening of the γ/δ boundary. This is clearly evident in Figure 5-85, which is taken from a high-ferrite, 5,000 h aged sample from the fatigue area between SCC and fracture toughness testing. Both transgranular fracture along the δ-ferrite and separation along the γ/δ boundary are visible. This is not seen in as welded material, as can be seen in Figure 5-55.

The environment also has an effect on the fatigue growth in weld metal. As shown in Figure 5-86, an as-welded low ferrite material. Figure 5-86A shows precracking in air, while Figure 5-86B shows fatigue precracking in the environment. In the air precracking, the fracture morphology is random and confused, not following a pattern linked to the microstructure. While in the environment, the fracture morphology is linked to the dendritic microstructure of the weld metal.

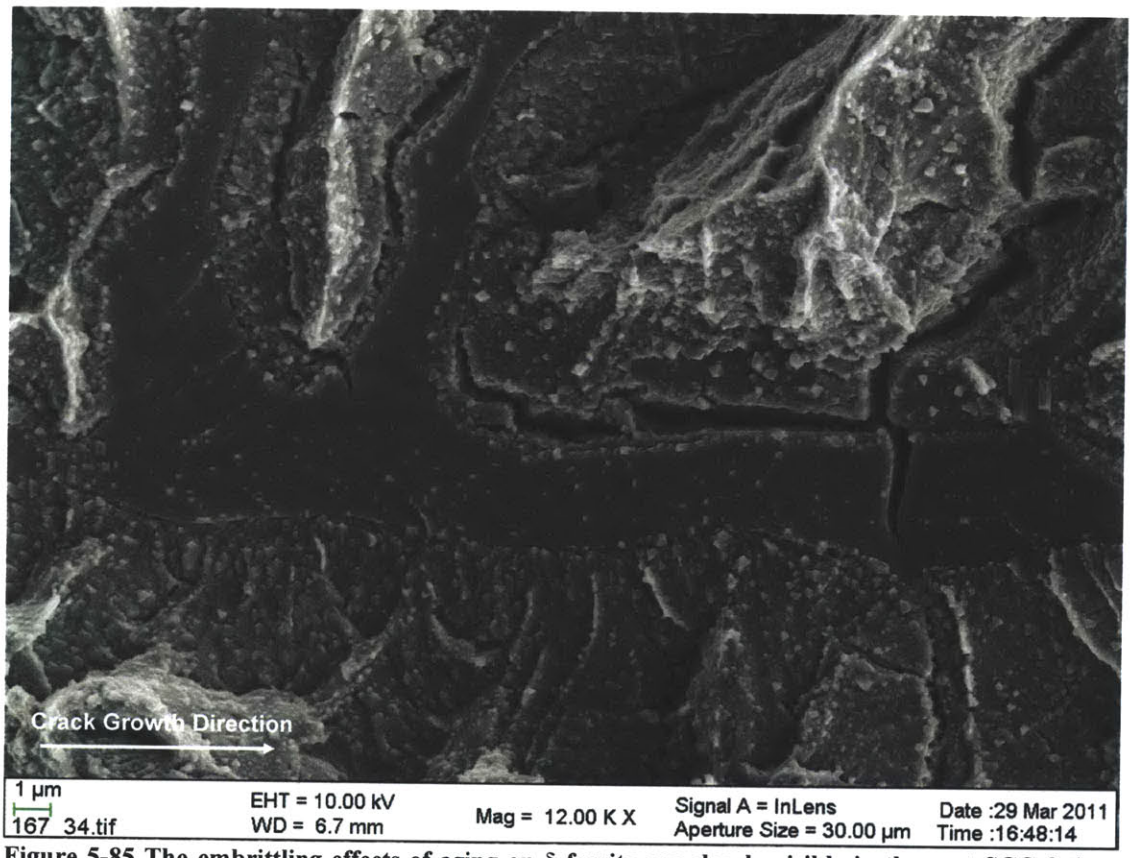

Figure 5-85 The embrittling effects of aging on δ-ferrite are clearly visible in the post SCC fatigue area in the 5,000 aged high-ferrite material. Both separation along the γ/δ boundary and transgranular fracture in the δ-ferrite are seen.

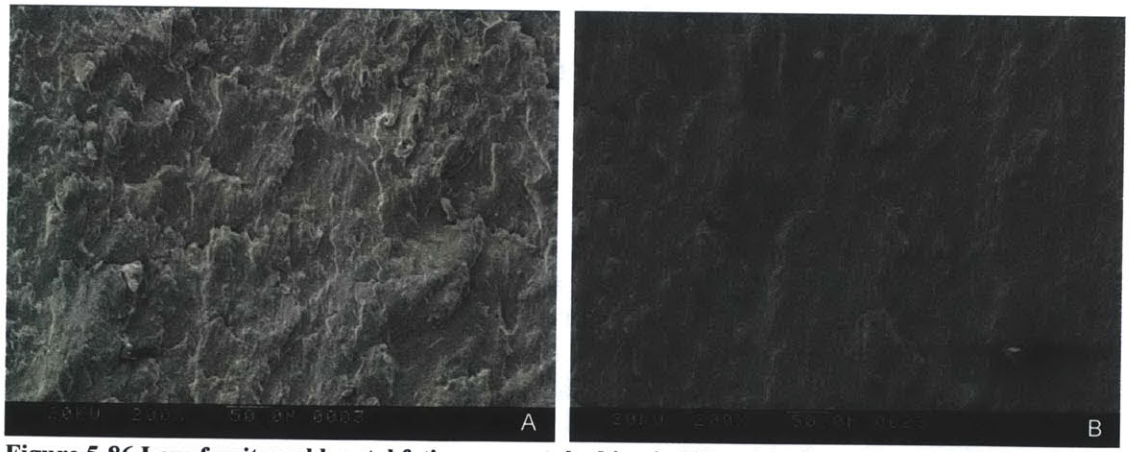

Figure 5-86 Low-ferrite weld metal fatigue precracked in air (A) and in the environment (B).

5.7 Sources of Error

It will be beneficial for better understanding of the results in the material properties section to summarize the error sources that can contribute to the scatter in data. Several

sources of error are likely to exist. However, those listed below are believed to provide the greatest impact. Uncertainty is manifested in the following ways:

- Material properties are highly dependent on the location taken from the weld blank. This is especially clear in the tensile data scatter. Considering that each sample contains different amounts of weld metal based on where the sample is taken yields difference in behavior.
- The dendrite structure changes significantly in the weld metal. In this sense, location dependant effects include the direction of the dendrites in reference to the principle stresses. However, at the weld centerline the dendrites are always parallel from bottom to top of the weld. This is one reason that it was important that fracture toughness and SCC testing was performed along the centerline.
- Fracture toughness and SCC behavior are dependant on the crack length as the weld properties change as a function of distance along the centerline of the weld. This occurs on the dendritic spacing scale.
- DCPD has inherent sources of error, including the effects of crack closure as well as oxide layer buildup.
- The residual stress field likely varies greatly across the cross-section of the weld.
- There are multiple scales of boundary interaction occurring. Listing these in order from largest to smallest:
    - Near fusion line effects, such as the HAZ, the weld metal/HAZ boundary, and the incipience of dendrites in this region. These occur along the entire length of the fusion line.
    - At approximately 1-3 mm in size, the individual weld passes create morphological changes in the structure as well as being a collection site for weld impurities.
    - The individual dendrite interactions between the austenite and the delta ferrite dendrite core. This occurs on a scale of the dendrite width, approximately 10-20 μm in size.
    - Finally the smallest boundary that should be present in our system is the spinodal decomposition which occurs in the delta ferrite on a wavelength of approximately 5-10 nm.

5.8 Experimental Summary

The primary goal of this thesis was to gain insight and understanding of the effects of aging and the environment on the behavior of weld metal properties. To this end, weld metal was prepared and evaluated using standard and adapted testing techniques to quantify material behavior. Analytical techniques, such as SEM, were utilized to elucidate the fundamental material processes occurring during characterization.

5.8.1 Thermal aging

There are two aging mechanisms occurring in the weld material. They are primarily affecting the δ-ferrite and γ/δ boundary. They are δ-ferrite embrittlement and precipitation on the γ/δ boundary. Embrittlement was only noted to occur in the δ-ferrite,

with the exception of SCC of the austenite, but in austenite this is not an age related effect and is present in all SCC conditions regardless of ferrite number or age. In fatigue and SCC, δ-ferrite becomes brittle after aging. In the tensile property evaluation, failure was completely ductile and in the fracture toughness testing, it was not possible to distinguish between the phases other than by dimple size and MnS inclusions. However, in the Charpy-V impact energy evaluation, the δ-ferrite started out brittle and gradually moved to ductile failure with some strain rate dependence noted. The least tough material was found to be one which is ductile at low strain rates but brittle at high strain rates. The primary embrittling mechanism is believed to be spinodal decomposition and the primary de-embrittling mechanism was the diffusion of carbon and nitrogen from the δ-ferrite system. However, residual stress relaxation also works favorably with aging.

Precipitation and carbide size growth was not conclusively found in the material, however, sensitization was found to occur. First, surrounding the chromium-rich carbides there is preferential oxidation weakening the over all weld metal structure. This leads to preference of attack on the γ/δ boundary which increases with age. This is most readily observed in the SCC fractography. Furthermore, spinodal decomposition periodically lowers the chromium content to less than that required for passivation allowing for preferential oxidation on the phase boundary. Chromium carbide and spinodal decomposition effects on the phase boundary primarily account for the weakening of the γ/δ boundary with aging and encourage phase boundary cracking.

The impact of aging on the material, in many cases, was favorable for a stronger or tougher material than the initial weld metal. The only case where aging is consistently unfavorable is in SCC resistance where aging can lead to a doubling of average crack growth rate. As can be seen in the fractography from the Charpy-V material there are several mechanisms working in concert on the relevant scale of time.

5.8.2 Environment

The environmental effects are noticeable in both the data and the fractography. One of the key findings of this thesis is that the environmental fracture that is occurring is most probably due to diffusible hydrogen generated by oxidation on the material in the environment. This is manifested in fatigue, SCC and fracture toughness testing.

In fatigue, while the air crack growth rates were not recorded, the effect of the environment is clear on the fracture surface. In air, the material demonstrate a random and confused surface morphology, however, when there is fatigue loading in-situ the fracture surface begins to take on crystallographic direction. This is most evident when viewing material that was first precracked in air then placed in-situ for crack tip sharpening.

SCC is by nature an environmental phenomenon. In this series of experiments, crack growth rate increased with age and decreased with ferrite number. However, the increase with age was greatest with the high-ferrite material. This indicates that first, low-ferrite material is over all more susceptible and second, the age related mechanism for the

increase in SCC crack growth rate is related to the δ-ferrite. As stated above, the γ/δ boundary is one of the main areas where there is an increase in the rate of cracking due to the presence of carbides and the subsequent sensitization as well as spinodal decomposition effects on passivation kinetics.

The most dramatic effects of the environment come in the change on weld metal fracture toughness. The decrease of fracture toughness in-situ is undeniable and is clearly evident in both the data as well as the fractography. The three main differences between air and in-situ fracture toughness fractography are that in-situ there is a brittle zone prior to the onset of crack tip blunting, during blunting slip plane fracture is noted and in the stable tearing region crack arrestors are not active, decreasing any crack path meandering.

The following is a summary of additional conclusions that can be drawn from this section and will be helpful in discussion in the next section:

- The general trend of the data is such that there is a large change by 1,000 h of aging and then a gradual change, usually reversing but possibly just trailing asymptotically with further aging.
- The data from this study trends well with data from other relevant studies, however, due to the complexity of the weld system, only trending can be compared, not actual values.
- In all cases the dendritic properties play an important role in the respective fracture mechanisms.
    - In fatigue crack growth in the environment, the dendritic structure of the material is clearly visible.
    - In SCC there is preferential attack of the chromium carbide rich boundary along the δ-ferrite. Furthermore, the dendritic structure likely plays an important role in enhanced diffusion characteristics as it provides for a more direct interdendritic diffusion path. There exist two modes of SCC crack propagation, a faster one along δ-ferrite boundary and a slower one in the austenite. Finally, since the dendrites grow in a preferential crystallographic orientation, there are preferred slip planes that are aligned in a disadvantageous direction to the applied loading.
    - In the fracture toughness testing, the dendrite morphology creates crack arrestors that are active in the air tests resulting in crack meandering and tougher materials. In addition, load is normal to the direction of the dendrites, causing delamination.
    - Preferential slip mechanisms play an important role in the failure of tensile specimens. Furthermore, as the material hardens with age the necking and failure point is shifted from the weld metal to the HAZ.
    - The equiaxial crystallographic nature of the dendrite growth along the weld centerline is advantageous for study as it removes the randomness of grain orientation found in wrought materials.
    - Spinodal decomposition leads to a loss of passivity and hardening of the δ-ferrite.

- There are competing effects occurring in the material. In considering the fracture toughness properties and tensile properties it is clear that there is a large amount of residual stress that is likely playing a factor. This would explain why the higher temperature samples have lower toughness than the room temperature samples. In the Charpy-V testing, the diffusion of interstitial carbon and nitrogen with aging likely counteracted the effects of spinodal decomposition.
- There is an effect of the environment on the fracture of the material. This is clearly manifested in fatigue, SCC and fracture toughness.
    - In fatigue, the visible difference between the air precracking and the precracking performed in-situ shows that the cracking mechanism follows the structure of the dendrites when the material is placed in the environment.
    - SCC, by its very nature, is caused by an environmental effect.
    - There is a brittle region at the beginning of the stretch zone in the fracture toughness test, in-situ, which is not seen in air.
    - There are even differences in the environment at the crack tip as evident by the lack of oxide precipitation in the SCC and fracture toughness test fracture surfaces that is seen in fatigue.
    - Diffusible hydrogen can be responsible for nearly all of the noted environmental affects.
- Ferrite content plays a very important role in the interplay of material behavior. The ferrite number gives a direct quantification of the volume fraction of ferrite and austenite in the material. The effect is evident in all cases.
- Alloying elements that form inclusions and precipitates such as manganese sulfide and chromium carbide play important roles in all modes of fracture, both in-situ and in air.

After completion of SCC CGR, fatigue CGR, fracture toughness, tensile, hardness, residual stress testing and Charpy-V impact testing, there is a great deal of elucidation into the weld material properties. In the next section, the discussion will focus around the effects noted at the crack tip. Particular attention will be paid to the change in oxide precipitant noted in difference loading regimes, this points to the importance of crack tip chemistry. Crack tip chemistry, combined with the noted brittle nature observed in SCC and fracture toughness fractography is suggestive of the role of hydrogen in assisting the cracking. Finally the transition region from SCC to fatigue contains information about SCC propagation that will be used to derive a proportional relation to aid in the comparison of SCC crack growth rates.

6 Discussion

The two most significant results from this research were: 1) That the environment has a very significant, and negative, effect on the toughness of stainless steel welds, regardless of aging; and 2) that aging has a significant, through moderate, effect on SCC crack growth rate. With regard to fracture toughness, the results of this work have demonstrated for the first time in a systematic, rigorous manner that there is a reduction in fracture toughness of 40% in cases that is not an effect of thermal aging, environmental exposure is the only requirement. Moreover, in addition to the toughness reduction, the resistance to crack propagation, as measured by the tearing modulus (proportional to dJ/da), is also severely degraded, approaching zero, after the exposure to the environment. The reduction in toughness is accompanied by change in fracture morphology that suggests that hydrogen is playing an important role in the process. A complete discussion will be provided below.

With respect to SCC crack growth rate, the effect of aging is an increase in the crack growth rate by approximately a factor of 2. The results of this work represent the first systematic analysis of the details of the crack advance process through careful analysis of the role of weld microstructure on the micro-process involved, including the interaction between the ferrite and austenite phases. The nature of the testing protocol, which involved fatigue, SCC, and fracture toughness measurements on the same sample, allowed for the confirmation that crack tip chemistry is indeed very different for static (SCC), fatigue, and dynamic (fracture toughness) loading conditions. The effect of thermal aging on the evolution of the ferrite microstructure, which results in a decrease of local corrosion and film forming properties, was also characterized in detail as the most likely cause of the increase in SCC crack growth rate.

In the following sections, a more detailed discussion will be presented and the rational and evidence for hydrogen being the dominant contributor to the fracture toughness reduction will be presented. The same level of discussion will be given concerning the microstructural influence on SCC crack growth rate.

6.1 In-situ Fracture Toughness Reduction

The reduction of fracture toughness after exposure to the environment is evident in the fracture toughness data behavior and in the fractography. Optical analysis of the weld material following fracture toughness evaluation shows that there is less lateral contraction than in the material tested in air conditions as well as little crack meandering compared to the material test performed in the air conditions. This indicated in that the embrittling element has to be capable of diffusing through out the weld metal. Fractography, shown in Figure 6-1, of the surface of the material following fracture toughness testing indicated the presence of a brittle zone as well as larger slip plane spacing, shear fracture and the inactivity of crack arrestors. This evidence all points to hydrogen as being the embrittling element. Figure 6-1A shows the entire testing area and

Figure 6-1B shows only the brittle fracture zone. Additional fractography was presented in the results section.

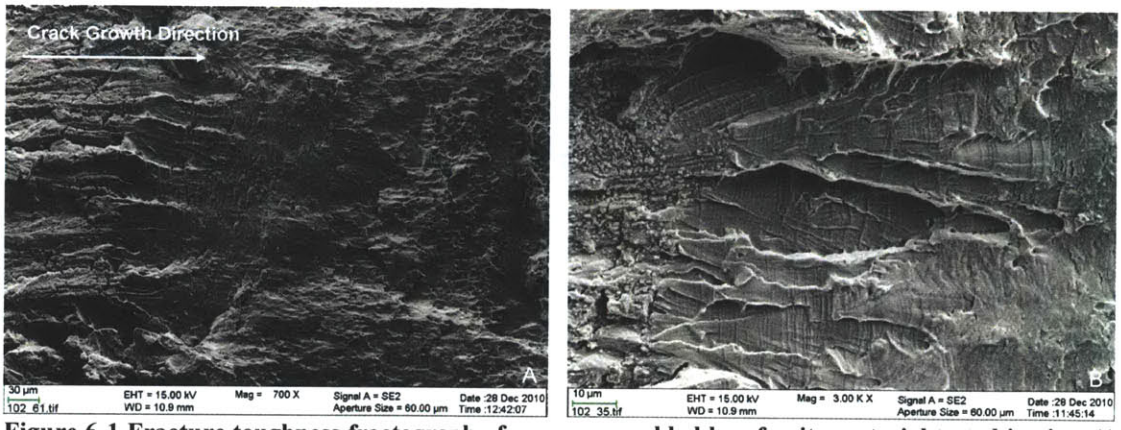

Figure 6-1 Fracture toughness fractography from an as-welded low-ferrite material tested in-situ. A) Overview of the entire fracture toughness test, showing the brittle zone and shear fracture. B) High magnification of the brittle fracture occurring prior to crack-tip blunting.

There have been several studies utilizing hydrogen charging of specimens and many of these have produced fractography very similar to those seen in this study. For example, Sommerday and Balch have seen fracture similar to the brittle plastic zone observed in fracture toughness testing. Aubert et al. have documented and quantified the slip step difference noted in crack tip blunting. Brooks and West, among others, have noted slip plane fracture, perpendicular to the direction of crack growth. Luppo made special note of fracture occurring in bending tests that illustrated fracture in ferrite. See Figure 6-2 for a sample of other's fractography. All of this is seen in the material being studied in-situ. There is however, one notable exception between this and the other studies, in the series of tests performed in-situ there was never any outside hydrogen charging, cathodically or otherwise.[71,72,73,74]

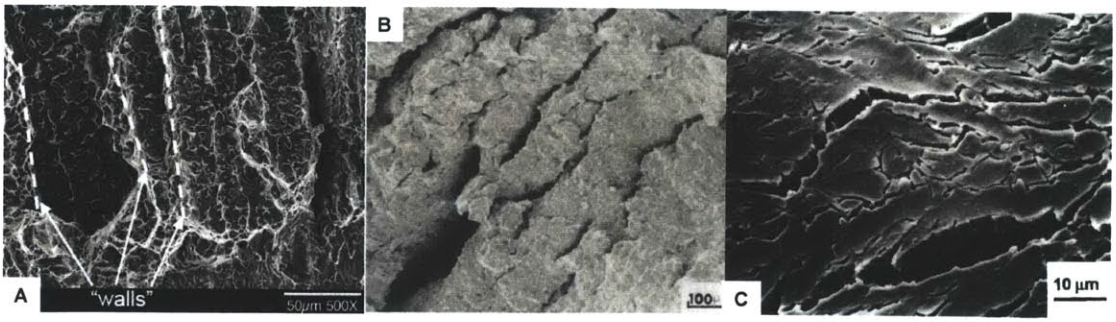

Figure 6-2 SEM fractographs from hydrogen charging studies showing similar microstructural impact as this study. A) Enhanced fracture along dendritic boundary [72], B) fracture on slip planes [71] and C) dendrite fracture [74].

The first indication of hydrogen's effect on the material fracture toughness is in a brittle zone noted prior to crack blunting. This indicates that the crack tip chemistry and the subsequent production, build up and diffusion of hydrogen is important in explaining

environmental fracture toughness. The difference in oxide precipitated on the fracture surface is important in identifying the change of environment at the crack tip. Merely noticing the change already points in the direction of crack tip chemistry and hydrogen evolution. Hydrogen evolved at the crack tip can diffuse throughout the material causing many of the noted environmental effects.

Following a discussion of oxide film formation at the crack tip, there will be a review of known effects of hydrogen on stainless steel weld metal. To show that hydrogen is responsible for environmental fracture, trapped hydrogen is measured, hydrogen production is quantified and the ability of hydrogen to diffuse through out the material is calculated. Once it has been shown that hydrogen, and particularly diffusible hydrogen, is produced in sufficient quantities, a discussion of the effects of hydrogen on fracture toughness in welds as observed in this study will be given.

6.1.1 Oxide Films

The difference in oxide deposition on the fracture surface between cyclic fatigue loading and static SCC loading is striking. Clearly there is an important process occurring that can serve as an agent for a better description of the crack tip. A difference in oxidation can be seen in the micrographs of other studies as well. See for example [64]. The change from one oxide to another is clear in welds as well as wrought material, but what is the driving factor to cause the change? In Figure 5-26 it is evident that when switching loading patterns from static to cyclic, there needs to be a few cycles before changing oxide precipitation. This indicates the environment flow to the crack tip is the source. The impact of the oxide thickness will have a large effect on the production of hydrogen at the crack tip, as will be shown below.

Beginning with a general half cell equation which describes the oxidation process [33]:

$$aA + mH^+ + ne^- = bB + dH_2O \qquad [6\text{-}1]$$

The potential e of the reaction above is found through the Nernst equation:

$$e = e^o - 2.303\frac{RT}{nF}\log\left[\frac{(A)^a\left(H^+\right)^m}{(B)^b\left(H_2O\right)^d}\right], \qquad [6\text{-}2]$$

where: e is reaction potential
e^0 is the standard potential
e^- is an exchange electron or equivalent
R is the gas constant
T is the absolute temperature
n is number of electrons exchanged
F is Faraday's constant, 96,500 coulombs per electron
(A) is the activity of product species A
a is the number of reactants A

(H^+) is the activity of hydrogen
(B) is the activity of product species B
b is the number of reactants B
(H_2O) is the activity of water
d is the number of water molecules

For the reaction of interest,

$$4H^+ + O_2 + 4e^- \longleftrightarrow 2H_2O \qquad [6\text{-}3]$$

it is shown in Appendix B that for a temperature of 561 K, the Nernst equation describing the system is:

$$e = 1.0V - 0.1114pH + 0.0279\log(O_2) \qquad [6\text{-}4]$$

This gives an expression for the reaction potential in terms of pH and oxygen concentration. Oxygen concentration is then expressed in atmospheres with 1 atm O_2 = 20,000 ppb O_2.

The outside environment is operating at a pH of 5.8 and an oxygen concentration of 300 ppb. In this case the e = 0.302 V, this is shown as point A on Figure 6-3, the Pourbaix diagram describing the iron-nickel-chrome system at 300°C [75].

In SCC, it is assumed that the system has become deaerated, leaving only the pH component, now eq. 6-4 is expressed as:

$$e = -0.1114pH, \qquad [6\text{-}5]$$

which is the expression for the hydrogen line in Figure 6-1. Solving again for a pH of 5.8 yields e = -0.646 V, noted as point B in Figure 6-4.

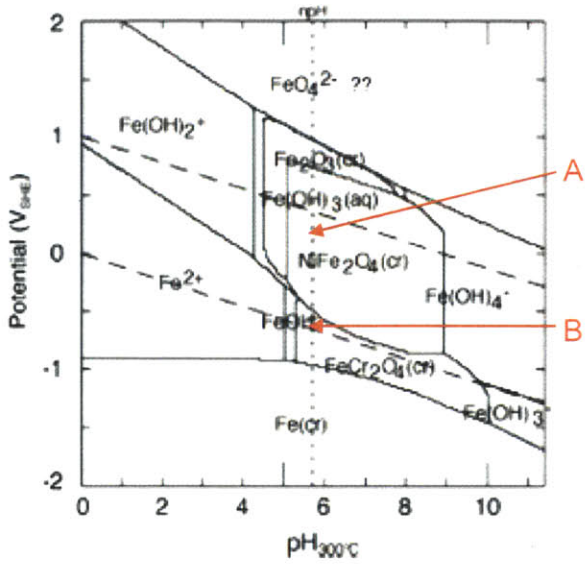

Figure 6-3 Pourbaix diagram for Fe-Ni-Cr system at 300°C. Point A is the potential during fatigue loading, while point B is the potential during SCC. Both points are at neutral pH [75].

Point A sits above the line defining $NiFe_2O_4$(cr) as the oxide that is thermodynamically stable, while point B is in the region where $FeCr_2O_4$(cr) is the stable oxide.

Considering that there is a transition between SCC and fatigue, visible in Figure 5-26 This figure also shows that there are a few striations of fatigue before changing oxide structure, this indicates that there is some pumping action needed to raise the oxygen concentration, that is to say, it does not just happen instantly, with the first fatigue cycle. Geometrically, consider first the calculation of the volume of the inside of the crack, shown schematically in Figure 6-4. Figure 6-5 illustrates the load line displacement, measured along the vertical axis of the center of the holes for the clamps which hold the sample. The final area to be calculated is diagramed in Figure 6-6.

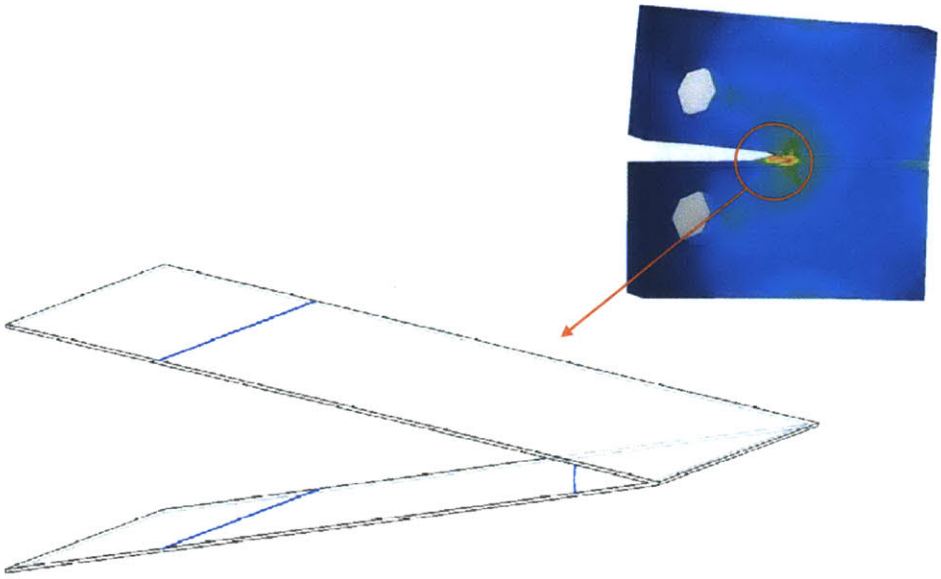

Figure 6-4 Exaggerated loading applied to 1T-CT specimen geometry, crack tip opening is shown as a triangular volume.

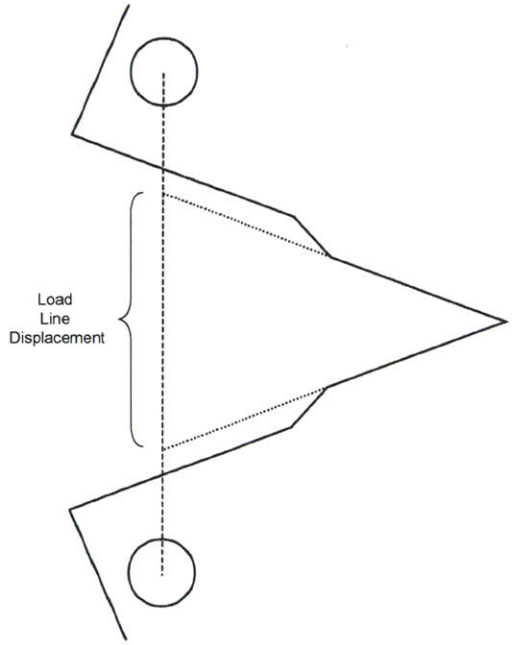

Figure 6-5 Schematic of load line displacement, exaggerated for clarity.

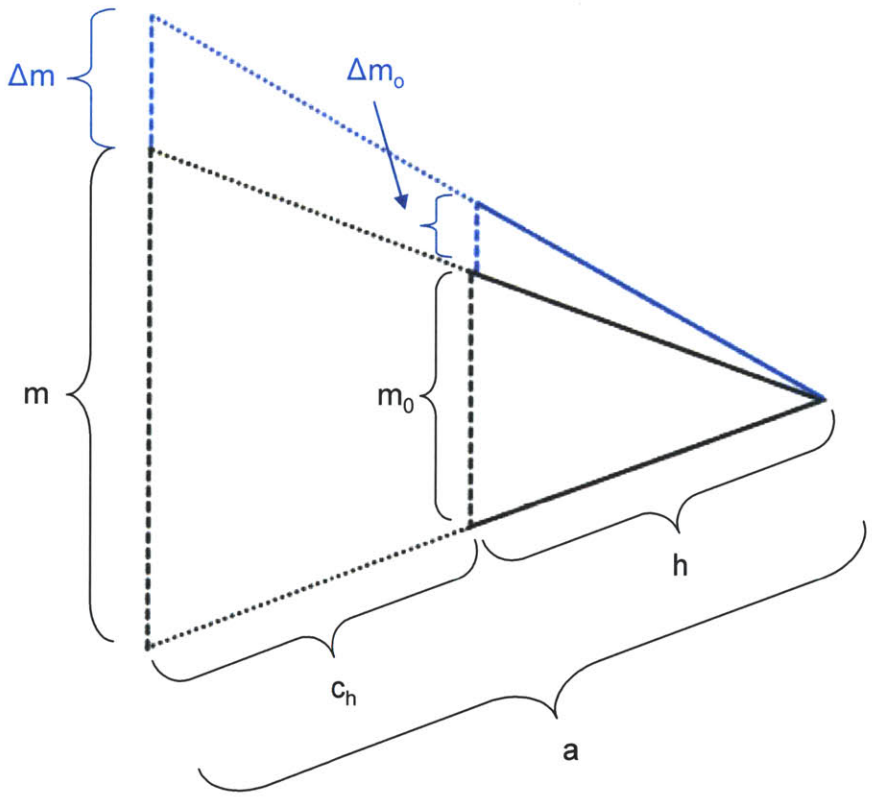

Figure 6-6 Triangular schematic representation of load line displacement effect on crack tip geometry.

Defining all of the labels:

a is the overall crack length
c_h is the length past the mouth of the actual crack
h is the actual crack length
m is the load line displacement
Δm is the small change in load line displacement applied in fatigue
m_0 is the actual crack mouth displacement
Δm_0 is the small change in actual crack mouth displacement applied in fatigue

Knowing that the sample has a thickness b, then everything that is needed is defined to calculate the volume of the actual crack based on crack length and load line displacement and is easily done geometrically. Once the exchange volume is known, then it is straight forward to calculate the change in oxygen content at the crack tip. The details of the derivation are given in Appendix B. This allows for the modification of eq. 6.4 to give the potential as a function of fatigue cycles:

$$e_N = 1.0V - 0.1114pH + 0.0279\log\left\{C_{ba}\left[1-\left(1-\frac{\Delta m}{M_f(\Delta m+m)}\right)^N\right]\right\} \qquad [6\text{-}6]$$

where: e_N is the potential after N cycles of fatigue,

M_f is the mixing factor.

The variable, M_f, is introduced in the derivation to provide a means for grading the strength of mixing. In the derivation of eq. 6-6, perfect mixing is assumed, but M_f is introduced as a correction for that assumption. The higher the number, the more difficult it is for the diluted bulk chemistry to reach the area where the oxide precipitates.

Next, inserting in some common numbers, easily found from the crack growth and displacement data:

$pH = 5.8$
$\Delta m = 0.1$ mm
$m = 0.6$ mm
$C_b = 300$ ppb
$C_{ba} = 0.015$

It is evident that any value for M_f which allows for even 2 striations to be visible, meaning $e_2 < -0.5$V, without changing from $FeCr_2O_4$(cr) to $NiFe_2O_4$(cr) oxide precipitation would have to be on the order of $1X10^{29}$. Such a large value needed to add to the mixing indicates that the oxidation must both occur very close to the crack tip, where the region is small enough that it cannot be thought of as a continuum and that oxidation occurs very quickly. The mixing factor is shown as function of the number of fatigue cycles in Figure 6-7.

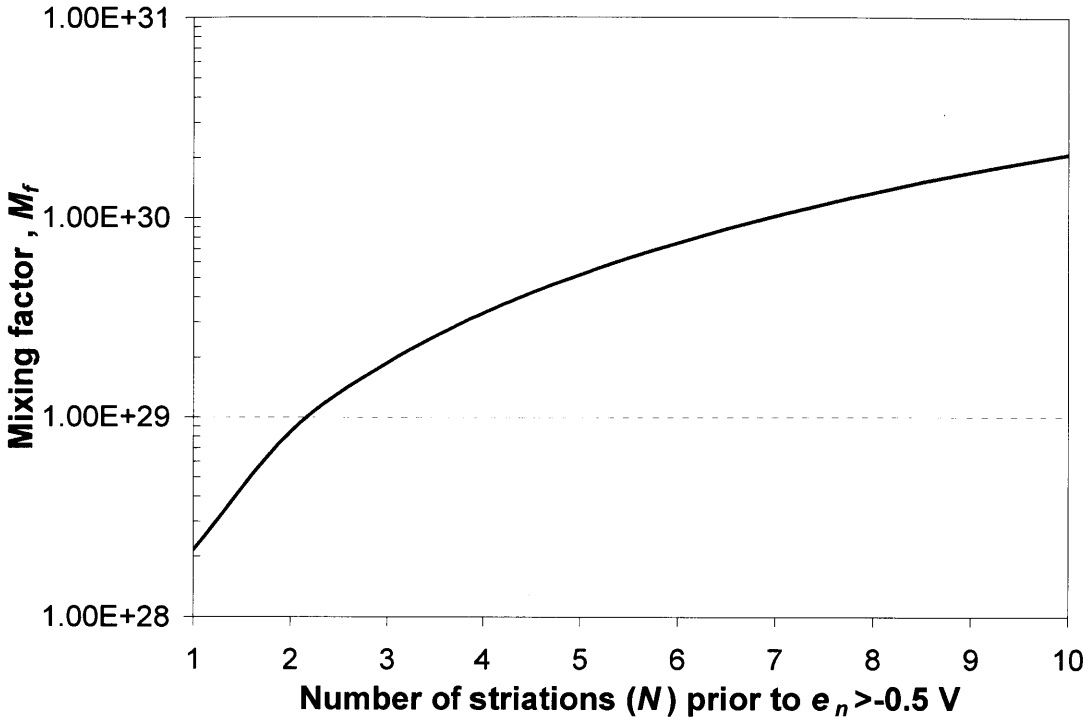

Figure 6-7 Mixing factor, M_f, as a function of striations, N, to cause e_n to be greater than -0.5 V.

In considering the concept of "tight cracks" as presented by [76], the physical mechanism for SCC shows that the oxidation must happen before a slip plane has opened up to the environment. Otherwise, the oxygen concentration would be high enough to change the stable oxide to $NiFe_2O_4$(cr) even in SCC. Furthermore, the bare surface created will provide the necessary available ions to produce an oxide film. That oxide precipitation is occurring at the crack tip, even in fatigue, is important for the production and diffusion of hydrogen.

6.1.2 Diffusible Hydrogen

Fracture toughness testing provided similar fractography to that which is seen in hydrogen charging studies. Hydrogen has long been known to have deleterious effects on the properties of metals. It can easily enter and diffuse through the crystalline structure of metals due to its small size. Hydrogen can become entrained in a material in traps or it can diffuse through the material. The high mobility means that it can quickly permeate a material so even a short exposure can be of issue. Traps in materials take the forms of single point elements, voids, interstitial and vacancy defects, as well as grain boundaries, dislocations, cracks and any other inconsistency. As the traps become full, the diffusivity of hydrogen increases. Hydrogen is known to cause a loss of ductility and lead to brittle cracking. [33]

Sources of hydrogen include aqueous dissolution, charging, initial solidification or irradiation. Depending on the environment that a metal is exposed to there may be the

possibility for hydrogen to evolve on the surface due to the dissociation of the water. In the case of this study the working fluid is water, which undergoes dissociation by:

$$2H_2O + 2e^- \rightarrow H_2 + 2OH^- \quad [6\text{-}7]$$

This occurs during general corrosion, during electrical charging (electrolysis), or during other chemical reactions. It can also occur radiolytically. If the hydrogen evolves on the surface it can easily migrate into the bulk material. Often times in studies, a specimen will be placed into a hydrogen bearing environment. For example, into a hydrogen gas, this is referred to as charging. Hydrogen may be present from the initial solidification process. This is particularly active in welds which are susceptible to exposure to humidity in the air as they solidify [33]. Irradiation of materials can lead to deposited hydrogen as well, either by transmutation and decay, or by direct proton irradiation where the proton slows down and picks up an electron.

The main method of removal is by means of bake out. The material is heated to a point that increases the mobility of the hydrogen to the point where it diffuses out of the material. Prior to a material first entering service, bake out is recommended if it is considered to be susceptible to hydrogen embrittlement. Furthermore, if there has been exposure to a hydrogen source during the life of a material, it can always be removed in this manner. [33]

Decohesion is the oldest explanation for hydrogen-induced cracking (HIC). Diffused hydrogen weakens the metallic bonds by electron capture. This causes the metal to undergo separation rather than slip. Hydrogen enhanced localized plasticity (HELP), previously known as enhanced plastic flow, was proposed first by Beachem in 1972 [77]. This explanation required the increase in dislocation velocity which leads to a reduction in the repulsive effects of dislocations, thus easing dislocation movement [77]. This theory explains why BCC crystal structure is most affected by hydrogen embrittlement, while there is a greater number of slip systems compared to FCC materials. The resistance to slip in BCC is greater so the effect of increasing dislocation mobility is greater. Surface absorption is the most recent theory and seems to be an extension of decohesion. In this model, the hydrogen is still weakening the interatomic bonds, however the idea is that dislocations initiate and flow from the crack tip, instead of the crack tip meeting them. This results in crack propagation rather than crack blunting [79]. The final model may not really be applicable to the scale of the crack tip. When the hydrogen concentration gets high enough, it can form bubbles and voids and result in blistering. The internal pressure created by this can be significant and depending on the size may exceed the yield point.

6.1.3 Hydrogen Extraction

Hydrogen analysis was performed on four materials that had undergone SCC and in-situ fracture toughness testing. As-welded base and weld metal were tested using a Leco tester. As-welded and 5,000 h aged at 400°C, high- and low-ferrite material was examined using hydrogen thermal desorption spectroscopy (TDS).

In TDS testing a constant heating rate of 6°C/min was used and the temperature ranged from 25°C to 650°C. Hydrogen was measured by the changing partial pressure in an ultra high vacuum apparatus. Vacuum is maintained less than 10^{-7} mbar. The results were compared to the automated Leco testing apparatus.

The total results of Leco and TDS are summarized in Table 6-1. Table 6-2, contains only TDS results of the tested material. Figure 6-8 shows the results for both the base metal and the weld metal for low-ferrite, as-welded material. The vertical dotted line represents the temperature of the experiment in this work. Interesting features that are noticeable in Figure 6-8 are that the weld metal has a double peak at 500 K and 650 K where as the base material only has one peak at 650 K. Furthermore, the magnitude of the 650 K peak is higher in the weld metal. Considering that the environmental system took up to 24 h to cool down from operating temperature, there was sufficient time for most of the hydrogen to diffuse out of the sample. It is conceivable that the amount of hydrogen in the weld metal was much higher and closer to the base metal while at steady state operating conditions due to the higher diffusion constant for hydrogen in the weld metal. This will be discussed in greater detail below. The first peak is believed to be due to the δ/γ boundary which is known to be a strong trap, and is not present in the base material. Figure 6-9 shows the results from only the weld metal for three materials: as-welded high-ferrite, aged 5,000 h at 400°C high-ferrite and low-ferrite material aged 5,000 h at 400°C. In each case the double peak is visible. Each material has a different test history. The time in-situ is relative to the time to reach equilibrium in the test system conditions, the time needed for crack growth and the time allowed for multiple SCC crack growth rate tests on an individual sample. Furthermore, a given test may have inadvertent shut downs and cool downs. Therefore, it is not reasonable to compare the effects of aging or ferrite content on hydrogen content.

Table 6-1 Hydrogen desorption results of un-aged base material.

Test Condition	TDS Hydrogen Content (wt.ppm)	LECO Hydrogen Content (wt.ppm)
25°C Air	5.87	3.94
288°C Air	3.02	3.00
In-Situ	0.08	0.68
In-Situ	0.14	0.47

Table 6-2 TDS hydrogen desorption results of weld material.

Material	Aging Time at 400°C (h)	Test Condition	Hydrogen Content (wt.ppm)
Low-Ferrite	0	25°C Air	0.66
	0	288°C Air	0.76
	0	In-Situ	0.18
	0	In-Situ	0.19
	5,000	In-Situ	0.09
High-Ferrite	0	25°C Air	0.92
	0	288°C Air	0.86
	0	In-Situ	0.14
	5,000	In-Situ	0.11

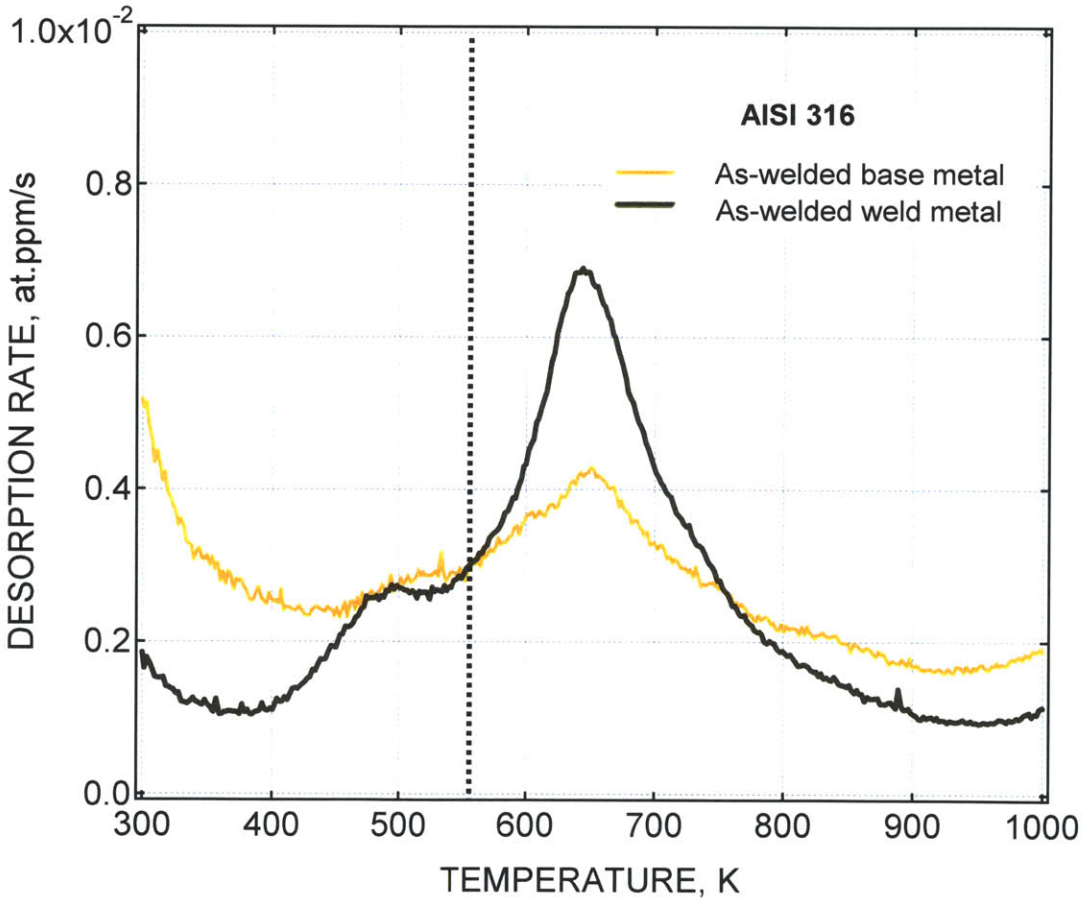

Figure 6-8 Hydrogen extraction results for base and weld metals in an as-welded low-ferrite material following SCC and in-situ fracture toughness testing, dotted line represents operating temperature of the SCC and fracture toughness experiment.

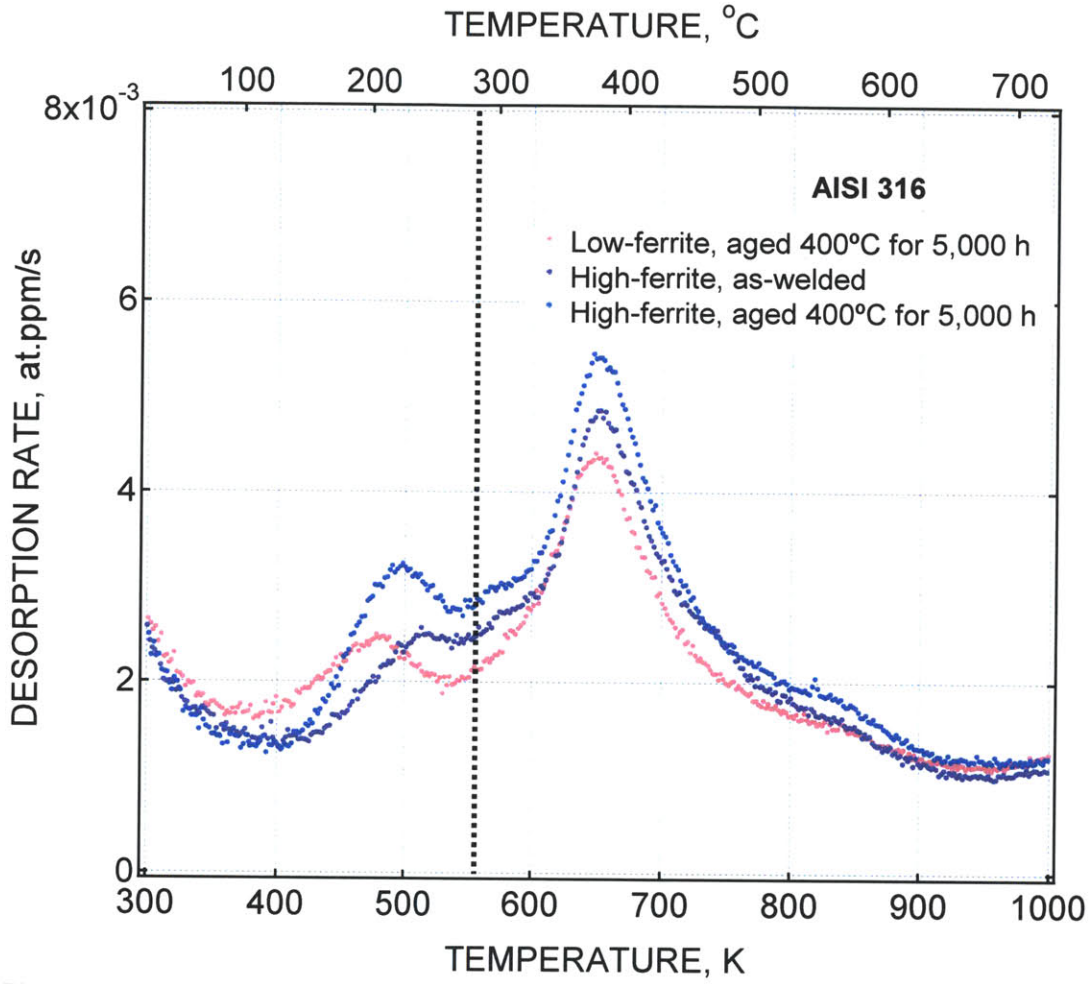

Figure 6-9 Hydrogen extraction results for as-welded high-ferrite, aged 5,000 h at 400°C high-ferrite and low-ferrite material aged 5,000 h at 400°C, following SCC and in-situ fracture toughness testing, dotted line represents operating temperature of the SCC and fracture toughness experiment.

6.1.4 Hydrogen Generation at the Crack Tip

It is already known that hydrogen can be evolved and absorbed into the metal at the crack tip [80]. The question concerning the effects of hydrogen on this material begins with the quantity of hydrogen evolved and absorbed in the material. Is there enough hydrogen being produced at the crack tip to cause the sort of changes in material properties that have been observed?

First consider the hydrolysis reaction:

$$3M + 4H_2O \rightarrow M_3O_4 + 4H_2 \qquad [6\text{-}8]$$

where: M is any metal species what will form the M_3O_4 oxide structure.

So immediately it is evident that hydrogen is being evolved if there is oxide being produced. The method of identifying the quantity of hydrogen produced will be to identify how much oxide is present on the surface for a given step size, or any growth in crack length, a. Once the quantity of oxide is known, then it is straight forward to show the amount of hydrogen produced. Some fraction of which will be adsorbed then absorbed into the metal where it can diffuse and cause effect. First calculating the volume of oxide which is evolved at a minimum, consider only one face of the fracture in one crack growth increment:

$$dV_{Ox} = da_s t_{Ox} b, \qquad [6\text{-}9]$$

where: V_{Ox} is the volume of oxide
a_s is the crack length increment
t_{Ox} is the thickness of the oxide layer
b is the thickness of the test specimen.

Next, finding the number of moles of oxide produced is straight forward:

$$dQ_{Ox} = \frac{dV_{Ox}\rho_{Ox}}{G_{Ox}}, \qquad [6\text{-}10]$$

where: Q_{Ox} is the number of moles of oxide
ρ_{Ox} is the density of the oxide
G_{Ox} is the molecular weight of the oxide.

Then hydrogen produced is just the ratio of number of moles of oxide to moles of hydrogen, 1 to 4 in this case. The above equations, 6-8, 6-9, and 6-10, can be combined to give the formula:

$$dN_{H2} = \frac{da_a t_{Ox} b \rho_{Ox} 4 N_A A}{G_{Ox}}, \qquad [6\text{-}25]$$

where: N_{H2} is the number of H_2 molecules produced
N_A is Avogadro's number
A is the absorption fraction, describing the fraction of hydrogen produced that is adsorbed onto the surface and then absorbed into the metal.

This quantity is then convenient to divide by da/dt or da/dN to give the amount of hydrogen produced per unit time or per fatigue step. Table 6-3 contains some values that have been taken from the experiments performed throughout the study or are assumed values. Figure 6-10 shows the production of hydrogen absorbed per length step as a function of the unknown absorbed fraction, A. Considering that the frequency in fatigue prior to a fracture toughness test is as high as 1 Hz, it is clear that there is considerable hydrogen being produced and absorbed leading up to the fracture toughness test. Furthermore, the step size for each test is the same, only the oxide thickness is changing,

but the rate of crack growth is much higher for fracture toughness testing, the effects of this are explored in greater detail below.

Table 6-3 Parameters used in calculating hydrogen content after one length step.

Parameter	Unit	Fatigue	SCC	Fracture Toughness
da_s	(μm)	0.1	0.1	0.1
t_{Ox}	(μm)	3	1	0.1
b	(mm)	23	23	23
ρ_{Ox}	(g/cm^3)	5	5	5
G_{Ox}	(g/mol)	200	200	200
N_A	(atoms/mol)	6.02E+23	6.02E+23	6.02E+23

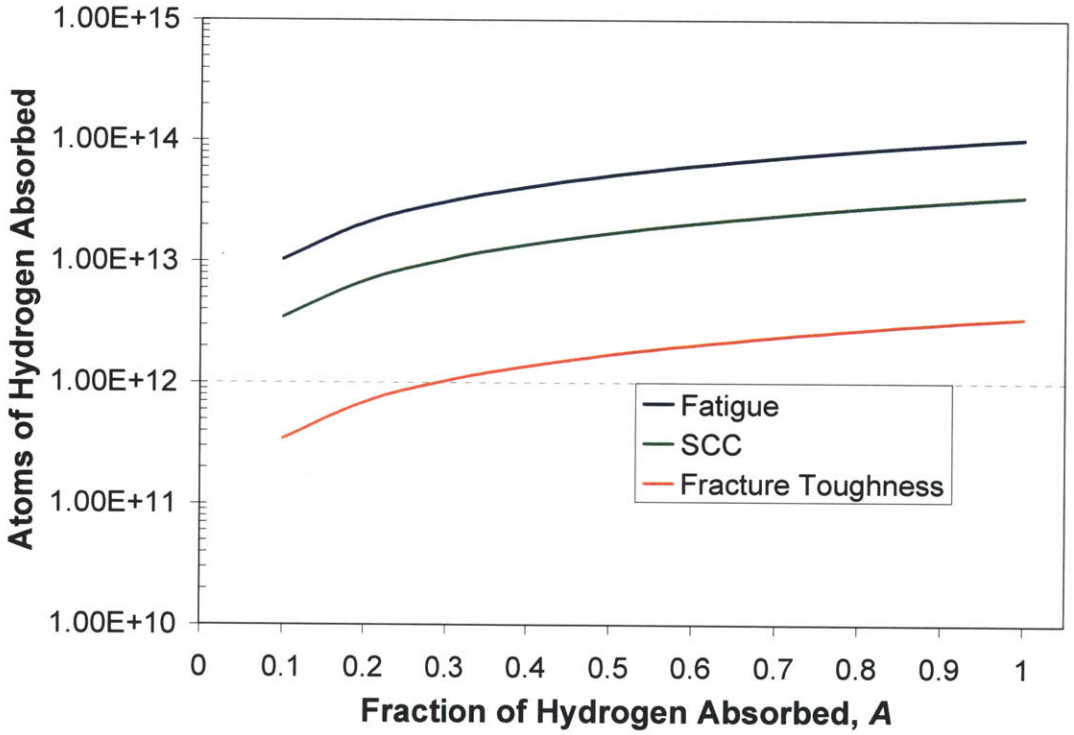

Figure 6-10 Number of atoms of hydrogen absorbed as a function of the fraction of hydrogen absorbed, *A*, after one length step.

6.1.5 Hydrogen Diffusion

Now that it is clear that there is sufficient hydrogen being produced and absorbed in a given unit of time to build up the quantity of hydrogen to sufficient levels to be of issue, the next question to answer is can it diffuse throughout the sample in a given amount of time? It is well known that the hydrogen builds up in the plastic zone [81], however, to fully explain the effects noted in this study, there must also be sufficient hydrogen diffusion to the extremities of the weld to cause a low contraction. From Habbashi [82] we obtain an expression for the diffusion constants for austenite:

$$D_\gamma = 1\times10^{-3} e^{\left(\frac{-5700}{T}\right)} \qquad [6\text{-}26]$$

and for ferrite:

$$D_\delta = 7.8\times10^{-4} e^{\left(\frac{-950}{T}\right)}, \qquad [6\text{-}27]$$

where: D_γ is the diffusion coefficient for hydrogen in austenite, in units of cm^2/s
D_δ is the diffusion coefficient for hydrogen in ferrite, in units of cm^2/s
T is the absolute temperature in degrees K.

For this system, solving for a T = 561 K, D_δ is 1.43 x 10^{-4} cm^2s^{-1} and D_γ is 3.87 x 10^{-8} cm^2s^{-1}. Since the weld system of interest is dealing with parallel diffusion paths along the weld, and the delta ferrite is essentially continuous, it is helpful for the bulk perspective to reduce the two diffusion constants into one. This is only valid in the FA mode of solidification, where the dendrites are grown parallel with continuous δ-ferrite cores. These diffusion constants can be reduced into one diffusion constant based on the following equation provided by Crank [83]:

$$D_T = f_\gamma D_\gamma + f_\gamma D_\gamma, \qquad [6\text{-}28]$$

where: D_T is the total diffusion constant
f_γ is the volume fraction of austenite
f_δ is the volume fraction of ferrite.

Finally:

$$f_\gamma = 1 - f_\delta \qquad [6\text{-}29]$$

Table 6-4 gives the individual and total diffusion coefficients for this weld structure.

Table 6-4 Individual volume fraction, *f*, and total hydrogen diffusion constant D_T, for low- and high-ferrite samples.

	f_γ	f_δ	D_T (cm^2/s)
Low-Ferrite	0.92	0.08	1.15E-05
High-Ferrite	0.88	0.12	1.72E-05

In the simplest geometry, the concentration will follow an error function, and this will cause the system to saturate on the order of hours. Furthermore, the weld material structure is complex enough that any more complex analysis would require a great deal of computing power and time. Consider then, the amount of hydrogen produced and absorbed for a normal crack growth rate, da/dt for fatigue, SCC and fracture toughness. The parameters for this are given in Table 6-5 and shown graphically in Figure 6-11. This demonstrates that because the rate is so much higher for fracture toughness testing, and

assuming the oxidation happens instantly, there is a much greater rate of hydrogen generation.

Table 6-5 Parameters used in calculating the change of hydrogen content with time.

Parameter	Unit	Fatigue	SCC	Fracture Toughness
da_s	(μm)	0.1	0.1	0.1
t_{Ox}	(μm)	3	1	0.1
b	(mm)	23	23	23
ρ_{Ox}	(g/cm^3)	5	5	5
G_{Ox}	(g/mol)	200	200	200
N_A	(atoms/mol)	6.02E+23	6.02E+23	6.02E+23
da/dt	(mm/s)	2.00E-06	5.00E-08	1.00E-04

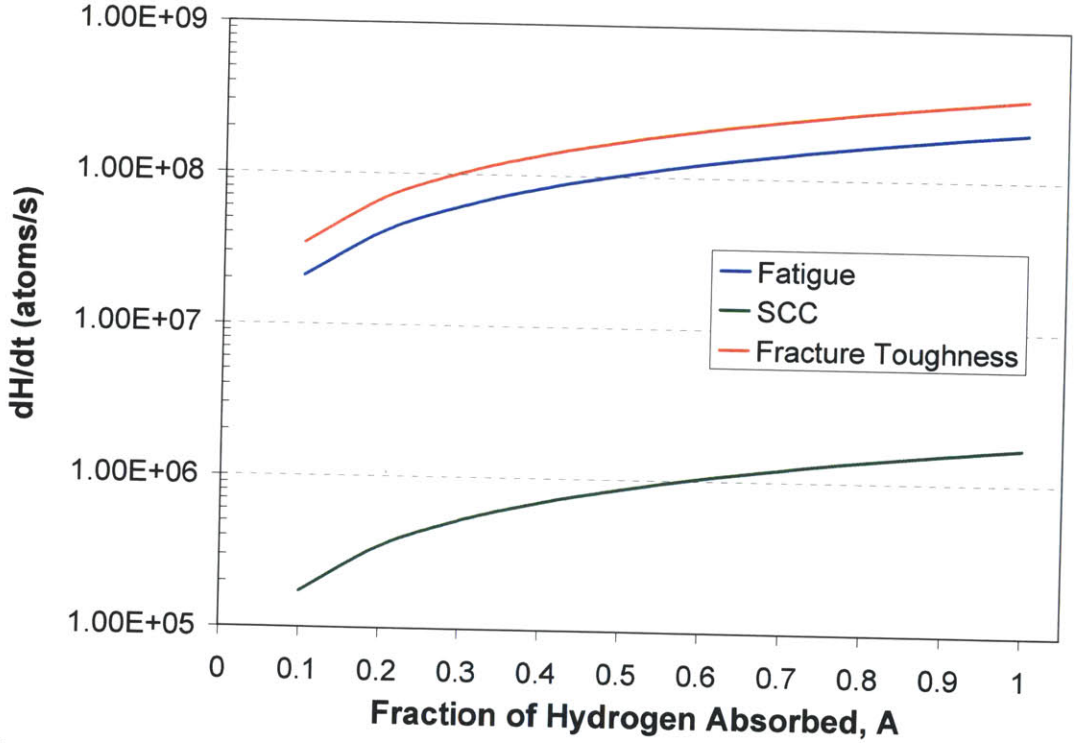

Figure 6-11 Change of hydrogen content with time as a function of fraction of absorbed hydrogen, *A*.

Finally, the entire length of each in-situ step is taken into account, fatigue, SCC and fracture toughness testing lengths, and the total amount of diffusible hydrogen is calculated. Next, it is known that in the triaxial stress zone, there can be as much as a 50x concentration factor, this is immediately ahead of the crack tip, an area adjacent to the hydrogen source [84]. This value is calculated using the values in Table 6-6 and then normalized over the amount of affected metal in the sample. This is shown graphically in Figure 6-12. The diffusible hydrogen concentration by weight parts per million (wppm) ranges from 0.1 to 10, depending on the step. It is greatest in every case from fatigue due

to the step size and thickness of the oxide layer. In the range from 1-10 wppm this becomes significant as it has been shown that as little as 4 wppm can cause enhanced crack growth rates [85].

Table 6-6 Parameters used in calculating hydrogen content after each loading method.

Parameter	Unit	Fatigue	SCC	Fracture Toughness
da_s	(μm)	2000	1000	4000
t_{Ox}	(μm)	3	1	0.1
b	(mm)	23	23	23
ρ_{Ox}	(g/cm^3)	5	5	5
G_{Ox}	(g/mol)	200	200	200
N_A	(atoms/mol)	6.02E+23	6.02E+23	6.02E+23

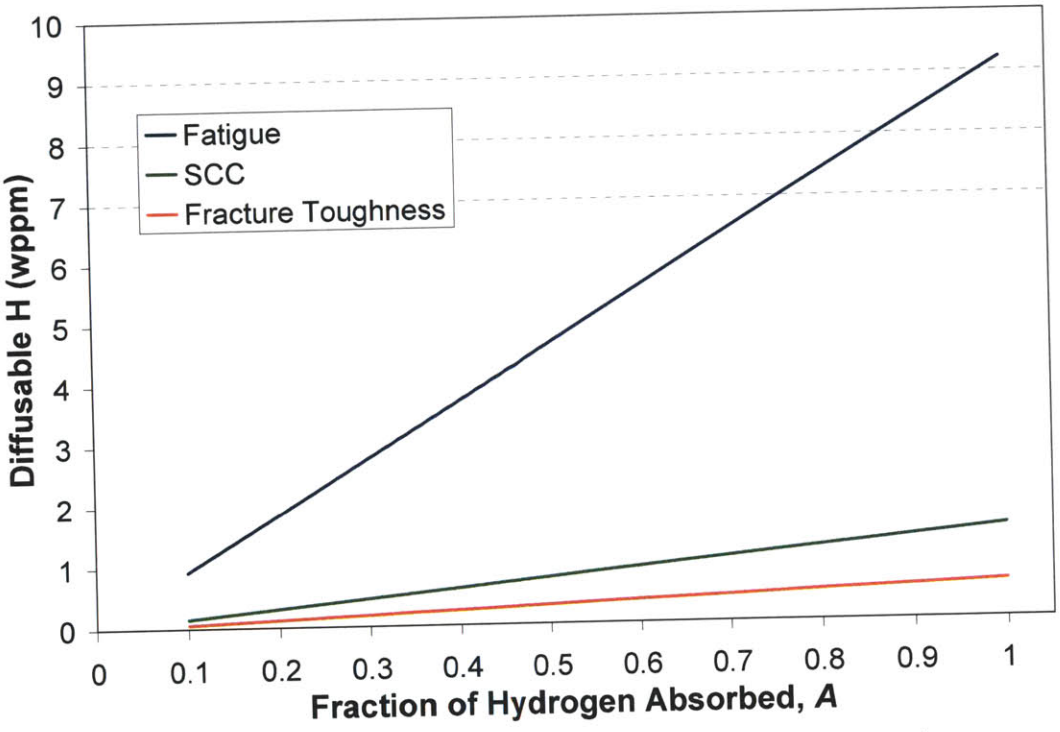

Figure 6-12 Total hydrogen content as a function of fraction of absorbed hydrogen, *A*.

Reconciliation of the hydrogen desorption data presented in Figures 6-8 and 6-9 and that calculated in Figure 6-12 is important. To a first approximation, the average desorption rate for 288°C to room temperature is approximately 2×10^{-3} at.ppm/s with a heating rate of 6°C/min. This means that the total amount of hydrogen released in a given sample in hydrogen desorption analysis was about 5 at.ppm, or about 0.1 wppm. Considering that the cool down time is up to 24 h for the autoclave system then there was at least 3.2 wppm of trapped hydrogen, and more diffusible hydrogen that can not be measured. The ratio of trapped to diffusible hydrogen is unknown. Since there is a large concentration of

the hydrogen in the plastic zone, it is most probable that autogenous hydrogen is at sufficient levels to cause the observed decrease in K_{IC}. Furthermore, the simple oxidation model above agrees well with the measured values from hydrogen desorption analysis. In addition, that the brittle zone noted prior to crack tip blunting is on the order of the cyclic plastic zone size is further evidence that hydrogen is building up in the plastic zone.

6.1.6 Hydrogen Effects on Fracture Toughness

There are several effects that the environment is having, which are especially visible during the fracture toughness testing. Figure 6-2 above shows fractography from purposeful hydrogen charging studies. These studies usually charge much more hydrogen than is produced by the environment and may have much more dramatic effects. As an example, Figure 6-13 below shows a micrograph taken from [64]. In this micrograph, the brittle zone is clear, however, this was not pointed out by the research as hydrogen was not the focus of the study. Toivonen's material was 304 stainless steel weld metal, with similar strain rates and environment to this study.

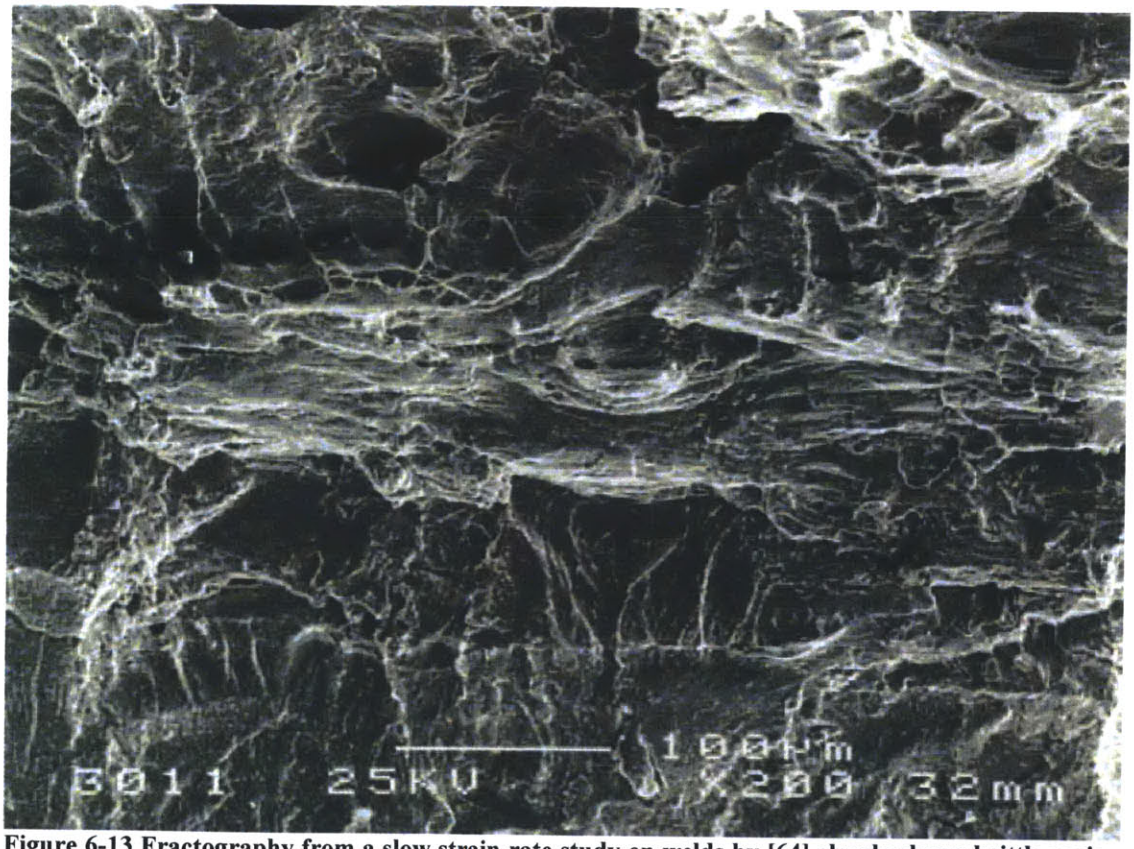

Figure 6-13 Fractography from a slow strain rate study on welds by [64] clearly shows brittle region at the onset of fracture toughness testing.

The concentration of diffusible hydrogen to get the same effect need not be as high due to the ability of the diffusible hydrogen to buildup in the plastic zone versus becoming trapped throughout the sample. [84]. Figure 6-14 below is a schematic of what hydrogen is doing to the sample, using fracture toughness testing to illustrate the process. The

illustration has two materials, one of which is in air and the other in-situ conditions. The initial conditions at time t_0 are that there were previously crack tip sharpening procedures carried out, so the immediate prior step was fatigue. In the hydrogen case, there is assumed to be a build up immediately inside the material from the sharp crack tip. In each case, load is applied vertically. At time t_1, the load is applied, in the case of the air sample, there is the beginning of blunting occurring at the crack tip. In the in-situ sample, at time t_1, there is first immediate brittle fracture, followed by blunting. The size of the brittle zone should be on the order of between the triaxial stress state and the plastic zone, 50-100 μm as calculated for this material. Indeed the measured value of this brittle zone in SEM analysis places the size of the brittle region in this range of magnitude. At t_2, the air sample has blunted and the end of the crack front is near vertical, the horizontal face of the crack is showing very close slip spacing. In the in-situ sample at time t_2, the active slip plane spacing has enlarged and cracks form along the slip plane in the direction perpendicular to the crack growth. However, at time t_3, both materials transition from crack blunting to stable tearing. In this region, fracture is analogous to a continuum of tensile specimens. The ductile crack growth is primarily controlled by manganese sulfide inclusions. However, at time t_4, the air sample tears along a weld boundary, causing a larger and more strenuous meandering fracture path with a great deal of plastic deformation. This mechanism is noticeable absent in the in-situ sample, indicating that the energy required to fracture of the base material is lower than the energy required for tearing along the weld bead boundary.

Nearly all of these effects have been shown to be the result of hydrogen in purpose built hydrogen-charging studies. There is no hydrogen charging occurring in this study, the only option for a hydrogen source is production during oxidation. As the trapped hydrogen data shows, there is a very low trap density, leaving the only possible cause for the noted effects to be diffusible hydrogen. Circumstantially, diffusible hydrogen is the agent of environmental fracture as has been identified in this thesis. In the future, more study is needed to quantify true production and diffusion of autogenous hydrogen in reference to the environmental exposure and degradation of materials.

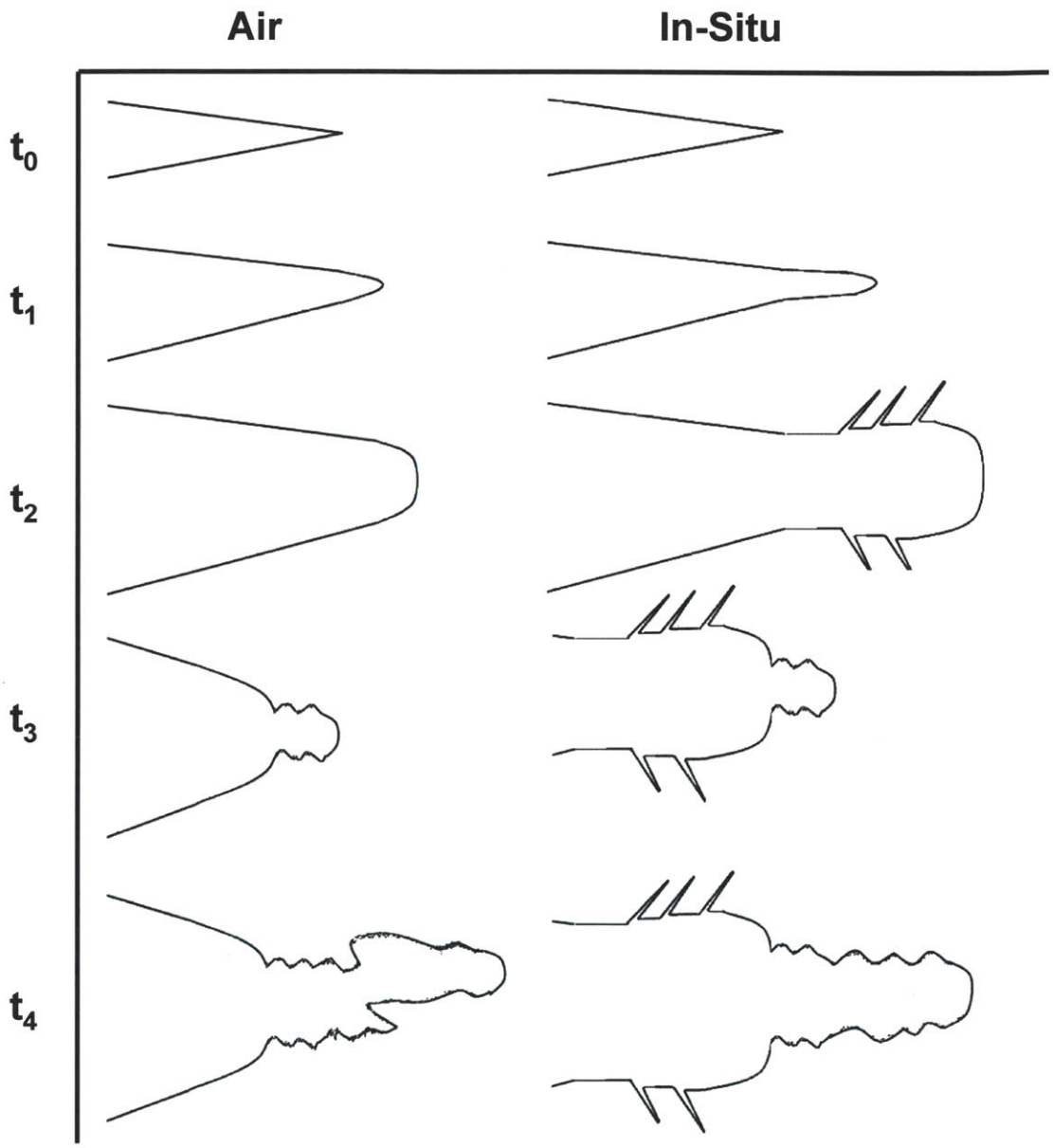

Figure 6-14 Schematic of the evolution of fracture during fracture toughness testing for air and in-situ environments.

6.2 Geometric Effects on SCC

The results of the SCC crack growth rate behavior measurements showed that there was as much a 2 fold increase in crack growth rate in the high-ferrite material with 5,000 h of aging at 400°C. There is a large amount of fractography discussed in the results section, however, the important features can be shown in Figure 6-15. In Figure 6-15 the effects of aging on SCC fractography is clearly visible. In Figure 6-15A, As-welded low-ferrite material, showed no γ/δ boundary oxidation, but did show preferential cracking at the γ/δ boundary. 5,000 h aged at 400°C low-ferrite material, illustrated in Figure 6-15B, showed oxide precipitation on δ-ferrite. Figure 6-15C demonstrates as-welded, low-ferrite material showed ductile failure of δ-ferrite and brittle fracture of austenite, while Figure 6-15 D, 5,000h aged at 400°C high-ferrite material, showed brittle δ-ferrite fracture with a chevron pattern and a smooth separation of the γ/δ boundary. Both the oxide precipitation and the change in γ/δ fracture mechanism can be attributed to spinodal decomposition embrittling the δ-ferrite and weakening the passivation ability of the δ-ferrite.

Common features in SCC fractography regardless of aging or ferrite content are shown in Figure 6-16. This material is as-welded, low-ferrite weld metal. In Figure 6-16A, the γ/δ boundary is a preferential site for SCC crack growth, demonstrated by the triangular nature of the crack front. A PN plane cross section, shown in Figure 6-16B, shows secondary cracking preference of the γ/δ boundary as well as the δ-ferrite cores and austenite highlighted by the etching process. The γ/δ boundary is a preferred site for cracking based on the presence of chromium-rich carbides.

For the purpose of this discussion, the geometry affects on SCC, all of the features shown here are of importance. The following discussion will highlight the importance of the preferential cracking along the γ/δ boundary and demonstrate how aging effects and ferrite number affect the SCC crack growth rate of the material in a quantitative way.

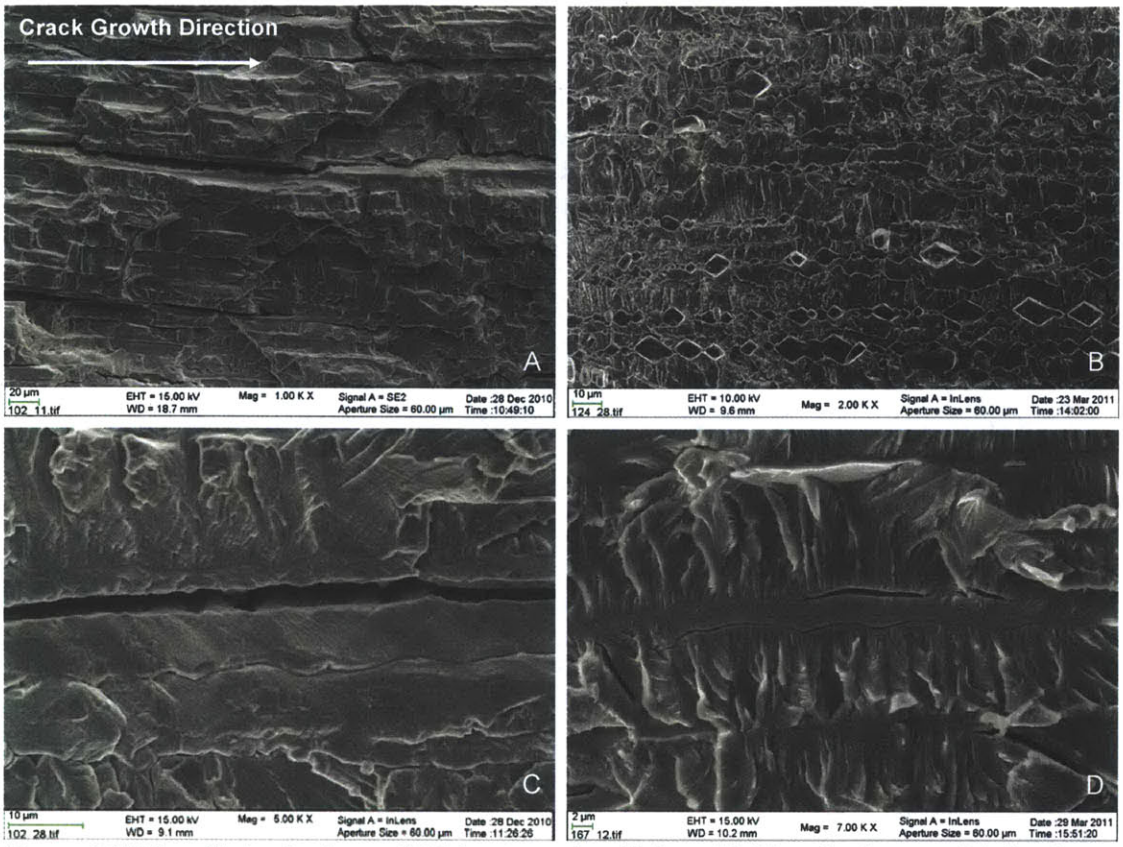

Figure 6-15 The effects of aging on SCC fractography. A) As-welded low-ferrite material showing no γ/δ boundary oxidation, B) 5,000 h aged at 400°C low-ferrite material showing oxide precipitation on δ-ferrite, C) as-welded low-ferrite material showing ductile failure of δ-ferrite and brittle fracture of austenite, D) 5,000h aged at 400°C high-ferrite material showing brittle δ-ferrite fracture with a chevron pattern and a smooth separation of the γ/δ boundary.

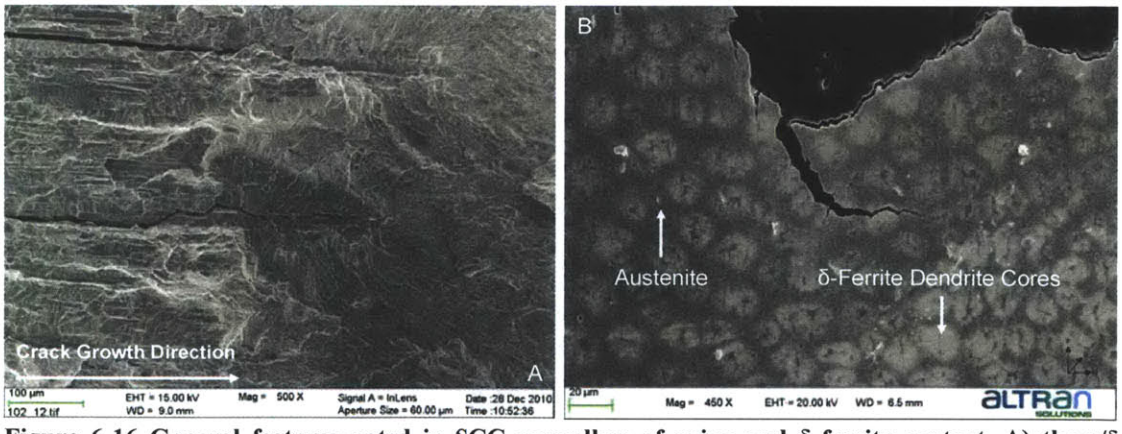

Figure 6-16 General features noted in SCC regardless of aging and δ-ferrite content, A) the γ/δ boundary is a preferential site for SCC crack growth, demonstrated by the triangular nature of the crack front, B) PN plane cross section showing secondary cracking preference of the γ/δ boundary as well as the δ-ferrite cores and austenite highlighted by the etching process.

6.2.1 Dendrite Cell Simplification

In order to properly understand the impact of the weld metal microstructure on SCC, it is first important to quantify the structure of the δ-ferrite and austenite into a simplified unit cell. Once this is understood, the impact will be elaborated and ultimately an explanation for the impact of weld metal microstructure on SCC will be given. The ultimate goal is to express the crack growth rate in terms of the volume fraction of δ-ferrite, α_δ, and the ratio of applied stress intensity, K_I, compared to the fracture toughness stress intensity calculated from the fracture toughness testing, K_{IC}. This takes into account the mechanical aging effects of spinodal decomposition.

First consider that there are two phases and an interphase region in the weld metal. The first phase is the δ-ferrite phase. The second phase is the austenite. The interphase region is the δ-ferrite boundary containing the chromium-rich carbides. Also there is a lighter etched area in Figure 6-16B,that is electrochemically different, as shown by the preferential etching, this indicates that the region is cathodic compared to the anodic δ-ferrite. Anymore information than this about the lightly etched region is not needed. It is just assumed that this region exists with in a radius R_C, and outside of this radius, there is no longer an effect. This is shown in Figure 6-17 below. Figure 6-17 will serve as the starting point for the critical discussion on the effect of ferrite number, or the more useful volume percent, on SCC.

Consider that the secondary dendrite arms have a length and width, which can be measured and averaged, L_δ and W_δ, respectively. These are a function of the chemistry and cooling rate. Furthermore, the δ-ferrite core is surrounded by the cathodic area with radius R_C, and then by austenite beyond the lightly etched areas. Since the dendrites exist in a periodic manner, dictated by cooling rate and chemistry, a simplified square unit cell can be defined having a length on one side of X. Finally, assume that the relation of R_C to the δ-ferrite arm spacing can be expressed through a constant B, which is also dictated by chemistry and cooling rate. Thus: L_δ, W_δ, R_C and B are functions of cooling rate and chemistry. For the purpose of this discussion, the function is assumed complex enough to not be discussed, but instead, measured values of these parameters will be substituted as needed. Common observed values for L_δ, W_δ, and B are given in Table 6-7.

Table 6-7 Common measured values used in calculating δ-ferrite area.

Parameter	Value
L_δ	4 μm
W_δ	1 μm
B	1.2

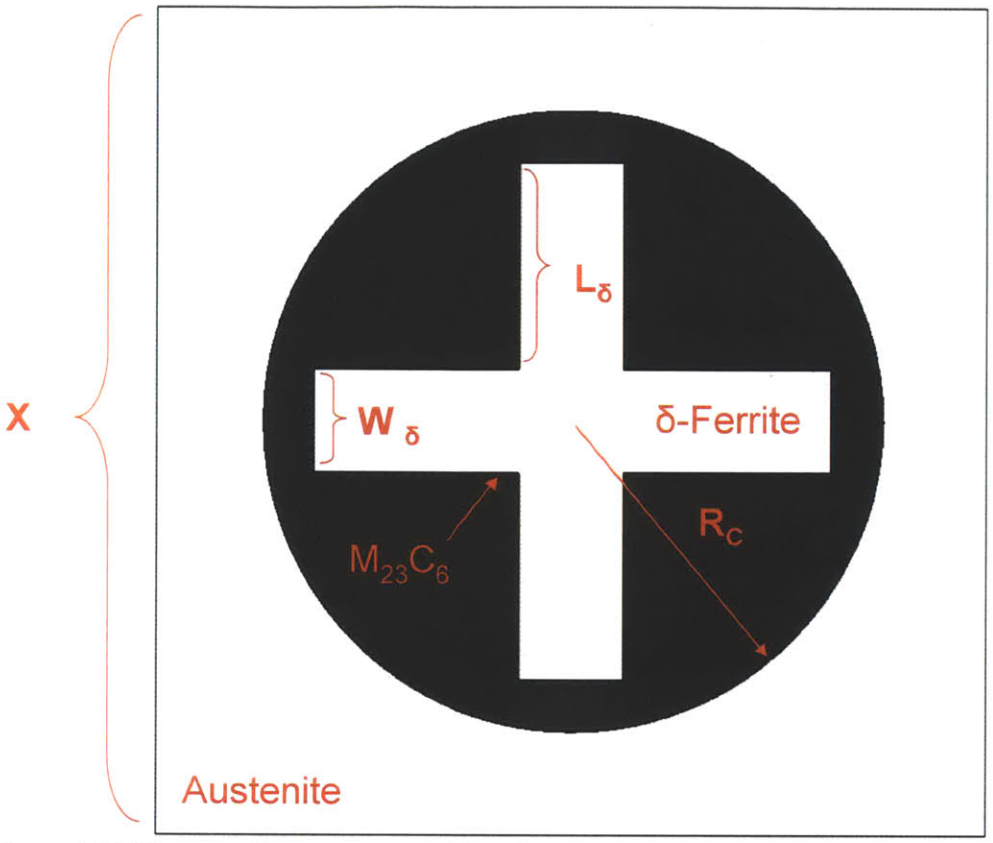

Figure 6-17 Diagram of parameters used in calculated geometric effects of a two phase system on SCC.

6.2.2 Microstructure Impact on SCC

From the above very simplified geometrical model, the next extension is to return the unit cell dendrite to an actual volume from an area. Extending over an arbitrary length, shown in Figure 6-18, the unit cell dendrite is then assembled into essentially an infinite array as shown in the left side of Figure 6-19. Representing the material in the experiment this way is not too large of an assumption. Figure 6-16B shows a similar arrangement of dendrites. When exposed to the environment as well as a loading, SCC ensues, the cracking comes in the form of slight oxidation, and little plastic deformation, as shown in the right side of Figure 6-19. It is important to note that the two fracture surfaces will match almost exactly. This will become the basic schematic for SCC growth rate comparisons as a function of α_δ, which ultimately relates to FN.

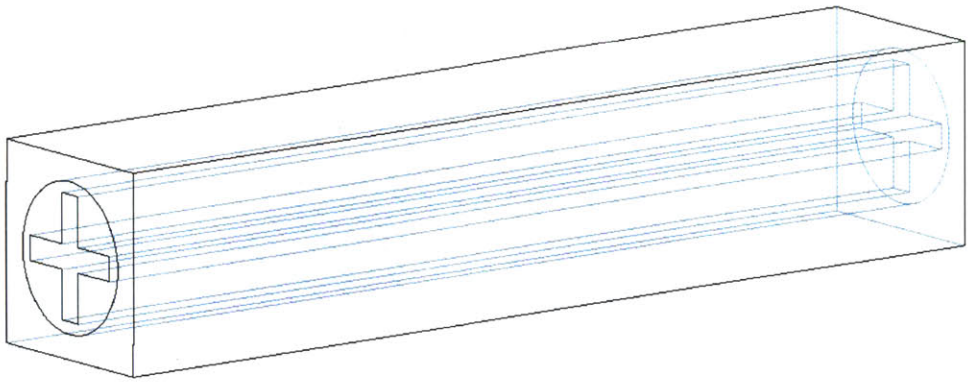

Figure 6-18 Dendrite unit cell of arbitrary length.

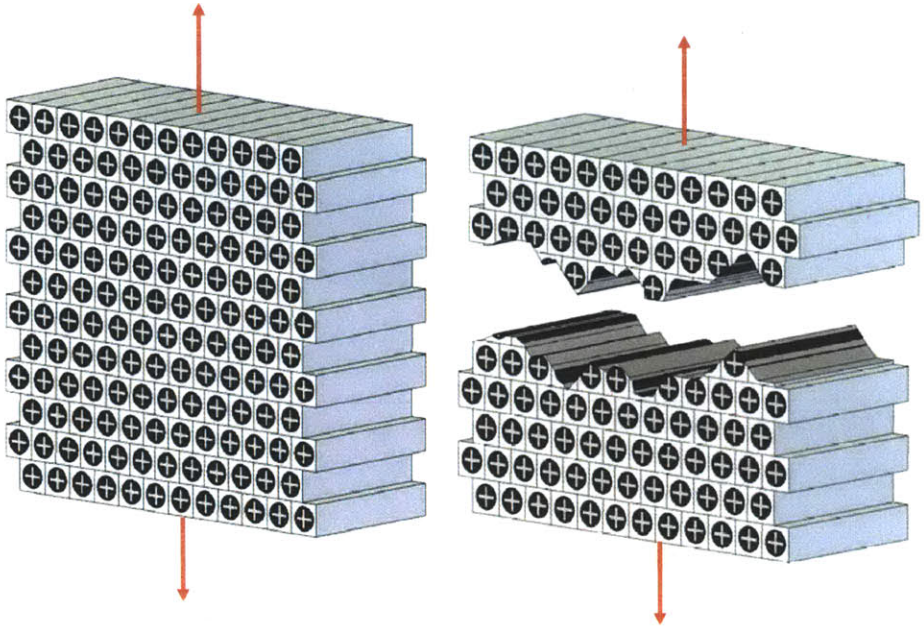

Figure 6-19 Schematic of SCC in dendrite cell structure.

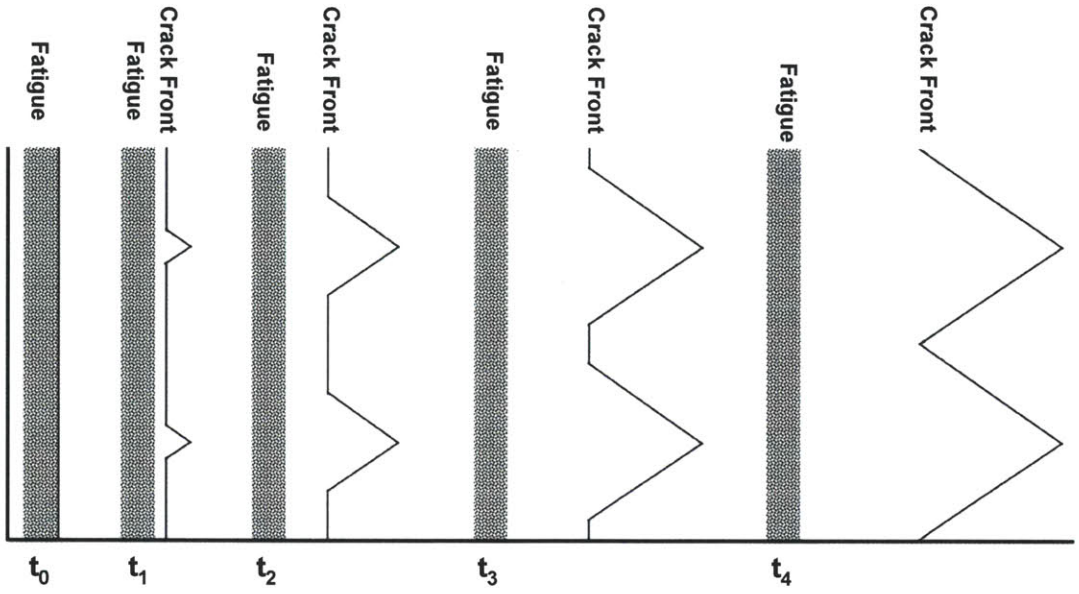

Figure 6-20 The evolution of the SCC front in a two-phase parallel system, as is present in the weld metal.

Consider the 2-dimensinal geometry of one side of the flattened fracture surface, shown in Figure 6-20. An explanation for the development of mature SCC will be now explained. At time t_0 in Figure 6-20, the loading pattern has shifted from fatigue to static loading. SCC begins with both austenite and the δ-ferrite phases as starting at the same crack length. The δ-ferrite represents an area that is more susceptible to SCC and consequently, crack growth rate is faster. However, austenite is still also undergoing SCC, albeit at a much slower rate. This is expressed in Figure 6-20, at time t_1. The center of the triangles represent the dendrite core and the area of the triangle represents austenite that is fracturing perpendicular to crack growth direction. This is evident in the fractograph in Figure 5-12 where the fan-shaped transgranular fracture in austenite point to fracture direction occurring parallel with the dendrite cores. However, the fan-shaped, transgranular fracture immediately surrounding the dendrite-core fracture perpendicular to the overall crack growth direction. This triangle will be the focus of discussion and is further explained in Figure 6-21 below. The flat, vertical front moving away from the fatigue region represents the austenite fracturing in the direction of crack growth. The angle of the point of the triangle is dictated by the uniform crystallographic nature of the dendrites. This continues at time t_2 and t_3, however, SCC in the δ-ferrite region is growing much faster than the austenite front. At time t_4, the crystallographic controlled triangle is now able to reach the nearest neighbor triangle and crack growth rate is controlled by the rate of perpendicular cracking of austenite. This is what is seen through out the fractographic analysis beginning in Figure 5-24 and in 6-16 above.

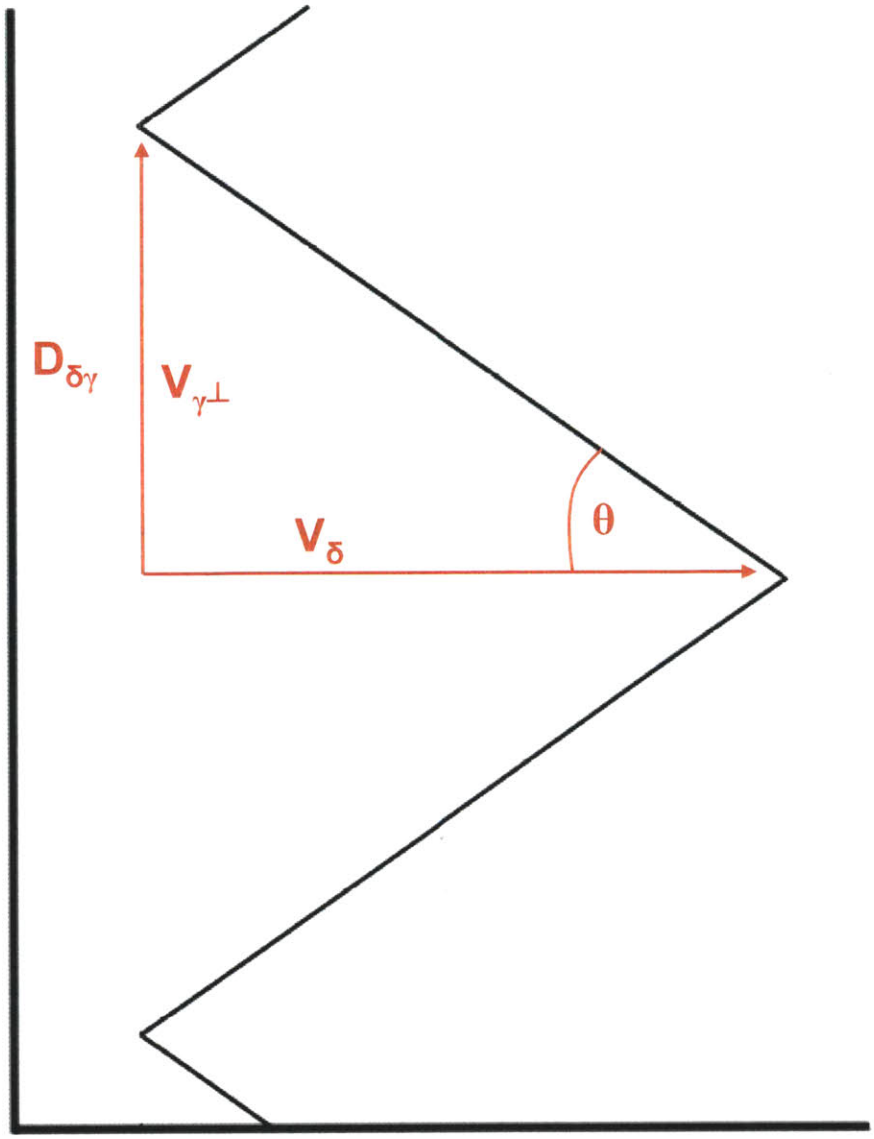

Figure 6-21 Geometric representation of fully developed crack front in a two phase system.

Fully developed SCC, that is, when the rate of cracking is controlled by the austenite perpendicular growth rate, occurs very quickly, probably in the first 30-50 μm, as seen in Figure 5-12. In terms of the SCC crack growth rates, that is about 800-1000 h, which is roughly equivalent to the incubation time seen in the crack growth rate data. This correlation is not meant to imply anything about the mechanism of SCC initiation, only that by the time SCC is reaching steady state crack growth, the vertical front of forward cracking austenite SCC has ended.

Figure 6-21 is focusing on just one of the triangles created during fully developed SCC. The four parameters shown describe the physical situation at the crack front. First, V_δ is the crack growth rate of the δ-ferrite phase boundary. Since this is limited, as discussed

above, it is moving with the same relative rate as the average crack growth front, and so it can also describe the overall crack growth rate. $V_{\gamma\perp}$ is the crack growth rate of the austenite in the perpendicular direction. These two vectors are linked by angle θ, which is defined crystallographically by the active slip system in FCC austenite and the Kurdjumov-Sachs relationship for the γ/δ interaction angle [65]. The final quantity, $D_{\delta\gamma}$ represents the distance between the dendrite cores and the center of the austenite, which is also the dendrite boundary, where another dendrite begins.

The above model allows for the development of proportionality of the crack growth rate to the material structure and property as well as test conditions. For the complete derivation of eq. 6-30, see Appendix B. The corrosion current is expressed as i_C.

$$V_\delta \propto \frac{2L_\delta W_\delta C_M i_C}{b \tan\theta} \frac{K_I}{K_{IC}} \frac{1}{\alpha_\delta} \qquad [6\text{-}30]$$

The equation developed gives a proportional relation of V_δ to α_δ and K_I/K_{IC}, achieving the goal. Introducing a convenient variable, C_{MEM}, a material-electrochemical-mechanical variable, to substitute for the first half of the equation in 6-30 and then rewriting equation 6-30 as:

$$V_\delta \propto C_{MEM} \frac{K_I}{K_{IC}} \frac{1}{\alpha_\delta} \qquad [6\text{-}31]$$

Now it is very straight forward to compare the effect of FN of the material tested in this study. Assuming that C_{MEM} is constant for two materials of the same age but different ferrite numbers, a ratio of crack growth rates can be obtained from eq. 6-31:

$$\frac{V_{\delta L}}{V_{\delta H}} \propto \left(\frac{\alpha_{\delta H}}{\alpha_{\delta L}}\right)\left(\frac{K_{IC}}{K_I}\right)_H \left(\frac{K_I}{K_{IC}}\right)_L, \qquad [6\text{-}32]$$

where the subscript: L denotes low-ferrite material
H denotes high-ferrite material.

The known values of $\alpha_{\delta L}$ and $\alpha_{\delta H}$ are 0.07 and 0.1, respectively, and K_I is 30 MPa$\sqrt{m}$ for each material. K_{IC} for each material can be found in Table 9. For as-welded material, the measured V_δ ratio is 1.78 and the correlated value is 1.64. For 5,000 h aged material, the actual ratio is 1.41 and predicted ratio is 1.44. This shows that there is relatively good agreement with the developed correlation and experimental data. Especially considering the high degree of variability and uncertainty in welds.

Now, consider the implications of the C_{MEM} and C_M. The constant C_M is contained in C_{MEM} so the discussion will begin there. The purpose of C_M is to describe unknown differences in the material, particularly in reference to aging. Aging likely affects high- and low-ferrite through the same method, however, there are clearly differences between

the two materials in terms of aged and initial mechanical properties. This was shown in the data in the material characterization section. It is also likely that the in-situ fracture toughness of the material, is an important factor in C_M. However, there is very little plastic deformation in the SCC fracture surface, giving priority to the elastic portion in calculating J or K during the SCC growth period. Thus, the ratio of K_I/K_{IC} expanded into C_{MEM}. The other parameter taken into account by C_{MEM} that is worthy of comment is the current density, i_C, applied to the sample. Multiplication of i_C by the area gives the total current, I. Consider the crack growth system as an electrical circuit. In the circuit, there is a potential, the voltage on the surface of the material and at the crack tip itself and there are two resistances of importance. It is straight forward to draw an equivalent circuit, shown in Figure 6-22. Expressing the cathodic and anodic potential difference as E_d and defining the material resistance, including the oxide, as R_M and the electrolyte resistance as R_E, then to solve for I by Ohm's law:

$$I = \frac{E_d}{R_E + R_M} \qquad [6\text{-}34]$$

This is greatly simplified, and in order to accurately describe the circuit and resulting current in a realistic three dimensional test geometry, it would be necessary to invoke a higher order differential expression based on geometry and proper boundary conditions, but this will suffice for purposes of explanation. In the BWR environment, E_d is about 0.7 V as this is the difference between the deaerated crack tip and the 300 ppb oxygen sample surface. If, for example, the chemistry was changed from BWR chemistry to PWR chemistry, where there is a hydrogen overpressure, one would expect the corrosion current to drop as E_d falls faster than the rate of resistance decrease. Weld metal, however, contains localized cathodes at the crack tip, as expressed by the area encompassed in radius R_C. The impact of outside chemistry would be mitigated by the availability of the cathodic area, which becomes a function of the ferrite fraction. This then goes along way in explaining the differences between hydrogen water chemistry and BWR chemistry. The rate controlling variable is the conductivity of the electrolyte and the surface potential outside the deaerated crack.

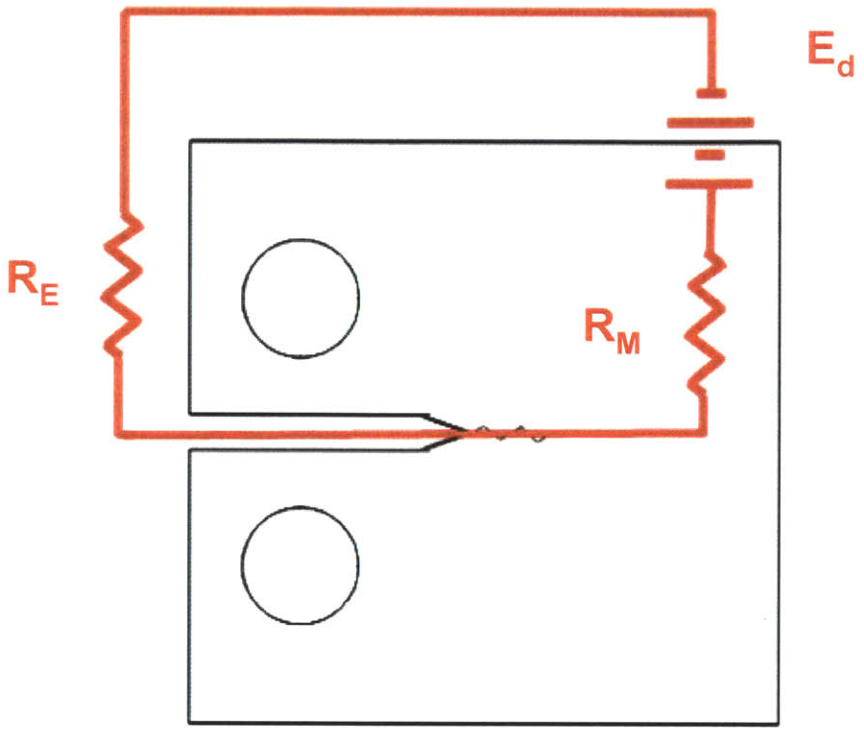

Figure 6-22 Corrosion circuit reduced to 1-line schematic for a 1T-CT specimen.

Finally, it is very important to consider what other models indicate about SCC in this material, as well as what the results of this study can say about their validity in this material.

In order for a model to accurately be applied to the weld system used in this study, it must be able to use and explain the phenomena seen through fractography, experimental data, and linking of the microstructure to the rate of crack growth. It must be able to explain or encompass:

- A very low level of oxygen concentration at the crack front, resulting in oxides that are stable around the hydrogen line in the Pourbaix diagram. These oxides are very thin and likely form in tight cracks as described by Staehle.
- The importance of slip and crystallographic planes in crack propagation.
- The impact of a 2-phase system, particularly the presence of carbides and the difference of crack propagation through chemically similar yet crystallographically different materials.
- Predict interdendritic SCC.
- Impact of crack front geometry on stress intensity.
- Effect of aging, even though the material remains chemically similar.

Beginning with the slip-oxidation model championed by Andresen et al. This model suggests that the rate is controlled primarily by the diffusion of external species to the crack tip, where the freshly exposed metal at the tip is oxidized. When slip occurs, the

oxide film is broken and the process starts over again. The importance is placed on slip and subsequent oxidation, as the model name suggests [34]. Part of the rate equations provided by Andresen is remarkably similar to the one developed above, but this is to be expected from taking into account corrosion current and crack tip strain rate. However, the diffusion required to change the oxide structure to be consistent with crack mouth oxidation potential is so small that oxidation may occur before slip. Furthermore, the slip-dissolution does not take into account carbides, as well as explaining the different rates associated with FCC vs. BCC crystal systems. It also is not meant to predict aging of materials, but would instead rely on adjustment of the strain rate.

The coupled environmental fracture model (CEFM), proposed by [40] is quite similar to the slip-dissolution model with some notable differences in accounting for the external environmental impact at the crack tip. Macdonald declares the rate limiting step to occur on the external surface of the crack rather than at the crack tip, however, he still promotes the idea of slip, then oxidation. In reference to a 2-phase system, such as is present in the welds in this study, it is hard to accept Macdonald's notion that the majority of cathodic reaction of importance occurs outside the crack. While it is very important to consider the external cathodic reactions, with the complex material structure of a weld there is certainly a large amount of local current exchange within the crack. However, to Macdonald's credit, electrically, and due to the large surface area difference, the cathodic surface reactions certainly play some role. In reference to this study, CEFM fails to provide a manner to of accounting for the multiple phases of the system. Furthermore, CEFM does little to account for crack tip stress intensity.

Internal oxidation suggested by [42] is normally applied to nickel-based alloys. The basic premise is that nickel is quite noble and any impurities or alloying elements which are less noble scavenge diffusing oxygen leaving the base metal unprotected. This is reasonable for nickel-based alloys but still may be applicable in the carbide rich γ/δ boundary of the weld metal. In this instance the protective chromium is tied up with the carbon atoms, allowing the iron to be attacked in preference to the nickel. Any remaining chromium is tied in with the iron to form $FeCr_2O_4$, the stable oxide in this chemistry. This also may have impact following spinodal decomposition.

Perhaps the Jones model provides the closest mechanism related at least to the austenite phase. The model simply states that vacancy migration as a result of strain and oxidation accumulates ahead of the crack tip resulting in weakened, strain-hardened material. This then undergoes brittle fracture.

It is entirely possible then that there are multiple mechanisms at work in the weld system. One for each dominant phase. Slip dissolution or some derivative may accurately describe the propagation through the austenite phase, while preferential oxidation is occurring in the chromium-rich carbide γ/δ boundary. Then generated hydrogen combined with vacancy migration embrittles the austenite phase that undergoes more brittle fracture as a result.

It is unlikely that there will ever be one single model to take into account all aspects of SCC in all materials and environments. However, weld metals offer a unique method of inspection due to the highly oriented crystallographic phases present. Furthermore, the concepts pertaining to SCC in welds can be extended to normal wrought materials through geometrical factors. That is to say that in wrought materials the random orientation of grains still presents material shape of significance. The tortuous intergranular diffusion path, for example, can be described geometrically. This ultimately affects flow of the outside environment in, and the removal of corrosion product out. Furthermore, the size of the wrought grains would affect the surface area available for interaction. When there has been greater elucidation on the mechanics of stress corrosion cracking, it is very likely that there will be several regimes of SCC mechanism dependant on the SCC-trifecta of the material, the stress and the environment.

7 Conclusions

This study has focused on the impact of aging and FN in Alloy 316L welds utilized in BWR components. At the outset of the project the goals were to evaluate SCC crack growth, fracture toughness behavior, and material properties in Alloy 316L stainless steel welds as a function of ferrite content and thermal aging. Furthermore, it was desired to establish structure-property relationships for SCC and in-situ fracture toughness behavior.

Alloy 316L stainless steel welds were constructed containing two different ferrite numbers and aged up to 40,000 h at three different temperatures to accelerate the aging mechanism. This allowed the simulation of total weld aging over BWR life. The material was then sectioned and machined into common test geometries for tensile, Charpy-V impact, hardness, fracture toughness and SCC testing. Residual stress was also explored using an instrumented hole drilling technique.

The major findings then concern both aging and ferrite content. To summarize first the material properties without environmental effects: tensile stress and yield strength in general demonstrated a sharp increase in the first 1,000 h of aging, this reached a maximum by 5,000 h and then gradually fell as the weld material aged. Vickers hardness, residual stress and Charpy-V impact toughness follow the same trends. Fracture toughness testing in air showed that there was an increase in fracture toughness by the first 1,000 h then negligible change with further aging, the notable exception being the high-ferrite material that showed a noticeable dip in fracture toughness at 5,000 h. In every case, higher FN material was harder, stronger and more tough.

Environmental impact on the weld material was characterized by SCC and in-situ fracture toughness testing. These experiments were performed in the BWR environment in a custom designed and built experimental facility that allowed the exact BWR chemistry, temperature and pressure to be maintained as well as performing load application for testing. Crack growth was measured utilizing the DCPD method. It was found that crack growth was higher in low-ferrite material and increased with aging. In-situ fracture toughness was shown to be notably lower than values obtained from air testing. In-situ fracture toughness increased in the low-ferrite material but decreased in the high-ferrite material with aging when compared to in-situ testing only, tests were conducted on as-welded and 5,000 h aged material. This is the first study specifically designed to test in-situ fracture toughness of austenitic stainless steel weld metal and systematically grade the impact of environmental fracture.

Microstructure of the weld metal was found to play a role in fracture toughness as well as SCC. High-ferrite numbers gave better performance, however, there is believed to be a limit improving performance based on raising FN. Furthermore, precipitates and inclusions such as chromium-rich carbides and MnS were important in the rate of SCC and fracture toughness, respectfully. New crack growth relations and insight have been elucidated in SCC of weld metal. It was shown that the SCC rate of propagation has an important geometric component that is not taken into account in many current models. In

addition, fracture was found to prefer the carbide-rich γ/δ boundary surrounding the δ-ferrite dendritic core. This accelerated growth was tempered by the slower crack growth of the austenite phase. Spinodal decomposition resulting in chromium depletion in δ-ferrite is believed to play an important role in SCC. Spinodal decomposition was also shown to harden the δ-ferrite. It is likely that the changes seen in the material properties can be correlated to both spinodal decomposition and stress relaxation, both of which are functions of aging time and temperature. Furthermore, the production of hydrogen in fatigue, SCC, and fracture toughness test crack propagation was shown to have a major impact and is believed to be the main source of environmental fracture. This is clearly demonstrated in fractography as well as through theoretical evaluation.

7.1 Contributions

There are many contributions of this study. In expanding the knowledge of fracture mechanics and SCC, as well as a general understanding of weld metal systems and the effects of aging time and temperature, the most important contributions are:

- Evaluated SCC crack growth behavior of Type 316L welds as a function of weld ferrite content and thermal aging.
  - Connected SCC crack growth rate to the weld microstructure via optical and SEM analysis.
  - Established the likelihood that diffusible hydrogen generated at the crack tip is responsible for the SCC crack growth when exposed to the LWR environment.
  - Identified previously unrecognized phenomenon of Fatigue/SCC oxide precipitation difference.
  - Provided a geometrical correlation linking FN to SCC growth rates for the FA solidification mode.
- Explored in a systematic way for the first time the phenomena of "Environmental Fracture" in LWR environments.
  - Established the likelihood that diffusible hydrogen generated at the crack tip is responsible for the reduction in toughness when exposed to the LWR environment.
  - Provided evidence that sufficient hydrogen can be produced and diffuse into the bulk material matrix to cause noted effects.
  - Identified previously undocumented brittle fracture occurring prior to the onset of crack blunting during in-situ fracture toughness testing.
- Expanded the data universe in reference to time, temperature, and ferrite number for thermal aging, utilizing high quality Alloy 316L welds, exactly duplicating those found in a BWR.

7.2 Future Work

The results and methods of this study bring about many new directions for future research. The original motivation was to understand the impact of the weld metal system in terms of BWR license extension. While it is beyond the scope of this study to provide

recommendation, the identification of environmental fracture following SCC and cyclic loading certainly holds merit in reference to rapid catastrophic loading, such as that experienced during earthquakes. In addition to immediate practical application in reactor environments, there is also the scientific impact of the study and the ability to continue the process of gaining new knowledge in the fields of fracture mechanics, SCC, and diffusion driven transformations such as spinodal decomposition and solidification modes in weld metal systems. Future work should focus on:

- Irradiation Studies: It is well known that irradiation of materials, particularly metals, deposits hydrogen. Furthermore, radiolyitic dissociation of water creates additional hydrogen. Additionally, irradiation of materials causes a decrease in toughness as well as possibly accelerating SCC. The weld material of interest is one that can be ultimately utilized in a neutron flux in reactor applications. As the impact of hydrogen is shown to be of major importance, and the mechanisms of SCC are already possibly accelerated over wrought materials, it is important to understand the symbiotic effect of radiation on the material. Of particular interest is if the impact has merely an additive effect over the noted environmental fracture and accelerated rates, or if a much worse case scenario is reality where there is a multiplicative effect by combining neutron damage and environmental effects. This is the next logical step in the study in terms of reactor applications.

- Standardized In-situ Fracture Toughness Tests: It will be worthwhile to perform fracture toughness tests directly from SCC conditions as this is what would likely be found in an operating reactor. A standard fracture toughness test begins with a precrack that has been fatigue generated. However, in actual service, it is more likely that cracks in the materials will be due to SCC and behavior may thus be more appropriately represented by SCC crack-initiated unstable fracture. This would serve to provide a realistic material/environment property.

- Purpose Built Hydrogen Experiments: The major contributor to environmental fracture in the weld metal system is thought to be diffusible hydrogen. This is difficult to measure directly due to the rapid removal of the hydrogen once generation has stopped. In the experiments conducted in this study, it was not possible to cool down the material fast enough to prevent outward diffusion and loss of the hydrogen. This meant that it was not possible to measure directly. Designing a purpose built experiment, which allows quenching of the specimen in liquid nitrogen immediately, thus reducing the diffusion rate to a negligible value, should provide direct insight into the quantities and dynamics of the diffusible hydrogen. This is by no means an easy endeavor, however, the knowledge gained from such an experiment would provide direct evidence for the arguments proposed in this study.

- Nano-indentation: Understanding the material property difference between the two phases in the weld metal system is essential to proper modeling of the material interaction of the phases in a composite sense. Nano-indentation provides a straightforward method of inspection on the same length scale as the material

microstructure. This would allow an understanding of the aging effects on each phase of the weld metal and the impact on localized material properties. This would also yield important specific mechanical properties of each phase that are not attainable otherwise.

- Atom Probe Microscopy: Recent advancement in analytical technique has allowed the three-dimensional placement of individual atoms. This is already showing profound impact on SCC understanding. See for example [86] or [87]. Understanding of the exact mechanisms at the crack tip will give refined models taking into account physical evidence over speculation of the interactions at the crack tip. Furthermore, atom probe microscopy is an excellent tool for analyzing spinodal decomposition and the impact that has on material properties as well as accurately gauging the diffusion dynamics predicted by Cahn and Hillard.

Physical systems find there ultimate limits in the materials chosen for their respective purposes. A better understanding of the materials used in the systems allows for a greater understanding of system life as well as system reaction to perturbation. In the case of welds, they are implemented as one of the key material joining processes. There are not many alternatives in many of the applications where welds are utilized, the nuclear reactor environment being no exception. The importance of understanding the impact of time and the environment on the weld metal system can not be overstated.

8 References

CH1

[1] E. S. Beckjord et al. "The Future of Nuclear Power, an interdisciplinary MIT study" Cambridge, MA 2003

[2] L.C. Shao and J.J. Burns "Stress-Corrosion Cracking Experience in Piping of Light Water Reactor Power Plants" Nuclear Engineering and Design 57 (1980) 133-140

[3] C. Jansson "Pipe Cracking Experience in Swedish BWRs" Int. J. Pres. Ves. & Piping 65 (1996) 227-282

[4] K. Ting "The evaluation of intergranular stress corrosion cracking problems of stainless steel piping in Taiwan BWR-6 nuclear power plant" Nuclear Engineering and Design 191 (1999) 245-254

[5] "Reactor Coolant System Weld Issues" US NRC, www.nrc.gov accessed Feb 1, 2011

[6] "Weld flaw at Iowa nuclear plant repaired" Globe Gazette, www.globegazette.com accessed Feb 1, 2011

[7] R.L. Tapping "Materials performance in CANDU reactors: The first 30 years and the prognosis for life extension and new designs" Journal of Nuclear Materials 383 (2008) 1-8

[8] "EAR ATL 090-004; Heavy Water Leak From Reactor Vessel" WANO, www.cogonline.org, accessed Feb 11, 2011

[9] J. Lippold and D. Kotecki "Welding Metallurgy and Weldability of Stainless Steels" John Wiley & Sons, Inc., Hoboken, New Jersey, 2005

[10] US Energy Information Administration, "World Nuclear Reactor Summaries" www.eia.gov, accessed March 15, 2011

[11] Terms and Terminology for weld Creep Testing, ECCC Recommendations, Volume 2, part IIb (2), *European Creep Collaborative Committee,* (2001) Rotherham, UK

[12] J. Lancaster "Handbook of Structural Welding", Woodhead Publishing LTD, Cambridge, England, 1993

[13] J.M. Vitek, S.A. David, D.J. Alexander, J.R. Keiser and R.K. Nanstad "Low temperature ageing behavior of type 308 stainless steel weld metal" Acta metal. mater. 39 (4), (1991) 503-516

[14] I Hamamda and K. Yamauchi "Intergranular stress corrosion cracking behavior of types 308 and 316 stainless steel weld metals in a simulated boiling water reactor environment" Metallurgical and Materials Transactions A 33A, (2002)

[15] Elmer, J.W., Allen, S.M. , Eager, T.W., "Microstructural Development during Solidification of Stainless Steel Alloys" MetTrans A, 20A October (1979)

[16] A.L. Schaeffler "Constitution diagram for stainless steel weld metal" Metal Progress, 56(11), (1949) 680-680B

[17] W.T. Delong, G.A. Ostrom and E.R. Szumachowski "Measurement and calculation of ferrite in stainless-steel weld metal" Welding Journal, 35(11) 521-528, 1956

[18] Long C.J. and DeLong, W.T. "The ferrite content of austenitic stainless steel weld metal" Metal Progress, 56 (11) 680-680B

[19] D.J. Kotecki and T.A. Siewart "WRC-1992 constitution diagram for stainless steel weld metals: a modification of the WRC-1988 diagram" Welding Journal, 71(5). (1992) 171-178

[20] Chopra et. al.: Effects of Thermal Aging on Fracture Toughness and Charpy-Impact Strength of Stainless Steel Pipe Welds. U.S. Nuclear Regulatory Commission NUREG/CR-6428. (1995)

[21] M.H. Hillert "A theory of nucleation for solid metal solutions" Sc.D Thesis, MIT, 1956

[22] J.W. Cahn and J.E. Hillard "Free energy of a non-uniform system-I Interfacial free energy" journal of Chemical Physics, 28, (1958) 258-267

[23] Metals Handbook, by the American Society for Metals, Ohio, 1948

[24] Peter Haasen, "Physical Metallurgy", third edition, Cambridge University Press, New York, 1996

[25] W.C. Carter, Thermodynamics of materials, MIT open course ware http://ocw.mit.edu/courses/materials-science-and-engineering/3-00-thermodynamics-of-materials-fall-2002/lecture-notes/lecture_32_oneside.PDF accessed April 1, 2011

[26] S. Brenner, M. Miller and W. Soffa, "Spinodal Decomposition of Fe-32at%Cr at 470 °C", Scripta Metall, (1982)

[27] M.I.M. Coetti and C.M. Elliot "Kinetics of phase processes: numerical solutions to Cahn-Hilliard equation" Materials Science and Technology, 6, (1990)

[28] H. Kubo, I. Cornelis and C.M. Wayman, Morphology and Characteristics of Spinodally Decomposed β-brass, Acta Metall., 28 (3), (1980) 405-416

[29] J.E. Brown and G.D.W. Smith "Atom probe studies of spinodal processes in duplex stainless steels and single- and dual-phase Fe-Cr-Ni alloys" Surface Science 246 (1991) 285-291

[30] H. Abe, Y. Watanabe, "Low Temperature Aging Characteristics of Type 316L Stainless Steel Welds: Dependence on Solidification Mode", Met. and Metal. Trans. A, 39A, (2008). 1392-1398.

[31] M Hättestrand,P Larssona, G Chaia, J Nilssona and J Odqvista, Study of decomposition of ferrite in a duplex stainless steel cold worked and aged at 450–500 °C Materials Science and Engineering: A, 499, (1-2), (2009) 489-492

[32] J.R. Hixon, J.H. Kim, R.G. Ballinger "Effect of Thermal Aging on SCC and Mechanical Properties of Stainless Steel Weld Metals" 13th International conference on Environmental Degradation of Materials, Whistler, BC, (2007)

[33] D. Jones "Principles and Prevention of Corrosion, 2nd Edition" Prentice Hall, Inc, Upper Saddle River, NJ 1992

[34] P.L. Andresen and F. P. Ford "Fundamental modeling of environmental cracking for improved design and lifetime evaluation in BWRs" Int. Journal Pres. Des. & Piping 59 (1994) 61-70

[35] M.M. Hall "An alternative to the Shoji crack tip strain rate equation" Corrosion Science 50 (2008) 2902-2905

[36] M.M. Hall "Critique of the Ford-Andresen film rupture model for aqueous stress corrosion cracking" Corrosion Science 51 (2009) 1103-1106

[37] T. Shoji, Z. Lu H. Murakami "Formulating stress corrosion cracking growth kinetics by combination of crack tip mechanics and crack tip oxidation kinetics" Corrosion Science 52 (2010) 769-779

[38] M.M. Hall "Film rupture model for aqueous stress corrosion cracking under constant and variable stress intensity factor" Corrosion Science 51 (2009) 225-233

[39] R. G. Raicheff, A. Damjanovic, and J. O'M. Bockris "Dependence of the Velocity of the Anodic Dissolution of Iron on Its Yield Rate under Tension" Journal of Chemical Physics 47, (1967) 2198

[40] D.D. Macdonald, et al, "Theoretical estimation of crack growth rates in type 304 stainless steel in LWR environments" corrosion Science 32 (1991), 51-81

[41] Aaltonen et al "Facts and Views on the role of anionic impurities, crack tip chemistry and oxide films in environmentally assisted cracking" VTT industrial systems, Finland, 2002

[42] P.M. Scott, M. Le Calvar "Some Possible Mechanisms of Intergranular Stress Corrosion Cracking of Alloy 600 in PWR Primary Water" Sixth International Symposium on Environmental Degradation of Materials in Nuclear Power Systems-Water Reactors; San Diego, (1993) 657-667

[43] D.A. Jones "A Unified Mechanism of Stress Corrosion and Corrosion Fatigue Cracking" Metalurgical Transactions A, 16A (1985)

[44] J.C. Scully "Stress Corrosion Crack Propigation: A Constant Charge Criterion" Corrosion Science, 15, (1975) 207-224

[45] Peter Andresen, GE Global Research & Development Center, Schenectady, NY, Used with Permission.

[46] JC Boreland "Generalized theory od super solidus cracking in welds (and castings)" British Welding Journal, 7, (1960) 508-512

[47] W.J. Mills, "Fracture toughness of type 304 and 316 stainless steels and their welds" International Materials Reviews 42 (2), (1997)

[48] J. Nayak, K. R. Udupa, K.R. Hebbar and H.V.S. Nayak, Estimation of Embrittlement During Ageing of AISI 316 Stainless Steel TIG Welds, Bulletin of Material Sciences, 27, (2004)

[49] G.L. Berry Jr., D.L. Olson and D.K Matlock "Influence of microcompositional gradients on stress corrosion crack propagation" Material Science and Engineering, A148 (1991) 1-6

[50] H. Shaikh, H.S. Khatak, S.K. Seshadri, J.B. Gnanamoorthy and P. Rodriguez "Effect of ferrite transformation on the tensile and stress corrosion properties of type 316 L stainless steel weld metal thermally aged at 873K" Metallurgical and Materials Transactions A 26A, (1995)

[51] Z. Lu, T.Shoji, Y. Takeda, Y. Ito, A. Kai, N. Tsuchiya "Effects of loading mode and water chemistry on stress corrosion crack growth of 316L HAZ and weld metal materials in high temperature pure water" Corrosion Science 50 (2008) 615-638

[52] S. Roychowdhury and V. Kain "Environmental effects on the fracture toughness of a duplex stainless steel" Corrosion 2006, NACE paper No. 06492

[53] P.H. Pumphrey and K.N. Akhurst "Aging kinetics of CF3 cast stainless steel in temperature range 300-400°C" Materials Science and Technology, 6, (1990)

[54] M. Strangwood and S.G. Druce "Aging effects in weldsed CF3 stainless steel" Materials Science and Technology. 6, (1990)

[55] H. M. Chung and T.R. Leax "Embrittlement of laboratory and reactor aged CF3,CF8, and CF*m duplex stainless steels" Materials Science and Technology, 6, (1990)

[56] M.Bethmont, Y. Meyzaud, and P. Soulat "Properties of cast austenitic materials for light water reactors" Int. J. Pres. Ves. Piping 65 (1996) 221-229

[57] J. Hixon, The Effects of Thermal Aging on SCC and Mechanical Properties of Stainless Steel Weld Metals, Master's Thesis, Massachusetts Institute of Technology, August 2006

[58] ASTM, Standard Test Methods for Tension Testing of Metallic Materials, ASTM E 8 – 04, ASTM International, 2004

[59] ASTM, Standard Method for Measurement of Fracture Toughness, ASTM E 1820 – 01, ASTM International, 2001

[60] ASTM, Standard Method for Measurement of Fatigue Crack Growth, ASTM E 647 – 00, ASTM International, 2000

[61] R. Hertzberg, "Deformation and Fracture Mechanics of Engineering Materials" Fourth Edition, John Wiley & Sons, Inc., Hoboken, New Jersey, 1996

[62] ASTM, Standard Test Methods for Notched Bar Impact Testing of Metallic Materials, ASTM E 23 – 02a, ASTM International, 2002

[63] JSME S NA1-2002, "Code for Nuclear Power Generation Facilities, Rules on Fitness-for-Service for Nuclear Power Plants", The Japan Society of Mechanical Engineers, October 2002

[64] A. Toivonen "Stress corrosion crack growth rate measurements in high temperature water using small precracked bend specimens", PhD Thesis, Helsinki University of Technology, June 2004

[65] Robert Reed-Hill and Reza Abbaschian "Physical Metallurgy Principles" third edition, PWS Publishing Co, Boston, 1994

[66] T. Saukkonen, U. Ehrstein, H. Hänninen, "Microsturcture and Plastic Strain Distribution of an AISI 304 Stainless Steel Power Plant Pipe Weld Studied by EBSD" VTT Technical Research Center, Finland

[67] M. Morra, GE Global Research & Development Center, Schenectady, NY, Used with Permission.

[68] ASTM, Standard Method for Measurement for Determining Residual Stress by the Hole-Drilling Strain Gage Method, ASTM E 837 – 01, ASTM International, 2001

[69] I. Ripyar, R. Kahkov "The Impact of DnS on Metals Testing Performance" Indian Institute of Technology, August, 2008

[70] A.C.T.M. Zwieten and J.H. Bulloch "The Influence of Interstitial Solute Level on the Charpy Toughness Properties of a 40% Cr-Fe Stainless Steel" International Journal of Vessel and Piping, 56, (1993) 69-91

[71] J.A. Brooks, A.J. West and A.W. Thompson "Effect of weld composition and microstructure on hydrogen assisted fracture of austenitic stainless steels" Metallurgical Transactions A, 14A, (1983)

[72] B.P. Somerday, M Dadfarnia , D.K.Balch, K.A. Nibur, C.H. Cadden, and P. Sofronis "Hydrogen-assisted crack propagation in austenitic stainless steel fusion welds" Metallurgical and Materials Transactions, 40A, (10), (2009) Science Module

[73] I. Aubert, J.M. Olive, N. Saintier, "The effect of internal hydrogen on slip surface localization on polycrystalline AISI 316L stainless steel" Material Science and Engineering, A 527, (2010) 5858-5866

[74] M.I. Luppo, A. Hazarabedian, J. Ovejero-Garcia "Effects of delta ferrite on hydrogen embrittlement of austenitic stainless steel welds" Corrosion Science 41 (1999) 87-102

[75] B. Beverskig and I. Puigdomenech, "Pourbaix Diagrams for the Ternary System of Iron-Chromium-Nickel" Corrosion, 55, (11), (1999) 1077-1087

[76] R. W. Staehle "Critical Analysis of 'Tight Cracks'", 13th International conference on Environmental Degradation of Materials in Nuclear Power Systems, Whistler, BC, August, 2007

[77] C.D. Beacham "A new model for hydrogen-induced cracking" Metallurgical Transactions B, 3. (1972) 437.

[78] H.K. Birnbaum and P. Sofronis "Hydrogen-enhanced localized plasticity-a mechanism for hydrogen related fracture" Materials Science and Engineering, A176, (1994) 191-202

[79] S.P. Lynch "A fractographic study of gaseous hydrogen embrittlement and liquid-metal embrittlement in a tempered-martnesitic steel" Acta Metallurgical, 32, (1984) 79-90

[80] Y. F. Cheng " Thermodynamically modeling the interactions of hydrogen, stress and anodic dissolution at crack-tip during near-neutral pH SCC in pipelines" Journal of Material Science, 42, (2007) 2701-2705

[81] S. X. Mao and M. Li "Mechanics and thermodynamics on the stress and hydrogen interaction in crack tip stress corrosion: experiment and theory" J. Mech. Phys. Solids, 46, (6),(1998) 1125-1137

[82] Habashi M., Galland J. "Considerations on the Hydrogen Embrittlement of Austenitic Stainless Steels" Memoires et Etudes Scientifiques Revue de Metallurgie, 79 (6), (1982) 311-323

[83] J. Crank, "The Mathematics of Diffusion" Clarendon Press, Oxford, 1975

[84] R. P. Gangloff "Hydrogen Assisted Cracking of High Strength Alloys", Compressive Structural Integrity, 6, Elsevier Science, New York, 2003

[85] Y. Huang, et al. "Hydrogen-induced cracking by nano-voids in 310 stainle steel" Science in China, (E) 41, (4), (1998)

[86] J. Gibbs "Stress Corrosion Cracking and Crack tip Characterization of alloy X-750 in Light Water Reactor Environments

[87] S.Lozano-Perez, P. Rogrigo, L.C. Gontard "Three-dimensional characterization of stress corrosion cracks" Journal of Nuclear Materials 408, (2011) 289-295

Appendix A SCC and Fracture Toughness Testing

SCC Crack Growth rate has been evaluated on eight samples representing 400°C high and low ferrite, as welded and 5,000 Hr aged points on the testing matrix. In-situ fracture toughness was also evaluated. The results along with a brief description are presented below.

A.1 Low Ferrite, As-Welded Test, Sample 38

Table A-1 shows the test sequence as well as the crack growth rates for each test step and illustrates the procedure necessary to achieve stable SCC crack growth for sample 38, low-ferrite, as welded material. Figures A-1 through A-3 show the detailed test variable plots. The numbers in Figure A-1 correspond to test sequence steps. Also shown in Figures A-1 through A-3 are the data for the chemistry of the system during the test.

Table A-1Test Sequence for As-Welded SS316L (low delta ferrite, FN = 10) Crack Growth Specimen #38

Step	R	Waveform	Frequency (Hz)	Kmax (Mpa√m)	a/W	da/dt (mm/s)
1	0.3	sine	1	25	0.4598	6.95E-05
2	0.5	sine	1	27	0.4658	5.03E-05
3	0.6	sine	1	30	0.4718	4.03E-05
4	0.7	sine	1	30	0.4778	2.01E-05
5	0.7	sine	0.1	30	0.4818	4.02E-06
6	0.7	sine	0.01	30	0.4858	9.95E-07
7	0.7	sine	0.001	30	0.4898	2.04E-07
8	0	cnst		30	0.4958	7.72E-08

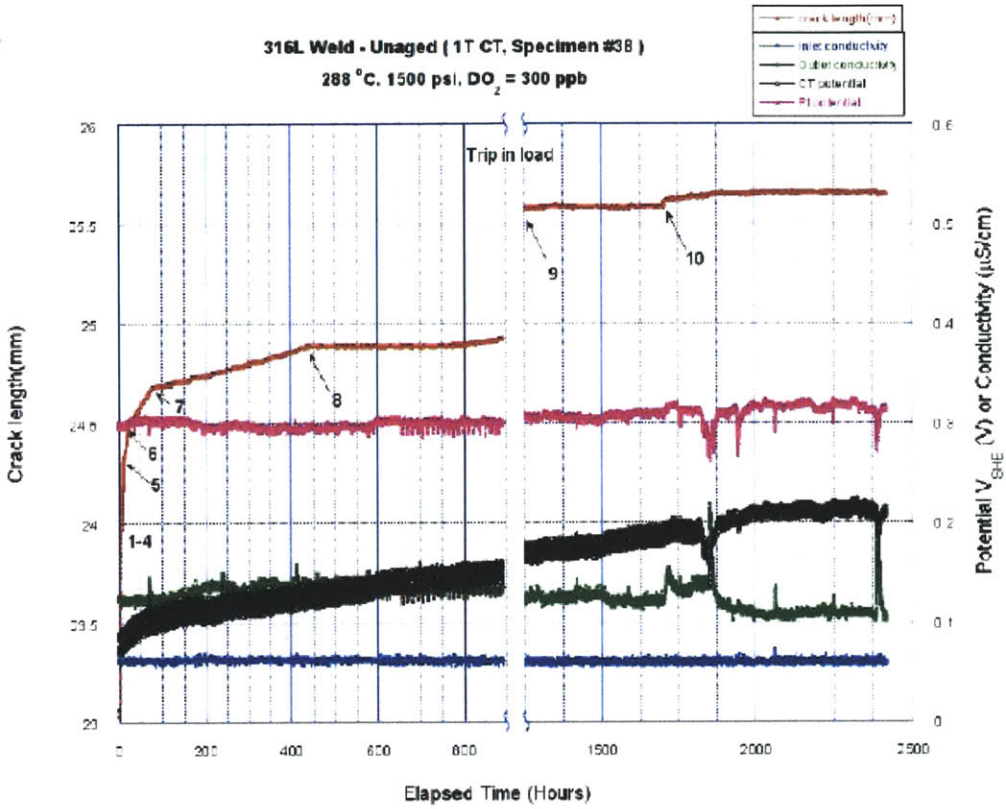

Figure A-1 Complete detailed test results for Specimen #38

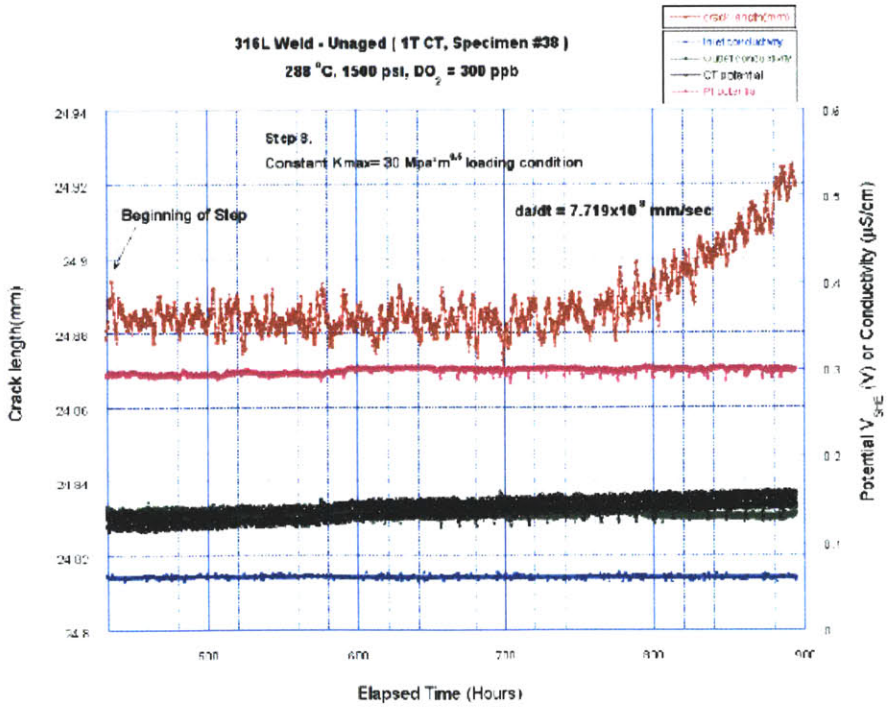

Figure A-2 Detailed test results for Step 8 in Specimen #38

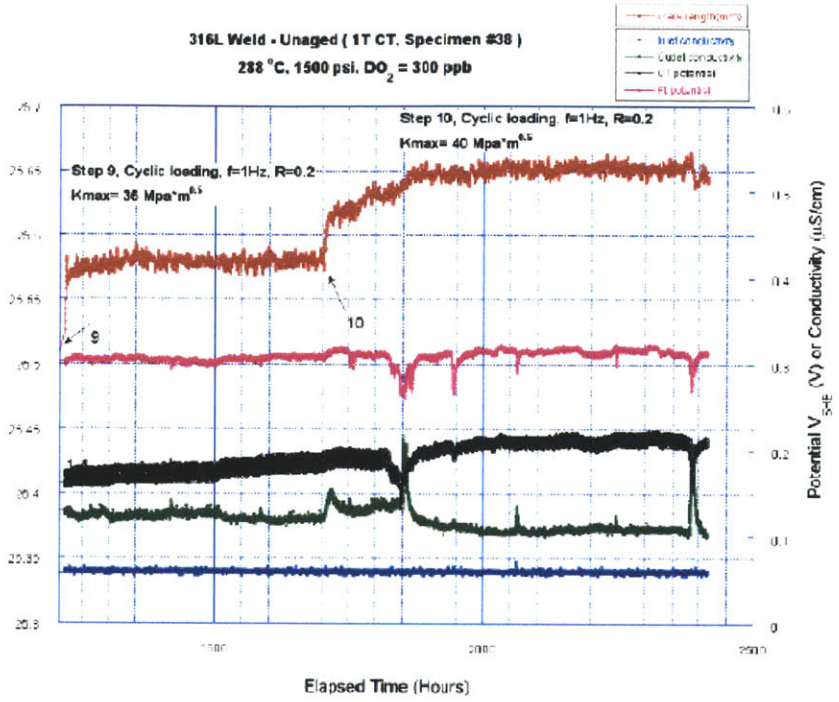

Figure A-3 Detailed test results for steps 9-10 in Specimen #38

A.2 Low Ferrite, As-Welded, Sample 102

Crack Growth rate testing was also completed on an unaged, low ferrite, 1T-CT sample - sample 102. The complete test ran for just under 2500 hours and was finished with an in-situ fracture toughness test. The sample was then removed from the autoclave and split in half for post-mortem analysis. The test was quite successful with few inadvertent shutdowns and even fewer cool downs.

Routine in air precracking was conducted. This was followed by cyclic loading with successive decreases in K_{max} until the final a/W was reached. Figure A-4 shows the test plan and crack growth plot as well as an accompanying micrograph of the in-situ crack growth region. The crack was conditioned for stress corrosion and cracking (SCC) through 8 steps, initially increasing K_{max} and R and then logarithmically decreasing frequency of fatigue. The only issue of note is the flat area occurring in Step 3 between approximately 50 and 300 hours. During this time a filter became clogged and the test was unloaded until repair was available. Finally in the 8th step a trapezoid approach to constant loading was used. Step 9 was constant loading and SCC was noted after approximately 500 hours of hold time. The maximum crack growth rate that was seen in

the SCC region was 8.33 mm/sec at a K value of 30.41 MPa. The observed crack growth rate has been plotted in Figure A-4 as well. In order to validate DCPD data and to analyze the crack front, an SEM micrograph montage is shown in Figure A-5. The step changes are highlighted in red. During the CGR experiment, chemistry is also recorded. Figure A-6 shows the chemistry during the test was constant and acceptable. Figure A-7 is the J-R curve derived from in-situ fracture toughness evaluation. The strain rate was 0.02 mm/min.

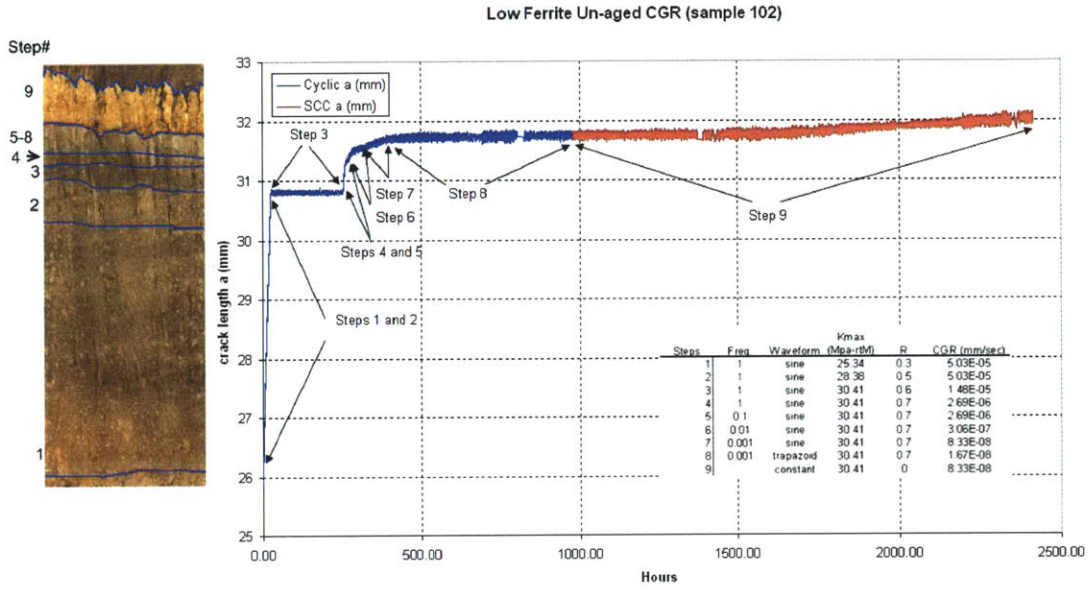

Figure A-4 Crack Growth Rate (CGR) data for unaged, low ferrite sample 102

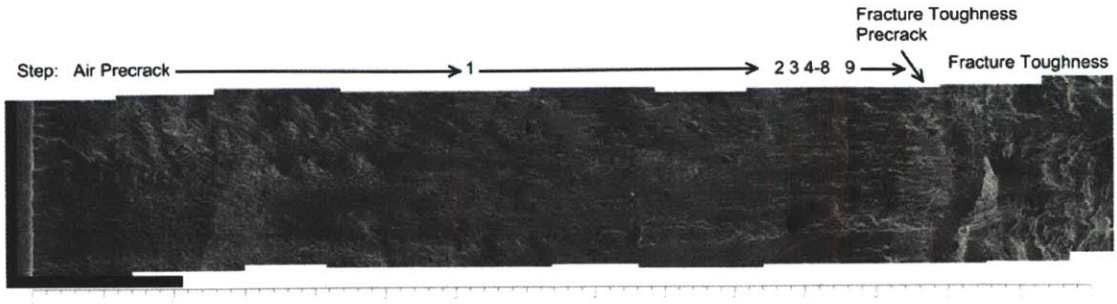

Figure A-5 SEM Micrograph montage showing crack front progression through all stages of precracking and testing

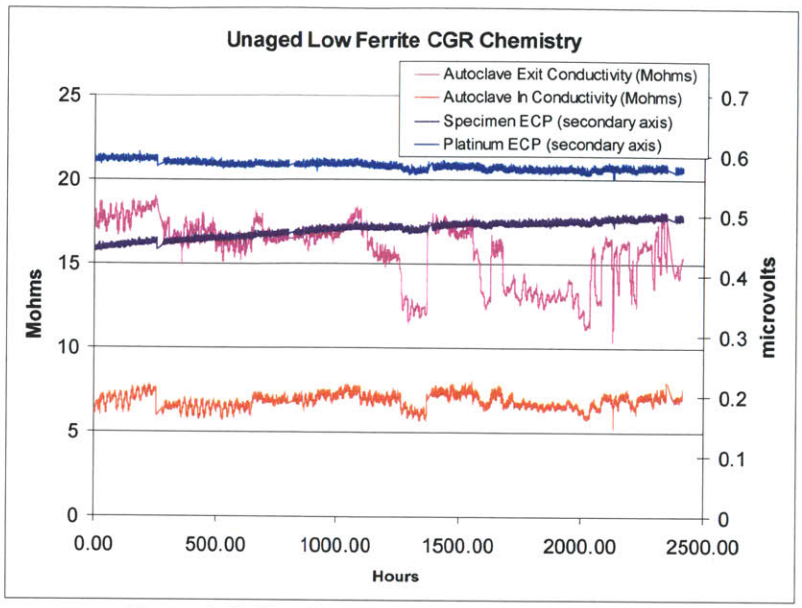

Figure A-6 Chemistry during the CGR experiment

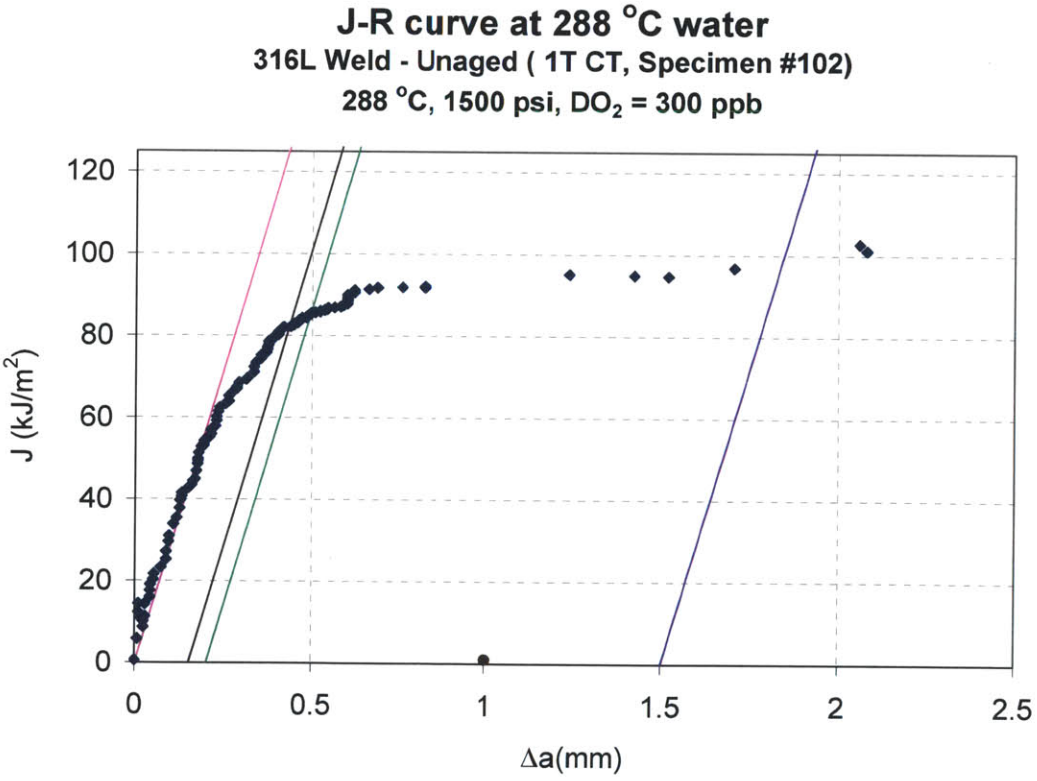

Figure A-7 J-R curve for low-ferrite, as welded material, sample 102

A.3 Low Ferrite 5,000 Hr Aged, Specimen #118

Table A-2 shows the detailed test sequence for a 5,000h aged at 400°C aged low-ferrite sample 118. Figures A-8 and A-9 show the details of the test. Figure A-10 shows optical and SEM fractographs of the fractured specimens.

Table A-2 Test Sequence for 5,000hr aged at400°C, SS316L (low delta ferrite, FN = 10) Crack Growth Specimen 118

Specimen 118 316L weld, aged (400°C, 5,000hrs)				
R	Waveform	Frequency (Hz)	Kmax (Mpa√m)	da/dt (mm/s)
0.3	sine	1	25	6.51E-05
0.5	sine	1	28	3.93E-05
0.6	sine	1	30	3.56E-05
0.7	sine	1	30	1.97E-05
0.7	sine	0.1	30	3.90E-06
0.7	sine	0.01	30	8.77E-07
0.7	sine	0.001	30	1.36E-07
n/a	const	n/a	30	7.95E-08

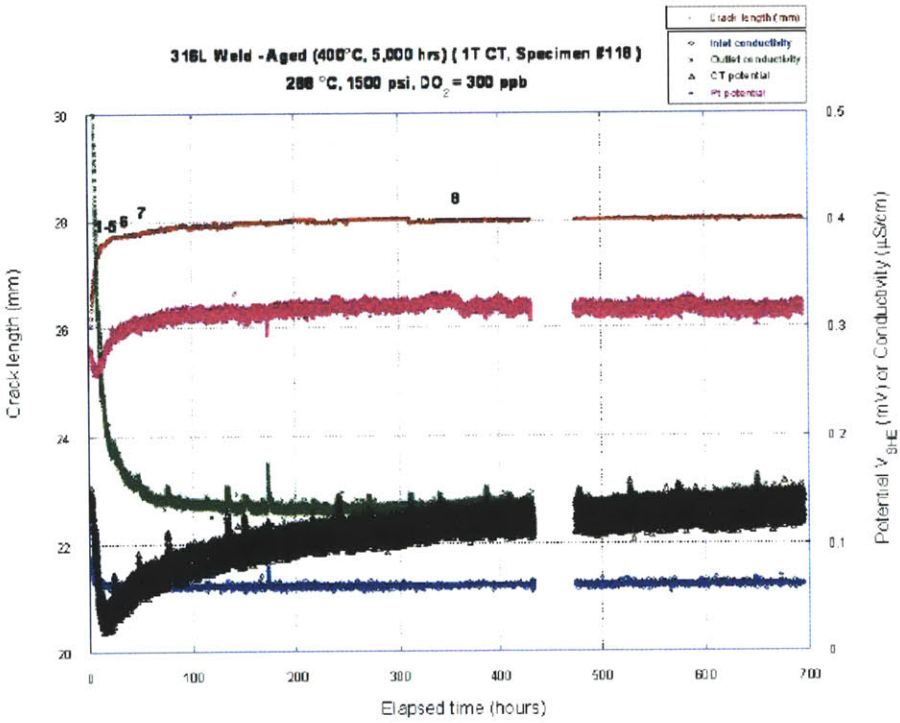

Figure A-8 Detailed test record for low-ferrite, 5,000 h aged, sample 118.

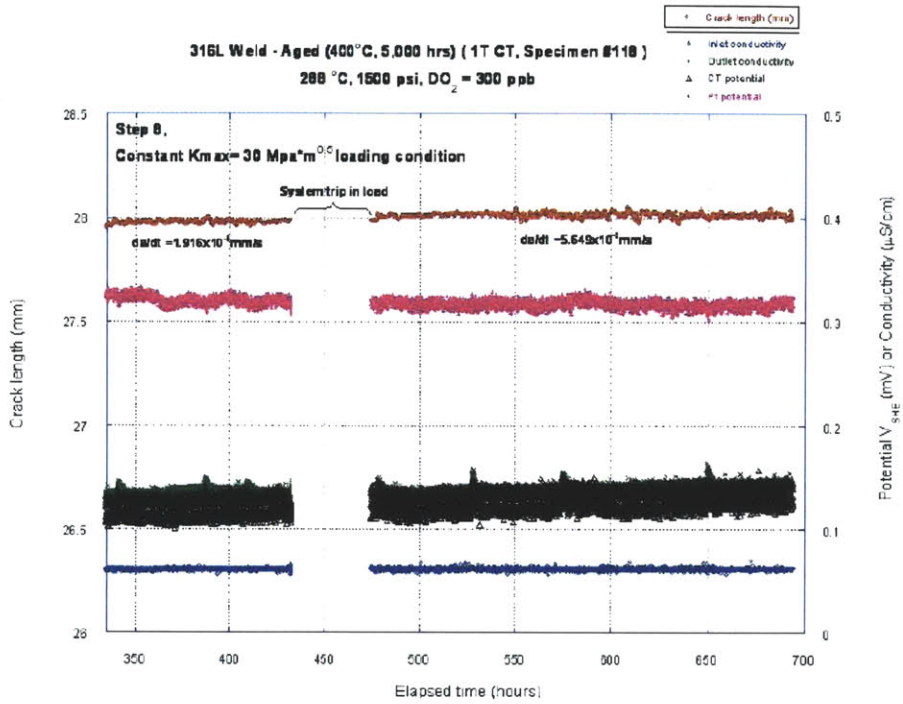

Figure A-9 Expanded test record for low-ferrite, 5,000 h aged, sample 118.

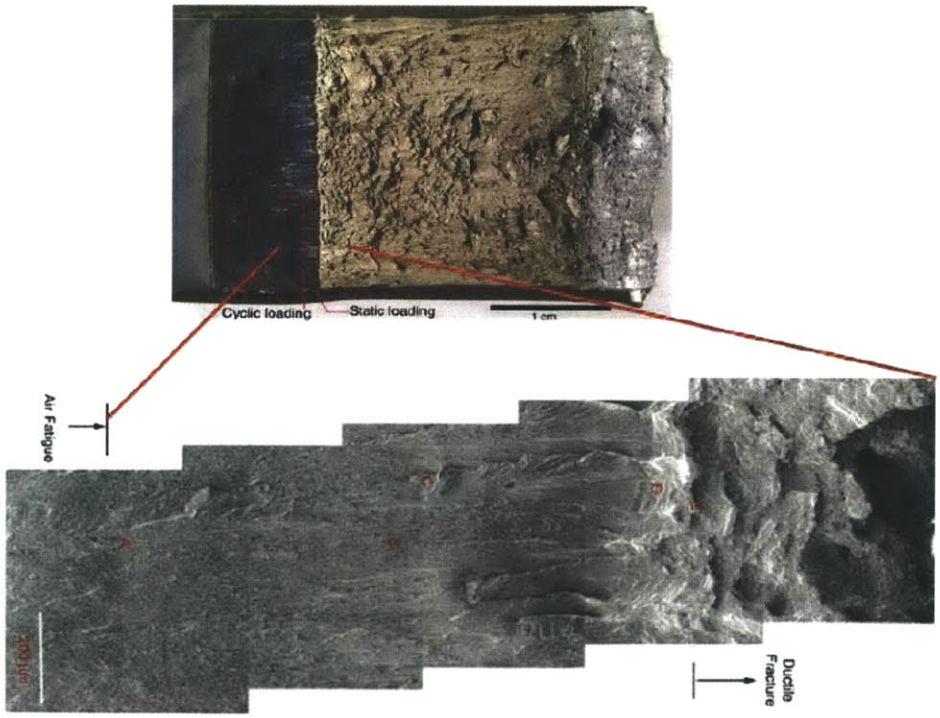

Figure A-10 Optical micrograph (upper) and SEM fractograph for low-ferrite, 5,000 h aged, sample 118 showing regions of test sequence.

A.4 Low-Ferrite 5,000 Hr Aged, Specimen 124

Table A-3 shows the detailed test sequence for low-ferrite, 5,000 h aged at 400°C material, sample 124. Figures A-11 through A-14 show the details for this test. A fracture toughness test was run at the end of the test for Specimen #124, with the J-R curve shown in Figure A-15. For this test, at the end of Step 16, the crack was grown in fatigue with load shedding until a K of 20 MPa$\sqrt{m}$ was achieved. Figures A-16 and A-17 show the fractography. The aged material exhibited a fracture toughness of approximately 150 MPa$\sqrt{m}$.

Table A-3 Test Sequence for 5,000h aged at 400°C, SS316L (low delta ferrite, FN = 10) Crack Growth Specimen 124

Step	R	Waveform	Frequency (Hz)	Hold (s)	Kmax (Mpa$\sqrt{m}$)	a/W	da/dt (mm/s)
1	0.3	sine	1	n/a	30	0.4602	6.09E-05
2	0.5	sine	1	n/a	33	0.4662	1.27E-04
3	0.6	sine	1	n/a	35	0.4722	1.12E-04
4	0.7	sine	1	n/a	35	0.4782	2.69E-05
5	0.7	sine	0.1	n/a	35	0.4822	5.92E-06
6	0.7	sine	0.01	n/a	35	0.4862	1.52E-06
7	0.7	sine	0.001	n/a	35	0.4902	2.94E-07
8	n/a	const	n/a	n/a	35	0.4905	1.00E-08
9,10	n/a	const	n/a	n/a	35	0.4962	1.89E-07
11	0.7	trapezoidal	0.001	9,000	35	0.4982	5.82E-07
12	n/a	cnst	n/a	n/a	35	0.5042	2.09E-07
13	0.7	sine	0.001	n/a	30	0.5302	4.59E-07
	n/a	cnst	n/a	n/a	30	0.5362	9.40E-08
14	n/a	cnst	n/a	n/a	30	0.5362	9.80E-08
15	0.7	trapezoidal	0.001	9,000	30	0.5382	1.78E-07
	n/a	cnst	n/a	n/a	30	0.5442	8.15E-08
16	n/a	cnst	n/a	n/a	30	0.5442	7.49E-08

(1) load ratio, P_{min}/P_{max}, (2) frequency, (3) corrected K, (4) corrected a/W after test, (5) trip in load in segment, (6) trip in temperature in segment

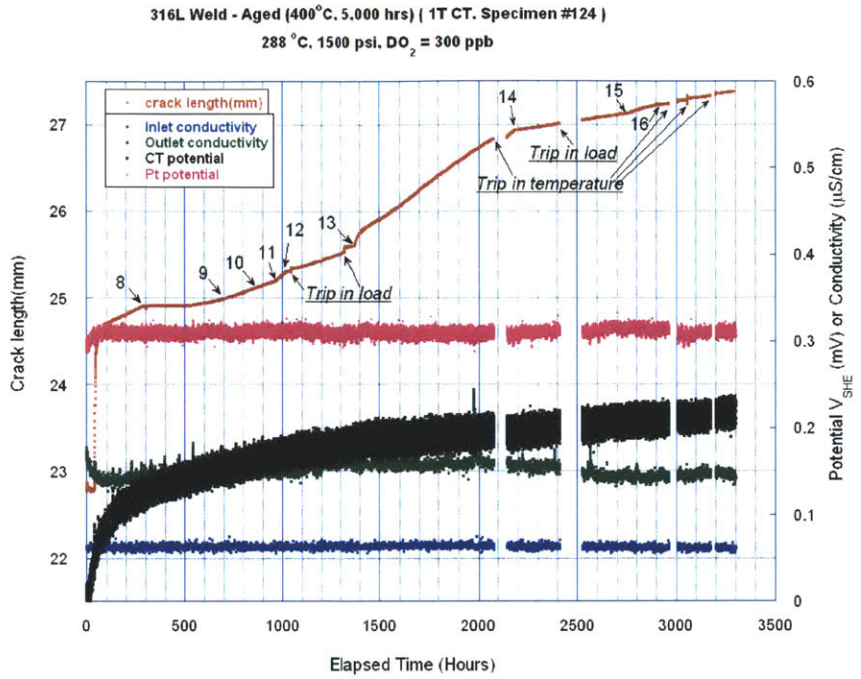

Figure A-11 Complete test sequence for 5,000 h aged at 400 °C low-ferrite 316L weld specimen 124.

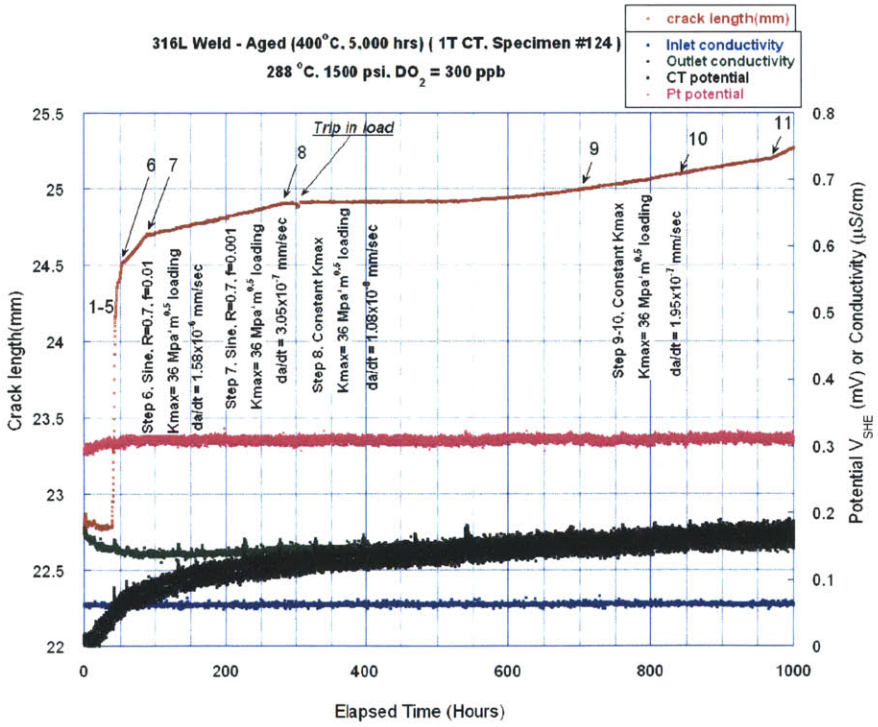

Figure A-12 Expanded initial 1,000 h of in-situ loading for 5,000 h aged at 400 °C low-ferrite 316L weld specimen 124.

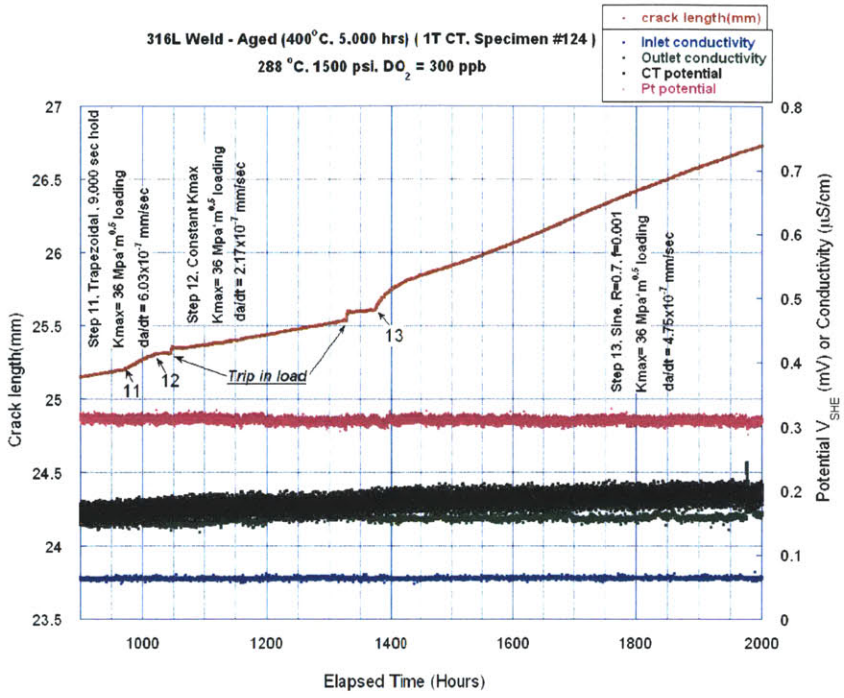

Figure A-13 Expanded second 1,000 hours for 5,000 h aged at 400 °C low-ferrite 316L weld specimen 124.

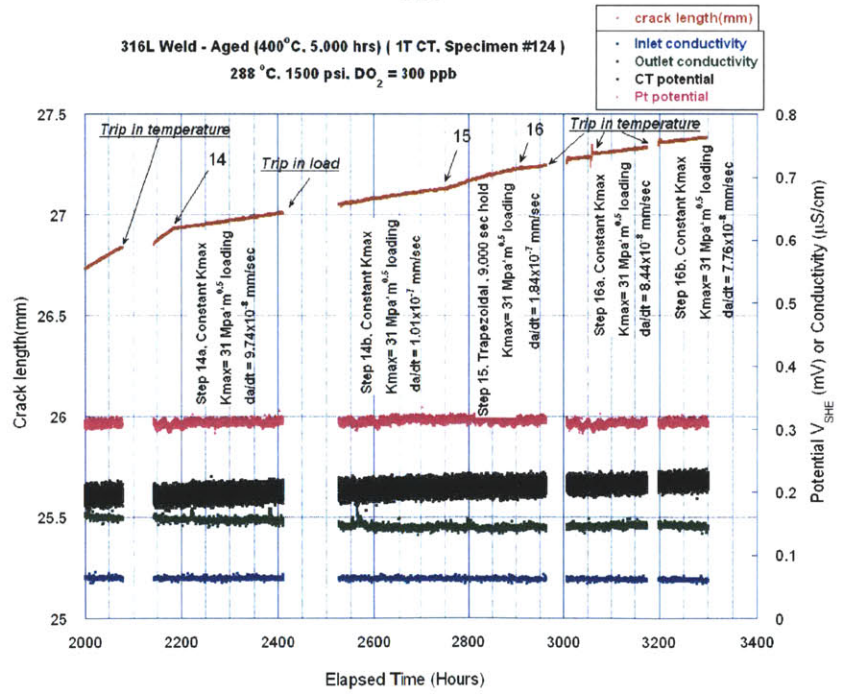

Figure A-14 Expanded third 1,000 hours for 5,000 h aged at 400 °C low-ferrite 316L weld specimen 124.

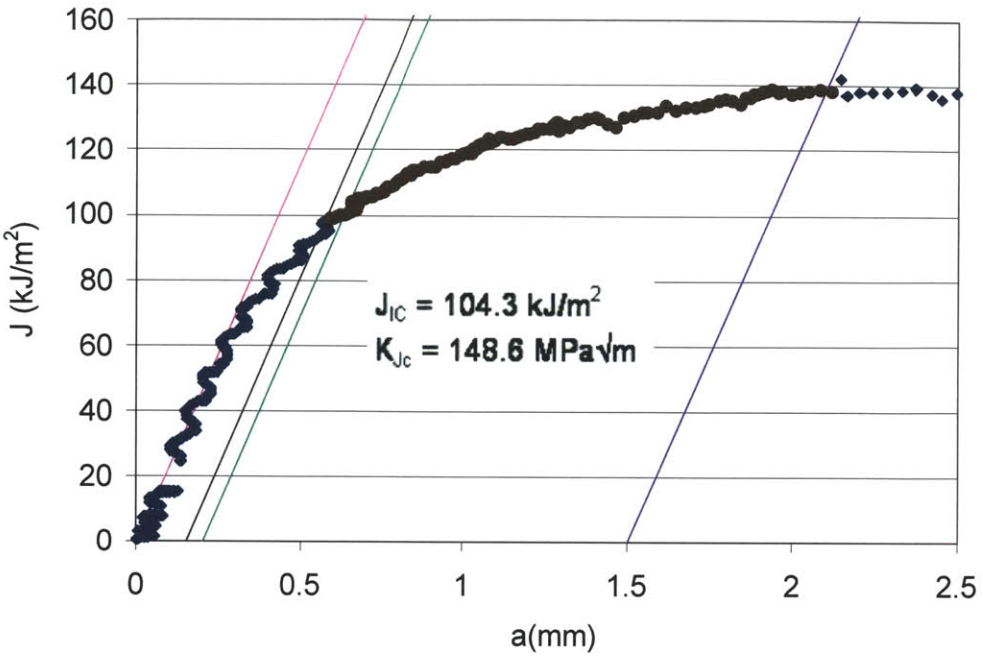

Figure A-15 J-R curve for 5,000 h aged at 400 °C low-ferrite 316L weld specimen 124.

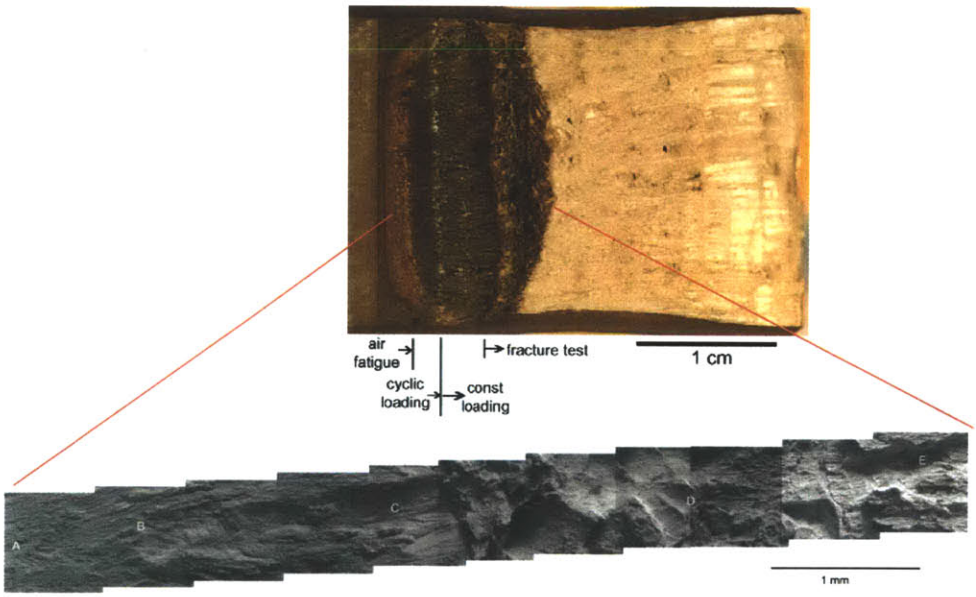

Figure A-16 Macro and SEM fractograph series for 5,000 h aged at 400 °C low-ferrite 316L weld specimen 124.

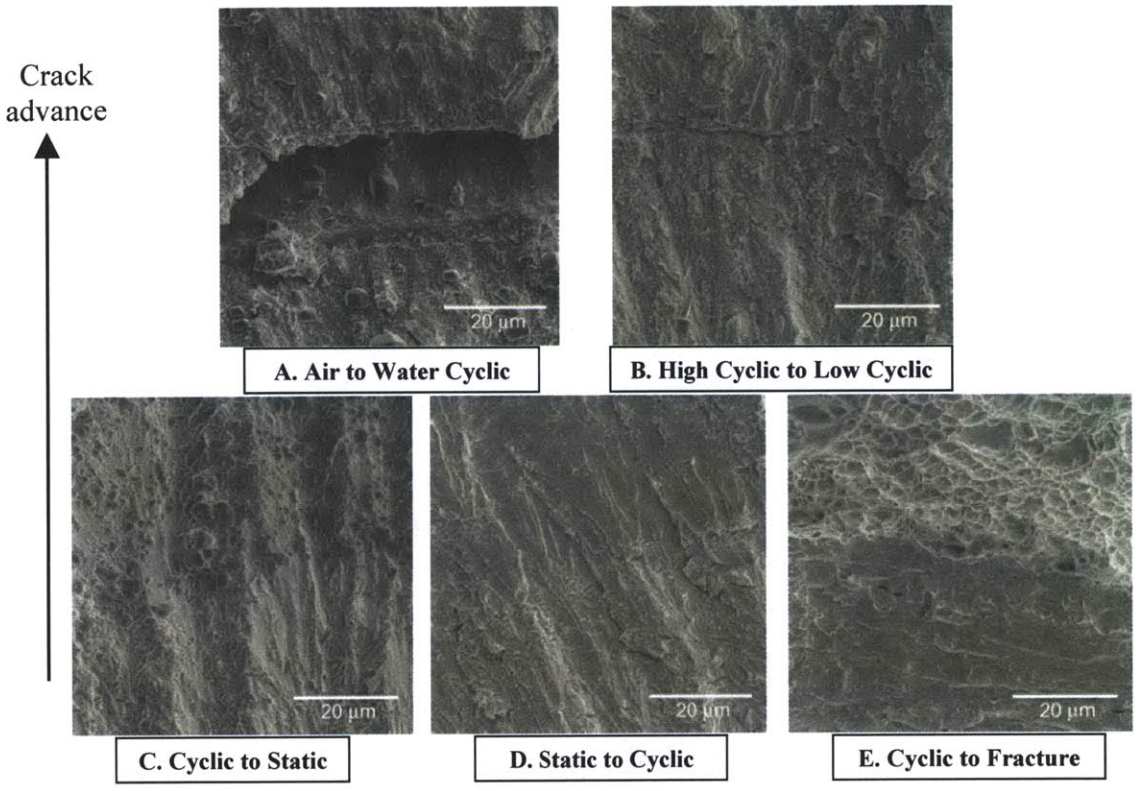

Figure A-17 Higher magnification SEM micrographs of selected regions for 5,000 h aged at 400 °C low-ferrite 316L weld specimen 124.

A.5 High Ferrite, As-Welded, Specimen # 238

Table A-4 shows the overall test plan for high-ferrite, as-welded material in sample 238. Figures A-18 and A-19 show the detailed test variable plots. In this test a valid J-R test was performed as the last step in the test program, with the plot shown in Figure A-20. However, the full test sequence that was performed lasted 8,700 hours. As a result of this the actual material condition was one in which the weld was aged at 288°C for 8,500 hours before the J-R test. Figure A-21 shows a montage of the fracture surface with the locations of each test step identified. The test sequence was designed such that the uncracked ligament remaining at the start of the fracture toughness measurement satisfied the requirements of ASTM E-1820-01. Prior to this test, a reference correlation between

COD and machine stroke was determined. During the test the correlation was used to transform stroke data to load line displacement. The J-R curve was then determined according to ASTM E 1820-01, Appendix A2.4.2.2. The results of the test indicate that the as-welded material has an approximate toughness value of 175 Mpa$\sqrt{m}$. This value represents a significant reduction in resistance to unstable crack propagation. Also, it should be noted once again that while the material discussed thus far are technically unaged, in actuality these materials are aged at 288°C for the duration of their particular test. Thus, Specimen # 238 was aged at 288°C for 8,700 hours prior to the toughness test.

Table A-4 Test sequence for the high-ferrite, as-welded material in sample 238.

Steps	Frequency (Hz)	Waveform	Hold Time (s)	Kmax (MPa$\sqrt{m}$)	R	a/W	da/dt (mm/s)
1	1	sine	n/a	25	0.3	0.4598	5.63E-05
2	1	sine	n/a	27	0.5	0.4658	4.47E-05
3	1	sine	n/a	30	0.6	0.4718	3.22E-05
4	1	sine	n/a	30	0.7	0.4778	1.97E-05
5	0.1	sine	n/a	30	0.7	0.4818	3.92E-06
6	0.01	sine	n/a	30	0.7	0.4858	6.66E-07
7	0.001	sine	n/a	30	0.7	0.4898	1.57E--7
8		cnst	n/a	30	0	0.4958	2.70E-08
9	0.001	trap	9000	30	0.7	0.4978	
10		cnst	n/a	30	0	0.5038	2.70E-09
11	0.001	sine	n/a	32	0.7	0.5078	
12		cnst	n/a	35	0	0.5138	5.50E-09
13	1	sine	n/a	35	0.3	0.53878	
14		cnst	n/a	9.6	0	0.9	1.60E-08

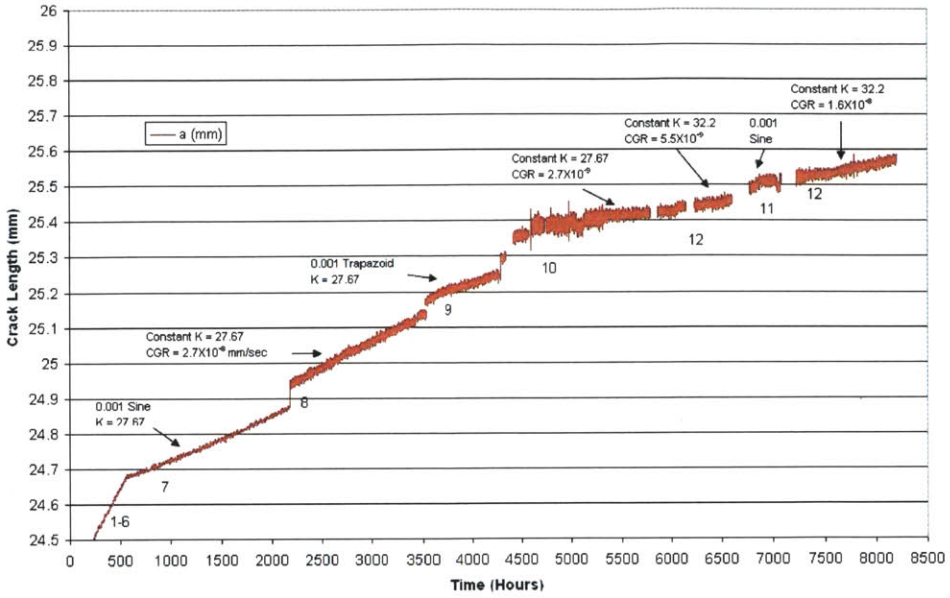

Figure A-18 Detailed test record for the high-ferrite, as-welded material in sample 238.

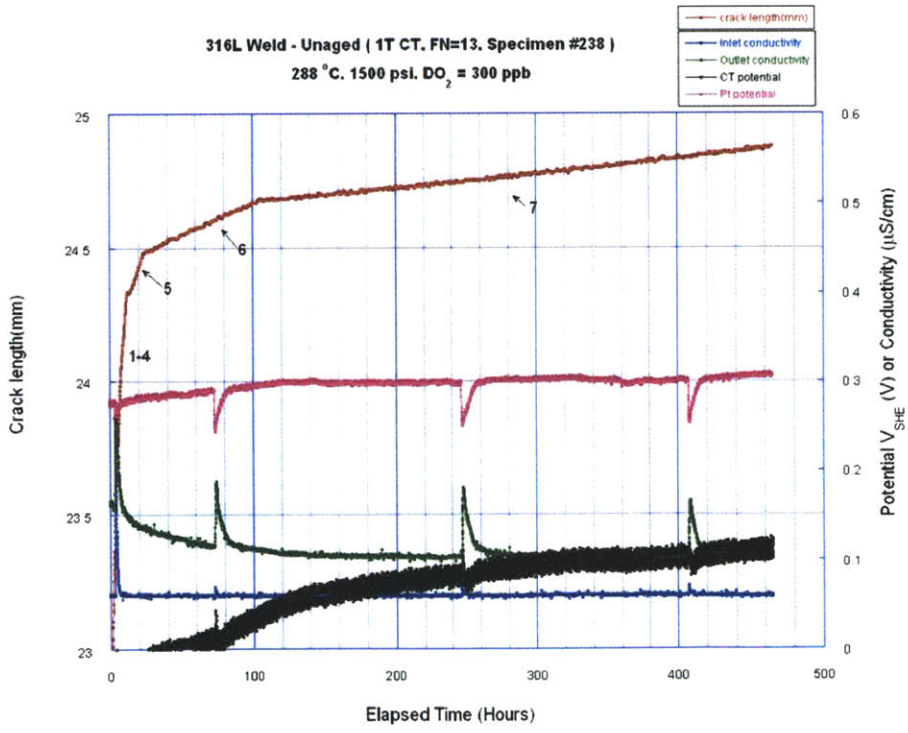

Figure A-19 Detailed test record for the high-ferrite, as-welded material in sample 238 for first part of test.

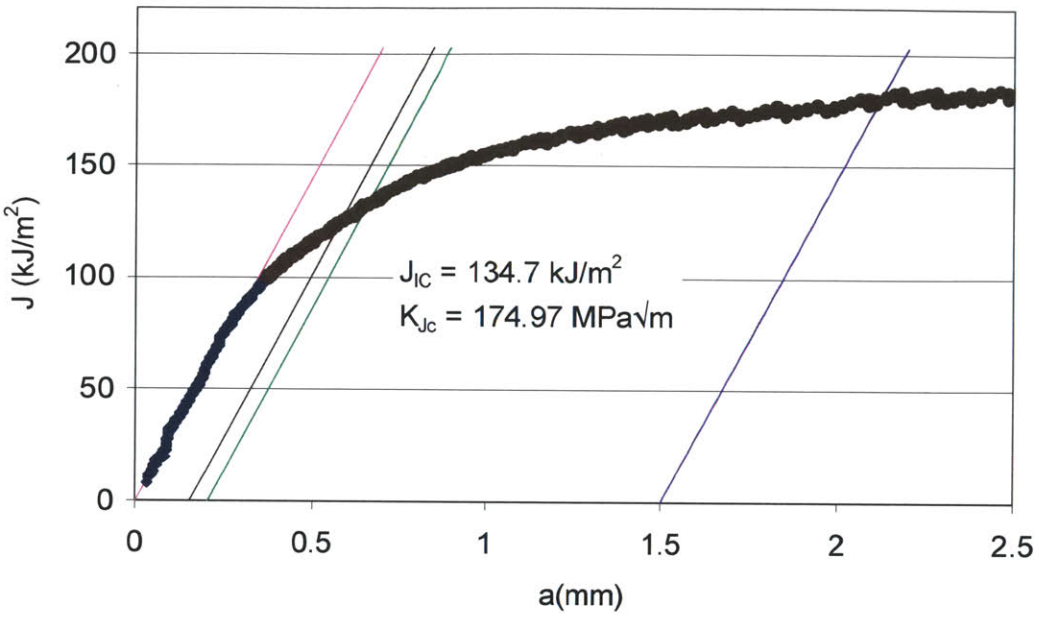

Figure A-20 J-R curve for the high-ferrite, as-welded material in sample 238.

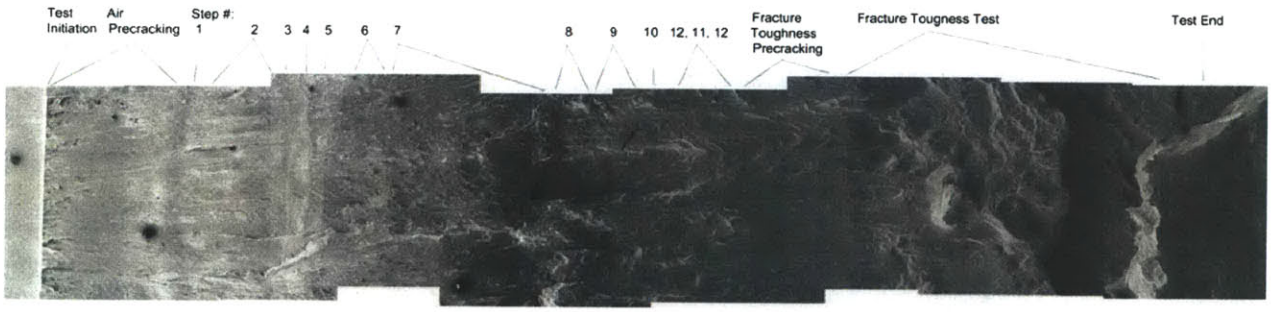

Figure A-21 Fracture montage for the high-ferrite, as-welded material in sample 238.

A.6 High-Ferrite, 5,000 h Aged at 400°C, Sample 167

The final specimen, sample 167, is a high-ferrite 400°C 5000 hr aged sample. The sample spent approximately 600 hours at BWR temperature pressure and chemistry prior to starting the actual test summarized in figures A-22 and A-23. The delay was due to DAQ program upgrades. Figure A-22 shows the stable SCC area with a stress intensity of 32 MPa$\sqrt{m}$ and a sustained CGR of 6.5 X 10^{-8} mm/s. The areas with no data represent portions where computer problems occurred. Crack growth rate is steady. Furthermore, there was only 1 inadvertent shutdown and cool down although there have been occasions where data was not being taken due to DAQ system malfunctions. Specimen

#167 was completed with an in-situ fracture toughness test, with the J-R curve shown in Figure A-24. The results of the fracture toughness test are a J of 106 KJ/m^2 and a K value of 143 MPa/√M.

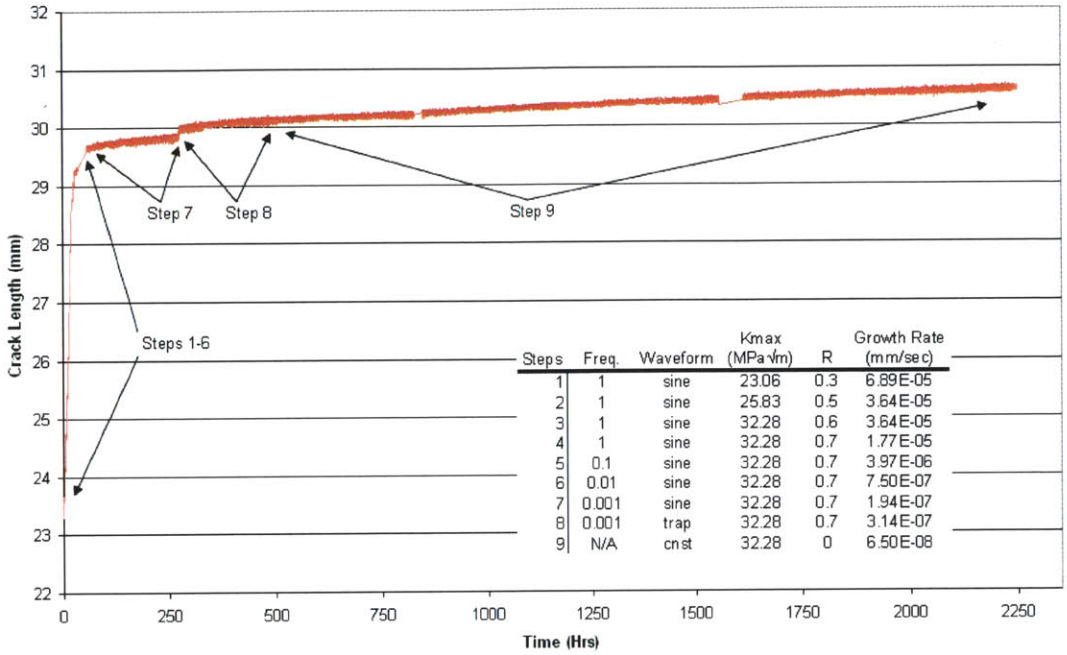

Figure A-22 Summary of SCC crack growth rate data for the high-ferrite 5,000 h aged at 400°C material in sample 167.

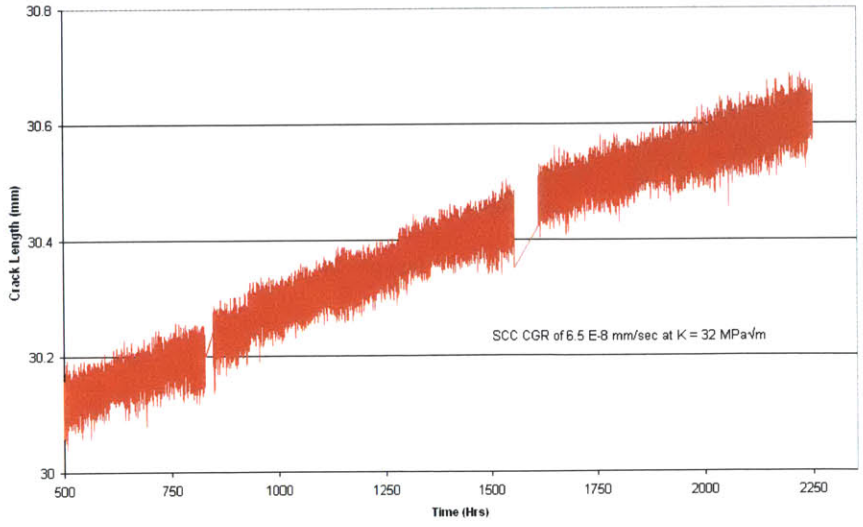

Figure A-23 SCC portion of in-situ testing for the high-ferrite 5,000 h aged at 400°C material in sample 167.

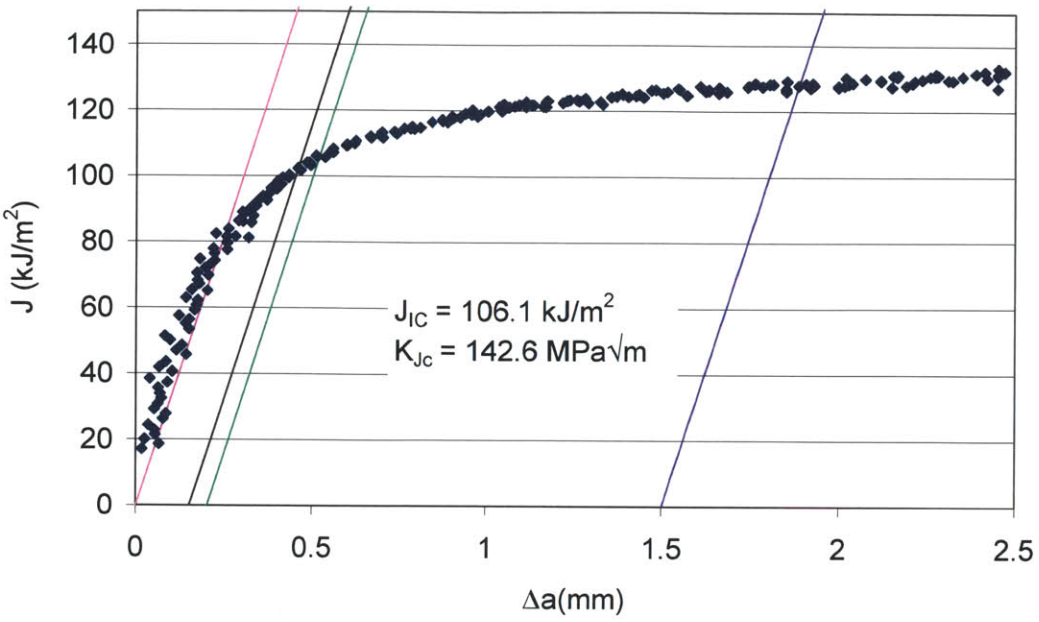

Figure A-24 J-R curve for the high-ferrite 5,000 h aged at 400°C material in sample 167.

A.7 Fracture Toughness Results

Fracture toughness evaluations have been completed on high- and low- ferrite material aged at 400°C samples for both room temperature (25°C) and 288°C in air. Where applicable, these results are then compared to the in-situ testing of high and low ferrite welds at 288°C, 300ppb O_2 after more than 2000 hr exposure in the environment. The fracture toughness measurement was performed using DCPD and in accordance with ASTM 1820-01. All results are shown in the main body of the thesis. Figures A-25 shows an example J-R curve for low-ferrite, as-welded material tested in air at 288°C. The strain rate was .15 mm/min.

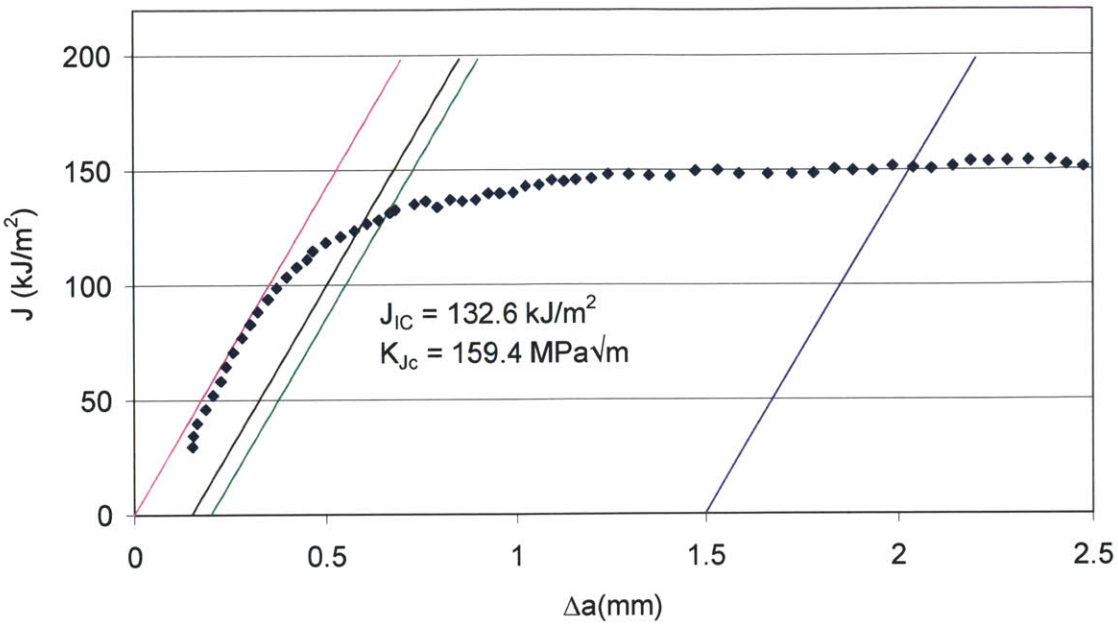

Figure A-25 A sample fracture toughness J-R curve for low-ferrite, as welded material in sample 92, tested at 288°C in air.

A.8 Anomalous J-R Behavior

There was one particular test that showed anomalous behavior and as a result was not considered a valid fracture toughness test under ASTM 1820-01. Sample #234 is a high ferrite sample aged 5,000 h at 400°C and tested in air at 25°C. The test seemed to proceed as normal, however at approximately 0.75 mm crack extension after the sample reached stable tearing the load began to increase significantly. This resulted in a second, yet non-standard, fracture point. Following this anomaly, the sample returned to a normal stable tearing mode. The actual material cause for this is not known. This does, however, illustrate the difficulty with weld characterization based on the inhomogeneity of the material. Figure A-26 shows the J-R curve for this test.

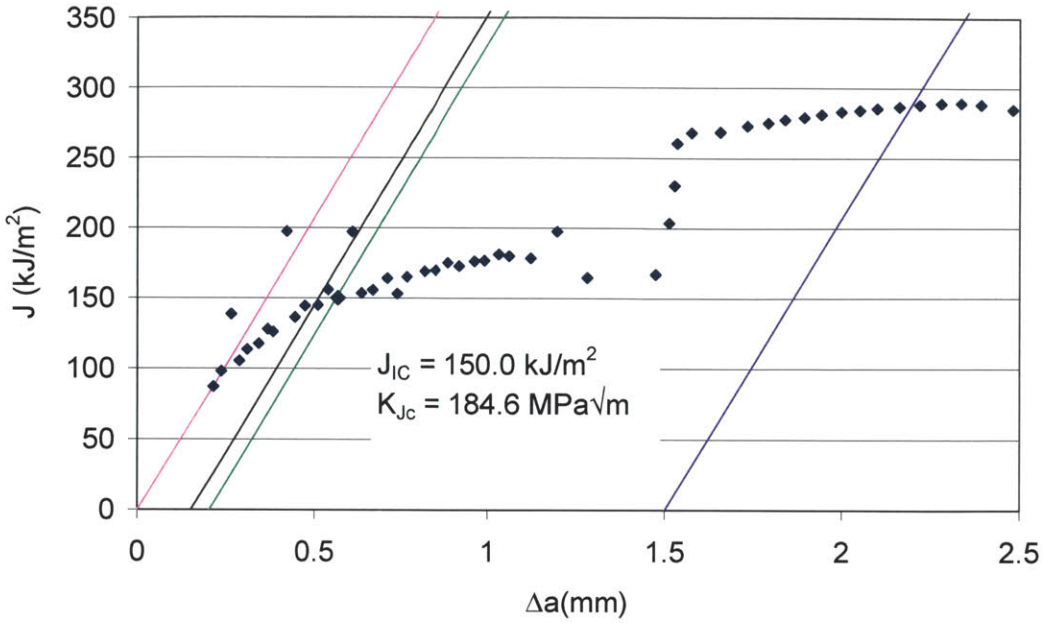

Figure A-26 J-R curve showing anomalous fracture behavior in 5,000 h aged at 400°C, high-ferrite material.

Appendix B Derivation of eq. 6-6 and eq. 6-30

B.1 Oxide Films

The difference in oxide deposition on the fracture surface between cyclic fatigue loading and static SCC loading is striking. Clearly there is an important process occurring that can serve as an agent for a better description of the crack tip In Figure 5-36 it is evident that when switching loading patterns from static to cyclic, there needs to be a few cycles before changing oxide precipitation. This indicates the environment flow to the crack tip is the source. Beginning with a general half cell equation which describes the oxidation process [33]:

$$aA + mH^+ + ne^- = bB + dH_2O \qquad \text{[B-1]}$$

The potential e of the reaction above is found through the Nernst equation:

$$e = e^o - 2.303\frac{RT}{nF}\log\left[\frac{(A)^a(H^+)^m}{(B)^b(H_2O)^d}\right], \qquad \text{[B-2]}$$

where: e is reaction potential
e^0 is the standard potential
e^- is an exchange electron or equivalent
R is the gas constant
T is the absolute temperature
n is number of electrons exchanged
F is Faraday's constant, 96,500 coulombs per electron
(A) is the activity of product species A
a is the number of reactants A
(H^+) is the activity of hydrogen
(B) is the activity of product species B
b is the number of reactants B
(H_2O) is the activity of water
d is the number of water molecules

For the reaction of interest,

$$4H^+ + O_2 + 4e^- \longleftrightarrow 2H_2O \qquad \text{[B-3]}$$

Inserting eq. B-3 into B-2:

$$e = e_0 - 2.303\frac{RT}{4F}\log\left[\frac{(H_2O)^2}{(O_2)(H^+)^4}\right] \qquad \text{[B-4]}$$

Solving for a temperature of 561K which is 288°C, and inserting the constants gives:

$$e = 1.0V - \frac{0.1114}{4}\log\left[\frac{(H_2O)^2}{(O_2)(H^+)^4}\right] \qquad \text{[B-5]}$$

It is known that:

$$pH = -\log(H^+) \qquad \text{[B-6]}$$

Next inserting eq. B-6 and the concentration of H_20 as equal to 1, eq. 6.5 can be reduced to:

$$e = 1.0V - 0.1114pH + 0.0279\log(O_2) \qquad \text{[B-7]}$$

This gives an expression for the reaction potential in terms of *pH* and oxygen concentration. Oxygen concentration is then expressed in atmospheres with 1 atm O_2 = 20,000 ppb O_2.

In SCC, it is assumed that the system has become deaerated, now eq. B-7 is expressed as:

$$e = -0.1114pH, \qquad \text{[B-8]}$$

which is the expression for the hydrogen line in Figure B-1.

In order to quantify the pumping importance geometrically, consider first calculation the volume of the inside of the crack, shown schematically in Figure B-1.

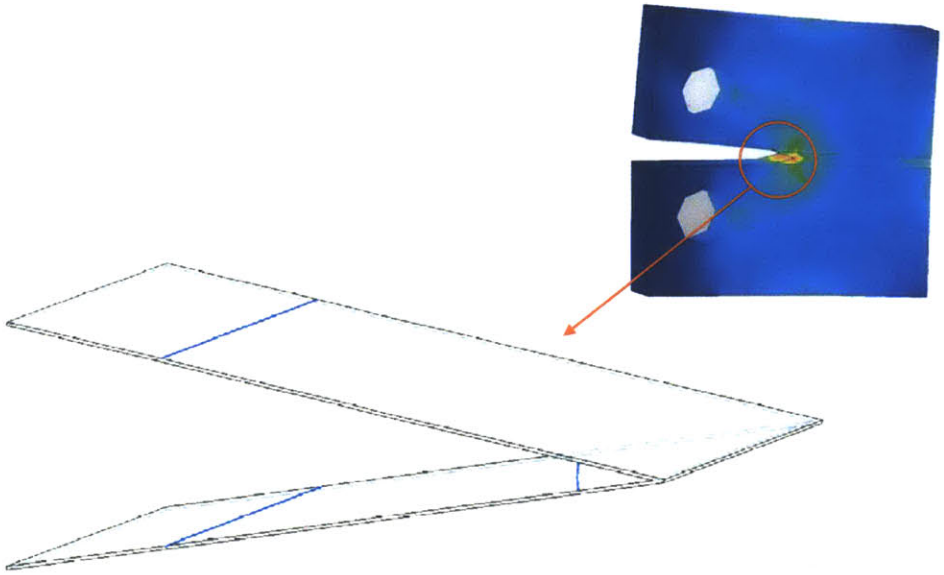

Figure B-1 Exaggerated loading applied to 1T-CT specimen geometry, crack tip opening is shown as a triangular volume.

First consider the load line displacement, measured along the vertical axis of the center of the holes for the clamps which hold the sample. This is shown in Figure B-2.

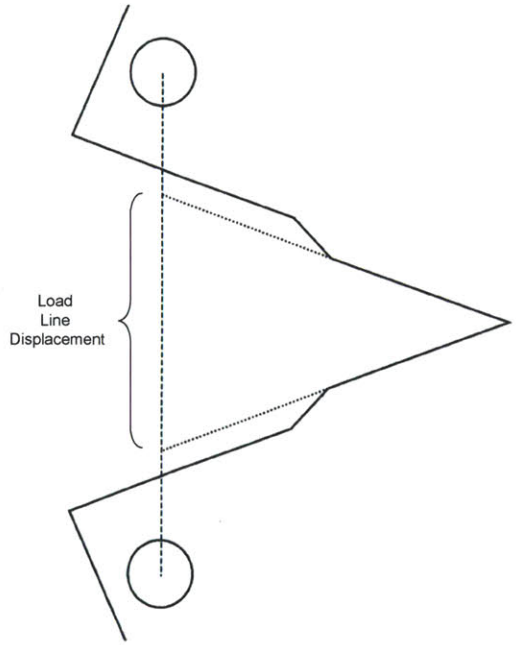

Figure B-2 Schematic of load line displacement, exaggerated for clarity.

In the following diagram, the final area to be calculated is shown, Figure B-3.

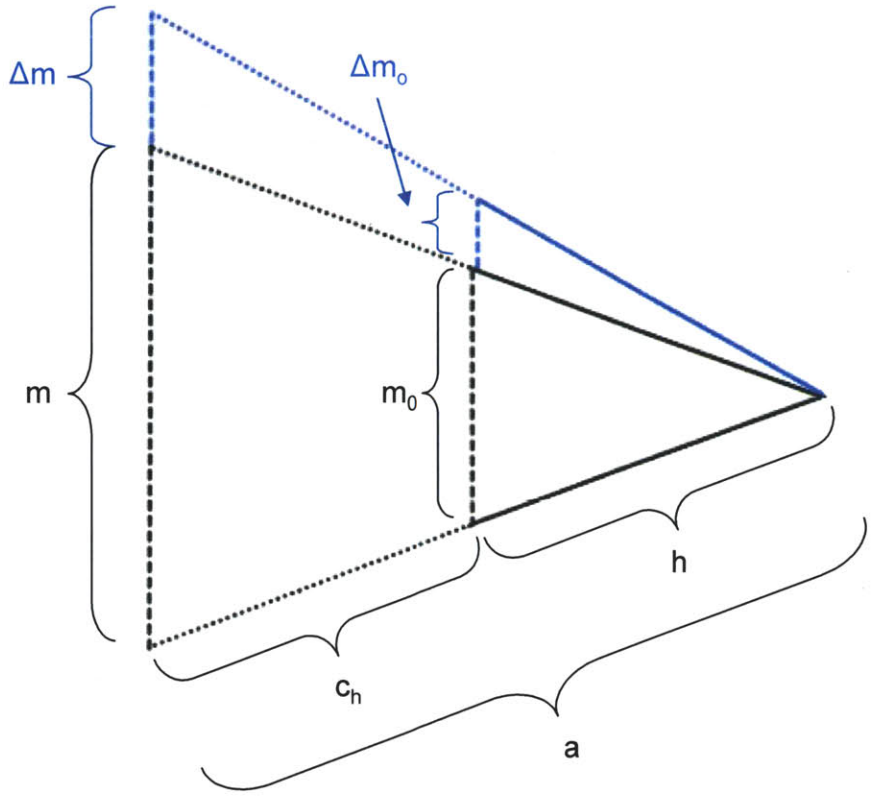

Figure B-3 Triangular schematic representation of load line displacement effect on crack tip geometry.

Defining all of the labels:

a is the overall crack length
c_h is the length past the mouth of the actual crack
h is the actual crack length
m is the load line displacement
Δm is the small change in load line displacement applied in fatigue
m_0 is the actual crack mouth displacement
Δm_0 is the small change in actual crack mouth displacement applied in fatigue

Knowing that the sample has a thickness b, then everything that is needed is now defined to calculate the volume of the actual crack based on crack length and load line displacement and is easily done geometrically.

Since m is very small for the sample geometry, it can be assumed that a and h are representative of the heights of the triangles. This approximation is only valid for $m/a \ll 1$.

Beginning with similar triangles, it is evident that:

$$\frac{m_0}{h} = \frac{m}{a} \qquad \text{[B-9]}$$

and:

$$h = a - c_h \qquad \text{[B-10]}$$

Solving for m_o yields:

$$m_0 = \frac{m(a - c_h)}{a} \qquad \text{[B-11]}$$

Volume of the crack interior, V_0, can then be calculated by:

$$V_0 = \frac{1}{2} h m_0 b \qquad \text{[B-12]}$$

Inserting eq. B-11 into B-12 gives:

$$V_0 = \frac{1}{2}\frac{m}{a} b(a - c_h)^2 \qquad \text{[B-13]}$$

Similarly the additional volume created by cyclic fatigue, Δm, is:

$$\Delta V_0 = \frac{1}{2}\frac{\Delta m}{a} b(a - c_h)^2 \qquad \text{[B-14]}$$

Next, it is relevant to know how the chemistry inside the crack changes with fatigue. Now that the volume and the volume exchange are known, therefore the impact of the addition of dissolved oxygen can be found. For a first approximation, consider a simple static solution-dilution problem after one complete fatigue cycle, expressed as:

$$\Delta V_0 C_b + V_0 C_0 = (V_0 + \Delta V_0) M_f C_1, \qquad \text{[B-15]}$$

where: C_b is the oxygen concentration in the bulk
M_f is the mixing fraction
C_0 is the initial concentration in the crack volume
C_1 is the concentration in the crack volume following one fatigue cycle

In this simplification of the dynamics of mixing, the mixing fraction, M_f, is a substitute for the driving force required for the dissolved oxygen to reach the crack tip. Thus, the higher the value of M_f then the farther into the crack the oxygen has to diffuse to have an impact.

Solving for C_1 yields:

$$C_1 = \frac{\Delta V_0 C_b + V_0 C_0}{(V_0 + \Delta V_0) M_f} \qquad \text{[B-16]}$$

Substituting eqs. B-13 and B-14 and simplifying yields

$$C_1 = \frac{\Delta m C_b + m C_0}{(m + \Delta m) M_f} \qquad \text{[B-17]}$$

To simplify formulation, it is convenient to introduce k where:

$$k = M_f \left(1 + \frac{m}{\Delta m}\right) \qquad \text{[B-18]}$$

Substituting eq. B-18, and generalizing for any number of fatigue cycles N, equation B-17 becomes:

$$C_{N+1} = C_N + \frac{C_b + C_N}{k} \qquad \text{[B-19]}$$

which can be shown to have the solution:

$$C_N = C_b \left[1 - \left(\frac{k-1}{k}\right)^N\right] \qquad \text{[B-20]}$$

which converges to $C_N = C_b$ as $N \rightarrow \infty$, which is correct for the system.

Recalling that 1 atm O_2 = 20,000 ppb O_2, and introducing the conversion:

$$C_{ba} = \frac{C_b}{20{,}000} \qquad \text{[B-21]}$$

Replacing k, and inserting eqs. B-19 and B-20 into eq. B-7 from above gives the analytical expression:

$$e_N = 1.0V - 0.1114pH + 0.0279 \log\left\{C_{ba}\left[1 - \left(1 - \frac{\Delta m}{M_f(\Delta m + m)}\right)^N\right]\right\} \qquad \text{[B-22]}$$

where: e_N is the potential after N cycles of fatigue.

B.2 Dendrite Cell Simplification

First consider that there are two phases and an interphase region in the weld metal. The first phase is the δ-ferrite phase. The second phase is the austenite. The interphase region is the δ-ferrite boundary containing the chromium-rich carbides. Also there is a lighter etched area in Figure 5-22, that is electrochemically different, as shown by the preferential etching, this indicates that the region is cathodic compared to the anodic δ-ferrite. Anymore information than this about the lightly etched region is not needed. It is just assumed that this region exists with in a radius R_C, and outside of this radius, there is no longer an effect. This is shown in Figure B-4 below. Figure B-4 will serve as the starting point for the critical discussion on the effect of ferrite number, or the more useful volume percent, on SCC.

Consider that the secondary dendrite arms have a length and width, which can be measured and averaged, L_δ and W_δ, respectively. These are a function of the chemistry and cooling rate. Furthermore, the δ-ferrite core is surrounded by the cathodic area with radius R_C, and then by austenite beyond the lightly etched areas. Since the dendrites exist in a periodic manner, dictated by cooling rate and chemistry, a simplified square unit cell can be defined having a length on one side of X. Finally, assume that the relation of R_C to the δ-ferrite arm spacing can be expressed through a constant B, which is also dictated by chemistry and cooling rate. Thus: L_δ, W_δ, R_C and B are functions of cooling rate and

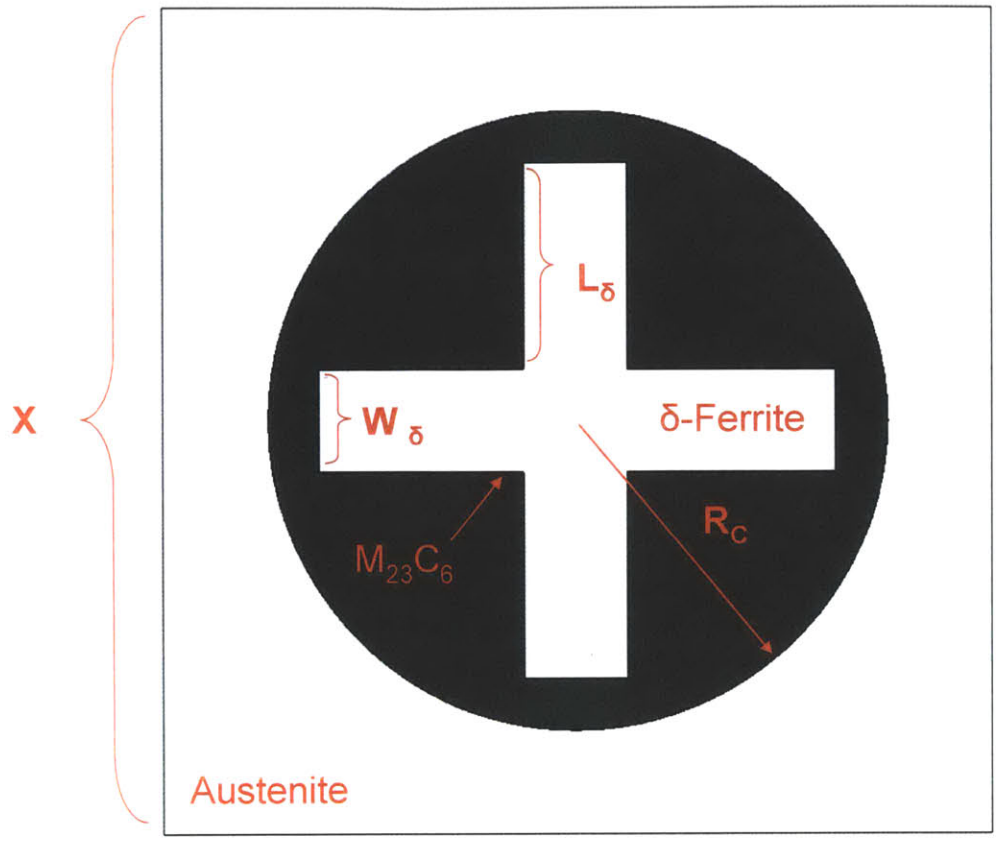

Figure B-4 Diagram of parameters used in calculated geometric effects of a two phase system on SCC.

chemistry. For the purpose of this discussion, the function is assumed complex enough to not be discussed, but instead, measured values of these parameters will be substituted as needed. Defining the system mathematically is an exercise in simple geometry. Beginning with area arguments:

$$A_T = X^2 \qquad \text{[B-9]}$$

$$A_\delta = 4L_\delta W_\delta \qquad \text{[B-11]}$$

$$A_C = \pi R_C^2 - A_\delta \qquad \text{[B-12]}$$

$$A_\gamma = X^2 - \pi R_C^2 \qquad \text{[B-13]}$$

$$R_C = B(L_\delta + .5W_\delta) \qquad \text{[B-14]}$$

where: A_T is the total area

A_δ is the area of the δ-ferrite
A_C is the area of cathodic region
$A\gamma$ is the area of the austenite outside the cathodic region

and it is assumed in eq. B-10, that $W_\delta^2 << A_\delta$.

Next it is helpful to describe each phase in terms of the volume fraction of that phase. However, since the consideration is only for a two dimensional surface, and there is no change over the length of the volume, volume fraction will be the same as an area fraction. So each phase will be given an area fraction, α, which for this purpose will be considered the same as the volume fraction. This will allow the expressions of interest to be shown as functions of the area fraction, particularly of the δ-ferrite, since that is one of the key variables in this study. The defining area equations are:

$$\frac{A_\delta}{A_T} = \alpha_\delta \qquad \text{[B-14]}$$

$$\frac{A_C}{A_T} = \alpha_C \qquad \text{[B-15]}$$

$$\frac{A_\gamma}{A_T} = \alpha_\gamma \qquad \text{[B-16]}$$

where: α_δ is the area fraction of the δ-ferrite
α_C is the area fraction of the austenite acting as the cathodic region
α_γ is the area fraction of the austenite outside the cathodic region.

Substituting eq. B-14 into eq. B-9 and solving for X gives the length of the unit cell, or the spacing of the dendrites as a function of α_δ and A_δ.

$$X = \sqrt{\frac{A_\delta}{\alpha_\delta}} \qquad \text{[B-17]}$$

There is a scenario of interest that will be discussed - the point where the secondary ferrite arms touch. The relationship is developed and expressed as functions of α_δ. The point when δ-ferrite arms touch, making a continuum of ferrite is of interest because it should roughly predict where the change of solidification mode from FA to F occurs. This provides some validation to the simplified model presented here. In order for the δ-ferrite arms to touch:

$$2L_\delta = X \qquad \text{[B-18]}$$

Inserting eq. B-17 into eq. B-18:

$$2L_\delta = \sqrt{\frac{A_\delta}{\alpha_\delta}} \qquad \text{[B-19]}$$

and solving for α_δ:

$$\alpha_\delta = \frac{W_\delta}{L_\delta} \qquad \text{[B-20]}$$

Finally, in order to provide some validation to the simple model, we can see that our assumption of $W_\delta^2 << A_\delta$ is true from common values measured for L_δ, W_δ and B, shown in Table B-1. Further validation comes in the accurate prediction of the change from FA to F solidification modes. This is predicted from eq. B-20 as occurring around 25% δ-ferrite, and indeed this is where the WRC-92 welding diagram predicts the transition, as shown in Figure 3-5. The final model validation is the accurate prediction of dendritic spacing, which is predicted as 15 to 20 μm for the range of FN in this study, and this matches measured values from SEM metallography. The simple geometrical arguments made above will help in showing the impact of FN on SCC.

Table B-1 Common measured values used in calculating δ-ferrite area.

Parameter	Value
L_δ	4 μm
W_δ	1 μm
B	1.2

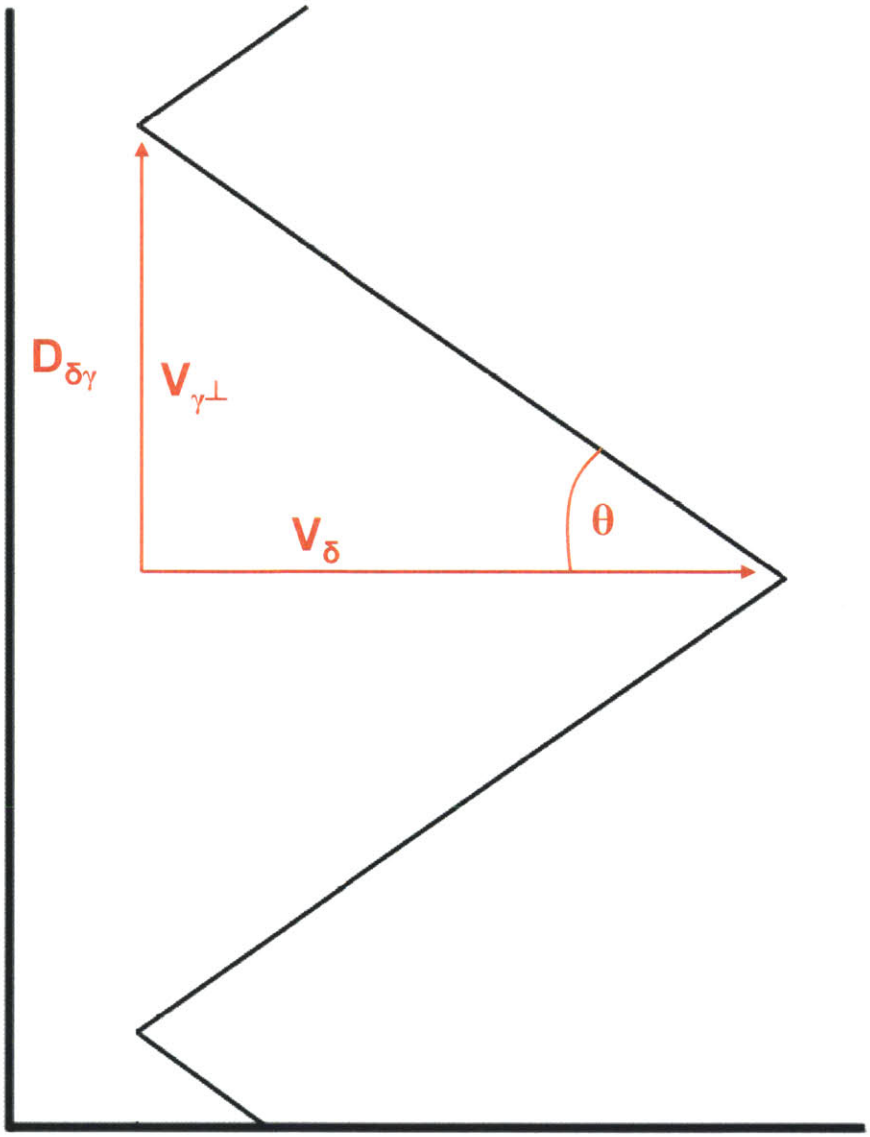

Figure B-5 Geometric representation of fully developed crack front in a two phase system.

Figure B-5 is focusing on just one of the triangles created during fully developed SCC. The four parameters shown describe the physical situation at the crack front. First, V_δ is the crack growth rate of the δ-ferrite phase boundary. Since this is limited, as discussed above, it is moving with the same relative rate as the average crack growth front, and so it can also describe the overall crack growth rate. $V_{\gamma\perp}$ is the crack growth rate of the austenite in the perpendicular direction. These two vectors are linked by angle θ, which is defined crystallographically as a preferred slip plane in FCC austenite. The final quantity, $D_{\delta\gamma}$ represents the distance between the dendrite cores and the center of the austenite, which is also the dendrite boundary, where another dendrite begins.

The goal of the following derivation is to find V_δ in terms of α_δ. Beginning with the velocity $V_{\gamma\perp}$:

$$V_{\gamma\perp} = \frac{D_{\delta\gamma}}{\Delta t} \qquad \text{[B-21]}$$

where: Δt is the time that it takes to transverse the distance, $D_{\delta\gamma}$.

Expressing $D_{\delta\gamma}$ in terms of α_δ is straight forward. However, Δt takes more manipulation. Assume that the time it takes to transverse the $D_{\delta\gamma}$ is controlled by the stress intensity factor of the applied stress intensity to fracture toughness, a factor accounting for the number of triangles in a sample, the corrosion current and material and mechanistic unknowns. The time Δt can then be expressed as the proportion:

$$\Delta T \propto = \frac{nK_{IC}}{C_M K_I i_C} \qquad \text{[B-22]}$$

where: C_m is the mechanistic constant describing unknown differences in the material, it has units of (mm^2-s^2/C)
n is the factor accounting for the number of triangles in a sample
K_I is the stress intensity factor
K_{IC} is stress intensity based fracture toughness
i_C is the corrosion current.

The parameter n is related to the width of the sample, b, by:

$$n = \frac{b}{2D_{\delta\gamma}} \qquad \text{[B-23]}$$

Combining eqs. B-22 and B-23 gives:

$$\Delta T \propto \frac{bK_{IC}}{2D_{\delta\gamma} C_M K_I i_C} \qquad \text{[B-24]}$$

Inserting eqs. B-24 into B-23 provides:

$$V_{\gamma\perp} \propto \frac{2D_{\delta\gamma}^2 C_M K_I i_C}{bK_{IC}} \qquad \text{[B-25]}$$

Geometrically it is intuitive that $D_{\delta\gamma}$ is related to the cell parameter X by:

$$D_{\delta\gamma} = \frac{X}{2} \qquad \text{[B-26]}$$

Replacing X according to eq. B-17:

$$D_{\delta\gamma} = \frac{1}{2}\sqrt{\frac{A_\delta}{\alpha_\delta}} \qquad \text{[B-27]}$$

Inserting eq. B-10 gives:

$$D_{\delta\gamma} = \sqrt{\frac{L_\delta W_\delta}{\alpha_\delta}} \qquad \text{[B-28]}$$

and it is known that:

$$\tan\theta = \frac{V_{\gamma\perp}}{V_\delta} \qquad \text{[B-29]}$$

Solving for V_δ gives:

$$V_\delta = \frac{V_{\gamma\perp}}{\tan\theta} \qquad \text{[B-30]}$$

Finally, inserting eqs. B-28 and B-25 into B-30 reveals:

$$V_\delta \propto \frac{2L_\delta W_\delta C_M i_C}{b\tan\theta}\frac{K_I}{K_{IC}}\frac{1}{\alpha_\delta} \qquad \text{[B-31]}$$